HELMHOLTZ ZENTRUM
DRESDEN ROSSENDORF

ANNUAL REPORT 2020

Institute of Ion Beam Physics and Materials Research

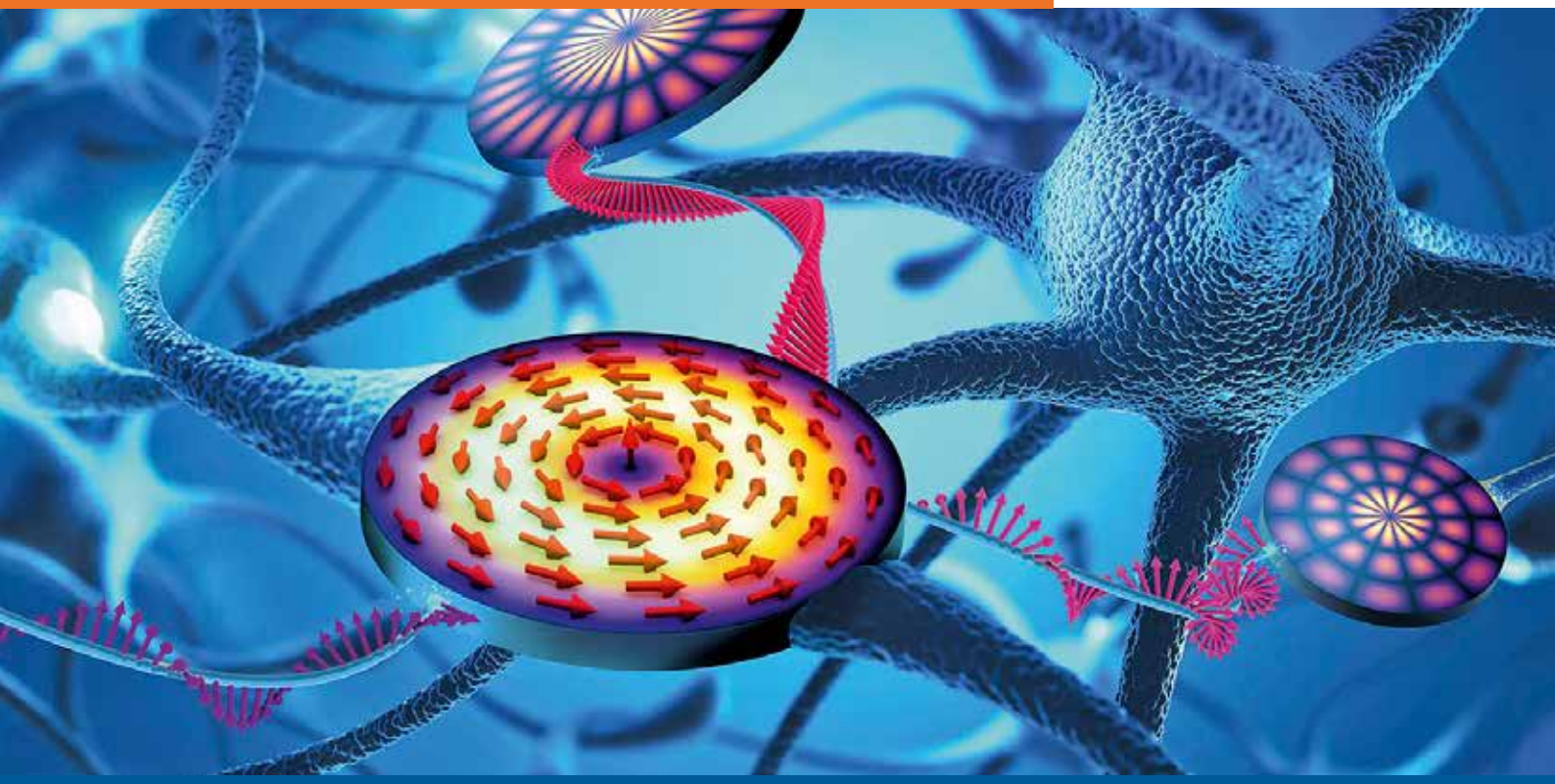

HZDR-112

Wissenschaftlich-Technische Berichte
HZDR–112

Annual Report 2020

Institute of Ion Beam Physics and Materials Research

Editors

J. Fassbender, M. Helm,
P. Zahn

HELMHOLTZ ZENTRUM
DRESDEN ROSSENDORF

Cover Picture - Spin waves in magnetic vortices as artificial neurons

As artificial intelligence (AI) and machine learning are employed in an increasing fashion to address modern-day problems, over the last decade, artificial neural networks have found their way into countless parts of our lives. These incredibly sophisticated networks are currently mostly software based, which, although they rely on state-of-the-art CMOS technology, limits their speed and leads to an ever-increasing energy consumption. To address these issues, current research efforts are exploring the possibilities of hardware-based neuromorphic computing, where typical AI applications, such as pattern recognition, are executed by some physical system. These physical systems need to be nonlinear and possess a so-called fading memory, which can be provided by internal damping.

Both of these qualities are perfectly met by magnons, the elementary excitations in ferromagnetic media. The illustration on the cover page schematically shows the magnons in small ferromagnetic disks interacting with each other. These disks are magnetized in a flux-closure (vortex) state. When excited with a large-enough microwave-field power, the magnons in such a vortex disk start to interact with each other in well-defined channels via a process called three-magnon splitting. This process can be controlled to great extent by stimulating it actively, for example, using the dynamic stray fields of magnons propagating in a waveguide adjacent to an individual vortex disk. Having well-defined, nonlinear and controllable scattering channels between them makes these magnons suitable candidates to serve as neurons, or as a nonlinear reservoir, for hardware-based neuromorphic computing.

For further information see:
L. Körber et al., **Nonlocal Stimulation of Three-Magnon Splitting in a Magnetic Vortex**, Phys. Rev. Lett. **125**, 207203 (2020), DOI: 10.1103/PhysRevLett.125.207203

Many thanks for providing material and for technical assistance to: S. Gebel, S. Kirch, S. Facsko, R. Heller, C. Schneider, L. Körber, and M. Zahn.

Print edition: ISSN 2191-8708
Electronic edition: ISSN 2191-8716

urn:nbn:de:bsz:d120-qucosa2-756331
www.hzdr.de/publications/Publ-32192
Published by Helmholtz-Zentrum Dresden - Rossendorf e.V.

This report is also available at https://www.hzdr.de/FWI.

Helmholtz-Zentrum Dresden - Rossendorf e.V.
Institute of Ion Beam Physics and Materials Research
Bautzner Landstraße 400
01328 Dresden
Germany

Directors	Prof. Dr. M. Helm	Prof. Dr. J. Fassbender
Phone	+49 351 260 2260	+49 351 260 3096
Fax	+49 351 260 3285	+49 351 260 3285
Email	m.helm@hzdr.de	j.fassbender@hzdr.de

Preface by the directors

As for everybody else also for the Institute of Ion Beam Physics and Materials Research (IIM), the COVID-19 pandemic overshadowed the usual scientific life in 2020. Starting in March, home office became the preferred working environment and the typical institute life was disrupted. After a little relaxation during summer and early fall, the situation became again more serious and in early December we had to severely restrict laboratory activities and the user operation of the Ion Beam Center (IBC). For the most part of 2020, user visits were impossible and the services delivered had to be performed hands-off. This led to a significant additional work load on the IBC staff. Thank you very much for your commitment during this difficult period. By now user operation has restarted, but we are still far from business as usual. Most lessons learnt deal with video conference systems, and everybody now has extensive experience in skype, teams, webex, zoom, or any other solution available. Conferences were cancelled, workshops postponed, and seminar or colloquia talks delivered online. Since experimental work was also impeded, maybe 2020 was a good year for writing publications and applying for external funding. In total, 204 articles have been published with an average impact factor of 6.95, which both mark an all-time high for the institute. 13 publications from last year are highlighted in this Annual Report to illustrate the wide scientific spectrum of our institute. In addition, 20 new projects funded by EU, DFG, BMWi/AiF and SAB with a total budget of about 5.7 M€ have started. Thank you very much for making this possible.

Also, in 2020 there have been a few personalia to be reported. Prof. Dr. Sibylle Gemming has left the HZDR and accepted a professor position at TU Chemnitz. Congratulations! The hence vacant position as the head of department was taken over by PD Dr. Artur Erbe by Oct. 1st. Simultaneously, the department has been renamed to “Nanoelectronics”. Dr. Alina Deac has left the institute in order to dedicate herself to new opportunities at the Dresden High Magnetic Field Laboratory. Dr. Matthias Posselt went to retirement after 36 years at the institute. We thank Matthias for his engagement and wish him all the best for the upcoming period of his life.

However, also new equipment has been setup and new laboratories founded. A new 100 kV accelerator is integrated into our low energy ion nanoengineering facility and complements our ion beam technology in the lower energy regime. This setup is particularly suited to perform ion implantation into 2D materials and medium energy ion scattering (MEIS).

Finally, we would like to cordially thank all partners, friends, and organizations who supported our progress in 2020. First and foremost we thank the Executive Board of the Helmholtz-Zentrum Dresden-Rossendorf, the Minister of Science and Arts of the Free State of Saxony, and the Ministers of Education and Research, and of Economic Affairs and Energy of the Federal Government of Germany. Many partners from universities, industry and research institutes all around the world contributed essentially, and play a crucial role for the further development of the institute. Last but not least, the directors would like to thank all members of our institute for their efforts in these very special times and excellent contributions in 2020.

Prof. Manfred Helm

Prof. Jürgen Fassbender

Contents

Selected Publications

Statistics

Selected Publications

Image: HZDR / R. Yankov († 2021)

Copyright remarks

The following journal articles and abstracts are reprinted with kind permission from:

Demonstration of a Broadband Photodetector Based on a Two-Dimensional Metal–Organic Framework
Arora, H.; Dong, R.; Venanzi, T.; Zscharschuch, J.; Schneider, H.; Helm, M.; Feng, X.; Cánovas, E.; Erbe, A.;
Advanced Materials **32**, 1907063 (2020)

DOI: 10.1002/adma.201907063

Alkali metals inside bi-layer graphene and MoS_2: Insights from first-principles calculations
Chepkasov, I.V.; Ghorbani-Asl, M.; Popov, Z.I.; Smet, J.H.; Krasheninnikov, A.K.
Nano Energy **75**, 104927 (2020)

DOI: 10.1016/j.nanoen.2020.104927

Helium Ion Microscopy for Reduced Spin Orbit Torque Switching Currents
Dunne, P.; Fowley, C.; Hlawacek, G.; Kurian, J.; Atcheson, G.; Colis, S.; Teichert, N.; Kundys, B.; Venkatesan, M.; Lindner, J.; Deac, A.M.; Hermans, T.M.; Coey, J.M.D.; Doudin, B.
Nano Letters **20**, 7036 (2020)

DOI: 10.1021/acs.nanolett.0c02060

Engineering telecom single-photon emitters in silicon for scalable quantum photonics
Hollenbach, M.; Berencen, Y.; Kentsch, U.; Helm, M.; Astakhov, G.V.
Optics Express **28** (18), 26111 (2020)

DOI: 10.1364/OE.397377

Nonlocal Stimulation of Three-Magnon Splitting in a Magnetic Vortex
Körber, L.; Schultheiss, K.; Hula, T.; Verba, R.; Fassbender, J.; Kákay, A.; Schultheiss, H.
Physical Review Letters **125**, 207203 (2020)

DOI: 10.1103/PhysRevLett.125.207203

Curvilinear One-Dimensional Antiferromagnets
Pylypovskyi, O.V.; Kononenko, D.Y.; Yershov, K.V.; Rößler, U.K.; Tomilo, A.V.; Fassbender, J.; van den Brink, J.; Makarov, D.; Sheka, D.D.
Nano Letters **20**, 8157 (2020)

DOI: 10.1021/acs.nanolett.0c03246

Up to 70 THz bandwidth from an implanted Ge photoconductive antenna excited by a femtosecond Er:fibre laser
Singh, A.; Pashkin, A.; Winnerl, S.; Welsch, M.; Beckh, C.; Sulzer, P.; Leitenstorfer, A.; Helm, M.; Schneider, H.
Light: Science & Applications **9**, 30 (2020)

DOI: 10.1038/s41377-020-0265-4

^{60}Fe deposition during the late Pleistocene and the Holocene echoes past supernova activity
Wallner, A.; Feige, J.; Fifield, L.K.; Froehlich, M.B.; Golser, R.; Hotchkis, M.A.C.; Koll, D.; Leckenby, G.; Martschini, M.; Merchel, S.; Panjkov, S.; Pavetich, S.; Rugel, G.; Tims, S.G.
PNAS **117** (36), 21873 (2020)

DOI:10.1073/pnas.1916769117

Intrinsic plasticity of silicon nanowire neurotransistors for dynamic memory and learning functions
Baek, E.; Das, N.R.; Cannistraci, C.V.; Rim, T.; Cañón Bermúdez, G.S.; Nych, K.; Cho, H.; Kim, K.; Baek, C.-K.; Makarov, D.; Tetzlaff, R.; Chua, L.; Baraban, L.; Cuniberti, G.
Nature Electronics **3**, 398 (2020)

DOI: 10.1038/s41928-020-0412-1

Efficient Modulation of Photonic Bandgap and Defect Modes in All-Dielectric Photonic Crystals by Energetic Ion Beams
Du, G.; Zhou, X.; Pang, C.; Zhang, K.; Zhao, Y.; Lu, G.; Liu, F.; Wu, A.; Akhmadaliev, S.; Zhou, S.; Chen, F.
Advanced Optical Materials **8**, 2000426 (2020)

DOI: 10.1002/adom.202000426

Engineering Self-Supported Noble Metal Foams Toward Electrocatalysis and Beyond
Du, R.; Jin, X.; Hübner, R.; Fan, W.; Hu, Y.; Eychmüller, A.
Advanced Energy Materials **10**, 1901945 (2020)

DOI: 10.1002/aenm.201901945

Inertial spin dynamics in ferromagnets
Neeraj, K.; Awari, N.; Kovalev, S.; Polley, D.; Zhou Hagström, N.; Arekapudi, S.S.P.K.; Semisalova, A.; Lenz, K.; Green, B.; Deinert, J.-C.; Ilyakov, I.; Chen, M.; Bawatna, M.; Scalera, V.; d'Aquino, M.; Serpico, C.; Hellwig, O.; Wegrowe, J.-E.; Gensch, M.; Bonetti, S.
Nature Physics **17**, 245 (2021)

DOI: 10.1038/s41567-020-01040-y

Direct nanoscopic observation of plasma waves in the channel of a graphene field-effect transistor
Soltani, A.; Kuschewski, F.; Bonmann, M.; Generalov, A.; Vorobiev, A.; Ludwig, F.; Wiecha, M.M.; Čibiraitė, D.; Walla, F.; Winnerl, S.; Kehr, S.C.; Eng, L.M.; Stake, J.; Roskos, H.G.
Light: Science & Applications **9**, 97 (2020)

DOI: 10.1038/s41377-020-0321-0

COMMUNICATION

ADVANCED MATERIALS
www.advmat.de

Demonstration of a Broadband Photodetector Based on a Two-Dimensional Metal–Organic Framework

Himani Arora, Renhao Dong, Tommaso Venanzi, Jens Zscharschuch, Harald Schneider, Manfred Helm, Xinliang Feng, Enrique Cánovas,* and Artur Erbe**

Metal–organic frameworks (MOFs) are emerging as an appealing class of highly tailorable electrically conducting materials with potential applications in optoelectronics. Yet, the realization of their proof-of-concept devices remains a daunting challenge, attributed to their poor electrical properties. Following recent work on a semiconducting $Fe_3(THT)_2(NH_4)_3$ (THT: 2,3,6,7,10,11-triphenylenehexathiol) 2D MOF with record-high mobility and band-like charge transport, here, an $Fe_3(THT)_2(NH_4)_3$ MOF-based photodetector operating in photoconductive mode capable of detecting a broad wavelength range from UV to NIR (400–1575 nm) is demonstrated. The narrow IR bandgap of the active layer (≈0.45 eV) constrains the performance of the photodetector at room temperature by band-to-band thermal excitation of charge carriers. At 77 K, the device performance is significantly improved; two orders of magnitude higher voltage responsivity, lower noise equivalent power, and higher specific detectivity of 7×10^8 cm $Hz^{1/2}$ W^{-1} are achieved under 785 nm excitation. These figures of merit are retained over the analyzed spectral region (400–1575 nm) and are commensurate to those obtained with the first demonstrations of graphene- and black-phosphorus-based photodetectors. This work demonstrates the feasibility of integrating conjugated MOFs as an active element into broadband photodetectors, thus bridging the gap between materials' synthesis and technological applications.

Metal–organic frameworks (MOFs) represent a class of hybrid materials, where metal ions or clusters coordinate with organic linkers to form long-range ordered crystalline structures.[1] Due to their tunable porosity, large surface-to-volume ratios (up to 90% free volume) have been developed,[2–5] as a result MOFs have been primarily considered for applications in gas storage/separation,[6–8] catalysis,[9,10] and drug delivery[11,12] so far.

Though the majority of MOFs are known to be electrical insulators, advances in synthetic approaches over the past decade have revealed several examples of (semi)conductive MOFs,[13–25] an aspect that allows their use in (opto)electronic applications as an active element. While some works demonstrate their semiconducting behavior,[15–18] others have revealed them behaving as either metals or semimetals,[21,24–26] that is, lacking a bandgap. Among them, graphene-like MOF analogues, where 2D hexagonal lattices are obtained from trigonal organic ligands coordinated by square-planar atomic metal nodes, have emerged as a unique sub-class of electrically conducting materials. In general, these 2D MOF samples display a variety of electrical properties, which can be linked to intrinsic and/or extrinsic factors. In most cases, the samples are produced in powder form, and later pressed into pellets to characterize their conductive properties as a function of temperature. Broadly speaking, most works revealed thermally activated charge transport mechanisms and low charge carrier mobilities, which might be (to a large extent) linked to the polycrystalline nature of the produced pellets. MOFs with such features are particularly unsuitable for device prototyping, where large-area MOF thin films displaying semiconducting properties (with a defined bandgap) and delocalized charge carrier transport are required. These ideal features for device development were recently reported by us on a novel semiconducting $Fe_3(THT)_2(NH_4)_3$ (THT: 2,3,6,7,10,11-triphenylenehexathiol) 2D MOF produced by an interfacial synthesis

H. Arora, T. Venanzi, J. Zscharschuch, Dr. H. Schneider, Prof. M. Helm, Dr. A. Erbe
Institute of Ion Beam Physics and Materials Research
Helmholtz-Zentrum Dresden-Rossendorf
Dresden 01328, Germany
E-mail: h.arora@hzdr.de; a.erbe@hzdr.de

The ORCID identification number(s) for the author(s) of this article can be found under https://doi.org/10.1002/adma.201907063.

DOI: 10.1002/adma.201907063

H. Arora, T. Venanzi, Prof. M. Helm
Faculty of Physics and Center for Advancing Electronics Dresden
Technische Universität Dresden
Dresden 01062, Germany

Dr. R. Dong, Prof. X. Feng
Faculty of Chemistry and Food Chemistry and Center for Advancing Electronics Dresden
Technische Universität Dresden
Dresden 01062, Germany

Dr. E. Cánovas
Instituto Madrileño de Estudios Avanzados en Nanociencia (IMDEA Nanociencia)
Madrid 28049, Spain
E-mail: enrique.canovas@imdea.org

ADVANCED SCIENCE NEWS
www.advancedsciencenews.com
ADVANCED MATERIALS
www.advmat.de

protocol (ref. [17]). A spontaneous reaction at the $CHCl_3$/water interface allows the formation of large-area free-standing multilayered films with tunable thicknesses that can be readily controlled. More importantly, these samples are characterized by a direct bandgap in the IR region and a charge carrier mobility of 230 $cm^2 V^{-1} s^{-1}$ at room temperature (measured by Hall-effect over channel lengths of few hundreds micrometers). These appealing characteristics of the reported samples open the path to exploiting them as active elements in optoelectronic devices.

In this work, we demonstrate the ability of free-standing 2D MOF films of $Fe_3(THT)_2(NH_4)_3$ to serve as an active element in a two-terminal photodetector device. Changes in device conductance are revealed upon light exposure ranging from UV to NIR wavelengths (400–1575 nm). Temperature-dependent photocurrent measurements demonstrate that the photodetector shows a stronger photoresponse and higher sensitivity at liquid nitrogen temperatures (77 K) than at room temperature. In addition, a drastic improvement in photodetector's figures of merit, such as photosensitivity (defined as the ratio of photocurrent to dark current), voltage responsivity (R_v), noise equivalent power (NEP) and specific detectivity (D^*), is achieved on cooling the devices to 77 K. These results are consistent with the low IR bandgap of the samples, which causes strong thermally activated band-to-band population of free charge carriers at room temperature, described by $N \propto \exp[-E_g/2kT]$. Cooling the devices suppresses this thermal generation of charge carriers, which consequently leads to much improved device performance. Furthermore, the devices show stable and reproducible photoswitching behavior as a function of time. To the best of our knowledge, such broadband photoresponse is being reported for the first time for an entirely 2D MOF-based photodetector and demonstrates a reliable and robust device.

The thin films of $Fe_3(THT)_2(NH_4)_3$ are synthesized by a spontaneous reaction at the $CHCl_3$/water interface hosting iron precursors and THT, respectively, under argon atmosphere at room temperature. Depending on the reaction time, the film thickness can be widely tailored, from 20 nm up to several µm. An in-depth characterization and analysis of the material's structure has confirmed the high-quality polycrystalline nature of as-prepared $Fe_3(THT)_2(NH_4)_3$ MOF films as reported in our previous work (ref. [17]) (note that a detailed summary of the results obtained from characterization and analysis of the material's structure and electronic properties is provided in Supporting Information). Structurally, a monolayer of $Fe_3(THT)_2(NH_4)_3$ MOF film (shown in **Figure 1**a) possesses a planar hexagonal geometry extended into two directions, thus, forming a 2D network. Within a monolayer, the Fe metal and THT organic ligands are bonded in a honeycomb structure with a pore size of ≈1.9 nm, as shown in Figure 1b. When these 2D monolayers superimpose via van der Waals interactions, flat and crack-free multilayered structures with typical lateral dimensions of few millimeters are formed. In this study, free-standing 1.7 µm thick MOF films are used to fabricate the photodetector devices. As revealed by the Tauc plot in Figure 1c, the samples are characterized by a direct bandgap with an absorption edge of ≈0.45 eV. A two-terminal device (schematic in Figure 1d) is fabricated from a MOF flake bonded to an insulating glass substrate by using high-quality indium metal electrodes (chemPUR, 99.99% purity). The optical micrographs of actual devices are shown in Figure S1, Supporting Information. The device consists of a 1.7 µm thick MOF layer with an active area $A \approx 0.7$ mm^2, defined by channel length $L \approx 1$ mm, and width $W \approx 0.7$ mm.

The photoresponse of the developed MOF-based photodetector is initially characterized under 785 nm laser irradiation,

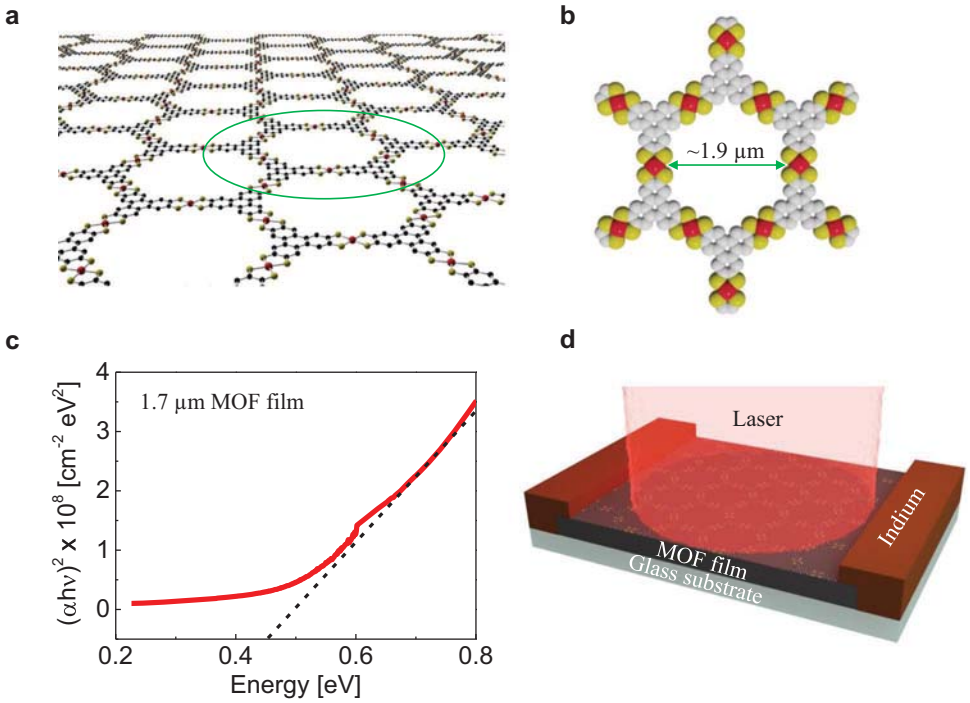

Figure 1. Material description and device fabrication. a) Schematic of a monolayer of $Fe_3(THT)_2(NH_4)_3$ 2D MOF film investigated in this study. b) Chemical structure of the MOF film, Fe metal and THT organic ligands are bonded via sulfur in a honeycomb structure with a pore size of ≈1.9 nm. Color code: red spheres represent iron atoms, yellow refers to sulfur atoms, and gray represents benzene rings. c) Tauc plot for 1.7 µm thick MOF film at room temperature, revealing an optical bandgap of ≈0.45 eV. d) Schematic of a two-terminal photodetector device based on 1.7 µm thick MOF layer with indium electrodes.

ADVANCED SCIENCE NEWS
www.advancedsciencenews.com
ADVANCED MATERIALS
www.advmat.de

and subsequently at 405, 633, and 1575 nm, at various power settings. The spot size of the laser is ≈2 mm in diameter, assuring full illumination of the device active area. All electrical characterizations, with and without illumination, are carried out in vacuum (<10^{-7} mbar) by applying a sweeping bias of ± 1 V in the temperature range of 77–300 K. For the whole temperature range, all analyzed MOF-devices are found to yield hysteresis-free current–voltage (*I*–*V*) characteristics, both in dark condition and under illumination.

Figure 2a,b shows the *I*–*V* characteristics of the MOF-device as a function of incident laser power densities (*P*) at 785 nm at 300 and 77 K, respectively. Both curves reveal an increase in the photocurrent with increasing photon density, demonstrating the operation of the active MOF layer as a photoconductor at both temperatures. In order to precisely interrogate the effect of temperature on the performance of the photodetector, we measured the photoresponse of the sample in the temperature range of 77–300 K under various fluences of 785 nm illumination. Figure 2c shows current (at a bias of –1 V) as a function of inverse temperature (1/*T*) measured in dark (black curve) and under different 785 nm light intensities ranging from 0.026 (red curve) to 0.60 (orange curve) W cm^{-2} (*I*–*V* curves measured in dark in the temperature range of 77–300 K are shown in Figure S2, Supporting Information). The obtained trend is consistent with the narrow IR bandgap of the samples, enabling thermally activated charge carrier population of the conduction and valence bands at higher temperatures (in agreement with our previous findings, where the 1.7 µm thick sample revealed a thermally activated carrier density population, described by $N \propto \exp[-E_g/2kT]$. From Hall measurements, a charge density of 6.2×10^{14} cm^{-3} was obtained at 300 K, which decreased to 2.0×10^{11} cm^{-3} at 100 K, ref. [17]). On fitting the exponential function, an activation energy of 0.35 ± 0.1 eV is extracted from *I* versus 1/*T* plot, which is comparable to the optical bandgap of 0.45 eV resolved for the samples. At higher temperatures ($T \geq 200$ K), the increase of thermally induced electronic transitions across the narrow bandgap results in larger dark currents, overshadowing the detection of optically generated

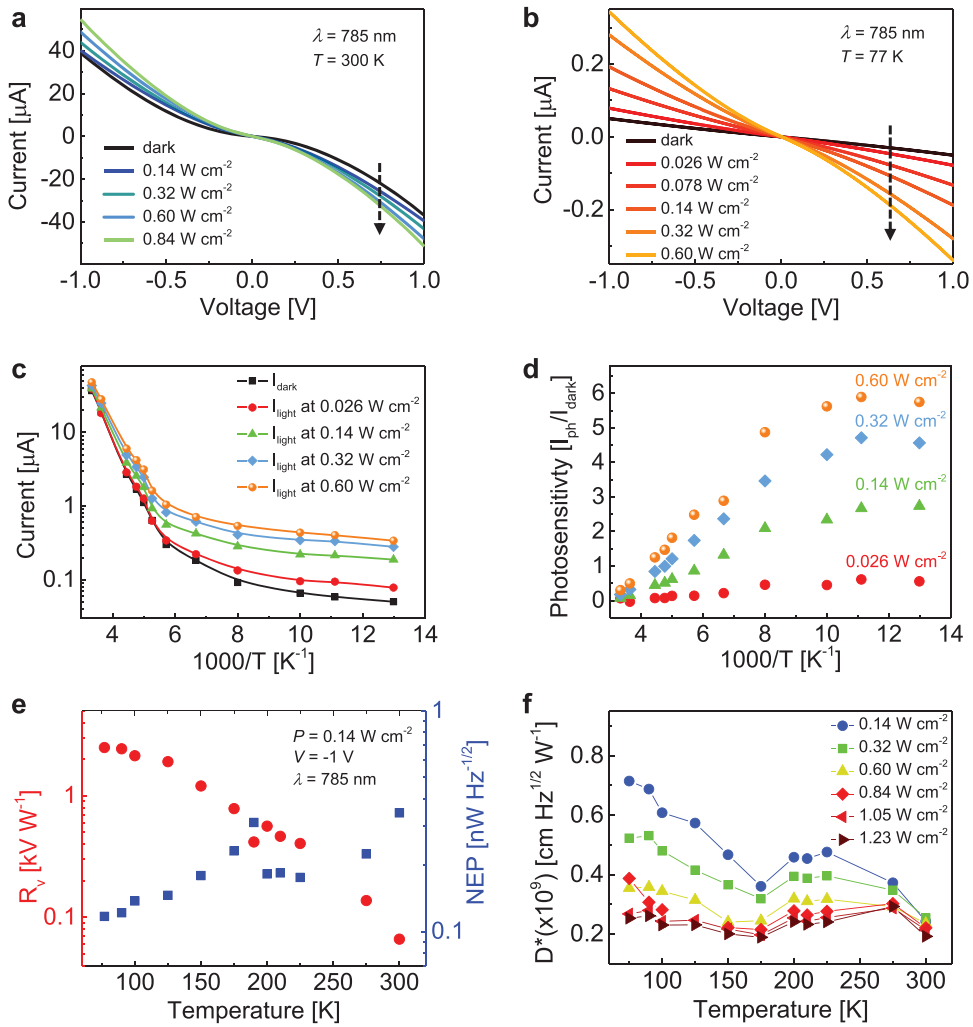

Figure 2. Device characterization under 785 nm illumination. a,b) *I*–*V* curves for different power densities of 785 nm wavelength at 300 and 77 K, respectively. c) Temperature dependence of current in dark (I_{dark}) and under illumination (I_{light}) for various power densities at a bias of –1 V. d) Photosensitivity (I_{ph}/I_{dark}) versus temperature at various laser power densities at an applied bias of –1 V. e) Temperature dependence of voltage responsivity and NEP at $P = 0.14$ W cm^{-2} and –1 V bias. f) Temperature dependence of detectivity at –1 V bias at various power densities.

ADVANCED SCIENCE NEWS
www.advancedsciencenews.com
ADVANCED MATERIALS
www.advmat.de

charge carriers upon light illumination. This reverses at lower temperatures (77 K ≤ T < 200 K) where photocurrent tends to remain constant and clearly dominates the dark current. In the low temperature range, the photodetector performance is, thus, governed mainly by optically generated charge carriers for the analyzed range of incident laser powers. To quantify these effects, photodetector photosensitivity (I_{ph}/I_{dark})[27,28] is plotted as a function of inverse temperature (Figure 2d). The photosensitivity is found to increase significantly with decreasing temperature; 6 at 77 K as opposed to 0.3 at 300 K (P = 0.60 W cm^{-2}, λ = 785 nm). While a notable change in the photosensitivity is observed at 77 K even for a low power density of 0.026 W cm^{-2}, at 300 K there is no measurable photocurrent until the incident power is increased tenfold, further affirming the improved performance at lower temperatures. In addition, photosensitivity also increases with laser power density, correlating to improved photocurrent generation. To reveal the device performance, we characterized other important figures of merit including responsivity, NEP, and D^*. Due to the linear and symmetric I–V characteristics, the MOF-photodetector operates in photoconductive mode. In a photoconductor, the absorption quantum efficiency (η_{abs}) can be defined as a function of absorption coefficient (α) and thickness of the active layer (t), $\eta_{abs} = (1 - r)(1 - \exp(-\alpha t))$, where r accounts for surface reflection losses.[29,30] From the estimated reflection losses of 5% ± 1% and α = 24 900 ± 3000 cm^{-1} (extracted from the Tauc plot in Figure 1c at λ = 866 nm), η_{abs} of 94% ± 1% is obtained for the 1.7 µm thick MOF-device. Assuming that all absorbed photons contribute to the photocurrent, the quantum efficiency η is considered the same as the absorption quantum efficiency, that is, $\eta = \eta_{abs}$. Since the Fourier-transform infrared spectroscopy (FTIR) measurements reveal an invariant and high absorption over the UV–NIR spectral region (reported elsewhere, ref. [17]), the absorption coefficient estimated above can be applied to the whole analyzed spectral range. The responsivity ($R = I_{ph}/(P \times A)$; P is incident power density, A is exposed device area)[31] is found to be 4 mA W^{-1} at 300 K (λ = 785 nm, P = 0.14 W cm^{-2}, V = −1 V), which is comparable to the values obtained for the first demonstrations of photodetectors based on black phosphorus (4.8 mA W^{-1})[32] and graphene (<6 mA W^{-1}).[33,34] However, in the present device configuration, responsivity is strongly dependent on device geometry and can vary significantly with the active area of the photodetector.[35] In this respect, we further analyzed the voltage responsivity R_v, defined as the change in voltage drop per unit incident power across the detector, since R_v is independent of the device area.[30] At low incident powers, it can be expressed as $R_v = (R \times V)/I_{dark}$, giving rise to R_v = 2.5 and 0.07 kV W^{-1} at 77 and 300 K, respectively. The temperature dependence of R_v is plotted in Figure 2e and shows a continuous increase with decreasing temperature. Another important parameter to evaluate the performance of the photodetector is NEP. It is defined as the detection limit of the photodetector and is a function of the detector's noise level, expressed as

$$\mathrm{NEP} = \frac{\overline{I_n^2}^{1/2}}{R} \tag{1}$$

where R is the responsivity and $\overline{I_n^2}^{1/2}$ is the root mean square of the total noise current.[36,37] The fundamental noise sources in a photoconductor are Johnson noise (I_j), generation–recombination (G–R) noise (I_{gr}), and $1/f$ noise (I_f), the latter being dominant at low frequencies.[29,30] From the photocurrent measurements, the Johnson noise is calculated as $[4kT\Delta f/R_d]^{1/2}$, where k is the Boltzmann constant, T is the absolute temperature, Δf is the bandwidth and R_d is the resistance of the device.[29,30] For the MOF-device, the values of I_j are found to be 7.81 × 10^{-13} A Hz$^{-1/2}$ at 300 K, which decreases to 1.44 × 10^{-14} A Hz$^{-1/2}$ at 77 K (P = 0.14 W cm^{-2}, λ = 785 nm). The G–R noise, calculated as $[4qGI_{dark}\Delta f]^{1/2}$, where q is the electronic charge, and G is the photoconductive gain (calculated as $G = Rhc/\eta q\lambda$),[30,38] is found to be ranging from 3.11 × 10^{-13} at 300 K to 2.60 × 10^{-15} A Hz$^{-1/2}$ at 77 K. While the Johnson noise and the G–R noise estimations are straightforward, the $1/f$ noise is difficult to analyze analytically and is currently out of the scope of this work. Therefore, only Johnson noise and G–R noise are considered for the calculation of NEP. An NEP value as low as possible is desirable for an efficient and sensitive photodetector, which for $Fe_3(THT)_2(NH_4)_3$ MOF-photodetectors is achieved by lowering the operating temperature (Figure 2e). Finally, we investigated the influence of temperature on the D^*, a measure of normalized signal-to-noise performance. D^* is derived by normalizing the inverse of NEP by detector area (A), $D^* = A^{1/2}/\mathrm{NEP}$, for various laser power densities.[37,39]

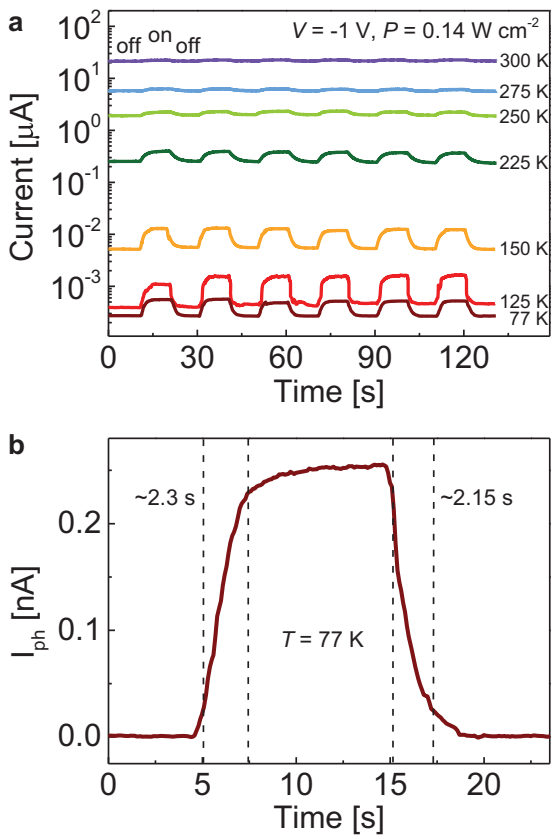

Figure 3. Photoswitching behavior under pulsed illumination of 785 nm laser. a) Temperature-dependent photoresponse as a function of time at P = 0.14 W cm^{-2} and V = −1 V. The device shows long-term stable photoswitching capability. b) Time-resolved response zoomed, for 77 K, showing a response time of ≈2 s.

ADVANCED SCIENCE NEWS
www.advancedsciencenews.com
ADVANCED MATERIALS
www.advmat.de

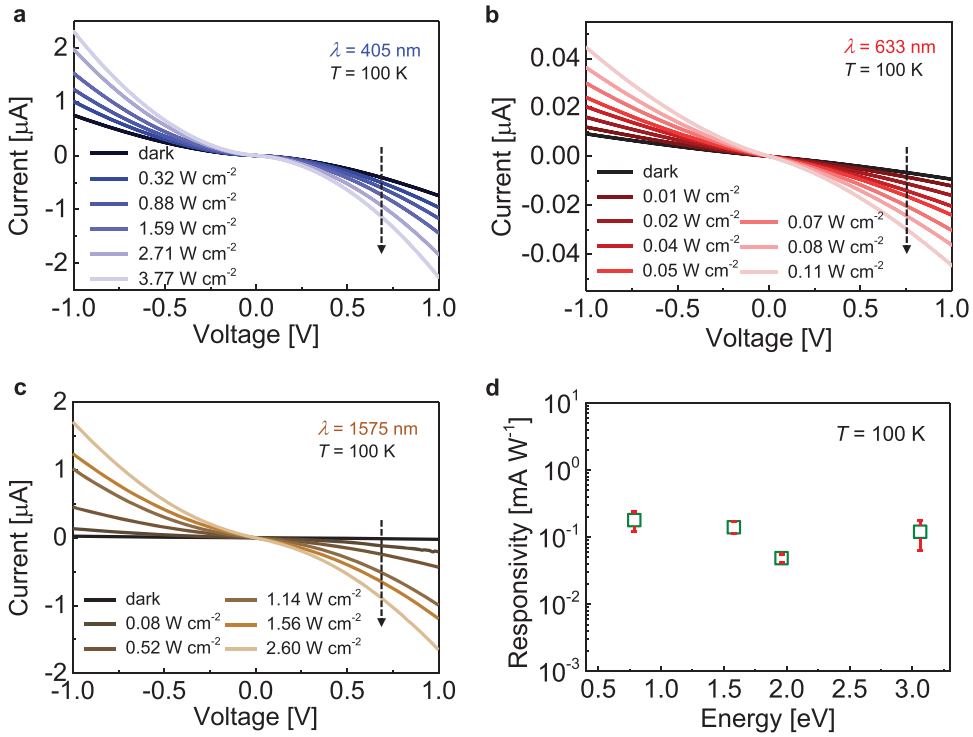

Figure 4. a–c) Photoresponse of the MOF detector at 100 K at 405 nm (a), 633 nm (b), and 1575 nm (c). d) Responsivity as a function of photon energy at a constant laser power density $P = 0.14$ W cm^{-2} and $T = 100$ K.

Figure 2f shows an increase in D^* of the photodetector as the temperature decreases, with a peak D^* of 7×10^8 cm Hz$^{1/2}$ W^{-1} achieved at 77 K. It should be noted that the estimated NEP values (and hence, D^*) depend on the assumption that all absorbed photons generate free charge carriers. There is a possibility that a part of the absorption is "parasitic", that is, some photons are lost without contributing to any photocurrent, leading to additional (typically, $1/f$) noise. Such a scenario would imply a higher gain, larger NEP, and smaller D^* values. Since this scenario is currently neglected, the estimations of NEP and D^* are valid only under the assumptions that the total noise comprises of only Johnson noise and G–R noise, and that the quantum efficiency equals the absorption efficiency. Therefore, our calculations provide a lower limit estimate of NEP and an upper limit of D^* values for the developed MOF-photodetectors.

The photoswitching performance of the MOF-photodetector is evaluated by testing the response of the MOF-device to light/dark cycles of illumination at 785 nm at various temperatures. Irrespective of temperature, a strong and reproducible switching behavior is revealed in **Figure 3**a, which demonstrates a stable operation of the MOF-device under pulsed irradiation. The response times for both rise and decay processes are extracted from the data as the time required by the photodetector to reach from 10% to 90% of the peak photocurrent after the illumination is turned on and vice versa after it is turned off, respectively.[31,32] From Figure 3b, the rise and decay times at 77 K are found to be 2.3 and 2.15 s, respectively, an increase from ≈1.7 s for both at 300 K. On testing multiple samples, response times in the range of 1–3 s are obtained. These response times are affected severely by the types and density of defects either intrinsic to the material and/or arising during device fabrication processes.[28,39,40] Previous reports have shown that by modulating these defects in a controlled manner, faster response times can be achieved.[28,39–42] A brief discussion of potential defects present in our samples and ways to mitigate them is included in Supporting Information.

The spectral response of the MOF-photodetector at other wavelengths is tested by laser irradiations at wavelengths of 405, 633, and 1575 nm. The results obtained at these wavelengths are summarized in **Figure 4**a–c. An enhancement of the current at all wavelengths confirms the broadband photodetection operation in the UV-to-NIR range. The photocurrent (I_{ph}) increases with the laser power density (P) in accordance with the power law, $I_{ph} \propto P^{\gamma}$ with the exponent (γ) ranging 0.92 ± 0.09 for all analyzed wavelengths. Temperature-dependent photocurrent and photoswitching measurements performed at these wavelengths are shown in Figures S3–S5, Supporting Information. These results further confirm the improvement in the detector's performance, once it is cooled to lower temperatures. While the response time lies in the range of 1–3 s, the detector demonstrates a stable and reproducible photoswitching behavior in the analyzed spectral range. The responsivity calculated for all impinging wavelengths at 100 K is plotted in Figure 4d. Since $Fe_3(THT)_2(NH_4)_3$ MOF has high absorption in the UV–NIR region, no significant change in the quantum efficiency at these wavelengths is expected, which is consistent with the observed wavelength-independent responsivity. At these wavelengths, NEP and D^* are calculated by using the approach described before. The NEP values at 100 K ($P = 0.14$ W cm^{-2}, $V = -1$ V) are found to be 2.8 nW Hz$^{-1/2}$ (405 nm), 0.33 nW Hz$^{-1/2}$ (633 nm), and 0.07 nW Hz$^{-1/2}$ (1575 nm). The corresponding D^* values are estimated to be

ADVANCED SCIENCE NEWS
www.advancedsciencenews.com

ADVANCED MATERIALS
www.advmat.de

3×10^7 cm $Hz^{1/2}$ W^{-1} (405 nm), 3×10^8 cm $Hz^{1/2}$ W^{-1} (633 nm), and 2×10^9 cm $Hz^{1/2}$ W^{-1} (1575 nm).

In summary, this work reports a proof-of-concept photodetector device based on semiconducting $Fe_3(THT)_2(NH_4)_3$ 2D MOF films operating in a broad spectral range (400–1575 nm). A systematic study of the photoresponse dependence on temperature, wavelength, and incident laser power is carried out for the first time to fully address the performance of the MOF-device. Significant improvements in the performance of the device are achieved by cooling the detector to lower temperatures, due to the suppression of thermally activated charge carriers. While our findings show a promising future for MOF-based photodetection, opportunities for further improvements by optimizing the device configuration, fabrication of reliable contacts, and structural engineering of the material still exist. Owing to synthetic flexibility, large-area coverage, and cost-effective production of 2D conjugated MOFs, these materials are promising candidates for a plethora of optoelectronic applications.

Experimental Section

FTIR Measurements: FTIR was performed using a Bruker Vertex 80v spectrometer. The spectral range was from 0.20 to 1.44 eV. The infrared source was a Globar. The thermal radiation emitted from the Globar was focused on the sample with a spot of around 2×2 mm^2. A nitrogen-cooled MCT was used as the detector.

Optoelectronic Properties Measurements: Low-temperature photocurrent measurements were performed in a cryogenic probe station (Lake Shore Model CPX-VF) equipped with a continuous-wave (cw)-laser diode at 405, 633, and 785 nm wavelengths (Toptica ultra compact diode laser, IBEAM-SMART-S). The laser was coupled with an optical fiber (FC/APC), which was connected to a vacuum feed through adapter inside the probe station to illuminate the samples. For all measurements, the fiber tip was kept orthogonal and at a fixed distance from the sample. The features of the laser were controlled by a software provided by Toptica. The IR measurements were performed under direct illumination of a 1575 nm wavelength InP laser diode (Thor Labs, L1575G1), controlled by an external power supply. All electrical measurements were carried out in vacuum ($<10^{-7}$ mbar) using a parameter analyzer (Agilent 4156C). The photoresponse was measured at regular temperature intervals while cooling down from 300 to 77 K.

Supporting Information

Supporting Information is available from the Wiley Online Library or from the author.

Acknowledgements

The authors thank S. Winnerl for subject matter discussion and J. Franke for drawing the schematics. E.C. acknowledges financial support from the Max Planck Society, the regional government of Comunidad de Madrid under projects 2017-T1/AMB-5207 & P2018/NMT-4511 and support from the "Severo Ochoa" Programme for Centres of Excellence in R&D (MINECO, Grant No. SEV-2016-0686). R.D. acknowledges the financial support from ERC Starting Grant (FC2DMOF, No. 852909), Coordination Networks: Building Blocks for Functional Systems (SPP 1928, COORNET), and MSCA-ITN-ETN (ULTIMATE, 813036). This work was supported by the Initiative and Networking Fund of the Helmholtz Association of German Research Centers through the International Helmholtz Research School for Nanoelectronic Networks, IHRS NANONET (VH-KO-606).

Conflict of Interest

The authors declare no conflict of interest.

Keywords

2D semiconductors, broadband photodetectors, low-temperature photodetection, metal–organic frameworks, photosensitivity

Received: October 28, 2019
Revised: December 14, 2019
Published online: January 23, 2020

[1] H. Li, M. Eddaoudi, M. O'Keeffe, O. M. Yaghi, *Nature* **1999**, *402*, 276.
[2] H. Deng, S. Grunder, K. E. Cordova, C. Valente, H. Furukawa, M. Hmadeh, F. Gándara, A. C. Whalley, Z. Liu, S. Asahina, H. Kazumori, M. O'Keeffe, O. Terasaki, J. F. Stoddart, O. M. Yaghi, *Science* **2012**, *336*, 1018.
[3] O. K. Farha, I. Eryazici, N. C. Jeong, B. G. Hauser, C. E. Wilmer, A. A. Sarjeant, R. Q. Snurr, S. T. Nguyen, A. Ö. Yazaydin, J. T. Hupp, *J. Am. Chem. Soc.* **2012**, *134*, 15016.
[4] O. K. Farha, A. Ö. Yazaydin, I. Eryazici, C. D. Malliakas, B. G. Hauser, M. G. Kanatzidis, S. T. Nguyen, R. Q. Snurr, J. T. Hupp, *Nat. Chem.* **2010**, *2*, 944.
[5] Q. L. Zhu, Q. Xu, *Chem. Soc. Rev.* **2014**, *43*, 5468.
[6] D. Farrusseng, *Metal-Organic Frameworks: Applications from Catalysis to Gas Storage*, John Wiley & Sons, Hoboken, NJ, USA **2011**.
[7] M. Eddaoudi, J. Kim, N. Rosi, D. Vodak, J. Wachter, M. O'Keeffe, O. M. Yaghi, *Science* **2002**, *295*, 469.
[8] Z. Chen, K. Adil, Ł. J. Weseliński, Y. Belmabkhout, M. Eddaoudi, *J. Mater. Chem. A* **2015**, *3*, 6276.
[9] F. X. Llabrés i Xamena, A. Abad, A. Corma, H. Garcia, *J. Catal.* **2007**, *250*, 294.
[10] J. Lee, O. K. Farha, J. Roberts, K. A. Scheidt, S. T. Nguyen, J. T. Hupp, *Chem. Soc. Rev.* **2009**, *38*, 1450.
[11] P. Horcajada, C. Serre, M. Vallet-Regí, M. Sebban, F. Taulelle, G. Férey, *Angew. Chem., Int. Ed.* **2006**, *45*, 5974.
[12] M. X. Wu, Y. W. Yang, *Adv. Mater.* **2017**, *29*, 1606134.
[13] M. G. Campbell, D. Sheberla, S. F. Liu, T. M. Swager, M. Dincă, *Angew. Chem., Int. Ed.* **2015**, *54*, 4349.
[14] M. G. Campbell, S. F. Liu, T. M. Swager, M. Dincă, *J. Am. Chem. Soc.* **2015**, *137*, 13780.
[15] G. Wu, J. Huang, Y. Zang, J. He, G. Xu, *J. Am. Chem. Soc.* **2017**, *139*, 1360.
[16] C. Yang, R. Dong, M. Wang, P. S. Petkov, Z. Zhang, M. Wang, P. Han, M. Ballabio, S. A. Bräuninger, Z. Liao, J. Zhang, F. Schwotzer, E. Zschech, H. H. Klauss, E. Cánovas, S. Kaskel, M. Bonn, S. Zhou, T. Heine, X. Feng, *Nat. Commun.* **2019**, *10*, 3260.
[17] R. Dong, P. Han, H. Arora, M. Ballabio, M. Karakus, Z. Zhang, C. Shekhar, P. Adler, P. S. Petkov, A. Erbe, S. C. B. Mannsfeld, C. Felser, T. Heine, M. Bonn, X. Feng, E. Cánovas, *Nat. Mater.* **2018**, *17*, 1027.
[18] R. Dong, Z. Zhang, D. C. Tranca, S. Zhou, M. Wang, P. Adler, Z. Liao, F. Liu, Y. Sun, W. Shi, Z. Zhang, E. Zschech, S. C. B. Mannsfeld, C. Felser, X. Feng, *Nat. Commun.* **2018**, *9*, 2637.
[19] A. A. Talin, A. Centrone, A. C. Ford, M. E. Foster, V. Stavila, P. Haney, R. A. Kinney, V. Szalai, F. El Gabaly, H. P. Yoon, F. Léonard, M. D. Allendorf, *Science* **2014**, *343*, 66.
[20] L. Sun, M. G. Campbell, M. Dincă, *Angew. Chem., Int. Ed.* **2016**, *55*, 3566.
[21] D. Sheberla, L. Sun, M. A. Blood-Forsythe, S. Er, C. R. Wade, C. K. Brozek, A. Aspuru-Guzik, M. Dincă, *J. Am. Chem. Soc.* **2014**, *136*, 8859.

ADVANCED SCIENCE NEWS
www.advancedsciencenews.com

ADVANCED MATERIALS
www.advmat.de

[22] V. Stavila, A. A. Talin, M. D. Allendorf, *Chem. Soc. Rev.* **2014**, *43*, 5994.
[23] I. Stassen, N. Burtch, A. Talin, P. Falcaro, M. Allendorf, R. Ameloot, *Chem. Soc. Rev.* **2017**, *46*, 3185.
[24] Y. Cui, J. Yan, Z. Chen, J. Zhang, Y. Zou, Y. Sun, W. Xu, D. Zhu, *Adv. Sci.* **2019**, *6*, 1802235.
[25] J. H. Dou, L. Sun, Y. Ge, W. Li, C. H. Hendon, J. Li, S. Gul, J. Yano, E. A. Stach, M. Dincă, *J. Am. Chem. Soc.* **2017**, *139*, 13608.
[26] A. J. Clough, J. M. Skelton, C. A. Downes, A. A. de la Rosa, J. W. Yoo, A. Walsh, B. C. Melot, S. C. Marinescu, *J. Am. Chem. Soc.* **2017**, *139*, 10863.
[27] A. F. Qasrawi, N. M. Gasanly, *Semicond. Sci. Technol.* **2005**, *20*, 446.
[28] B. Cao, X. Shen, J. Shang, C. Cong, W. Yang, M. Eginligil, T. Yu, *APL Mater.* **2014**, *2*, 116101.
[29] A. Rogalski, *Infrared Detectors*, Gordon and Breach Science Publishers, Amsterdam **2000**.
[30] G. D. Dereniak, E. L. Boreman, *Infrared Detectors and Systems*, John Wiley & Sons, New York **1996**.
[31] H. Arora, Y. Jung, T. Venanzi, K. Watanabe, T. Taniguchi, R. Hübner, H. Schneider, M. Helm, J. C. Hone, A. Erbe, *ACS Appl. Mater. Interfaces* **2019**, *11*, 43480.
[32] M. Buscema, D. J. Groenendijk, S. I. Blanter, G. A. Steele, H. S. J. van der Zant, A. Castellanos-Gomez, *Nano Lett.* **2014**, *14*, 3347.
[33] T. Mueller, F. Xia, P. Avouris, *Nat. Photonics* **2010**, *4*, 297.
[34] F. Xia, T. Mueller, Y. M. Lin, A. Valdes-Garcia, P. Avouris, *Nat. Nanotechnol.* **2009**, *4*, 839.
[35] R. Singh, V. Mittal, *Def. Sci. J.* **2003**, *53*, 281.
[36] H. Arora, P. E. Malinowski, A. Chasin, D. Cheyns, S. Steudel, S. Schols, P. Heremans, *Appl. Phys. Lett.* **2015**, *106*, 143301.
[37] X. Qiu, X. Yu, S. Yuan, Y. Gao, X. Liu, Y. Xu, D. Yang, *Adv. Opt. Mater.* **2018**, *6*, 1700638.
[38] V. D. Shadrin, V. V Mitin, V. A. Kochelap, K. K. Choi, *J. Appl. Phys.* **1995**, *77*, 1771.
[39] B. Y. Zhang, T. Liu, B. Meng, X. Li, G. Liang, X. Hu, Q. J. Wang, *Nat. Commun.* **2013**, *4*, 1811.
[40] O. Lopez-Sanchez, D. Lembke, M. Kayci, A. Radenovic, A. Kis, *Nat. Nanotechnol.* **2013**, *8*, 497.
[41] R. H. Bube, *Photoelectric Properties of Semiconductors*, Cambridge University Press, Cambridge, UK **1992**.
[42] A. Rose, *Concepts in Photoconductivity and Allied Problems*, Robert E. Krieger Publishing Company, Huntington, NY, USA **1978**.

Nano Energy 75 (2020) 104927

Contents lists available at ScienceDirect

Nano Energy

journal homepage: http://www.elsevier.com/locate/nanoen

Alkali metals inside bi-layer graphene and MoS_2: Insights from first-principles calculations

Ilya V. Chepkasov [a,b,c,**], Mahdi Ghorbani-Asl [a], Zakhar I. Popov [b,d,g], Jurgen H. Smet [e], Arkady V. Krasheninnikov [a,f,*]

[a] Institute of Ion Beam Physics and Materials Research, Helmholtz-Zentrum Dresden-Rossendorf, D-01328, Dresden, Germany
[b] National University of Science and Technology MISiS, 4 Leninskiy Pr, 119049, Moscow, Russia
[c] Khakas State University, 90 Lenin Pr, 655017, Abakan, Russia
[d] Emanuel Institute of Biochemical Physics RAS, Moscow, 199339, Russia
[e] Max Planck Institute for Solid State Research, Stuttgart, Germany
[f] Department of Applied Physics, Aalto University, P.O. Box 11100, FI-00076, Aalto, Finland
[g] Plekhanov Russian University of Economics, 36 Stremyanny per., 117997, Moscow, Russia

ARTICLE INFO

Keywords:
Alkali metal-ion batteries
Nanostructured materials
Intercalation
First-principles simulations

ABSTRACT

Contrary to a wide-spread belief that alkali metal (AM) atoms intercalated into layered materials form single-layer structures only, recent experiments [Nature 564 (2018) 234] showed that multi-layer configurations of lithium are possible in bi-layer graphene. Using state-of-the-art first-principles calculations, we systematically study the intercalation energetics for various AMs (Li, Na, K, Rb, Cs) in bi-layer graphene and MoS_2. We demonstrate that for bi-layer graphene as host the formation energy of multi-layer structures is negative for K, Rb and Cs and only slightly positive for both Li and Na. In view of the previous experimental data on lithium, a multi-layer of Na might therefore form, while it is well-known that single-layers of Na in graphitic hosts are energetically very unfavorable. In MoS_2, multi-layer structures are considerably higher in energy than the single-layer ones, but the formation of the former can still occur, especially for the AMs with the lowest electro-negativity. To rationalize the results, we assess the charge transfer from the intercalants to the host material and analyze the interplay between the ionic and covalent bonding of AM and host atoms. While our theoretical effort primarily focuses on the fundamental aspects of AM intercalation, our findings may stimulate experimental work addressing multi-layer intercalation to maximize the capacity of anode materials in AM ion batteries.

1. Introduction

A fossil fuel-free society is hardly possible without the development of light-weight but high-capacity rechargeable electrical power sources, such as alkali metal (AM)-ion batteries [1,2], which had extensively been studied since 1970s and entered the market in early 1990s. The significance of this scientific and technological breakthrough was reflected by the 2019 Nobel Prize in Chemistry awarded for the development of Li-ion batteries (LIBs). However, in spite of numerous applications of AM-ion batteries ranging from portable electronics to electric cars, they currently cannot match the growing demand for higher energy storage density, charging speed and cost reduction. At the same time, further improvements in their design and operation present a challenge, see Ref. [1,2] for an overview.

Specifically, modern LIBs have safety problems and narrow operating temperature ranges. Currently, graphite, which has a theoretical capacity of 372 $mAhg^{-1}$, is normally used as the anode material [1], but other layered materials have been studied both experimentally and theoretically, including transition metal dichalcogenides (TMDs), MXenes, black phosphorus, both in bulk and nano-structured forms, see Ref. [3–5] for an overview. Particular attention has been paid to bi-layer graphene (BLG), as intercalation into this system is interesting not only in the context of AM storage [6–10], but also superconductivity [11,12]. Bi-layers can potentially provide more space for intercalants than bulk systems. Notably, a macroscopic three-dimensional bi-layer graphene foam with few defects was recently manufactured [6], and its Li-storage

* Corresponding author. Institute of Ion Beam Physics and Materials Research, Helmholtz-Zentrum Dresden-Rossendorf, D-01328, Dresden, Germany.
** Corresponding author. Institute of Ion Beam Physics and Materials Research, Helmholtz-Zentrum Dresden-Rossendorf, D-01328, Dresden, Germany.
E-mail addresses: ilya_chepkasov@mail.ru (I.V. Chepkasov), a.krasheninnikov@hzdr.de (A.V. Krasheninnikov).

https://doi.org/10.1016/j.nanoen.2020.104927
Received 19 February 2020; Received in revised form 9 April 2020; Accepted 2 May 2020
Available online 30 May 2020

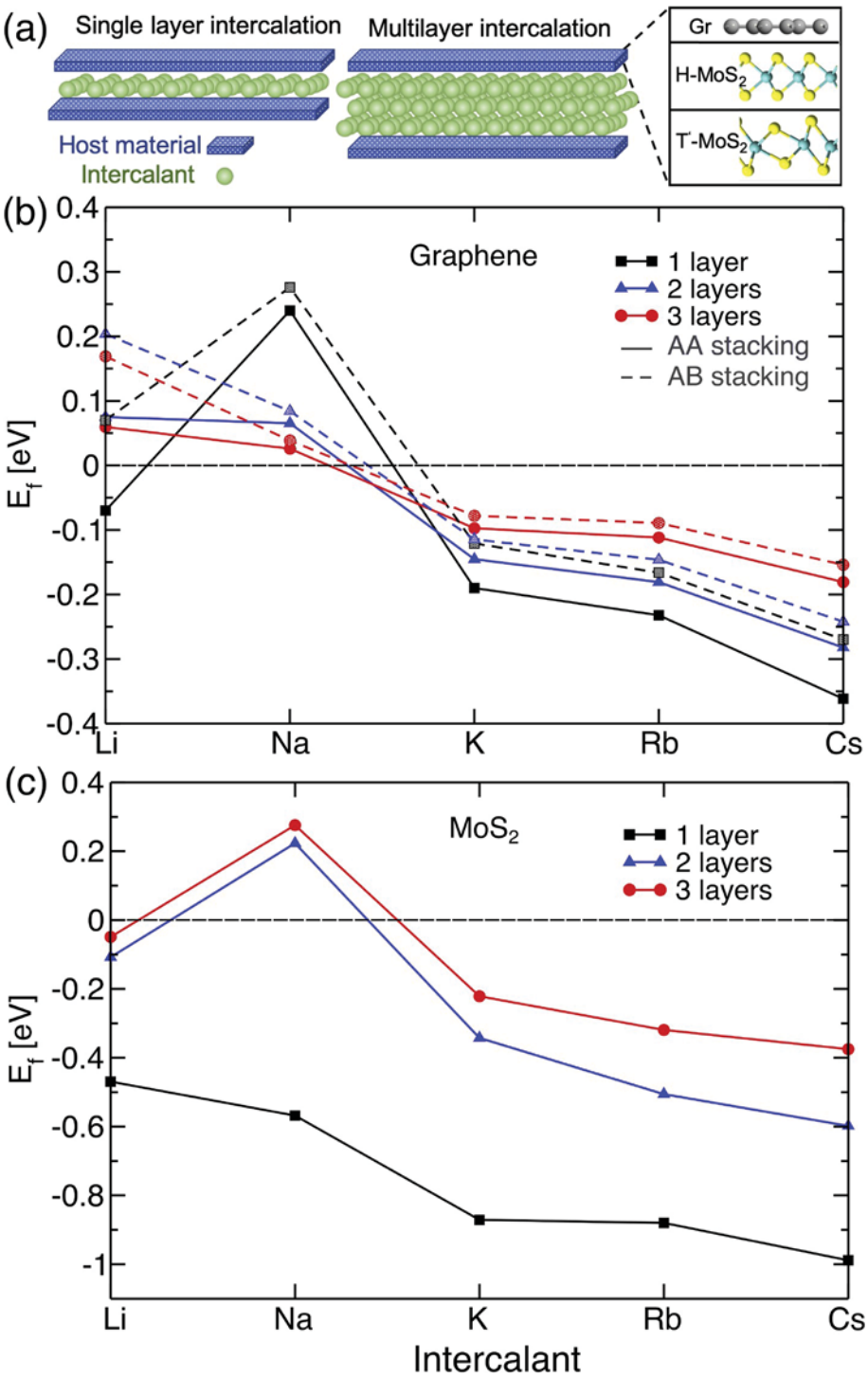

Fig. 1. (a) Schematic illustration of the single- and multi-layer structures of alkali metals (AMs) between two sheets of the host material. (b) Formation energy of single layers and multi-layers with the *bcc* structure of AMs (Li, Na, K, Rb, Cs) between AA- and AB-stacked bi-layer graphene. (c) The energetics of single- and multi-layer structures of AMs in a MoS_2 bi-layer.

capacity and intercalation kinetics were systematically studied. It was concluded that in BLG Li atoms can be stored only between the graphene sheets, not on the outer surfaces. As for TMDs, and first of all, MoS_2, the most common material in the TMD family, their layered structure and the weak van der Waals (vdW) interaction between the layers also enable the easy intercalation of Li ions without any significant increase in the volume and exhibit high Li storage capacities (up to 700 mAh/g) [13]. Understanding TMD behavior upon AM intercalation is important for controlling phase transitions from the semiconducting *H* to metallic *T* and *T'* phases as well [14–20]. Intercalation into heterostructures of these materials has also been investigated both experimentally [21] and theoretically [22,23].

All these studies on the intercalation of Li (or other AMs) into bulk and few-layer systems assumed that a *single* layer of the intercalant atoms is formed between the sheets of the host material. However, recent studies [24] employing in-situ transmission-electron microscopy (TEM), which is one of the most powerful techniques for getting insights into the dynamics of various processes in energy materials with atomic

resolution [25], showed the unexpected formation of multi-layer close-packed Li phases between graphene sheets, hinting at the possibility of increasing the areal Li storage capacity. This gives rise to a question: is the formation of multi-layer structures between bi-layers of other 2D materials possible? Moreover, as sodium-ion [26] and potassium-ion batteries [27] have also been rapidly developed, another important issue is to understand the behavior of these (much cheaper than Li) and other AM atoms in bi-layers formed by graphene and TMDs.

Here, using density functional theory (DFT) calculations, we theoretically study the intercalation of AM atoms into bi-layer graphene and MoS_2. We analyze the charge transfer and energetics of multi-layer configurations of various AMs between the layers of the host material and show that the formation of such structures should be possible with a few exceptions.

2. Computational methods

All our calculations were carried out using the VASP software package [28,29]. The exchange-correlation functional proposed by Björkman [30] was employed to account for the vdW interaction. An energy cut-off of 600 eV was used for the primitive cell calculations, for supercells we used 400 eV. The Brillouin zones of the primitive cells of the 2D materials and bulk AMs were sampled using 12x12x1 and 12x12x12 Monkhorst–Pack grid points [31]. The equivalent or better sampling was used for supercells consisting of up to 620 atoms (see Tables S1–S16). The maximum force on each atom was set to be less than 0.01 eV for the optimized configurations. The atomic structures and the charge densities were illustrated using the VESTA package [32]. Various initial configurations of AM atoms between graphene sheets (AA and AB stacking) and MoS_2 (H, T, T' - phases) were created, and then the geometry was fully optimized. In order to reduce the lattice mismatch for periodic structures, the optimum sizes of the supercells and rotational angles between surfaces were defined using the Virtual NanoLab software [33].

We assessed the stability of various AM structures between the sheets of graphene and MoS_2 by calculating their formation energy E_f per AM atom defined as

$$E_f = (E[Host + AM] - E[Host]) / n_{AM} - \mu_{AM}, \quad (1)$$

where $E[Host + AM]$ is the energy of the supercell containing bi-layer graphene (or MoS_2) and AM atoms, $E[Host]$ is the energy of pristine bi-layer (graphene or MoS_2), n_{AM} is the total number of AM atoms and μ_{AM} is their chemical potential. Eq. (1) gives the energy per atom required to take AM atoms from the bulk structure and place them between the host material. Negative values indicate that this process is energetically favorable. Charge transfer from AM atoms to graphene (MoS_2) was evaluated as a difference between the integrated electron densities of the composite structure and isolated 2D material and the equivalent AM structures.

3. Results and discussion

Following the previous work [24] on multi-layer structures of Li atoms between graphene sheets, we studied first the intercalation of AMs into BLG, as sketched in Fig. 1 (a). We considered both the AB and AA stacking in BLG, as our calculations, in agreement with the previous results [22,34], showed that the AA stacking is only slightly (about 10 meV per atom) higher in energy, so that both configurations are generally possible. AM atoms with various densities were placed between the graphene sheets as single- or multi-layered structures, as schematically illustrated in Fig. 1(a), and then the geometry of the system was optimized. Examples of the optimized configurations are shown in Figs. S1, S2, S5, S6.

We found that the arrangements of AM atoms (M) in single-layers were the same as in the AMC_6 phase in the bulk host materials, which formed a commensurate $(\sqrt{3} \times \sqrt{3})R30^o$ superstructure (Fig. S1). We did not consider the AMC_8 phase, as it has a lower concentration of AM atoms, and overall our goal was to compare the energetics of multi-layer and single-layer AM structures. As for the geometry optimization of the multi-layered AM configurations, the initial atom positions were cut from the bulk *fcc, hcp, bcc* metals along the low-energy directions (e.g. [111] for the fcc structures) and placed between the graphene layers. The orientation of the metal crystal lattice with regard to graphene and sizes of the supercells were chosen to minimize the strain in the system, which normally did not exceed 1%.

The results of our calculations are presented in Fig. S3 and a summary is shown in Fig. 1(b). As the *fcc, hcp, bcc* structures of AMs in BLG have very close energies (for the same number of layers), Fig. S3, and because many bulk AM are *bcc* crystals, we presented here only the results for the *bcc* arrangement of atoms in the multi-layers. Note that E_f for Li multi-layer configurations are slightly higher than those reported in Ref. [24], as they are for the bcc, not fcc/hcp arrangements of AM atoms.

It is evident that for all AMs, except for Na, E_f is negative for a single layer of AMs in AA-stacked BLG. The trend is the same in AB-stacked BLG, but the values of E_f are slightly higher due to the asymmetric positions of C atoms in the graphene planes with respect to AM atoms. Positive values of E_f for Na in the $C_6NaC_6(\sqrt{3} \times \sqrt{3})R30^o$ phase and negative values for K have been also previously reported for graphite [1,9,35,36]. Formation of multi-layer AM structures is less energetically favorable than single-layers (except for Na): the energy increases with the number of layers, but remains negative. E_f for two/three layers of Na atoms is positive, but it is comparable to that of Li, though, and as the latter have been experimentally observed [24], the multilayer Na structures may be experimentally realized in BLG. For K, Rb, and Cs, E_f for multilayer structures increases with the number of layers, making the intercalation energetically less favorable, but theoretically possible, as the values are still negative. We stress that when the number of AM atom layers increases, E_f should approach zero value, corresponding to an infinitely thick slab of AM atoms inserted between two graphene sheets. We note also that contrary to single-layer AM structures, multi-layers and graphene are incommensurate, as the spacing between AM atoms is governed by not only the interaction of AMs with the host material, but also between each other, as in the bulk crystal. Thus there are always AM atoms on top of different sites in graphene, but the 'net' effect is that the energies are lower for the A-A stacking in BLG.

For MoS_2 we considered both H and T/T' phases, as illustrated in Figs. S5 and S6. We found that the H phase had lower energy in most cases, as evident from Tables S7–S16 and Fig. S7. Although the T′-phase is expected to be energetically preferable at high concentrations of Li atoms, the concentration for single-layer structures we considered was always lower than the critical value (for Li, about 0.4 AM per formula unit [19,20]), while for multi-layer structures charge transfer into MoS_2 was in most cases not sufficient to make the T/T′ phases energetically favorable. We also note that a direct comparison of the energetics of the H and T phases was not always straightforward due to different sizes and thus different number of atoms in the supercells. Because our main goal was to look at the differences in the behavior of the system upon formation of multi-layer AM structures, we present results for the *H*-phase only, Fig. 1(c).

The behavior of AMs between MoS_2 sheets is qualitatively the same for all AMs, except for Na: E_f is smaller for a single layer of AMs than in multi-layers, and bonding becomes stronger from Na to Cs. Note a stronger bonding of AMs to MoS_2 as compared to graphene. For single layers of AMs in both graphene and MoS_2 bi-layers, our results are very close to those obtained for bulk graphite and MoS_2 serving as the hosts [36,37].

To get further insight into the energetics of the intercalants between the layers of the host material, E_f can be represented [37] as

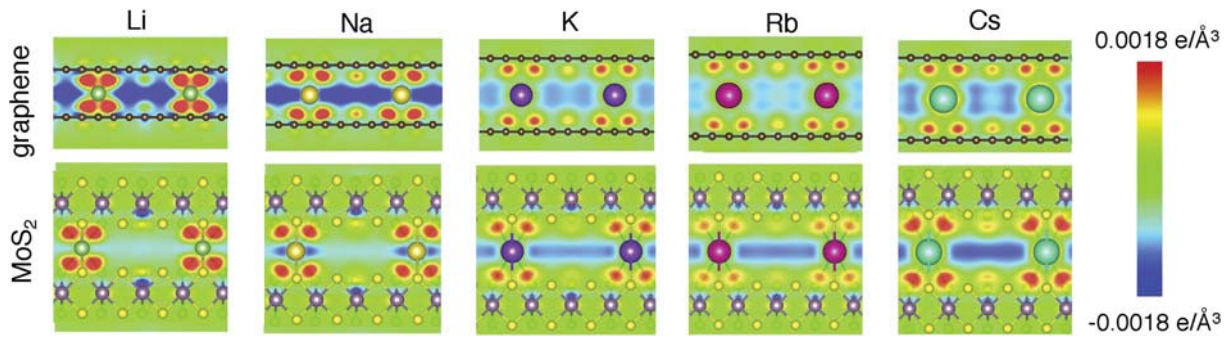

Fig. 2. Charge difference (cross-section through AM atoms perpendicular to the host material planes) for a single layer of AM atoms between the sheets of graphene and MoS_2 in the C_6MC_6 structure. Note a build-up of the electron density between Li atoms and graphene, illustrating a substantial contribution to the bonding from covalent interaction. Red color corresponds to density build-up, blue to depletion. (For interpretation of the references to color in this figure legend, the reader is referred to the Web version of this article.)

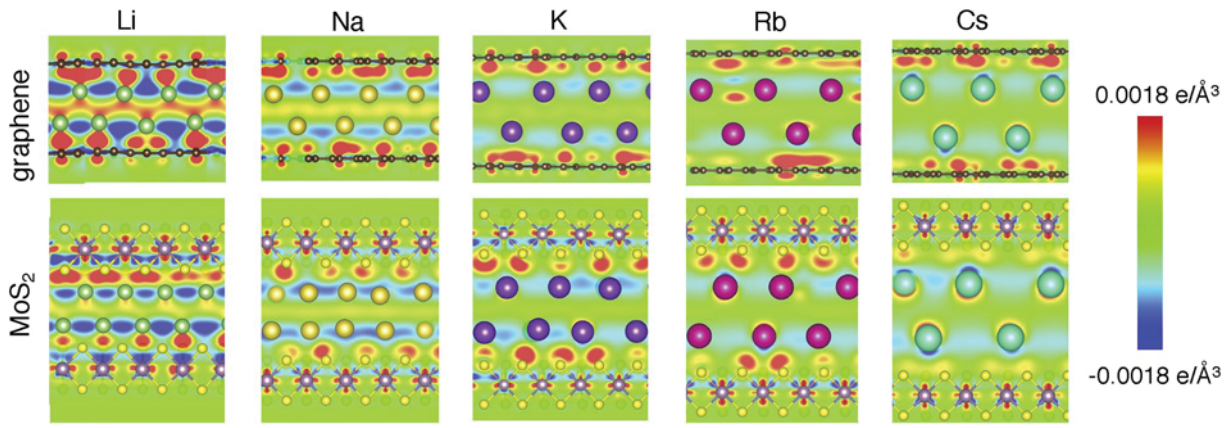

Fig. 3. Charge difference (cross-section through AM atoms perpendicular to the host material planes) for two layers of AM atoms in bi-layer graphene and MoS_2. Red color corresponds to density build-up, blue to depletion. (For interpretation of the references to color in this figure legend, the reader is referred to the Web version of this article.)

$$E_f \approx E_{coh} + E_{vdW} - E_b, \tag{2}$$

where E_{coh} is the cohesive energy of the bulk metal (energy required to split the bulk crystal into separate atoms, $E_{coh} > 0$), E_{vdW} is the loss in the vdW energy when the distance between the sheets of the host material is changed upon intercalation ($E_{vdW} > 0$), and E_b ($E_b > 0$) is the binding energy of an AM atom to the host material (adsorption energy).

The contributions to E_f are listed in Table S17. Similar to intercalation into bulk host materials, the behavior of E_f for all AMs, except for Li, is defined by the difference between E_{coh} and E_b, as E_{vdW} is much smaller. E_b depends on the interplay between the charge transfer related to the electronegativity of AMs and covalent bonding between AM atoms and the host material. As shown previously for bulk hosts [36,37], the covalent bonding between BLG and Li is very strong affecting charge transfer [38] and the ionic contribution.

To assess charge transfer in the bi-layer systems upon intercalation and to compare it to that in the corresponding bulk host materials, we calculated the difference $\Delta\rho$ between electron densities of the combined and separated systems as

$$\Delta\rho = \rho[Host + AM] - \{\rho[Host] + \rho[AM]\}, \tag{3}$$

where $\rho[Host + AM]$ is the total electron density of the host material and embedded AM atoms, and $\rho[Host]$ and $\rho[AM]$ are the electron densities of the isolated host structures and AM layers for the same positions of the atoms, respectively.

For BLG and a single layer of AM atoms, a cross-section of $\Delta\rho$ is presented in the top panel of Fig. 2, and the corresponding values for MoS_2 bi-layer are shown in the bottom panels. It is evident that strong covalent bonds between C and Li atoms have been formed, and although the electron density is depleted between the AMs, a substantial part of it is still localized near the atoms in the covalent bonds. For MoS_2 bi-layer as a host, the situation is different: the covalent interaction is roughly the same for all the AMs. It is also evident that charge transfer from AMs to the host materials should increase from Na to Cs in case of MoS_2, in agreement with the trend in the electro-negativity of these metals. However, for graphene the situation is more complicated, as discussed below.

We also visualized $\Delta\rho$ for double and triple layers of AMs between graphene and MoS_2 sheets. The results for double layers of AMs are presented in Fig. 3 and for triple layers in Fig. S8. It is evident that the interaction between Li and the host material for multi-layers is also rather strong, it even gives rise to a redistribution of the electron density between Li atoms, making the bond between them more 'covalent'. The overall charge transfer from AMs to the host material increases from Na to Cs as well, as expected, similar to the case of a single layer of AMs. It is also clear that the AM atoms facing the host material mostly donate the electrons, while the inner atoms (e.g., in the triple layer) preserve their charges.

Quantifying the charge transfer in these systems is not straightforward, and the results may depend on the methods used to evaluate it, as discussed at length previously [38]. The Bader analysis [39,40] based on finding the extrema in the electron density and splitting the space to atomic volumes accordingly is normally used. However, it accounts for the geometrical charge transfer which occurs in every system upon adding atoms, even when there is no physical charge transfer between

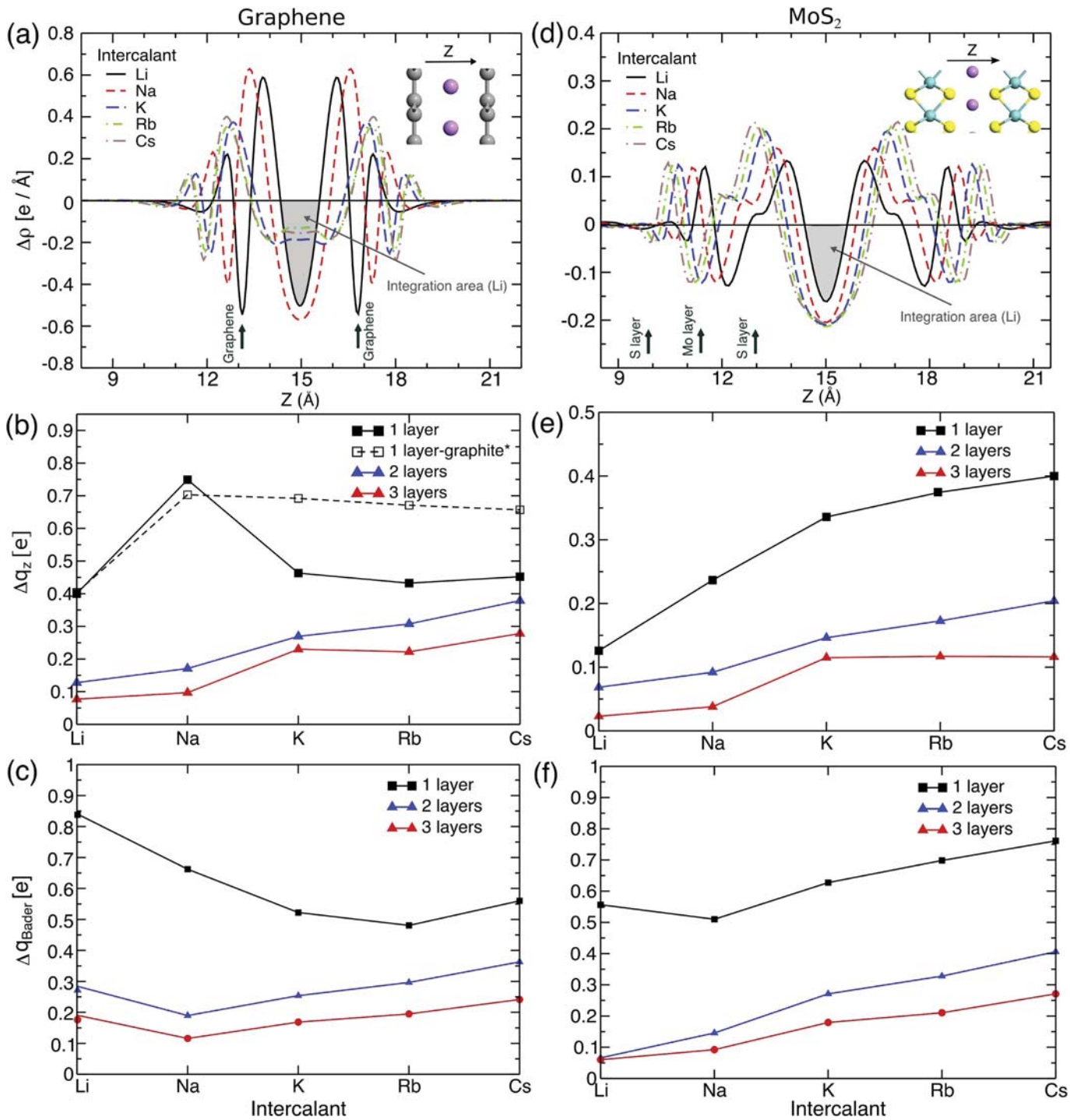

Fig. 4. (a) Electron density difference $\Delta\rho$ for single layers of AM atoms averaged in the planes parallel to the graphene sheets as a function of the z-coordinate (perpendicular to the planes). The geometry is schematically shown in the inset. (b) Total charge transfer Δq_z for single- and double-layers of AM atoms obtained by integrating over the range of z where $\Delta\rho < 0$, as illustrated for Li in panel (a). The results for a single layer of AM atoms in bulk graphite are also shown. The data is taken from Ref. [38]). (c) Charge transfer for single and multi-layer structures as calculated using the Bader method. (d) $\Delta\rho$ for single layers of AM atoms averaged in the planes parallel to the MoS_2 sheets as a function of the z-coordinate. (e) Total charge transfer Δq_z for single and double layers of AM atoms obtained by integrating over the range of z where $\Delta\rho < 0$, as illustrated for Li in panel (d). (f) Charge transfer for single and multi-layer structures obtained using the Bader method.

the host and the added atoms [38].

Thus, we evaluated charge transfer using two approaches: using the Bader method and by averaging $\Delta\rho$ within the planes parallel to the sheets of the host material, and plotting it as a function of z-coordinate (perpendicular to the planes) as schematically shown in the inset in Fig. 4(a). Charge difference for a single layer of AMs between graphene sheets is shown in Fig. 4(a). It is evident that the averaged electron density is depleted within the AM plane (compare it to the cross-section of $\Delta\rho$ shown in Fig. 2), and is increased considerably in the area between graphene sheets and the AM metals, especially for Li and Na. Note that the graphene planes are at different locations due to different atomic radii of the AM atoms. Then we evaluated the total charge transfer Δq_z by integrating over the range of z where $\Delta\rho$ is negative, as illustrated for Li in Fig. 4(a). We stress that the choice of the integration range is not

unique, but if the same criterion is used for all AMs, this approach makes it possible to analyze the trends.

The charge transfer Δq_z for single- and multi-layers of AMs between graphene sheets is shown in Fig. 4(b). We also present similar results (for the AMC_8 phase) for graphite taken from Ref. [38]. For a single layer of Li and Na atoms, when the covalent interaction is strong and atomic radii are small, the results for bi-layer graphene and the bulk system are very close, while the difference for AMs with larger atomic radii can be explained by the different geometry: there is no layer of AMs on the other side of the graphene plane and the system has more space to adjust its geometry. For the double layer of AM atoms, charge transfer increases from Li to Cs, and the same is true for triple layers.

The results obtained using the Bader method, Fig. 4(c), give qualitatively (and even quantitatively for all AMs, except for Li) the same picture for double and triple layers of AM atoms. However, for single layers our findings are somewhat counterintuitive, although the results for Li in BLG (0.84e per Li atom) agree well with the previous [41] Bader results (0.88e). They indicate that charge transfer decreases from Li to Rb, contrary to what one can expect from lower electronegativity of heavier AMs. The reason for that is the strong covalent bonding between graphene and light AM atoms, which gives rise to a redistribution of the electron density and its build-up in the covalent bonds between carbon and AM atoms. This is evident from 4(a): charge build-up is clearly observable, and even a part of the electron density from graphene sheets went into the new bonds. Charge transfer (per AM atom) decreases with the number of the AM layers, as only the top layers are depleted of electrons [7] and the inner layers mostly retain their metallic character.

In order to get further insight into the nature of chemical bonding between graphene and AMs, we also calculated the electron localization function (ELF) [42,43] for single layers of AMs. The ELF makes it possible to assess the distribution of the electron density in chemical bonds. The ELF for Li in graphene is shown in Fig. S9. It is evident that the picture is dominated by strong carbon-carbon bonds in graphene. Thus, in order to improve visualisation, we subtracted the values of the ELF obtained for isolated graphene sheets, following the approach previously used for other systems with different types of bonding [44]. The results are presented in Fig. S10. It is clear that the bonds between AM and carbon atoms, when moving from Li to Cs, become less and less covalent, confirming the picture obtained from the analysis of the electron density.

Having analyzed charge transfer in BLG, we moved on to MoS_2. Similar to graphene, we carried out averaging in the planes parallel to the sheets. The charge difference for a single layer of AMs between MoS_2 sheets is shown in Fig. 4(d). The averaged electron density is also depleted close to the AM plane, but its build-up in the covalent bonds with regard to the depletion area is smaller and rather uniform for all AMs. As a result of this, the total charge transfer Δq_z integrated over the range of z where $\Delta\rho$ is negative, increases from Li to Cs, Fig. 4 (e). The same is true for AM double and triple layers, and the charge transfer per AM atom is smaller. The results obtained using the Bader analysis in Fig. 4 (f) also indicate that Δq increases from Li to Cs, and gets smaller when the number of AM layers increases.

Using the calculated geometries for multi-layers of AMs in graphene and MoS_2 bi-layers, we estimated the theoretically achievable capacity of such systems, which is presented in Table S18. For triple-layered Li and Na structures in BLG it proved to be equal to 828 $mAhg^{-1}$ and 440 $mAhg^{-1}$ respectively. This indicates that the capacity of BLG with intercalated multi-layered Na structures can exceed that for graphite with lithium (372 $mAhg^{-1}$). In the case of lithium between double-layered MoS_2 the capacity reaches 251 $mAhg^{-1}$ for three layers of Li and could further be increased by adding more Li layers. The capacity of three-layered sodium in bi-layered-MoS_2 (157 $mAhg^{-1}$) is rather low, though. It should be pointed out that in general the capacity can be increased by making vertical vdW graphene-MoS_2 heterostructures [23]. Such heterostructures are expected to be beneficial for multi-layer AM storage due to the weight reduction of the host by using the lighter graphene and decrease of the formation energy due to the dichalcogenide layer. There have been only a few reports (see Ref. [45] for an overview) on vdW heterostructures used for energy storage due to many challenges in their fabrication processes.

4. Conclusions

By using first-principles calculations we have studied the energetics of various AMs (Li, Na, K, Rb, Cs) in bi-layer graphene and MoS_2. We have demonstrated that the formation energy of multi-layer AM structures between graphene sheets is negative for K, Rb and Cs. Both Li and Na multi-layer structures have positive formation energy, but the values are small. In MoS_2, AM multi-layer structures are considerably higher in energy than the single-layer ones. Multilayer structures can still occur, as intercalation is energetically favorable, especially for the AMs with the lowest electro-negativity. To rationalize the results, we assessed the charge transfer from the intercalants to the host material and analyzed the interplay between the ionic and covalent bonding of alkali metal and host atoms. Our results, in conjunction with the recent experimental discovery of multi-layer lithium in bi-layer graphene [24], raise hope that even for Na a multi-layer structure in bilayer graphene can form, although the single-layer configuration is energetically strongly unfavorable for this metal. This result is intriguing in the context of the recent progress in manufacturing macroscopic amounts of bi-layer graphene [6] and the low cost/abundance of Na, key prerequisites to envisage the implementation of Na-ion batteries based on nano-structured 2D materials. Thus, while our theoretical effort primarily focuses on the fundamental aspects of AM intercalation, our findings may stimulate experimental work addressing multi-layer intercalation to maximize the capacity of anode materials in AM ion batteries.

Declaration of competing interest

The authors declare that they have no known competing financial interests or personal relationships that could have appeared to influence the work reported in this paper.

Acknowledgements

We thank HLRS, Stuttgart, Germany (PRACE project 2018184458), TU Dresden (Taurus cluster), and CSC Finland for generous grants of CPU time. AVK acknowledges funding from the German Research Foundation (DFG) through Project No. KR 48661-1 and KR 48661-2. JHS acknowledges support from the European Graphene Flagship, core 3. The study was also funded by the Ministry of Education and Science of the Russian Federation and the German Academic Exchange Service (DAAD) program "Mikhail Lomonosov 2018" through research project No 57391663. The theoretical study of alkali metal between graphene sheets was supported by the Russian Science Foundation (project identifier, 17-72-20223). IVC further acknowledges the financial support of the Ministry of Education and Science of the Russian Federation in the framework of Increase Competitiveness Program of NUST "MISiS" (No. K2-2019-016). Finally, we thank A. Tkatchenko and P. Sorokin for discussions.

Appendix A. Supplementary data

Supplementary data to this article can be found online at https://doi.org/10.1016/j.nanoen.2020.104927.

References

[1] J. Xu, Y. Dou, Z. Wei, J. Ma, Y. Deng, Y. Li, H. Liu, S. Dou, Recent progress in graphite intercalation compounds for rechargeable metal (li, na, k, al)-ion batteries, Advanced Science 4 (10) (2017) 1700146.

[2] J. Janek, W.G. Zeier, A solid future for battery development, Nature Energy 1 (9) (2016) 16141.
[3] M.S. Stark, K.L. Kuntz, S.J. Martens, S.C. Warren, Intercalation of layered materials from bulk to 2D, Adv. Mater. 31 (2019) 1808213.
[4] Y.-P. Zhu, Y. Lei, F. Ming, E. Abou-Hamad, A.-H. Emwas, M.N. Hedhili, H. N. Alshareef, Heterostructured mxene and g-c3n4 for high-rate lithium intercalation, Nanomater. Energy 65 (2019) 104030.
[5] S. Shi, J. Gao, Y. Liu, Y. Zhao, Q. Wu, W. Ju, C. Ouyang, R. Xiao, Multi-scale computation methods: their applications in lithium-ion battery research and development, Chin. Phys. B 25 (2016), 018212.
[6] K. Ji, J. Han, A. Hirata, T. Fujita, Y. Shen, S. Ning, P. Liu, H. Kashani, Y. Tian, Y. Ito, J.-i. Fujita, Y. Oyama, Lithium intercalation into bilayer graphene, Nat. Commun. 10 (1) (2019) 275.
[7] M. Kühne, F. Paolucci, J. Popovic, P.M. Ostrovsky, J. Maier, J.H. Smet, Ultrafast lithium diffusion in bilayer graphene, Nat. Nanotechnol. 12 (9) (2017) 895–900.
[8] F.J. Sonia, M.K. Jangid, B. Ananthoju, M. Aslam, P. Johari, A. Mukhopadhyay, Understanding the li-storage in few layers graphene with respect to bulk graphite: experimental, analytical and computational study, J. Mater. Chem. 5 (18) (2017) 8662–8679.
[9] S. Yang, S. Li, S. Tang, W. Dong, W. Sun, D. Shen, M. Wang, Sodium adsorption and intercalation in bilayer graphene from density functional theory calculations, Theoretical Chemistry Accounts 135 (7) (2016) 164.
[10] E. Lee, K.A. Persson, Li absorption and intercalation in single layer graphene and few layer graphene by first principles, Nano Lett. 12 (9) (2012) 4624–4628.
[11] S. Ichinokura, K. Sugawara, A. Takayama, T. Takahashi, S. Hasegawa, Superconducting calcium-intercalated bilayer graphene, ACS Nano 10 (2) (2016) 2761–2765.
[12] A.P. Durajski, K.M. Skoczylas, R. Szcześniak, Superconductivity in bilayer graphene intercalated with alkali and alkaline earth metals, Phys. Chem. Chem. Phys. 21 (11) (2019) 5925–5931.
[13] H. Hwang, H. Kim, J. Cho, MoS2 nanoplates consisting of disordered graphene-like layers for high rate lithium battery anode materials, Nano Lett. 11 (2011) 4826–4830.
[14] S. Fan, X. Zou, H. Du, L. Gan, C. Xu, W. Lv, Y.-B. He, Q.-H. Yang, F. Kang, J. Li, Theoretical investigation of the intercalation chemistry of lithium/sodium ions in transition metal dichalcogenides, J. Phys. Chem. C 121 (25) (2017) 13599–13605.
[15] T. Zhao, H. Shu, Z. Shen, H. Hu, J. Wang, X. Chen, Electrochemical lithiation mechanism of two-dimensional transition-metal dichalcogenide anode materials: intercalation versus conversion reactions, J. Phys. Chem. C 123 (4) (2019) 2139–2146.
[16] J. Cherusseri, N. Choudhary, K.S. Kumar, Y. Jung, J. Thomas, Recent trends in transition metal dichalcogenide based supercapacitor electrodes, Nanoscale Horizons 4 (4) (2019) 840–858.
[17] X. Zhu, D. Li, X. Liang, W.D. Lu, Ionic modulation and ionic coupling effects in mos2 devices for neuromorphic computing, Nat. Mater. 18 (2) (2019) 141–148.
[18] J. Shuai, H.D. Yoo, Y. Liang, Y. Li, Y. Yao, L.C. Grabow, Density functional theory study of li, na, and mg intercalation and diffusion in mos2 with controlled interlayer spacing, Mater. Res. Express 3 (6) (2016), 064001.
[19] D. Nasr Esfahani, O. Leenaerts, H. Sahin, B. Partoens, F. Peeters, Structural transitions in monolayer mos2 by lithium adsorption, J. Phys. Chem. C 119 (19) (2015) 10602–10609.
[20] A.N. Enyashin, G. Seifert, Density-functional study of lixmos2 intercalates (0¡ x¡ 1), Computational and Theoretical Chemistry 999 (2012) 13–20.
[21] D.K. Bediako, M. Rezaee, H. Yoo, D.T. Larson, S.Y. Zhao, T. Taniguchi, K. Watanabe, T.L. Brower-Thomas, E. Kaxiras, P. Kim, Heterointerface effects in the electrointercalation of van der Waals heterostructures, Nature 558 (2018) 425–429.
[22] S.N. Shirodkar, E. Kaxiras, Li intercalation at graphene/hexagonal boron nitride interfaces, Phys. Rev. B 93 (24) (2016) 245438.
[23] X. Shao, K. Wang, R. Pang, X. Shi, Lithium intercalation in graphene/MoS2Composites: first-principles insights, J. Phys. Chem. C 119 (2015) 25860–25867.
[24] M. Kühne, F. Börrnert, S. Fecher, M. Ghorbani-Asl, J. Biskupek, D. Samuelis, A. V. Krasheninnikov, U. Kaiser, J.H. Smet, Reversible superdense ordering of lithium between two graphene sheets, Nature 564 (7735) (2018) 234–239.
[25] C. Zhang, K.L. Firestein, J.F.S. Fernando, D. Siriwardena, J.E. Treifeldt, D. Golberg, Recent progress of in situ transmission electron microscopy for energy materials, Adv. Mater. (2019) 1904094.
[26] Z. Jian, W. Luo, X. Ji, Carbon electrodes for k-ion batteries, J. Am. Chem. Soc. 137 (36) (2015) 11566–11569.
[27] W. Luo, J. Wan, B. Ozdemir, W. Bao, Y. Chen, J. Dai, H. Lin, Y. Xu, F. Gu, V. Barone, L. Hu, Potassium ion batteries with graphitic materials, Nano Lett. 15 (2015) 7671–7677.
[28] G. Kresse, J. Furthmüller, Efficient iterative schemes for ab initio total-energy calculations using a plane-wave basis set, Phys. Rev. B 54 (16) (1996) 11169.
[29] G. Kresse, D. Joubert, From ultrasoft pseudopotentials to the projector augmented-wave method, Phys. Rev. B 59 (3) (1999) 1758.
[30] T. Björkman, van der waals density functional for solids, Phys. Rev. B 86 (16) (2012) 165109.
[31] H.J. Monkhorst, J.D. Pack, Special points for brillouin-zone integrations, Phys. Rev. B 13 (12) (1976) 5188.
[32] K. Momma, F. Izumi, Vesta: a three-dimensional visualization system for electronic and structural analysis, J. Appl. Crystallogr. 41 (3) (2008) 653–658.
[33] S. Smidstrup, T. Markussen, P. Vancraeyveld, J. Wellendorff, J. Schneider, T. Gunst, B. Verstichel, D. Stradi, P.A. Khomyakov, U.G. Vej-Hansen, M.-E. Lee, S. T. Chill, F. Rasmussen, G. Penazzi, F. Corsetti, A. Ojanpera, K. Jensen, M.L. N. Palsgaard, U. Martinez, A. Blom, M. Brandbyge, K. Stokbro, QuantumATK: an integrated platform of electronic and atomic-scale modelling tools, J. Phys. Condens. Matter 32 (2019), 015901.
[34] J. Zhou, W. Zhou, C. Guan, J. Shen, C. Ouyang, M. Lei, S. Shi, W. Tang, First-principles study of lithium intercalated bilayer graphene, Sci. China Phys. Mech. Astron. 55 (8) (2012) 1376–1382.
[35] Z. Wang, S.M. Selbach, T. Grande, Van der waals density functional study of the energetics of alkali metal intercalation in graphite, RSC Adv. 4 (8) (2014) 4069–4079.
[36] H. Moriwake, A. Kuwabara, C.A. Fisher, Y. Ikuhara, Why is sodium-intercalated graphite unstable? RSC Adv. 7 (58) (2017) 36550–36554.
[37] Y. Liu, B.V. Merinov, W.A. Goddard, Origin of low sodium capacity in graphite and generally weak substrate binding of na and mg among alkali and alkaline earth metals, Proc. Natl. Acad. Sci. Unit. States Am. 113 (14) (2016) 3735–3739.
[38] C. Hartwigsen, W. Witschel, E. Spohr, Charge density and charge transfer in stage-1 alkali-graphite intercalation compounds, Phys. Rev. B 55 (1997) 4953–4959.
[39] R.F.W. Bader, Atoms in Molecules: a Quantum Theory, Oxford University Press, New York, 1990.
[40] W. Tang, E. Sanville, G. Henkelman, A grid-based bader analysis algorithm without lattice bias, J. Phys. Condens. Matter 21 (8) (2009), 084204.
[41] D.M. Guzman, H.M. Alyahyaei, R.A. Jishi, Superconductivity in graphene-lithium, 2D Mater. 1 (2014), 021005.
[42] A. Becke, E. K E, A simple measure of electron localization in atomic and molecular systems, J. Chem. Phys. 92 (1990) 5397–5403.
[43] A. Savin, O. Jepsen, J. Flad, O.K. Andersen, H. Preuss, H.G. von Schnering, Electron localization in solid-state structures of the elements: the diamond structure, Angew Chem. Int. Ed. Engl. 31 (1992) 187–188.
[44] Y. Zhang, H. Wang, Y. Wang, L. Zhang, Y. Ma, Computer-assisted inverse design of inorganic electrides, Phys. Rev. X 7 (2017), 011017.
[45] Y. Yang, X. Liu, Z. Zhu, Y. Zhong, Y. Bando, D. Golberg, J. Yao, X. Wang, The role of geometric sites in 2d materials for energy storage, Joule 2 (2018) 1075–1094.

Dr. Ilia V. Chepkasov received his PhD in Physics from Polzunov Altai State Technical University in 2013. From 2013 to 2018 he was a postdoctoral fellow at the Katanov Khakass State University. Since 2019 he is a Senior Research at the Laboratory of Inorganic Nanomaterials NUST "MISiS" and also a visiting scientist at Helmholtz-Zentrum Dresden-Rossendorf. His area of expertise is computational materials science with a focus on molecular dynamics and ab-initio methods. His scientific interests are the electronic and structural properties of two-dimensional materials and synthesis of nanoparticles.

Dr. Mahdi Ghorbani-Asl received his PhD in Physics with a special distinction from Jacobs University Bremen in 2014. He has received several scholarships and Marie Curie Fellowship for Early Stage Researchers. From 2014 to 2016, he was a postdoctoral fellow at the University of Cambridge. Since 2016, he is a Senior Research Associate in the group of Dr. Arkady Krasheninnikov at Helmholtz-Zentrum Dresden-Rossendorf. His area of expertise is computational materials science based on ab-initio methods. He is particularly interested in the electronic, transport and catalytic properties of two-dimensional materials. The results of his research are published in more than 30 peer-reviewed journals.

Dr. Zakhar I. Popov received his PhD in Physics from Kirensky Institute of Physics, Siberian Branch of the Russian Academy of Sciences, Krasnoyarsk, Russia in 2013. Currently, he is a senior researcher at the Emanuel Institute of Biochemical Physics, Russian Academy of Sciences, Moscow, Russia and a visiting researcher at NUST "MISiS", Moscow, Russia. His scientific interests lie in the areas of computational materials science, electronic structure calculations, two-dimensional materials, chemical reactions, and catalysis. Throughout his career, he has co-authored more than 60 peer-refereed papers.

Dr. Jurgen Smet received his PhD in Electrical Engineering and Computer Science from MIT in 1994. Currently he is the head of the Solid State Nanophysics Group at the Max Planck Institute for Solid State Research in Stuttgart, Germany. His scientific interests include Coulomb interaction, correlation and spin phenomena in two dimensional electron systems hosted by conventional semiconductor and van der Waals heterostructures as well as ionic transport in 2D materials. He has co-authored about 200 peer-refereed papers. Awards include the Walter Schottky Prize (DPG) and the Gerhard Hess (DFG) and Nano-Futur (BMBF) young investigator awards.

Dr. Arkady V. Krasheninnikov received his PhD in Physics from Moscow State Engineering Physics Institute in 1995. Currently he is a Group Leader at the Institute of Ion Beam Physics and Materials Research, Helmholtz-Zentrum Dresden-Rossendorf, Germany, and a Visiting Professor at Aalto University, Finland. His scientific interests lie in the areas of computational materials science, electronic structure calculations, two-dimensional materials, and irradiation effects in solids. Throughout his career, he has co-authored more than 200 peer-refereed papers. His awards and recognitions include HZDR Research Award, Highly Cited Researcher (Physics) from Clarivate Analytics (ex. Web of Science); American Physical Society "Outstanding Referee".

NANO LETTERS

pubs.acs.org/NanoLett Letter

Helium Ion Microscopy for Reduced Spin Orbit Torque Switching Currents

Peter Dunne,* Ciaran Fowley,* Gregor Hlawacek, Jinu Kurian, Gwenael Atcheson, Silviu Colis, Niclas Teichert, Bohdan Kundys, Munuswamy Venkatesan, Jürgen Lindner, Alina Maria Deac, Thomas M. Hermans, J. M. D. Coey, and Bernard Doudin

Cite This: *Nano Lett.* 2020, 20, 7036−7042 Read Online

ACCESS | Metrics & More | Article Recommendations | Supporting Information

ABSTRACT: Spin orbit torque driven switching is a favorable way to manipulate nanoscale magnetic objects for both memory and wireless communication devices. The critical current required to switch from one magnetic state to another depends on the geometry and the intrinsic properties of the materials used, which are difficult to control locally. Here, we demonstrate how focused helium ion beam irradiation can modulate the local magnetic anisotropy of a Co thin film at the microscopic scale. Real-time *in situ* characterization using the anomalous Hall effect showed up to an order of magnitude reduction of the magnetic anisotropy under irradiation, with multilevel switching demonstrated. The result is that spin-switching current densities, down to 800 kA cm^{-2}, can be achieved on predetermined areas of the film, without the need for lithography. The ability to vary critical currents spatially has implications not only for storage elements but also neuromorphic and probabilistic computing.

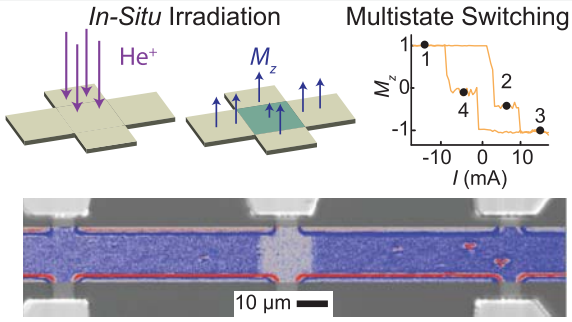

KEYWORDS: *spintronics, spin orbit torque switching, nanomagnetism, ion beam irradiation*

Spin transport across material interfaces is sensitive to the electronic and structural nature of the interface. Since the discovery of giant magnetoresistance in the late 1980s[1,2] the field of spintronics has grown steadily through to the theoretical[3] and experimental realisation of spin transfer torque,[4,5] with modern data storage already exploiting it to change magnetisation states in magnetic tunnel junctions.[6] Spin orbit torque (SOT) switching, on the other hand, is a relatively new topic,[7−9] relying on the spin Hall[9] and Rashba[10] effects to manipulate static and dynamic magnetization states by the flow of electrical current in adjacent heavy metal (HM) layers. In contrast to spin-transfer-torque MRAMs,[11] SOT devices require less demanding 3D fabrication, greatly simplifying their production. Moreover, their planar nature allows for easy visualization and easier exploitation of the stray magnetic fields in applications such as reprogrammable magnetic domain configurations for spin-wave logic.[12]

The present drive to reduce switching currents and energy consumption is constrained by the selection of materials necessary to switch a magnetic domain via SOT. Similarly, real devices require multistep nanofabrication to define memory storage cells. Here, we present a new method to both reduce the switching currents and to avoid multistep lithography by using He$^+$ irradiation to locally modify the material properties in a single layer. Consequently, we can reduce the critical current density in a macroscopic device by almost an order of magnitude. Furthermore, we demonstrate how *in situ* electrical measurement during irradiation allows precise control over the manipulation of the perpendicular magnetic anisotropy, capturing its evolution as a function of ion dose, making possible high-precision control and reproducibility of the process.

Light ion irradiation can lead to structural reorganization of stable material phases while preserving overall atomic composition with little to no topological damage.[13] This allows for the reduction of PMA in thin magnetic multilayers,[14,15] which is caused by the intermixing of layers and the increase of interfacial roughness.[13] Furthermore, He$^+$ and Ar$^+$ broad-beam irradiation have been used to tailor SOT driven domain-wall dynamics,[16] improve the spectral line width of SOT nano-oscillators,[17] and reduce the critical current density to switch the magnetization of extended thin films via SOT.[18] Patterned magnetic anisotropy using broad beam irradiation has been demonstrated using shadow masks, but the smallest patterned

Received: May 14, 2020
Revised: September 14, 2020
Published: September 15, 2020

https://dx.doi.org/10.1021/acs.nanolett.0c02060
Nano Lett. 2020, 20, 7036−7042

volumes are mostly determined by the lithography process rather than the ion-beam interaction volume.[15] On the contrary, focused helium ion beams allow precise control of perpendicular magnetic anisotropy[19,20] and magnetization[21] on the order of the size of the collision cascade ($\lesssim$10 nm).[22] With helium ion microscope (HIM) based He^+ irradiation, the lateral dimensions of the magnetic structures are limited only by the collision cascade[22] due to the minimal beam-size of only 0.5 nm.

Samples of Ta(5)/Pt(2)/Co(1.0)/W(1.5)/Pt(1.5)/Ta(1.5) were prepared by magnetron sputtering on Si wafers, and patterned into 10 μm Hall bar structures by a combination of UV lithography, ion milling, and lift-off. An asymmetric stack of Pt, Co, and W was chosen, as the opposite spin Hall angles of the Pt−Co and Co−W interfaces are known to maximize SOT switching efficiency.[23] SQUID magnetometry on unpatterned films with the substrate orientated parallel and perpendicular to the applied field indicated robust PMA (Figure 1a), as expected

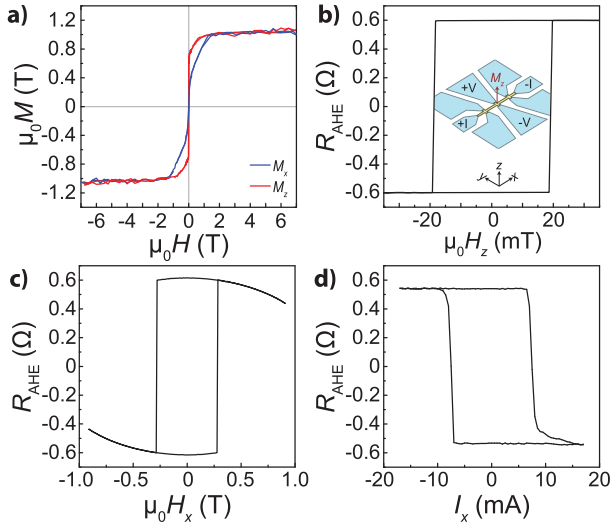

Figure 1. (a) SQUID-VSM magnetometry parallel (M_x) and perpendicular (M_z) to the substrate. The anomalous Hall resistance of virgin junctions versus (b) $\mu_0 H_z$; (c) $\mu_0 H_x$; and (d) applied DC pulse current, I_x, under a bias field of $\mu_0 H_x$ = 150 mT.

for a subnanometer Co film[24] with an effective anisotropy field of 1.28 T and a saturation magnetization $\mu_0 M_s$ of 1.02 T. Anomalous Hall effect measurements confirmed that the PMA remains intact on the patterned Hall bars (Figures 1b,c). Here, we found square hysteresis loops and coercivities of ∼20 mT (Figure 1b) for magnetic fields applied perpendicular to the film along z and effective magnetic anisotropies well over 1 T (Figure 1c) for hard axis measurements (along x). At positive saturation ($+m_z$), the anomalous Hall resistance is 0.59 Ω.

Current-induced (I_x) switching measurements under a bias field $\mu_0 H_x$ = 150 mT (Figure 1d) yield a critical current density, J_c, of 6.0 MA cm^{-2} for full magnetization reversal in the microfabricated structure. To minimize thermal effects while sweeping the current, I_x was pulsed for a duration of 2 ms with a delay of 1 s between subsequent pulses, that is, a duty cycle of 0.2%. Similar to the field driven switching in Figure 1b, there is only one step and the saturated state has a resistance of 0.57 Ω.

The patterned devices were locally irradiated with helium ions with a 30 kV acceleration voltage using an Orion Nanofab helium ion microscope system, while in real time we monitored the evolution of the anomalous Hall resistance *in situ*. This electrical characterization system consists of four Kleindieck MM3A micromanipulators which allow three-dimensional positioning of the contacting needles in a high vacuum environment (see Figure 2a). A Keithley 2400 source meter was used to apply current and read the voltage drop corresponding to the longitudinal and transverse resistances. A current of 1 mA applied along the x-axis is used to probe the evolution of the anomalous Hall resistance close to zero-applied magnetic field. The combination of the HIM with the possibility for *in situ* control of the magnetization state via Hall resistance measurements is unique in that it allows unprecedented spatial resolution and high flexibility in the patterning by avoiding high resolution but low yield lithography steps, resulting in a high turn around for explorative experiments. This compliments alternative approaches based on laser illumination with a 1.5 μm lateral resolution,[25] ion broad beam irradiation which requires thick photoresist masks that limit the achievable spatial resolution,[18] electric field control of anisotropy,[26] or even oxidation which is CMOS compatible but inflexible and not ideal for fundamental studies.[27]

During irradiation, the anomalous Hall resistance steadily decreases (Figure 2b) until a critical dose of 35 ions nm^{-2} is reached, and a sharp switching is observed. The sharp fall in ΔR is complete at 37 ions nm^{-2}. The total fall of resistance (0.52 Ω) is close to the full deflection observed in the *ex situ* measurements shown in Figure 1, marked as a gray dashed line, and indicates a reduced effective anisotropy field in the irradiated zone (H_{K2}) compared to that of the extended structure (H_{K1}) (Figure 2b). The layer intermixing introduced by irradiation gives control over K_{eff}, and H_{K2} thus becomes an experimentally tunable parameter. Although the irradiations were carried out over the complete area of the Hall cross, as shown in Figure 2c, the close proximity of the unirradiated areas allow for residual information from those regions to be gathered in the Hall loops, leading to the offset of ∼0.1 Ω in Figure 2b.

We selected four doses along this irradiation curve to demonstrate the ease of applying this technique to the reduction of critical currents for spin orbit torque switching. Figure 2d shows the corresponding anomalous Hall response versus $\mu_0 H_x$ for 1, 20, 30, and 50 ions nm^{-2}. Aside from the reduction in magnetic anisotropy field, evidenced by the saturation of R_{AHE} at lower in-plane applied fields, several steps are observed in the anomalous Hall loops for irradiation doses ≥30 ions nm^{-2}. The additional steps correspond to the unchanged anisotropy in the unirradiated adjacent regions. This offset is highly dependent on the accuracy of overlaying the irradiation box with the junction area, and the residual Hall resistance is never precisely the same for each junction. However, the multistep switching, as seen in Figure 2d, is always a result of the reversal of neighboring regions adjacent to the Hall cross.

Assuming coherent rotation of the magnetization, the normalized first quadrant magnetization, M_z', (Figure 2e) can be fitted with[28]

$$M_z' = \sqrt{1 - \left(\frac{\mu_0 H_x}{\mu_0 H_K}\right)^2} \tag{1}$$

which yields the magnetic anisotropy field, $\mu_0 H_K$, as a function of irradiation dose (Figure 2f). We observe a continuous decrease in the anisotropy field from 1.32 T for as-deposited films to only 0.12 T for samples irradiated beyond the critical dose of 35 ions nm^{-2}. The saturation magnetization, M_s, (Figure 2f) was

https://dx.doi.org/10.1021/acs.nanolett.0c02060
Nano Lett. 2020, 20, 7036−7042

Nano Letters pubs.acs.org/NanoLett Letter

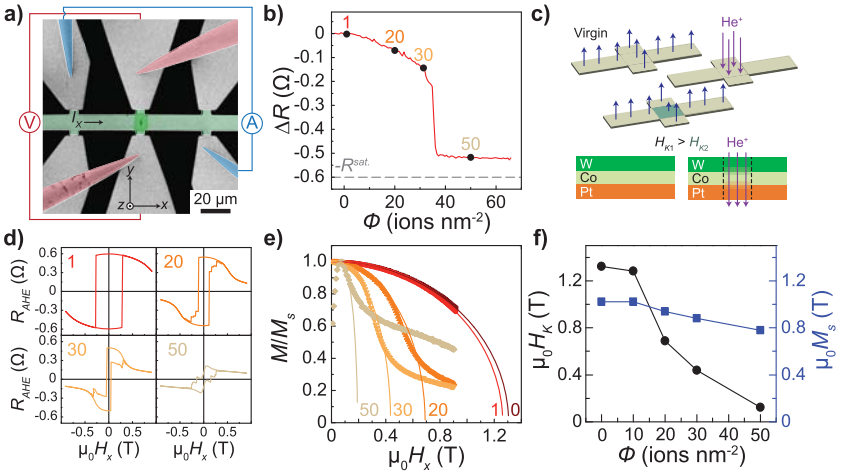

Figure 2. (a) False-colored helium ion microscopy image of the *in situ* contacting of a 10 μm Hall bar structure. The gray areas are the gold contact pads, the green stripe represents the magnetic multilayer under investigation, the red needle probes are for measuring the Hall voltage, while the blue ones are for applying the current. One such image corresponds to a dose of only 0.1 ions nm^{-2}. An overlay schematic shows the current and voltage lines used. (b) *In situ* change in anomalous Hall resistivity as a function of irradiation dose between 0 and 70 ions nm^{-2}. (c) Schematic of the local irradiation process, whereby the local anisotropy is reduced due to interface mixing of the upper and lower Co/HM interfaces. (d) *Ex situ* R_{AHE} versus $\mu_0 H_x$ curves at selected doses marked in (a): 1 ion nm^{-2}, 20 ions nm^{-2}, 30 ions nm^{-2}, and 50 ions nm^{-2}. (e) Normalized magnetization from (d) for all irradiated and virgin samples with solid line fits using eq 1 to determine the anisotropy field, as a function of irradiation dose. (f) Anisotropy field and saturation magnetization determined from *ex situ* anomalous Hall effect loops.

determined from the relative change in the saturation Hall resistance with ion dose when the magnetic field is applied out-of-plane along z (not shown here). M_s is reduced at higher ion doses due to alloying of the Co/HM interfaces but is less sensitive than the magnetic anisotropy field, H_K, only reducing to 86% of the initial value compared to 33% for the anisotropy field after a dose of 30 ions nm^{-2}.

Both the H_K and M_s play an important role in current-induced SOT switching. Under a macrospin approximation with the condition $H_x \ll H_K$, where H_x is a magnetic bias field applied in-plane, the critical current density, J_c, required to switch the magnetization direction of a magnetic state (in SI units) is[29]

$$J_c = \frac{2e\mu_0 M_s t_f}{\hbar\theta_{SH}}\left(\frac{H_K}{2} - \frac{H_x}{\sqrt{2}}\right) \tag{2}$$

where e is the electronic charge, $\hbar$ is the reduced Planck constant, t_f is the magnetic free-layer thickness, and θ_{SH} is the spin Hall angle. However, when the applied field is comparable to the anisotropy, as we find for increased ion doses, the critical current density can instead be written as[29]

$$J_c = \frac{2e\mu_0 M_s t_f}{\hbar\theta_{SH}}\left(\sqrt{\frac{H_K^2}{32}[8 + 20b^2 - b^4 - b(8 + b^2)^{3/2}]}\right) \tag{3}$$

where $b = \frac{H_x}{H_K}$. The effect of ion dose on J_c is initially minimal for doses up to 20 ions nm^{-2} (Figures 2f, 3a, and Table 1) with J_c^- reducing from −6.0 to −5.0 MA cm^{-2} (for $\mu_0 H_x$ = 150 mT). For 30 ions nm^{-2}, close to the critical dose, the critical current density is, however, reduced by almost 1 order of magnitude to −800 kA cm^{-2}. At larger doses, 50 ions nm^{-2}, we only observe the switching in the peripheral regions adjacent to the Hall cross.

Nonetheless, reducing the critical current density is not the sole criterion for improvement of SOT switching of magnetic states. Additionally, we define a SOT switching efficiency, η, as the ratio of the magnetic energy barrier (K_{eff}) per unit area (in

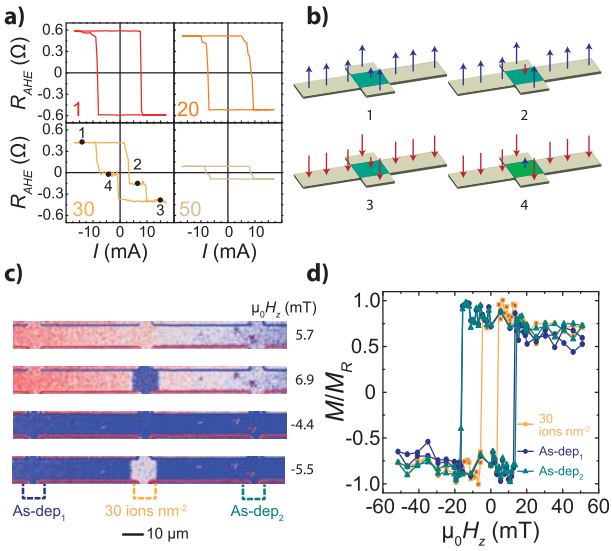

Figure 3. (a) Current driven SOT switching curves at the same doses as Figure 2 under a bias field of $\mu_0 H_x$ = 150 mT. (b) Schematic of four distinct magnetic configurations achievable through electric current switching, numbered 1−4 in 30 ions nm^{-2} subpanel of panel (a). (c) MOKE images of the Hall bar under four different external fields, $\mu_0 H_z$, displaying the four different magnetic states shown in panel b. (d) MOKE-acquired hysteresis loops for the device receiving a dose of 30 ions nm^{-2} at three different 10 × 10 μm^2 areas: one irradiated region and two nonirradiated regions as show in panel (c).

the magnetic free layer t_f) versus the electrical power (P) per unit area (in the entire stack thickness d) required to switch the magnetic state, in units of seconds

$$\eta = \frac{K_{eff} t_f}{Pd} = \frac{\mu_0 M_s (H_K - H_x) t_f}{2J_c^2 \rho d} \tag{4}$$

https://dx.doi.org/10.1021/acs.nanolett.0c02060
Nano Lett. 2020, 20, 7036−7042

Nano Letters pubs.acs.org/NanoLett Letter

Table 1. Irradiation Dose Dependency of the Thin Film Magnetic Properties[a]

Dose ions nm^{-2}	K_{eff} kJ m^{-3}	Δ	ρ $\mu\Omega$·cm	I_c^- mA	I_c^+ mA	J_c^- MA cm^{-2}	J_c^+ MA cm^{-2}	J_c^{th} MA cm^{-2}	η ps	η_i fs
0	537	133	214	−7.5	7.5	−6.0	6.0	459	7.1	1.2
1	521	129	214	−7.5	7.5	−6.0	6.0	442	6.9	1.2
20	257	64	219	−6.2	7.5	−5.0	6.0	184	4.3	2.5
30	153	39	224	−1.0	3.3	−0.8	2.7	85	86	4.2
50	38	9	235							

[a]The properties are effective anisotropy K_{eff}, thermal stability parameter Δ, negative and positive critical currents I_c^-, I_c^+, the corresponding experimental critical current densities J_c^-, J_c^+, the theoretical critical current density J_c^{th} determined using eq 3 with $\mu_0 H_x$ = 150 mT, and an effective spin hall angle measured to be θ_{SH} = 0.4, the switching efficiency η calculated from eq 4, and intrinsic efficiency η_i using eq 5. Note that for 50 ions nm^{-2}, only switching of adjacent unirradiated regions was detected.

Table 2. Comparing Switching Efficiencies

Stack	J_c[a] MA cm^{-2}	B_x mT	θ_{SH}[b]	Δ[c]	P[d] PW m^{-3}	η ps	η_i fs	ref
Pt 3/Co 0.6/AlO$_x$ 1.6	78	47.5	0.07	74	2330	0.02	0.09	10
Ta 3/Pt 5/Co 0.6/Cr 2/Ta 5	2.70	20	0.41	106	0.89	28	2.02	43
Ta 3/Pt 5/Co 0.8/W 3/TaO$_x$ 2	2.30	5	0.244	136	0.42	69	0.78	30
Ta 5/CoFeB 1.1/MgO 2/Ta 2	3.09	20	0.08	56	1.91	14	0.19	44
Bi_2Se_3 7.4[e]/CoTb 4.6/SiN$_x$ 3	3.0	100	0.16	73	2.48	6.2	0.23	45
Pt 5/$BaFe_{12}O_{19}$ 3[f]	5.7	123	0.07	232	6.26	18	0.04	31
Pt 4/Co 0.4/Ni 0.2/Co 0.4/Pt 2[g]	7.1	0	0.07	13	10.2	0.74	0.72	37

[a]If $J_c^- \neq J_c^+$, then the smaller of the two values is taken. [b]When not reported, literature values of θ_{SH} were taken from ref 46; for multilayers with adjacent layers of opposite θ_{SH}, the magnitude of the larger one was chosen. [c]Calculated for $\mu_0 H_x$ = 0. [d]When not reported, calculated using bulk resistivity values from ref 47 and then corrected using the M-S model.[48] [e]Topological insulator used for spin injection. [f]Ferromagnetic insulator. [g]Zero-field switching device, moving between a remnant state m_z = 0, and a downward pointing $-m_z$ state.

where ρ is the total resistivity of the device. The choice of units is deliberate; the minimum pulse length for deterministic SOT switching is not always reported, but if it is known then η can be divided by this duration to determine the dimensionless efficiency. Either way, a larger value of η implies a more stable magnetic element that requires less power to switch. Defined in this way, the switching efficiency of different material systems can be compared regardless of the pulse length, so long as the bias fields are similar. Furthermore, increasing N, the number of Pt/Co/W repeats, will not impact the efficiency if the relative amount of magnetic material remains the same, that is, t_f/d is constant. If the bias fields are not similar, substituting J_c from eq 2 into eq 4 under the condition $H_x \ll H_K$, leads to an intrinsic SOT efficiency for PMA systems

$$\eta_i = \frac{\hbar^2 \theta_{SH}^2}{2\mu_0 M_s H_K e^2 \rho d t_f} \tag{5}$$

The advantage of eq 5 is that it depends solely on intrinsic material properties and not on the experimental conditions, thus making it a more transparent comparator between different reported systems, particularly when the experimental current pulse may be much longer than the intrinsic switching time. Its drawback is that it is based on a macrospin approximation, which cannot envisage a multidomain response, and therefore overestimates the critical current density by a factor 10−100.

Nevertheless, eq 5 provides a theoretical guideline for optimum parameters when considering material systems. This expression illustrates that to achieve large switching efficiencies, a minimal amount of conductive material must be used, while retaining a large spin Hall angle and a small anisotropy field. We find that neither the calculated spin Hall angle nor resistivity change significantly upon irradiation with the former remaining ∼0.4 with the latter ranging from 215−235 $\mu\Omega$.cm. Similar to J_c, we find there is negligible change in the intrinsic switching efficiency, η_i, for irradiation doses <20 ion nm^{-2} which remains close to 2 fs (Table 1), increasing to a maximum of 4.2 fs at 30 ions nm^{-2}. In contrast, the experimental efficiency, η, is initially ∼7.1 ps and drops at 20 ions nm^{-2} to 4.3 ps before then increasing to its maximum of 86 ps at 30 ions nm^{-2}, an order of magnitude improvement upon the virgin state. The discrepancy between η and η_i is due to the breakdown of the macrospin approximation used to calculate the latter. In all cases, the switching efficiency compares favorably to the literature values listed in Table 2, where efficiencies are of order 0.01−10 ps with a maximum of 69 ps found for metallic Ta/Pt/Co/W/Ta multilayers[30] and 21 ps for insulating barium ferrite on Pt,[31] whereas zero-field switching devices[26] present much lower efficiencies (0.74 ps).

Returning to the SOT switching for 30 ions nm^{-2}, shown in Figure 3a, we sketch the magnetic states at points 1, 2, 3, and 4 in Figure 3b. As the interior of the Hall cross can be addressed separately from the rest of the device, this forms a two-state system that can be addressed electrically as shown in Figure 3a, or magnetically as shown in Figure 2c and Figure 3c,d. Electrical switching involves applying a bias in-plane field (here 150 mT) and pulsing currents in a range of ±3 mA to ensure switching of only the irradiated region. This leads to a switch between states 1 and 2 or 3 and 4 in (Figure 3a,b). Otherwise pulsing currents of order ±7.5 mA switches the magnetization of the entire device between states 1 and 3 (Figure 3a,b). Magneto-optic Kerr effect (MOKE) imaging under magnetic fields normal to the device ($\mu_0 H_z$) confirms that the entire irradiated region switches independently from the rest of the device, Figure 3c. Individual hysteresis loops for the irradiated (30 ions nm^{-2}) and nonirradiated regions (as-dep$_1$, as-dep$_2$) are shown in Figure 3d. The irradiated and unirradiated regions exhibit coercivities which are well spaced in magnetic field, $\mu_0 H_c$ = 5 mT and $\mu_0 H_c$ = 16 mT, respectively. The reader is directed to SI video 1 to view the full magnetization response during a field sweep.

Although there is an equivalence between electrical and magnetic switching, electrical SOT switching is more robust to

https://dx.doi.org/10.1021/acs.nanolett.0c02060
Nano Lett. 2020, 20, 7036−7042

variability in lithographic processing of the Hall bars than magnetic switching. This is because the former depends on the perpendicular magnetic anisotropy of a device, compared to coercivity for the latter. We find less than 1% variation in the magnetic anisotropy for the nonirradiated devices, $\mu_0 H_K = 1.32 \pm 0.01$ T, as the anisotropy is determined by the deposition process, which in bulk, nonpatterned, thin films is 1.28 ± 0.05 T. In contrast, we find a 26% variation of coercivity in the same devices, 14 ± 4 mT, reflecting the strong dependence of the coercivity on the lithographic processing and slight variations in dimensions of the Hall bars. Since we address the anisotropy directly with ion irradiation, this illustrates the advantageous precision and robustness of focused ion beam irradiation for magnetic element patterning compared to material removal.

In order to assess the suitability of the device as a memory storage element, we discuss the effect of He^+ irradiation on the thermal stability of the created magnetic bits. As expected, the reduction in J_c does come at the cost of thermal stability, defined by a parameter $\Delta = K_{eff}V/k_BT$, where V is the magnetic element volume, k_B is Boltzmann's constant, and T is temperature. However, even for a 1 nm thick, 32 nm sided element, that is, a 1024 nm^3 volume, $\Delta = 64$ for doses as high as 20 ions nm^{-2}, more than the 10 year stability criterion of $\Delta = 60$ used in magnetic recording.[32] Close to the critical dose at 30 ions nm^{-2}, Δ drops to 38, which is the equivalent of 95% data retention for 16 days,[33] but unlike data storage long-term stability is not critical to all applications. In fact, weakly bistable devices can be suitable for spin Hall oscillators, where the strength and modulation of spin wave propagation depends on the magnetic anisotropy.[34] An easy way to improve the thermal stability would be to add N Pt/Co/W repeats to the system. Δ will increase linearly with N while not impacting η (eq 4), as stated previously. Furthermore, the reduction in local magnetic anisotropy allows for minimal losses during magnetization switching. This level of control highlights the effectiveness of this method to tailor the switching current density in PMA multilayers. Although only two steps are shown in Figure 3, one can also write switching current spatial gradients of almost any value directly. This allows for complex tailoring of not only field-free memory elements[35−38] but even permits the control of spin-wave waveguide locations coupled with on-and-off spin-wave transmission control.[12,39] Such switching current spatial gradients can be used to tailor the synaptic-like response from PMA memory elements[40] when applied to neuromorphic computing or even logic elements.[27] Extremely low thermal stability would mean metastable 0 and 1 states which can be applied to probabilistic computing[41] or random number generation.[42]

In summary, a He^+ microscope has been used to perform maskless light-ion irradiation on perpendicular magnetic anisotropy stacks for local control of the SOT switching properties. *In situ* electrical measurements of anisotropy reduction provides real-time control of the anisotropy, allowing accurate determination of the critical dose needed to reach a desired, up-to-the-transition-to in-plane magnetic anisotropy. The corresponding reduction in critical current densities for SOT switching are nearly linear with decreasing anisotropy. Irradiation at doses just below the critical dose allows us to achieve almost an order of magnitude control over the critical current required for robust switching, and DC switching current densities as low as 800 kA cm^{-2} are achieved, which we believe is the lowest to date. Moreover, the switching efficiency of 86 ps is larger than the previous state of the art. It illustrates the unique advantages of this approach and opens the door to preferential switching of predetermined areas of a device, limited only by the nanometer-resolution of the He^+ ion beam microscopy, while preserving the flat topography of the initial magnetic stack.

■ ASSOCIATED CONTENT

Supporting Information

The Supporting Information is available free of charge at https://pubs.acs.org/doi/10.1021/acs.nanolett.0c02060.

Derivation of eq 1 using a macrospin approximation, and an example fit to the sample irradiated with 20 ions nm^{-2}; anomalous Hall resistance plots for eight nonirradiated samples for $\mu_0 H_z$ and $\mu_0 H_x$; discussion of the Mayadas−Shatzkes model used for applying thickness dependent corrections to bulk resistivities (PDF)

Supporting movie of *ex situ* normalized magnetization of a 10 μm wide Hall bar under a magnetic field sweep from −50 mT to +50 mT and then back to −50 mT using a MOKE microscope. The central 10×10 μm^2 area was irradiated with a dose of 30 ions/nm^2 (MP4)

■ AUTHOR INFORMATION

Corresponding Authors

Peter Dunne − *Université de Strasbourg, CNRS, IPCMS UMR 7504, F-67034 Strasbourg, France; Université de Strasbourg, CNRS, ISIS, 67000 Strasbourg, France;* orcid.org/0000-0003-2370-2059; Email: peter.dunne@ipcms.unistra.fr

Ciaran Fowley − *Institute of Ion Beam Physics and Materials Research, Helmholtz-Zentrum Dresden - Rossendorf, 01328 Dresden, Germany*; Email: c.fowley@hzdr.de

Authors

Gregor Hlawacek − *Institute of Ion Beam Physics and Materials Research, Helmholtz-Zentrum Dresden - Rossendorf, 01328 Dresden, Germany;* orcid.org/0000-0001-7192-716X

Jinu Kurian − *Université de Strasbourg, CNRS, IPCMS UMR 7504, F-67034 Strasbourg, France*

Gwenael Atcheson − *AMBER and School of Physics, Trinity College, Dublin 2, Ireland*

Silviu Colis − *Université de Strasbourg, CNRS, IPCMS UMR 7504, F-67034 Strasbourg, France*

Niclas Teichert − *AMBER and School of Physics, Trinity College, Dublin 2, Ireland*

Bohdan Kundys − *Université de Strasbourg, CNRS, IPCMS UMR 7504, F-67034 Strasbourg, France*

Munuswamy Venkatesan − *AMBER and School of Physics, Trinity College, Dublin 2, Ireland*

Jürgen Lindner − *Institute of Ion Beam Physics and Materials Research, Helmholtz-Zentrum Dresden - Rossendorf, 01328 Dresden, Germany*

Alina Maria Deac − *Institute of Ion Beam Physics and Materials Research, Helmholtz-Zentrum Dresden - Rossendorf, 01328 Dresden, Germany*

Thomas M. Hermans − *Université de Strasbourg, CNRS, ISIS, 67000 Strasbourg, France*

J. M. D. Coey − *AMBER and School of Physics, Trinity College, Dublin 2, Ireland*

Bernard Doudin − *Université de Strasbourg, CNRS, IPCMS UMR 7504, F-67034 Strasbourg, France*

Complete contact information is available at: https://pubs.acs.org/10.1021/acs.nanolett.0c02060

https://dx.doi.org/10.1021/acs.nanolett.0c02060
Nano Lett. 2020, 20, 7036−7042

Author Contributions

The manuscript was written through contributions of all authors. All authors have given approval to the final version of the manuscript.

Funding

We acknowledge the support of the Labex NIE 11-LABX-0058_NIE within the Investissement d'Avenir program ANR-10-IDEX-0002-02, and the International Center for Frontier Research in Chemistry (icFRC). This project has received funding from the European Union's Horizon 2020 research and innovation program under the Marie Skłodowska-Curie Grant Agreement 766007.

Notes

The authors declare no competing financial interest.

Source data for Figures 1−3 and any other data that support the findings of this study and the Python scripts used to process the data are available on the Zenodo data repository: https://zenodo.org/communities/mami-h2020/

■ ACKNOWLEDGMENTS

We thank Fabien Chevrier for technical support, and the staff of the STnano nanofabrication facility. The nanofabrication facilities (NanoFaRo) at the Ion Beam Center at the HZDR are also gratefully acknowledged.

■ ABBREVIATIONS

HM	heavy metal
MRAM	magnetic random-access memory
PMA	perpendicular magnetic anisotropy
SOT	spin orbit torque

■ REFERENCES

(1) Baibich, M. N.; Broto, J. M.; Fert, A.; Van Dau, F. N.; Petroff, F.; Etienne, P.; Creuzet, G.; Friederich, A.; Chazelas, J. Giant Magnetoresistance of (001)Fe/(001)Cr Magnetic Superlattices. *Phys. Rev. Lett.* **1988**, *61* (21), 2472−2475.

(2) Binasch, G.; Grünberg, P.; Saurenbach, F.; Zinn, W. Enhanced Magnetoresistance in Layered Magnetic Structures with Antiferromagnetic Interlayer Exchange. *Phys. Rev. B: Condens. Matter Mater. Phys.* **1989**, *39* (7), 4828−4830.

(3) Slonczewski, J. C. Current-Driven Excitation of Magnetic Multilayers. *J. Magn. Magn. Mater.* **1996**, *159* (1), L1.

(4) Myers, E. B.; Ralph, D. C.; Katine, J. A.; Louie, R. N.; Buhrman, R. A. Current-Induced Switching of Domains in Magnetic Multilayer Devices. *Science* **1999**, *285* (5429), 867−870.

(5) Kiselev, S. I.; Sankey, J. C.; Krivorotov, I. N.; Emley, N. C.; Schoelkopf, R. J.; Buhrman, R. A.; Ralph, D. C. Microwave Oscillations of a Nanomagnet Driven by a Spin-Polarized Current. *Nature* **2003**, *425* (6956), 380−383.

(6) *IBM Unveils 19TB SSD With Everspin MRAM Data Cache | Everspin*. https://www.everspin.com/news/ibm-unveils-19tb-ssd-everspin-mram-data-cache (accessed Nov 19, 2019).

(7) Miron, I. M.; Garello, K.; Gaudin, G.; Zermatten, P.-J.; Costache, M. V.; Auffret, S.; Bandiera, S.; Rodmacq, B.; Schuhl, A.; Gambardella, P. Perpendicular Switching of a Single Ferromagnetic Layer Induced by In-Plane Current Injection. *Nature* **2011**, *476* (7359), 189.

(8) Gambardella, P.; Miron, I. M. Current-Induced Spin−Orbit Torques. *Philos. Trans. R. Soc., A* **2011**, *369*, 3175−3197.

(9) Liu, L.; Pai, C.-F.; Li, Y.; Tseng, H. W.; Ralph, D. C.; Buhrman, R. A. Spin-Torque Switching with the Giant Spin Hall Effect of Tantalum. *Science* **2012**, *336* (6081), 555−558.

(10) Miron, I. M.; Gaudin, G.; Auffret, S.; Rodmacq, B.; Schuhl, A.; Pizzini, S.; Vogel, J.; Gambardella, P. Current-Driven Spin Torque Induced by the Rashba Effect in a Ferromagnetic Metal Layer. *Nat. Mater.* **2010**, *9* (3), 230.

(11) Perrissin, N.; Lequeux, S.; Strelkov, N.; Chavent, A.; Vila, L.; Buda-Prejbeanu, L. D.; Auffret, S.; Sousa, R. C.; Prejbeanu, I. L.; Dieny, B. A Highly Thermally Stable Sub-20 Nm Magnetic Random-Access Memory Based on Perpendicular Shape Anisotropy. *Nanoscale* **2018**, *10* (25), 12187−12195.

(12) Wagner, K.; Kákay, A.; Schultheiss, K.; Henschke, A.; Sebastian, T.; Schultheiss, H. Magnetic Domain Walls as Reconfigurable Spin-Wave Nanochannels. *Nat. Nanotechnol.* **2016**, *11* (5), 432−436.

(13) Fassbender, J.; Ravelosona, D.; Samson, Y. Tailoring Magnetism by Light-Ion Irradiation. *J. Phys. D: Appl. Phys.* **2004**, *37* (16), R179−R196.

(14) Hoshi, Y.; Naoe, M. Differences between Sputtering Methods in The Formation of Amorphous Magnetic Alloy Films. *MRS Online Proceedings Library Archive* **1985**, *58*. DOI: 10.1557/PROC-58-75.

(15) Chappert, C.; Bernas, H.; Ferré, J.; Kottler, V.; Jamet, J.-P.; Chen, Y.; Cambril, E.; Devolder, T.; Rousseaux, F.; Mathet, V.; Launois, H. Planar Patterned Magnetic Media Obtained by Ion Irradiation. *Science* **1998**, *280* (5371), 1919−1922.

(16) Zhao, X.; Zhang, B.; Vernier, N.; Zhang, X.; Sall, M.; Xing, T.; Diez, L. H.; Hepburn, C.; Wang, L.; Durin, G.; Casiraghi, A.; Belmeguenai, M.; Roussigné, Y.; Stashkevich, A.; Chérif, S. M.; Langer, J.; Ocker, B.; Jaiswal, S.; Jakob, G.; Kläui, M.; Zhao, W.; Ravelosona, D. Enhancing Domain Wall Velocity through Interface Intermixing in W-CoFeB-MgO Films with Perpendicular Anisotropy. *Appl. Phys. Lett.* **2019**, *115* (12), 122404.

(17) Jiang, S.; Khymyn, R.; Chung, S.; Le, T. Q.; Diez, L. H.; Houshang, A.; Zahedinejad, M.; Ravelosona, D.; Åkerman, J. Reduced Spin Torque Nano-Oscillator Linewidth Using He + Irradiation. *Appl. Phys. Lett.* **2020**, *116* (7), 072403.

(18) Yun, J.; Zuo, Y.; Mao, J.; Chang, M.; Zhang, S.; Liu, J.; Xi, L. Lowering Critical Current Density for Spin-Orbit Torque Induced Magnetization Switching by Ion Irradiation. *Appl. Phys. Lett.* **2019**, *115* (3), 032404.

(19) Franken, J. H.; Hoeijmakers, M.; Lavrijsen, R.; Kohlhepp, J. T.; Swagten, H. J. M.; Koopmans, B.; van Veldhoven, E.; Maas, D. J. Precise Control of Domain Wall Injection and Pinning Using Helium and Gallium Focused Ion Beams. *J. Appl. Phys.* **2011**, *109* (7), 07D504.

(20) Fowley, C.; Diao, Z.; Faulkner, C. C.; Kally, J.; Ackland, K.; Behan, G.; Zhang, H. Z.; Deac, A. M.; Coey, J. M. D. Local Modification of Magnetic Anisotropy and Ion Milling of Co/Pt Multilayers Using a He + Ion Beam Microscope. *J. Phys. D: Appl. Phys.* **2013**, *46* (19), 195501.

(21) Röder, F.; Hlawacek, G.; Wintz, S.; Hübner, R.; Bischoff, L.; Lichte, H.; Potzger, K.; Lindner, J.; Fassbender, J.; Bali, R. Direct Depth- and Lateral- Imaging of Nanoscale Magnets Generated by Ion Impact. *Sci. Rep.* **2015**, *5*, 16786.

(22) Hlawacek, G.; Veligura, V.; van Gastel, R.; Poelsema, B. Helium Ion Microscopy. *J. Vac. Sci. Technol., B: Nanotechnol. Microelectron.: Mater., Process., Meas., Phenom.* **2014**, *32* (2), 020801.

(23) Woo, S.; Mann, M.; Tan, A. J.; Caretta, L.; Beach, G. S. D. Enhanced Spin-Orbit Torques in Pt/Co/Ta Heterostructures. *Appl. Phys. Lett.* **2014**, *105* (21), 212404.

(24) Carcia, P. F. Perpendicular Magnetic Anisotropy in Pd/Co and Pt/Co Thin-film Layered Structures. *J. Appl. Phys.* **1988**, *63* (10), 5066−5073.

(25) Cao, Y.; Sheng, Y.; Edmonds, K. W.; Ji, Y.; Zheng, H.; Wang, K. Deterministic Magnetization Switching Using Lateral Spin−Orbit Torque. *Adv. Mater.* **2020**, *32* (16), 1907929.

(26) Lee, K.-Y.; Jo, S.; Tan, A. J.; Huang, M.; Choi, D.; Park, J. H.; Ji, H.-I.; Son, J.-W.; Chang, J.; Beach, G. S. D.; Woo, S. Fast Magneto-Ionic Switching of Interface Anisotropy Using Yttria-Stabilized Zirconia Gate Oxide. *Nano Lett.* **2020**, *20* (5), 3435−3441.

(27) Baek, S. C.; Park, K.-W.; Kil, D.-S.; Jang, Y.; Park, J.; Lee, K.-J.; Park, B.-G. Complementary Logic Operation Based on Electric-Field Controlled Spin−Orbit Torques. *Nat. Electron* **2018**, *1* (7), 398−403.

(28) Fowley, C.; Ouardi, S.; Kubota, T.; Yildirim, O.; Neudert, A.; Lenz, K.; Sluka, V.; Lindner, J.; Law, J. M.; Mizukami, S.; Fecher, G. H.; Felser, C.; Deac, A. M. Direct Measurement of the Magnetic Anisotropy

https://dx.doi.org/10.1021/acs.nanolett.0c02060
Nano Lett. 2020, 20, 7036−7042

Field in Mn−Ga and Mn−Co−Ga Heusler Films. *J. Phys. D: Appl. Phys.* **2015**, *48* (16), 164006.
(29) Lee, K.-S.; Lee, S.-W.; Min, B.-C.; Lee, K.-J. Threshold Current for Switching of a Perpendicular Magnetic Layer Induced by Spin Hall Effect. *Appl. Phys. Lett.* **2013**, *102* (11), 112410.
(30) Zhang, X.; Mao, J.; Chang, M.; Yan, Z.; Zuo, Y.; Xi, L. Current-Induced Magnetization Switching in Pt/Co/W and Pt/Co/$W_{0.82}Pt_{0.18}$ Structures with Perpendicular Magnetic Anisotropy. *J. Phys. D: Appl. Phys.* **2020**, *53*, 225003.
(31) Li, P.; Liu, T.; Chang, H.; Kalitsov, A.; Zhang, W.; Csaba, G.; Li, W.; Richardson, D.; DeMann, A.; Rimal, G.; Dey, H.; Jiang, J. S.; Porod, W.; Field, S. B.; Tang, J.; Marconi, M. C.; Hoffmann, A.; Mryasov, O.; Wu, M. Spin−Orbit Torque-Assisted Switching in Magnetic Insulator Thin Films with Perpendicular Magnetic Anisotropy. *Nat. Commun.* **2016**, *7*, 12688.
(32) Evans, R. F. L.; Chantrell, R. W.; Nowak, U.; Lyberatos, A.; Richter, H.-J. Thermally Induced Error: Density Limit for Magnetic Data Storage. *Appl. Phys. Lett.* **2012**, *100* (10), 102402.
(33) Weller, D.; Moser, A. Thermal Effect Limits in Ultrahigh-Density Magnetic Recording. *IEEE Trans. Magn.* **1999**, *35* (6), 4423−4439.
(34) Fulara, H.; Zahedinejad, M.; Khymyn, R.; Awad, A. A.; Muralidhar, S.; Dvornik, M.; Åkerman, J. Spin-Orbit Torque−Driven Propagating Spin Waves. *Science Advances* **2019**, *5* (9), No. eaax8467.
(35) Yu, G.; Upadhyaya, P.; Fan, Y.; Alzate, J. G.; Jiang, W.; Wong, K. L.; Takei, S.; Bender, S. A.; Chang, L.-T.; Jiang, Y.; Lang, M.; Tang, J.; Wang, Y.; Tserkovnyak, Y.; Amiri, P. K.; Wang, K. L. Switching of Perpendicular Magnetization by Spin−Orbit Torques in the Absence of External Magnetic Fields. *Nat. Nanotechnol.* **2014**, *9* (7), 548−554.
(36) Lau, Y.-C.; Betto, D.; Rode, K.; Coey, J. M. D.; Stamenov, P. Spin−Orbit Torque Switching without an External Field Using Interlayer Exchange Coupling. *Nat. Nanotechnol.* **2016**, *11* (9), 758.
(37) Cai, K.; Yang, M.; Ju, H.; Wang, S.; Ji, Y.; Li, B.; Edmonds, K. W.; Sheng, Y.; Zhang, B.; Zhang, N.; Liu, S.; Zheng, H.; Wang, K. Electric Field Control of Deterministic Current-Induced Magnetization Switching in a Hybrid Ferromagnetic/Ferroelectric Structure. *Nat. Mater.* **2017**, *16* (7), 712−716.
(38) Sheng, Y.; Edmonds, K. W.; Ma, X.; Zheng, H.; Wang, K. Adjustable Current-Induced Magnetization Switching Utilizing Interlayer Exchange Coupling. *Adv. Electron. Mater.* **2018**, *4* (9), 1800224.
(39) Sluka, V.; Schneider, T.; Gallardo, R. A.; Kákay, A.; Weigand, M.; Warnatz, T.; Mattheis, R.; Roldán-Molina, A.; Landeros, P.; Tiberkevich, V.; Slavin, A.; Schütz, G.; Erbe, A.; Deac, A.; Lindner, J.; Raabe, J.; Fassbender, J.; Wintz, S. Emission and Propagation of 1D and 2D Spin Waves with Nanoscale Wavelengths in Anisotropic Spin Textures. *Nat. Nanotechnol.* **2019**, *14* (4), 328−333.
(40) Cao, Y.; Rushforth, A. W.; Sheng, Y.; Zheng, H.; Wang, K. Tuning a Binary Ferromagnet into a Multistate Synapse with Spin−Orbit-Torque-Induced Plasticity. *Adv. Funct. Mater.* **2019**, *29* (25), 1808104.
(41) Borders, W. A.; Pervaiz, A. Z.; Fukami, S.; Camsari, K. Y.; Ohno, H.; Datta, S. Integer Factorization Using Stochastic Magnetic Tunnel Junctions. *Nature* **2019**, *573* (7774), 390−393.
(42) Lee, H.; Ebrahimi, F.; Amiri, P. K.; Wang, K. L. Design of High-Throughput and Low-Power True Random Number Generator Utilizing Perpendicularly Magnetized Voltage-Controlled Magnetic Tunnel Junction. *AIP Adv.* **2017**, *7* (5), 055934.
(43) Cui, B.; Li, D.; Yun, J.; Zuo, Y.; Guo, X.; Wu, K.; Zhang, X.; Wang, Y.; Xi, L.; Xue, D. Magnetization Switching through Domain Wall Motion in Pt/Co/Cr Racetracks with the Assistance of the Accompanying Joule Heating Effect. *Phys. Chem. Chem. Phys.* **2018**, *20* (15), 9904−9909.
(44) Li, S. K.; Zhao, X. T.; Liu, W.; Song, Y. H.; Liu, L.; Zhao, X. G.; Zhang, Z. D. Interface Effect of Ultrathin W Layer on Spin-Orbit Torque in Ta/W/CoFeB Multilayers. *Appl. Phys. Lett.* **2019**, *114* (8), 082402.
(45) Han, J.; Richardella, A.; Siddiqui, S. A.; Finley, J.; Samarth, N.; Liu, L. Room-Temperature Spin-Orbit Torque Switching Induced by a Topological Insulator. *Phys. Rev. Lett.* **2017**, *119* (7), 077702.
(46) Sinova, J.; Valenzuela, S. O.; Wunderlich, J.; Back, C. H.; Jungwirth, T. Spin Hall Effects. *Rev. Mod. Phys.* **2015**, *87* (4), 1213−1260.
(47) *CRC Handbook of Chemistry and Physics*, 97th ed.; Haynes, W. M., Ed.; CRC Press: Boca Raton, 2016; Section 12, pp 42−46.
(48) Mayadas, A. F.; Shatzkes, M. Electrical-Resistivity Model for Polycrystalline Films: The Case of Arbitrary Reflection at External Surfaces. *Phys. Rev. B* **1970**, *1* (4), 1382−1389.

https://dx.doi.org/10.1021/acs.nanolett.0c02060
Nano Lett. 2020, 20, 7036−7042

Research Article Vol. 28, No. 18 / 31 August 2020 / Optics Express 26111

Optics EXPRESS

Engineering telecom single-photon emitters in silicon for scalable quantum photonics

MICHAEL HOLLENBACH,[1,2,3] YONDER BERENCÉN,[1,3] ULRICH KENTSCH,[1] MANFRED HELM,[1,2] AND GEORGY V. ASTAKHOV[1,*]

[1] *Helmholtz-Zentrum Dresden-Rossendorf, Institute of Ion Beam Physics and Materials Research, Bautzner Landstrasse 400, 01328 Dresden, Germany*
[2] *Technische Universität Dresden, 01062 Dresden, Germany*
[3] *These authors contributed equally to this work*
[*] *g.astakhov@hzdr.de*

Abstract: We create and isolate single-photon emitters with a high brightness approaching 10^5 counts per second in commercial silicon-on-insulator (SOI) wafers. The emission occurs in the infrared spectral range with a spectrally narrow zero phonon line in the telecom O-band and shows a high photostability even after days of continuous operation. The origin of the emitters is attributed to one of the carbon-related color centers in silicon, the so-called G center, allowing purification with the ^{12}C and ^{28}Si isotopes. Furthermore, we envision a concept of a highly-coherent scalable quantum photonic platform, where single-photon sources, waveguides and detectors are integrated on an SOI chip. Our results provide a route towards the implementation of quantum processors, repeaters and sensors compatible with the present-day silicon technology.

1. Introduction

Single-photon sources are key building blocks for photonic quantum information processing and optical quantum computing [1,2]. Quantum photonic states are the preferred candidates to encode quantum information among the several physical systems [3], such as trapped ions [4], superconducting devices [5] and atomic defects [6]. They provide a myriad of advantages with respect to their counterparts due to the lack of interaction with the external environment that makes them robust against decoherence times.

In photonics, silicon and its mature technology have been demonstrated to be instrumental for applications in integrated optics, sensing and long-range telecommunications [7]. Due to its stable oxide (SiO_2) with which it forms high-quality interfaces with a high contrast of the refractive index, SOI is the material platform of choice for the realization of photonic integrated circuits containing optical waveguides, switches, multiplexers, optical modulators, among others [8]. Therefore, in terms of manufacturability, functionality and scalability, silicon photonics would provide a crucial advantage in building integrated photonic quantum devices. Recently, an impressive breakthrough has been accomplished in integrated photonic quantum circuits adopting the state-of-the-art developments from the realm of silicon photonics [9,10]. For instance, a large-scale SOI quantum circuit with 671 optical components has been demonstrated, that is used for the generation of photon-pairs, manipulation and measurement of multidimensional entanglement [11]. To this date, silicon quantum photonics only makes use of telecom photon-pair sources whose mechanism of photon generation is probabilistic in lieu of on demand [12]. The scalability using these probabilistic two-photon sources is not viable since they are not intrinsically coupled to quantum matter systems. Alternatively, the hybrid integration of on-demand III-V quantum dots single-photon sources on Si-based quantum photonic circuits [13,14] is nowadays the solution of choice due to the lack of an on-demand telecom single-photon emitter in Si.

In this work, we demonstrate that silicon can host single-photon emitters in the telecom O-band of fiber-optic communication, allowing monolithic integration with photonic circuits.

#397377 https://doi.org/10.1364/OE.397377
Journal © 2020 Received 11 May 2020; revised 16 Jul 2020; accepted 17 Jul 2020; published 20 Aug 2020

Research Article Vol. 28, No. 18 / 31 August 2020 / Optics Express 26112
Optics EXPRESS

Based on the spectral properties, we attribute the origin of these emitters to the well-known carbon-related defect in silicon, the so-called G center. We discuss a scalable architecture where these single-photon emitters are incorporated into basic blocks of quantum photonic circuits, serving as an interface between flying and stationary qubits.

2. Experiment

2.1. Engineering single G centers

Our experiments are performed on a commercial SOI wafer purchased from IceMOS. It consists of a 12 μm-thick Si device layer separated by a 1 μm-thick buried oxide layer from the substrate, as schematically shown in Fig. 1(a). We use a home-built low-temperature confocal microscope with the photoluminescence (PL) sensitivity optimized in the spectral range from 1.26 to 1.63 μm, which covers all telecom bands of fiber-optic communication. A 637 nm-laser diode pigtailed with a single-mode optical fiber (Thorlabs, LP637-SF70) is coupled into a variable fiber optical attenuator. The incident laser beam is focused by a cryocompatible objective (Attocube LT-APO-IR, NA=0.81), providing a minimal spot diameter of about 1 μm. The SOI wafer is mounted into an oxygen-free copper sample holder inside a customized Attocube DR800 closed-cycle cryostat that ensures a stable base temperature of $T = 4.6$ K. The temperature measured underneath the sample is $T = 5.7$ K.

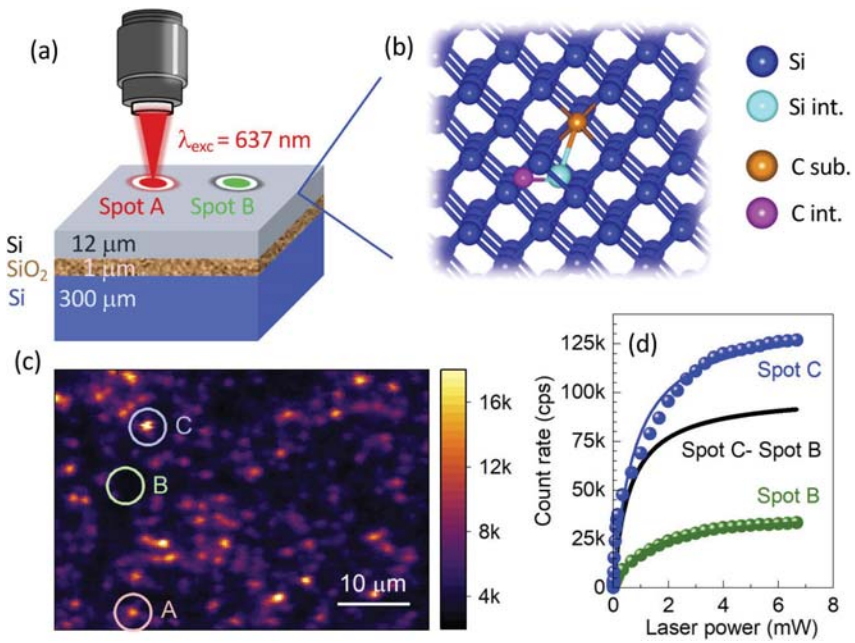

Fig. 1. Engineering single G centers in SOI wafers. (a) Schematic of the SOI wafer under study. The PL from the G centers is excited by a 637 nm laser. (b) A scheme of the Si crystal structure with one G center. (c) PL XY raster scan at $Z = 0\,\mu$m showing many isolated single G centers after C implantation to a fluence $\Phi = 1 \times 10^9\,\text{cm}^{-2}$. The laser power is 170 μW. (d) Photon count rate of a single G center (spot C) and the background (spot B) as a function of excitation power. The solid lines are fits to Eq. (2). The black thick line shows a fit to Eq. (2) of the difference between the spots C and B, yielding $I_{max} = 99$ kcps. The sample temperature is $T = 5.7$ K.

Research Article Vol. 28, No. 18 / 31 August 2020 / Optics Express 26113
Optics EXPRESS

A superconducting nanowire single-photon detector (SNSPD) from Single Quantum is used for the spectrally integrated PL measurements. The SNSPD has a detection efficiency of >90% and <60% at the wavelengths of 1.3 μm and 1.6 μm, respectively. The dark count rate is below 100 counts per second (cps) and the timing jitter is less than 50 ps. Using two linear nanopositioners anchored to the sample holder, two-dimensional (XY) lateral PL mappings over 6 mm with a positioning accuracy of 200 nm are obtained. To perform in-depth (Z) PL scans, the microscope objective is mounted into the third linear nanopositioner. The PL is collected by the same objective and then coupled to a single-mode fiber fed to the SNSPD after imaging through a 75 μm confocal pinhole. Two long-pass filters (830 nm and 1250 nm) are used to completely suppress the contribution of the reflected laser light and the Si bandgap emission from the PL signal.

The G center can be represented as a carbon-silicon molecule occupying a single lattice site [15], as schematically depicted in Fig. 1(b). There are several possible configurations of the C atoms in the Si lattice and not all of them are optically active. It is generally accepted that in the optically active configuration, the G center consists of an interstitial-substitutional C pair (C_iC_s) coupled to an interstitial Si atom (Si_i) [16,17]. To create single G centers in a controllable way, we perform C implantation and vary the fluence from 1×10^9 to 3×10^{14} cm^{-2}. The implanted C energy of 5.5 keV corresponds to the mean implantation depth of 20 nm below the surface of the Si device layer. The most prominent results are obtained for $\Phi = 1 \times 10^9$ cm^{-2}. A XY confocal PL scan at nominally $Z = 0$ μm (corresponds to the sample surface) for this fluence is presented in Fig. 1(c). There is a number of nearly diffraction-limited spots, which demonstrate a photon count rate above 10 kcps for a relatively low excitation power ($P = 170$ μW).

To determine the number of emitters in these spots, we perform the Hanbury Brown and Twiss interferometry experiment. This is a frequently used method to verify single-photon emission [18]. To this end, we use a 50/50 fiber optic wideband beamsplitter (Thorlabs, TW1300R5F1) and two SNSPDs. The PL is collected in the entire spectral range from 1.25 (the cut-off edge of the long-pass filter) to approximately 1.6 μm (limited by the SNSPD sensitivity). The photon statistics are recorded with a time-to-digital converter (Time Tagger, Swabian Instruments).

A standard evaluation method for the single photon nature of a quantum emitter is the second order intensity correlation function $g^{(2)}(\tau) = \langle I(t)I(t+\tau)\rangle / \langle I(t)\rangle^2$, where $I(t)$ is the photon count rate at time t. This function represents the measure for a photon detection at time $t + \tau$ if a previous photon is recorded at time t. The correlation function is derived from a time-delayed coincidence histogram, which is recorded as described above. The background signal from the surface centers has a strong influence on the measured second-order correlation function $g^{(2)}_{meas}(\tau)$. Therefore, we apply a standard correction procedure $g^{(2)}(\tau) = [g^{(2)}_{meas}(\tau) - (1-\rho^2)]/\rho^2$ [19]. The constant factor $\rho = (A - B)/A$ considers the count rate from a potential single photon emitter (spot A) and the background (spot B). For the spot C, this factor is $\rho = (C - B)/C$. In order to take into account the non-zero value at $\tau = 0$, we fit $g^{(2)}_{meas}(\tau)$ after correction to [20]

$$g^{(2)}(\tau) = \frac{N-1}{N} + \frac{1}{N}\left[1 - (1+a)e^{-|\tau|/\tau_1} + ae^{-|\tau|/\tau_2}\right]. \quad (1)$$

Here, N corresponds to the number of single-photon emitters.

The results for $g^{(2)}(\tau)$ obtained from the spot A are presented in Fig. 2(a). The dip at zero-time delay ($\tau = 0$) is a fingerprint of the non-classical behavior of the emitter. A fit to Eq. (1) yields $g^{(2)}(0) = 0.07(4)$, pointing at a single photon emitter $N = 1.07(4)$. The characteristic anti-bunching time $\tau_1 = 3.8(2)$ ns corresponds to the relaxation time from the excited state (ES) to the ground state (GS) of the G center. It reduces with the excitation laser power and the upper limit is the radiative recombination time [18,20]. Therefore, the obtained value reasonably agrees with the PL lifetime of 5.9 ns reported for an ensemble of G centers [21]. The parameter a in

Research Article Vol. 28, No. 18 / 31 August 2020 / Optics Express 26114
Optics EXPRESS

Eq. (1) describes the bunching behavior and is indistinguishable from zero within the error bar. The characteristic bunching time τ_2 is undefined in this case.

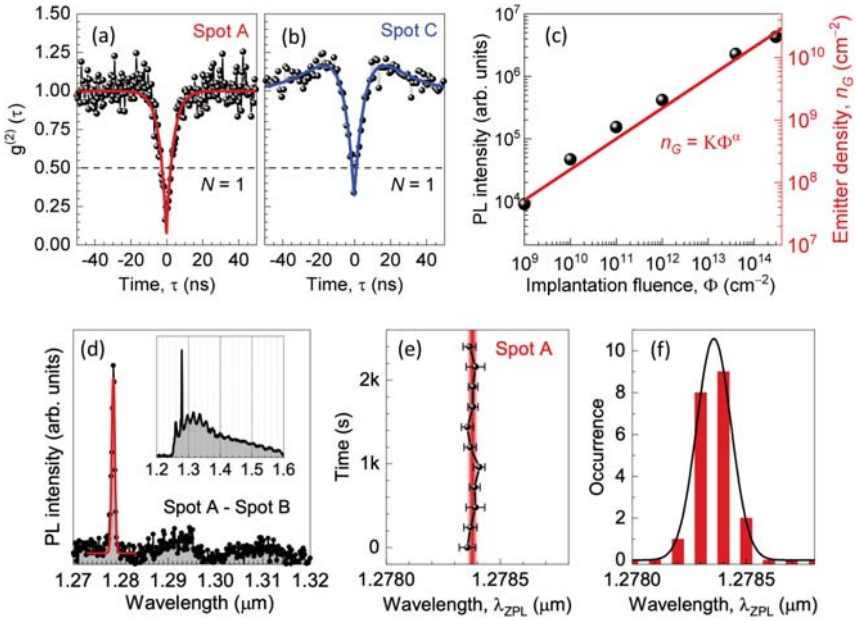

Fig. 2. Spectral properties of single G centers. (a,b) Correlation function $g^{(2)}(\tau)$ obtained at two different spots A and C in Fig. 1(c), respectively. The solid lines are fits to Eq. (1). (c) Symbols show the PL intensity as a function of the C implantation fluence, obtained with defocused excitation. The emitter density n_G is obtained from Fig. 1(c) by counting the number of single spots and then calculated for higher Φ assuming linear scaling with the PL intensity. The solid line is a fit to $n_G = K\Phi^{\alpha}$ with $\alpha = 0.5$. (d) Symbols represent a PL spectrum from a single G center after subtraction of the PL background. The solid line is a fit to a Gauss function. Inset: a PL spectrum in a larger spectral range without background correction. (e) Spectral trajectory of the ZPL in a single G center. The shaded area represents λ_{ZPL} averaged over 11 measurements. (f) Distribution of λ_{ZPL} over 20 individual G centers. The solid line is a fit to a normal distribution.

We examine the photon statistics in more than 20 random spots and they all show $g^{(2)}(0)<0.5$ after background correction. We thus conclude that all spots in Fig. 1(c) are single photon emitters, created by the C implantation. In two of the examined spots, which account for 10%, we also observe bunching $a \neq 0$, as shown for the spot C in Fig. 2(b). A fit to Eq. (1) yields $\tau_2 \sim 15$ ns and a large uncertainty for a.

The power dependence for the count rate at the spots C and B (background) is presented in Fig. 1(d). The difference between them gives the count rate of a single photon emitter. As expected for color centers, the PL intensity I saturates with increasing excitation power P, following

$$I(P) = \frac{I_{max}}{1 + P_0/P}\,. \tag{2}$$

From a fit to Eq. (2), we find the saturation count rate $I_{max} = 99$ kcps and the saturation power $P_0 = 500\,\mu$W. The latter corresponds to a power density of 70 kW cm^{-2}. Taking into account the wavelength dependence of the excitation efficiency, it is very similar to that reported for an ensemble of G centers [21]. This value is also within the same order of magnitude of the

Research Article Vol. 28, No. 18 / 31 August 2020 / Optics Express 26115
Optics EXPRESS

saturation power density for the nitrogen-vacancy defect in diamond [22] and silicon vacancy defect in silicon carbide [20].

To determine the creation efficiency of the G centers using C implantation, we first count individual spots in Fig. 1(c) and obtain the areal density $n_G = 5 \times 10^7\,\mathrm{cm}^{-2}$. We then move the sample away from the focal plane of the objective ($Z = -20\,\mu$m) and collect the PL from an area of roughly 800 $\mu\mathrm{m}^2$ with approximately 400 G centers. The PL intensity I is measured under the same conditions for different C implantation fluences Φ. The left axis in Fig. 2(c) shows $I(\Phi)$ after subtraction of the PL intensity in the pristine sample. Assuming that I is proportional to the G center density n_G , we then calculate n_G for other Φ (the right axis in Fig. 2(c)). The fluence dependence is well fitted to a power law $n_G = K\Phi^\alpha$ with $\alpha = 0.50(1)$. A sub-linear dependence (α<1) is expected because the G center is a complex radiation-induced defect consisting of two C atoms and one Si atom. The coefficient K should depend on the intrinsic C concentration. Indeed, we perform C implantation in two other Si wafers with unspecified but expected lower intrinsic C concentration than that of the SOI wafer under study. In these cases, it is found that G centers are created with significantly lower efficiency or are not created using only the C implantation step. A systematic analysis on how the intrinsic C concentration influences the G center creation efficiency is needed, but this is beyond the scope of this work.

2.2. Spectral properties of single G centers

To analyze the spectral properties of single G centers created by C implantation, the PL spectra are measured by using a Shamrock Kymera 193i spectrograph equipped with an iDus InGaAs front-illuminated photodiode array (PDA) detector. The PL spectrum of the G center consists of a phonon sideband (PSB) superimposed by the zero-phonon line (ZPL) and phonon-related peaks [23,24]. A PL spectrum from a single spot (the inset of Fig. 2(d)) reveals a well-pronounced spectrally-narrow line at about 1.28 μm, which is a spectroscopic fingerprint of the G center [23]. Figure 2(d) shows a PL spectrum from a single spot after background subtraction. A fit to a Gauss function yields the ZPL spectral position $\lambda_{\mathrm{ZPL}} = 1.27838(2)\,\mu$m and the full width at half maximum (FWHM) $\Delta_{\mathrm{ZPL}} = 0.5$ nm. The spectral trajectory of the ZPL presented in Fig. 2(e) indicates spectral stability over hours as required for quantum applications. However, we are limited by the spectral resolution of our spectrometer while the lifetime-limited FWHM is three orders of magnitude smaller [25]. The λ_{ZPL} spectral distribution for 20 individual G centers is presented in Fig. 2(f). A fit to a normal distribution gives a standard deviation of 0.1 nm. This result is in agreement with the observation of the ensemble Δ_{ZPL} ($\Phi = 1 \times 10^{12}\,\mathrm{cm}^{-2}$) to be nearly equal to that of single G centers.

As the background correction factor for the engineered G centers $\rho \leqslant 0.75$ differs from the ideal case $\rho = 1$, it is necessary to improve it for future quantum photonic applications. Its origin is not clear and could be the tail of the Si bandgap emission or the emission from surface/interface defects. A possible way to suppress the background signal is to use another excitation wavelength with higher excitation efficiency than that used in our experiments, for instance 590 nm or 420 nm [21]. Another way is to use resonant excitation into the ZPL using a tunable laser with narrow-linewidth or to couple single G centers into an optical cavity with a high Q-factor. We hope that our findings will stimulate further research in this direction.

2.3. Pristine SOI wafers

The G centers are activated when a Si wafer containing C impurities (incorporated either during growth or by implantation) is annealed and subsequently irradiated with high-energy protons [24]. For this reason, G centers are inherent to SOI substrates fabricated by the smart-cut technique, in which the annealing and proton irradiation are the essential steps [26]. In the pristine sample, the concentration of the G centers is expected to be non-monotonically distributed along the depth. The projected range of the implanted protons during the SOI fabrication process [26] results in

Research Article Vol. 28, No. 18 / 31 August 2020 / Optics Express 26116
Optics EXPRESS

a higher background signal close to the top surface. Therefore, we perform a XY confocal PL scan at some depth below the surface ($Z = 12\,\mu$m) as presented in Fig. 3(a). Several bright spots can be clearly discriminated above the background signal. A fit to Eq. (1) for the spot D yields $N = 1.7(2)$ (Fig. 3(b)) and the fulfilled condition $N<2$ denotes a single-photon emitter. Other parameters, i.e., the characteristic anti-bunching time $\tau_1 = 3.7(6)$ ns and the absence of bunching $a = 0$, are similar to the spot A in the implanted SOI wafer presented in Fig. 2(a).

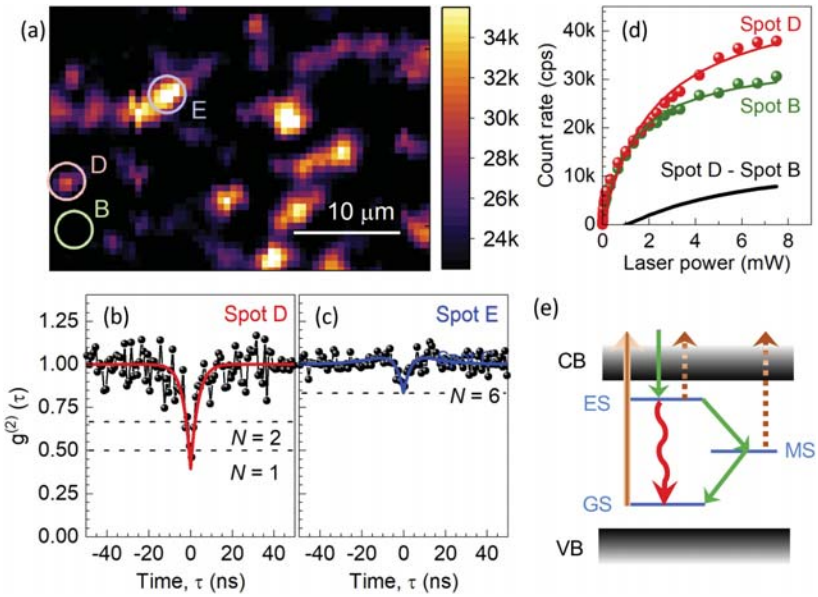

Fig. 3. Single-photon emitters in a pristine SOI wafer. (a) PL XY raster scan at $Z = 12\,\mu$m showing isolated single (spot A) and few (spot C) G centers. The laser power is 4 mW. (b,c) Correlation function $g^{(2)}(\tau)$ obtained at two different spots D and E, respectively. The solid lines are fits to Eq. (1). (d) Photon count rate of a single G center (spot D) and the background (spot B) as a function of excitation power. The solid lines are fits to Eq. (2). The black thick line shows the difference between the fitting curves for the spots D and B. (e) A three-level model of the G center, as explained in the text. The sample temperature is $T = 5.7$ K.

Figure 3(c) shows $g^{(2)}(\tau)$ obtained at the spot E, which is brighter than the spot D. A fit to Eq. (1) yields the number of single emitters in this spot $N = 6(1)$. The characteristic anti-bunching time $\tau_1 \sim 3$ ns corresponds to τ_1 for other spots in pristine and implanted samples. Furthermore, we additionally observe the bunching behavior with a non-zero parameter $a = 0.6(5)$ and a characteristic time $\tau_2 \sim 15$ ns. This behavior can be explained by a three-level model [18,27], where in addition to the radiative recombination from the ES to the GS there is a non-radiative relaxation channel through the metastable state (MS), as schematically depicted in Fig. 3(e). The photophysics of the G center can be even more complex. The 637 nm-laser excites an electron from the GS of the G center into the conduction band (CB). In addition, the deshelving process of the ES or MS into the CB promoted by the same laser may occur (the dashed lines in Fig. 3(e)), which can be described by a four-level model [20,28]. Finally, the direct excitation from the valence band (VB) to the CB may lead to the recharging of the G center. The detailed investigation of these processes, including the determination of all transition rates, is beyond the scope of this work.

The saturation power for the spot D in the pristine SOI is found to be $P_0 = 2.2$ mW. This corresponds to a power density of 300 kW cm^{-2}, which is by a factor of 4 higher than for

Research Article Vol. 28, No. 18 / 31 August 2020 / Optics Express 26117
Optics EXPRESS

the irradiated sample of Fig. 1(d). A possible explanation is that the PL is collected close to the Si/SiO_2 interface and the laser absorption should be taken into account. Indeed, the low-temperature penetration depth at a wavelength of 637 nm is about 10 μm [29]. The thick solid line in Fig. 3(d) represents the difference between the fitting curves for the spots D and B. By extrapolating the experimental data to higher powers, the saturation count rate for a single G center is estimated to be I_{max} = 14 kcps.

The PL spectrum from the spot D at Z = 12 μm is presented in Fig. 4(a). It is spectrally broadened and no ZPL is observed. One can recognize small oscillations in the spectrum of the PSB, corresponding to the interference of light within the device layer of our SOI wafer. The spectral shape of the PSB is caused by the deformation potential interaction with the longitudinal acoustic (LA) phonons [21], and the calculated LA PSB is shown by the dashed line in Fig. 4(a). The perfect agreement with the measured PL spectrum indicates that the observed emission also originates from the G centers but with pure optical properties.

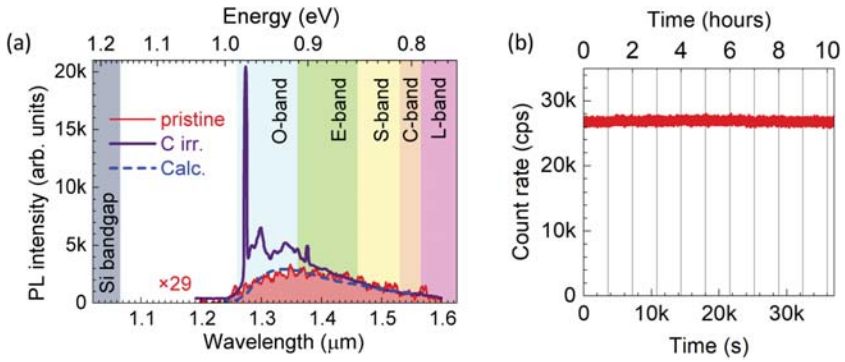

Fig. 4. Optical properties of G centers. (a) The thin solid red line represents a PL spectrum in a pristine SOI wafer and the thick solid violet line represents a PL spectrum after C implantation to a fluence $\Phi = 1 \times 10^{12}$ cm^{-2}. The dashed line represents the calculated LA PSB of the G center [21]. (b) PL time trace of a single G center.

The low count rate and the absence of the ZPL compared to the implanted samples is because the SOI fabrication process is not optimized for the creation of G centers with high optical quality [24]. Using the C implantation, we can create G centers close to the surface with a pronounced ZPL. The 5.5 keV-energy of the implanted C ions corresponds to a projected C range of 20 nm. However, we cannot exclude that the G centers are created deeper because of the influence of the tail of the implant profile and the displacement of lattice Si atoms during the implantation. For example, the W-centers in Si have been shown to emit at a depth that is around double the average projected range of the implanted ions [30]. Nevertheless, the G centers are expected to be created within 100 nm below the surface, as required for photonic applications (Fig. 5).

The thick solid line in Fig. 4(a) shows the PL spectrum for an implanted fluence of 1×10^{12} cm^{-2}. As expected for the G centers [23], the ZPL appears at a wavelength of about 1.28 μm (O-band) and dominates. The obtained Debye-Waller (DW) factor of 11% (the ratio between the light emitted into the ZPL and the all emitted light) is only slightly smaller compared to the earlier reported value for the optimized fabrication protocol [21]. These data demonstrate that the G centers can be efficiently created using a single-step implantation. The well-documented method is based on three steps: C implantation, annealing and proton irradiation for the activation [24]. In our approach with a relatively high substitutional C atoms in pristine wafers, the first and second steps can be omitted. The third step is then replaced by the C implantation, simultaneously providing interstitial C atoms and creating interstitial Si atoms, as required for the creation of G centers.

Research Article Vol. 28, No. 18 / 31 August 2020 / Optics Express 26118
Optics EXPRESS

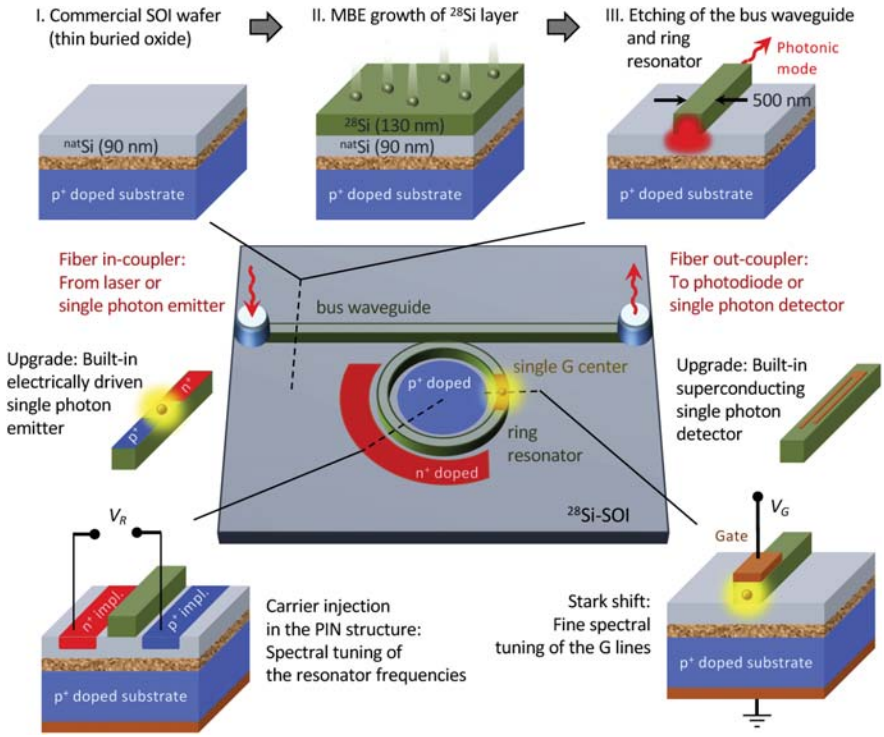

Fig. 5. A cartoon of the scalable quantum architecture with a single G center in an isotopically purified ^{28}Si-SOI photonic structure. Possible upgrades include built-in electrically driven single-photon emitters and superconducting single-photon detectors integrated on the same chip.

Photostability is an important characteristic of a single-photon emitter. The PL time trace from one of the spots with a single G center at $P = 4$ mW is shown in Fig. 4(b). The count rate remains constant over one day without any indication of blinking. At higher laser powers $P>5$ mW, the count rate drops to a low value within several minutes due to local heating. However, the count rate restores if the laser power is reduced. We performed measurements at the same spot over one week and no photobleaching was observed, indicating long-term optical stability of the G center at moderate laser powers and low temperature $T = 5.7$ K. Similar results are obtained for all the measured spots in pristine and C implanted samples.

3. Scalable quantum photonic architecture

It has recently been shown that an ensemble of G centers in isotopically purified ^{28}Si wafers possesses an extremely spectrally narrow ZPL [25]. The inhomogeneous linewidth of 0.2 μeV (50 MHz) – exceeding the Fourier limit by a factor of 2 only – implies marginal spectral diffusion of the ZPL line associated with a single G center. This unique feature can be used to generate indistinguishable photons on demand in the telecom O-band, which builds a solid basis for quantum communication and computing [31–33]. To achieve this goal, it is necessary to develop a complementary-metal-oxide-semiconductor (CMOS)-compatible route to monolithically integrate the telecom single-photon source into isotopically purified ^{28}Si-SOI photonic structures. A possible procedure is presented in Fig. 5. The first step is to grow a high-quality ^{28}Si layer on top of a commercial SOI wafer using molecular beam epitaxy (MBE).

Research Article Vol. 28, No. 18 / 31 August 2020 / Optics Express 26119
Optics EXPRESS

The second step is to use well-established etching protocols for the fabrication of SOI photonic circuits, which comprise bus waveguides and ring resonators. A very challenging task is the creation of single G center in the desired position of the ring resonators with optimized optical properties, i,e., with a high DW factor and high-photon emission rate. A possible protocol is based on the previous approach [24] and can include a broad-beam implantation with either ^{12}C (zero nuclear spin for ultra-long quantum coherence [34]) or ^{13}C isotopes (non-zero nuclear spin for quantum storage [35]) followed by a rapid thermal annealing at 1000 °C. For the local activation of the single G centers, a focused proton beam irradiation at the desired position [36] can be used instead of a broad-beam proton irradiation [24].

A single G defect coupled to a ring resonator mode can serve as an ideal basic module for scalable quantum-optical processors and networks due to several reasons. (i) The path of a single photon is unambiguously linked to the spin state of a single defect [33]. It requires a high-fidelity spin-photon interface. Though optically detected magnetic resonance in G centers was reported more than three decades ago [37], the interface is yet to be realized. (ii) The detection of a single photon in the exit port generates heralded entanglement between defect spins [31]. (iii) The wavelengths of the resonator modes and the G center ZPL can be tuned independently, as schematically presented in Fig. 5. In the former, one can use carrier injection in a PIN structure [38], and in the latter, the tuning can be realized via the Stark effect [39]. Such a reconfigurable photonic quantum circuit allows controlling the single-photon path injected from the entrance port. This is a basis for the implementation of two-bit quantum gates with selectively addressable single G centers, which can be located on the same or separated SOI chips. Furthermore, built-in electrically driven [40,41] single-photon emitters based on a G center and superconducting single-photon detectors [42,43] (Fig. 5) provide a route towards a fully integrated quantum photonic platform.

4. Conclusion

We have demonstrated for the first time that commercial SOI wafers can host telecom single-photon emitters based on one of the carbon-related point defects in silicon. They have been shown to possess a spectrally stable zero-phonon line in the O-band and exhibit a long-term photostability over days of continuous excitation. Using C implantation, these telecom single-photon emitters are engineered in a controllable way within tens nm below the surface of the device layer in a SOI wafer. Inspired by these findings, we have envisioned a feasible concept for the realization of an integrated photonic platform with single-photon emitters, which is compatible with the current silicon technology. The implementation of this platform could enable scalable quantum processors and networks.

Funding

Deutsche Forschungsgemeinschaft (AS 310/5-1).

Acknowledgments

We thank Slawomir Prucnal and Shengqiang Zhou for stimulating discussions. Support from the Ion Beam Center (IBC) at Helmholtz-Zentrum Dresden-Rossendorf (HZDR) is gratefully acknowledged.

Disclosures

The authors declare no conflicts of interest.

Research Article Vol. 28, No. 18 / 31 August 2020 / *Optics Express* 26120

Optics EXPRESS

References

1. M. D. Eisaman, J. Fan, A. Migdall, and S. V. Polyakov, "Invited Review Article: Single-photon sources and detectors," Rev. Sci. Instrum. **82**(7), 071101 (2011).
2. J. L. O'Brien, "Optical Quantum Computing," Science **318**(5856), 1567–1570 (2007).
3. T. D. Ladd, F. Jelezko, R. Laflamme, Y. Nakamura, C. Monroe, and J. L. O'Brien, "Quantum computers," Nature **464**(7285), 45–53 (2010).
4. R. Blatt and C. F. Roos, "Quantum simulations with trapped ions," Nat. Phys. **8**(4), 277–284 (2012).
5. G. Wendin, "Quantum information processing with superconducting circuits: a review," Rep. Prog. Phys. **80**(10), 106001 (2017).
6. J. R. Weber, W. F. Koehl, J. B. Varley, A. Janotti, B. B. Buckley, C. G. Van de Walle, and D. D. Awschalom, "Quantum computing with defects," Proc. Natl. Acad. Sci. **107**(19), 8513–8518 (2010).
7. C. R. Doerr, "Silicon photonic integration in telecommunications," Front. Phys. **3**, 952 (2015).
8. R. Won, "Integrating silicon photonics," Nat. Photonics **4**(8), 498–499 (2010).
9. J. Wang, F. Sciarrino, A. Laing, and M. G. Thompson, "Integrated photonic quantum technologies," Nat. Photonics **14**(5), 273–284 (2020).
10. A. W. Elshaari, W. Pernice, K. Srinivasan, O. Benson, and V. Zwiller, "Hybrid integrated quantum photonic circuits," Nat. Photonics **14**(5), 285–298 (2020).
11. J. Wang, S. Paesani, Y. Ding, R. Santagati, P. Skrzypczyk, A. Salavrakos, J. Tura, R. Augusiak, L. Mančinska, D. Bacco, D. Bonneau, J. W. Silverstone, Q. Gong, A. Acín, K. Rottwitt, L. K. Oxenløwe, J. L. O'Brien, A. Laing, and M. G. Thompson, "Multidimensional quantum entanglement with large-scale integrated optics," Science **360**(6386), 285–291 (2018).
12. X. Qiang, X. Zhou, J. Wang, C. M. Wilkes, T. Loke, S. O'Gara, L. Kling, G. D. Marshall, R. Santagati, T. C. Ralph, J. B. Wang, J. L. O'Brien, M. G. Thompson, and J. C. F. Matthews, "Large-scale silicon quantum photonics implementing arbitrary two-qubit processing," Nat. Photonics **12**(9), 534–539 (2018).
13. I. E. Zadeh, A. W. Elshaari, K. D. Jöns, A. Fognini, D. Dalacu, P. J. Poole, M. E. Reimer, and V. Zwiller, "Deterministic Integration of Single Photon Sources in Silicon Based Photonic Circuits," Nano Lett. **16**(4), 2289–2294 (2016).
14. J.-H. Kim, S. Aghaeimeibodi, C. J. K. Richardson, R. P. Leavitt, D. Englund, and E. Waks, "Hybrid Integration of Solid-State Quantum Emitters on a Silicon Photonic Chip," Nano Lett. **17**(12), 7394–7400 (2017).
15. L. W. Song, X. D. Zhan, B. W. Benson, and G. D. Watkins, "Bistable interstitial-carbon–substitutional-carbon pair in silicon," Phys. Rev. B **42**(9), 5765–5783 (1990).
16. D. Timerkaeva, C. Attaccalite, G. Brenet, D. Caliste, and P. Pochet, "Structural, electronic, and optical properties of the C-C complex in bulk silicon from first principles," J. Appl. Phys. **123**(16), 161421 (2018).
17. H. Wang, A. Chroneos, C. A. Londos, E. N. Sgourou, and U. Schwingenschlögl, "Carbon related defects in irradiated silicon revisited," Sci. Rep. **4**(1), 4909 (2015).
18. C. Kurtsiefer, S. Mayer, P. Zarda, and H. Weinfurter, "Stable Solid-State Source of Single Photons," Phys. Rev. Lett. **85**(2), 290–293 (2000).
19. R. Brouri, A. Beveratos, J.-P. Poizat, and P. Grangier, "Photon antibunching in the fluorescence of individual color centers in diamond," Opt. Lett. **25**(17), 1294–1296 (2000).
20. F. Fuchs, B. Stender, M. Trupke, D. Simin, J. Pflaum, V. Dyakonov, and G. V. Astakhov, "Engineering near-infrared single-photon emitters with optically active spins in ultrapure silicon carbide," Nat. Commun. **6**(1), 7578 (2015).
21. C. Beaufils, W. Redjem, E. Rousseau, V. Jacques, A. Y. Kuznetsov, C. Raynaud, C. Voisin, A. Benali, T. Herzig, S. Pezzagna, J. Meijer, M. Abbarchi, and G. Cassabois, "Optical properties of an ensemble of G-centers in silicon," Phys. Rev. B **97**(3), 035303 (2018).
22. F. Jelezko and J. Wrachtrup, "Single defect centres in diamond: A review," Phys. Status Solidi A **203**(13), 3207–3225 (2006).
23. G. Davies, "The optical properties of luminescence centres in silicon," Phys. Rep. **176**(3-4), 83–188 (1989).
24. D. D. Berhanuddin, M. A. Lourenço, R. M. Gwilliam, and K. P. Homewood, "Co-Implantation of Carbon and Protons: An Integrated Silicon Device Technology Compatible Method to Generate the Lasing G-Center," Adv. Funct. Mater. **22**(13), 2709–2712 (2012).
25. C. Chartrand, L. Bergeron, K. J. Morse, H. Riemann, N. V. Abrosimov, P. Becker, H. J. Pohl, S. Simmons, and M. L. W. Thewalt, "Highly enriched 28Si reveals remarkable optical linewidths and fine structure for well-known damage centers," Phys. Rev. B **98**(19), 195201 (2018).
26. M. Bruel, B. Aspar, and A.-J. Auberton-Hervé, "Smart-Cut: A New Silicon On Insulator Material Technology Based on Hydrogen Implantation and Wafer Bonding," Jpn. J. Appl. Phys. **36**(Part 1, No. 3B), 1636–1641 (1997).
27. I. Aharonovich, S. Castelletto, D. A. Simpson, A. D. Greentree, and S. Prawer, "Photophysics of chromium-related diamond single-photon emitters," Phys. Rev. A **81**(4), 043813 (2010).
28. E. Neu, D. Steinmetz, J. Riedrich-Möller, S. Gsell, M. Fischer, M. Schreck, and C. Becher, "Single photon emission from silicon-vacancy colour centres in chemical vapour deposition nano-diamonds on iridium," New J. Phys. **13**(2), 025012 (2011).
29. S. M. Sze and K. K. Ng, *Physics of Semiconductor Devices* (Wiley, 2006).
30. S. M. Buckley, A. N. Tait, G. Moody, B. Primavera, S. Olson, J. Herman, K. L. Silverman, S. Papa Rao, S. Woo Nam, R. P. Mirin, and J. M. Shainline, "Optimization of photoluminescence from W centers in a silicon-on-insulator," Opt. Express **28**(11), 16057–16072 (2020).

Research Article Vol. 28, No. 18 / 31 August 2020 / *Optics Express* 26121

Optics EXPRESS

31. K. Nemoto, M. Trupke, S. J. Devitt, A. M. Stephens, B. Scharfenberger, K. Buczak, T. Nöbauer, M. S. Everitt, J. Schmiedmayer, and W. J. Munro, "Photonic Architecture for Scalable Quantum Information Processing in Diamond," Phys. Rev. X **4**(3), 031022 (2014).
32. M. Atatüre, D. Englund, N. Vamivakas, S.-Y. Lee, and J. Wrachtrup, "Material platforms for spin-based photonic quantum technologies," Nat. Rev. Mater. **3**(5), 38–51 (2018).
33. A. Sipahigil, R. E. Evans, D. D. Sukachev, M. J. Burek, J. Borregaard, M. K. Bhaskar, C. T. Nguyen, J. L. Pacheco, H. A. Atikian, C. Meuwly, R. M. Camacho, F. Jelezko, E. Bielejec, H. Park, M. Loncar, and M. D. Lukin, "An integrated diamond nanophotonics platform for quantum-optical networks," Science **354**(6314), 847–850 (2016).
34. K. Saeedi, S. Simmons, J. Z. Salvail, P. Dluhy, H. Riemann, N. V. Abrosimov, P. Becker, H. J. Pohl, J. J. L. Morton, and M. L. W. Thewalt, "Room-Temperature Quantum Bit Storage Exceeding 39 Minutes Using Ionized Donors in Silicon-28," Science **342**(6160), 830–833 (2013).
35. J. J. Pla, F. A. Mohiyaddin, K. Y. Tan, J. P. Dehollain, R. Rahman, G. Klimeck, D. N. Jamieson, A. S. Dzurak, and A. Morello, "Coherent Control of a Single ^{29}Si Nuclear Spin Qubit," Phys. Rev. Lett. **113**(24), 246801 (2014).
36. H. Kraus, D. Simin, C. Kasper, Y. Suda, S. Kawabata, W. Kada, T. Honda, Y. Hijikata, T. Ohshima, V. Dyakonov, and G. V. Astakhov, "Three-Dimensional Proton Beam Writing of Optically Active Coherent Vacancy Spins in Silicon Carbide," Nano Lett. **17**(5), 2865–2870 (2017).
37. K. M. Lee, K. P. O'Donnell, J. Weber, B. C. Cavenett, and G. D. Watkins, "Optical Detection of Magnetic Resonance for a Deep-Level Defect in Silicon," Phys. Rev. Lett. **48**(1), 37–40 (1982).
38. Y. Tian, Z. Liu, H. Xiao, G. Zhao, G. Liu, J. Yang, J. Ding, L. Zhang, and L. Yang, "Experimental demonstration of a reconfigurable electro-optic directed logic circuit using cascaded carrier-injection micro-ring resonators," Sci. Rep. **7**(1), 6410 (2017).
39. L. C. Bassett, F. J. Heremans, C. G. Yale, B. B. Buckley, and D. D. Awschalom, "Electrical Tuning of Single Nitrogen-Vacancy Center Optical Transitions Enhanced by Photoinduced Fields," Phys. Rev. Lett. **107**(26), 266403 (2011).
40. E. Rotem, J. M. Shainline, and J. M. Xu, "Electroluminescence of nanopatterned silicon with carbon implantation and solid phase epitaxial regrowth," Opt. Express **15**(21), 14099–14106 (2007).
41. J. Bao, M. Tabbal, T. Kim, S. Charnvanichborikarn, J. S. Williams, M. J. Aziz, and F. Capasso, "Point defect engineered Si sub-bandgap light-emitting diode," Opt. Express **15**(11), 6727–6733 (2007).
42. G. N. Gol'tsman, O. Okunev, G. Chulkova, A. Lipatov, A. Semenov, K. Smirnov, B. Voronov, A. Dzardanov, C. Williams, and R. Sobolewski, "Picosecond superconducting single-photon optical detector," Appl. Phys. Lett. **79**(6), 705–707 (2001).
43. W. H. P. Pernice, C. Schuck, O. Minaeva, M. Li, G. N. Gol'tsman, A. V. Sergienko, and H. X. Tang, "High-speed and high-efficiency travelling wave single-photon detectors embedded in nanophotonic circuits," Nat. Commun. **3**(1), 1325 (2012).

PHYSICAL REVIEW LETTERS **125,** 207203 (2020)

Nonlocal Stimulation of Three-Magnon Splitting in a Magnetic Vortex

L. Körber,[1,2,*] K. Schultheiss,[1,†] T. Hula,[1,3] R. Verba,[4] J. Fassbender,[1,2] A. Kákay,[1] and H. Schultheiss[1,2]
[1]*Helmholtz-Zentrum Dresden - Rossendorf, Institut für Ionenstrahlphysik und Materialforschung, D-01328 Dresden, Germany*
[2]*Fakultät Physik, Technische Universität Dresden, D-01062 Dresden, Germany*
[3]*Institut für Physik, Technische Universität Chemnitz, D-09126 Chemnitz, Germany*
[4]*Institute of Magnetism, Kyiv 03142, Ukraine*

(Received 27 May 2020; accepted 5 October 2020; published 12 November 2020)

We present a combined numerical, theoretical, and experimental study on stimulated three-magnon splitting in a magnetic disk in the vortex state. Our micromagnetic simulations and Brillouin-light-scattering results confirm that three-magnon splitting can be triggered even below threshold by exciting one of the secondary modes by magnons propagating in a waveguide next to the disk. The experiments show that stimulation is possible over an extended range of excitation powers and a wide range of frequencies around the eigenfrequencies of the secondary modes. Rate-equation calculations predict an instantaneous response to stimulation and the possibility to prematurely trigger three-magnon splitting even above threshold in a sustainable manner. These predictions are confirmed experimentally using time-resolved Brillouin-light-scattering measurements and are in a good qualitative agreement with the theoretical results. We believe that the controllable mechanism of stimulated three-magnon splitting could provide a possibility to utilize magnon-based nonlinear networks as hardware for neuromorphic computing.

DOI: 10.1103/PhysRevLett.125.207203

With the first experiments on ferromagnetic resonance at large excitation powers by Bloembergen, Damon, and Wang [1–3], nonlinear effects in magnetization dynamics have often been regarded as parasitic, leading to additional losses, frequency shift, or linewidth broadening of the ferromagnetic resonance and of the magnon modes therein. On the other hand, this nonlinearity leads to many interesting phenomena such as multimagnon scattering, parametric pumping, formation of solitons, or phase locking [4,5]. Some of these effects have analogs in other fields, like nonlinear optics [6,7].

In recent years, nonlinear systems have been given increasing attention, for example, as candidates for hardware implementations of neuromorphic computing [8–11]. One of the most important working principles of neuromorphic networks in order to achieve complexity is that the individual neurons are activated in a nonlinear way. Suitably, magnons (spin waves) in ferromagnets are strongly coupled and, above a certain threshold amplitude, undergo spontaneous scattering processes with each other, leading to information transport in wave-vector space. In addition to this, magnons generate high-frequency magnetic fields and, thus, provide a potential interface between nonlinear networks and spin-qubit-based quantum systems. As a result, the study of nonlinear magnon dynamics is of both fundamental and technological interest.

Recently, we provided the direct experimental evidence for three-magnon splitting (3MS), i.e., the splitting of one primary magnon in two secondary magnons, in magnetic disks in the vortex state [12]. But typically, a certain microwave power is necessary to overcome the threshold of spontaneous splitting. This is, in addition, accompanied with a characteristic time delay which cannot be precisely controlled, since it relies on the instantaneous amplitudes of the thermal magnons. Recently, Zhang and co-workers predicted numerically the stimulation of such processes in domain walls [13]. However, up to now, there was no experimental demonstration of an active stimulation of magnon splitting in confined systems which allows us to not only trigger nonlinear dynamics below threshold but also to control the time when the splitting sets in.

In this Letter, we use rate-equation calculations, micromagnetic simulations, and Brillouin-light-scattering microscopy (μBLS) to predict and verify that 3MS can be triggered nonlocally even below threshold by exciting one of the secondary modes via the long-range dipolar magnetic fields of magnons propagating in a waveguide which is spatially separated from the disk [Fig. 1(a)]. The experiments show that stimulation is possible at low powers and in a wide frequency range around the frequencies of the secondary modes. Furthermore, we demonstrate the instantaneous response to stimulation and the possibility to prematurely trigger 3MS above threshold.

Magnon eigenmodes in vortex-state magnetic disks have been examined in numerous experimental [12,14–16], theoretical, [16–24] as well as numerical works [25–27]. Their confinement leads to a discrete spectrum which is categorized by a radial index $n \geq 0$, counting the nodes in the radial (ϱ) direction, and an azimuthal index $m \in \mathbb{Z}$, counting the periods in the azimuthal ϕ direction

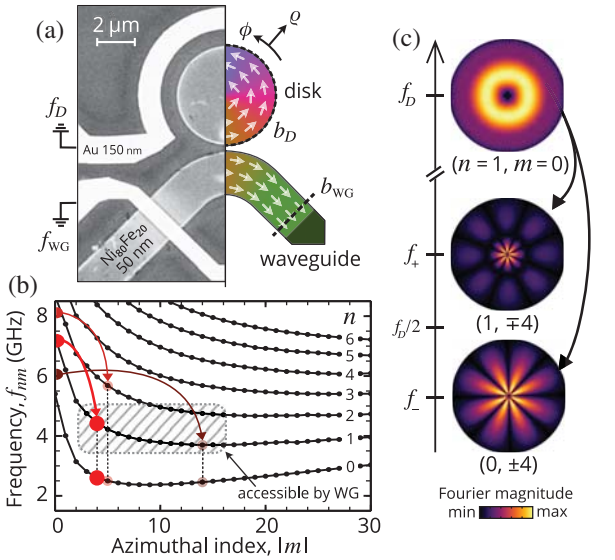

FIG. 1. (a) Experimental realization (left) and simulation model (right) of the vortex-state permalloy disk and of the longitudinally magnetized 2 μm wide waveguide. The experimental image has been acquired using scanning electron microscopy. An Ω-shaped antenna is used to excite the disk with a rf field b_D at frequency f_D. Additionally, a strip-line antenna is used to excite magnons in the waveguide with a rf field b_{WG} at frequency f_{WG}. (b) Dispersion of the vortex disk calculated using micromagnetic simulations. Exemplary scattering channels for three different excitation frequencies are marked on the dispersion. The hatched rectangular region represents an approximate frequency and wave-vector interval in which the waveguide can efficiently excite magnons in the disk. (c) Numerically obtained spatial profiles of the magnons taking part in a 3MS channel: the directly excited radial mode with frequency f_D and the secondary azimuthal modes with f_+ and f_-.

[see coordinate system in Fig. 1(a)]. These modes appear in degenerate duplets. For large enough disks, two modes with the same n but opposite m share the same frequency, with the exception of $m = \pm 1$ for which hybridization with the gyrotropic mode of the vortex appears [14,17,18,28]. Figure 1(b) shows the spectrum of the vortex magnons obtained by micromagnetic simulations for a permalloy ($Ni_{80}Fe_{20}$) disk of 50 nm thickness and 5.1 μm diameter [29]. The slope of the dispersion is negative in the azimuthal direction (increasing $|m|$) and positive in the radial direction (increasing n), which is characteristic for dipolar-dominated spin-wave propagation parallel and perpendicular to the equilibrium magnetization in thin magnetic films [14,15,32].

A radial mode ($m = 0$), that is excited by an azimuthally symmetric out-of-plane microwave (rf) field at frequency f_D and with a large enough power, may decay into two secondary modes via 3MS [12], as shown using micromagnetic simulations in Fig. 1(c) for an excitation frequency of $f_D = 7.2$ GHz. Experimentally, such a rf field can be achieved by an Ω-shaped microwave antenna around the magnetic disk. The 3MS in magnetic vortices obeys certain selection rules [12]: Because of the cylindrical symmetry, the angular momentum in ϕ direction must be conserved, resulting in secondary modes of opposite azimuthal index $\pm m$. Moreover, the two secondary modes must have different radial indices which leads to a pronounced splitting in frequency $2\Delta f$ between them. Finally, energy conservation demands for the frequencies of the secondary modes $f_\pm = f_D/2 \pm \Delta f$. Simultaneously, the mirrored process with exchanged signs of the azimuthal indices is equally probable. We associate these two equivalent processes with one scattering channel and speak of secondary duplets instead of secondary modes. This symmetry leads to standing waves which can be observed, e.g., by μBLS [12,33]. Depending on the excitation frequency of the radial mode f_D, a variety of scattering channels can be observed, some of which are marked on the dispersion in Fig. 1(b).

For all channels, the frequency split $2\Delta f$ between the secondary duplets can be exploited to access them individually using an additional rf field at the respective frequency f_+ or f_-. It is well known that 3MS leads to a considerable feedback on the directly excited mode at f_D. This interconnection together with the fact that the secondary duplets could be excited individually raised the question of whether stimulated splitting could be realized even below threshold. In other words, what happens if we excite one of the secondary duplets directly (e.g., at f_+), taken that the radial mode at f_D is excited below threshold? A direct evidence for stimulated 3MS would be an instant response at f_-.

To answer this question, we have performed micromagnetic simulations using a custom version of MUMAX[3] [34,35] and verified these numerical results by μBLS. In order to resonantly excite one of the secondary duplets (with $|m| > 0$), it is not possible to use an Ω-shaped antenna. The reason is that these modes possess no net magnetic moment and, therefore, cannot couple to the azimuthally symmetric rf field produced by such an antenna. Instead, we use an adjacent, 2 μm wide waveguide (WG) of the same material and thickness as the disk. In this waveguide, we inject propagating magnons at frequency f_{WG} that couple to the azimuthal modes within the disk. A curved waveguide is used to allow for a better surrounding of the disk by the Ω-shaped antenna. To maximize their intensity within the waveguide, magnons are excited at both ends resulting in standing waves in the vicinity of the disk. The experimental and numerical sample design is shown in Fig. 1(a). An approximate frequency and wave-vector regime, in which azimuthal modes in the disk can be excited by the waveguide, is marked in the spectrum in Fig. 1(b).

Without loss of generality, stimulated 3MS is shown for the channel at $f_D = 7.20$ GHz, introduced in Fig. 1(c), with the secondary duplets at $f_+ = 4.46$ GHz and

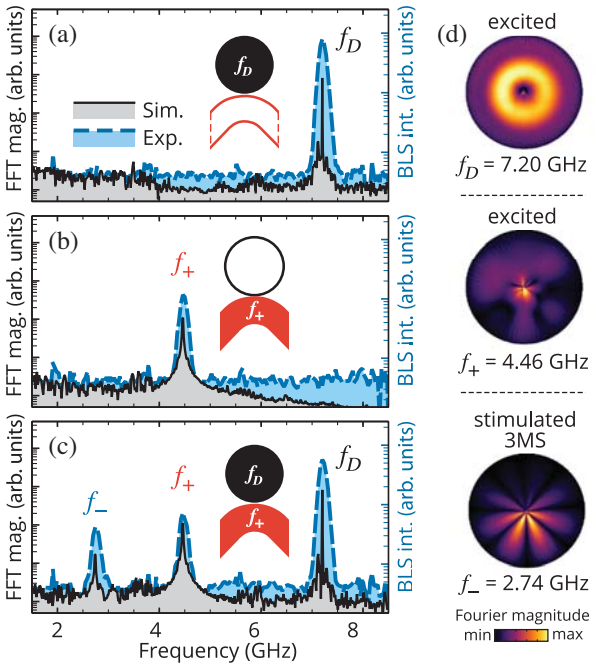

FIG. 2. Spectra of the vortex disk obtained by micromagnetic simulations and μBLS experiments for three cases: (a) exciting only the disk below threshold at frequency f_D, (b) exciting only the waveguide at frequency f_+, and (c) both combined, showing an additional signal at f_-. (d) Mode profiles obtained from the simulation in (c).

$f_- = 2.74$ GHz. Confirmation for other channels is found in the Supplemental Material [29].

As a first sanity check, we excite (using the Ω-shaped antenna in the experiments) the radial mode (1,0) in the disk at frequency f_D with a low power to verify that the direct excitation is below threshold and no secondary duplets are observed [36]. The corresponding numerical and experimental spectra are shown in Fig. 2(a). In the simulations, the spectrum of the disk was obtained by performing a Fourier transform at each cell in the disk whereas the experimental spectrum was obtained by measuring and integrating the μBLS spectra at 14 different points on the disk.

Next, to verify that magnons in the waveguide can couple to the azimuthal modes in the disk, we pump the waveguide at the frequency of the higher duplet $f_{WG} = f_+$. By again measuring the spectral response in the disk [Fig. 2(b)], we observe a signal at f_+, confirming a successful coupling. Here, no rf field at the Ω-shaped antenna was applied.

Finally, we combine both schemes by exciting at the frequency of the radial mode $f_D = 7.20$ GHz in the disk and at $f_+ = 4.46$ GHz in the waveguide. As seen in Fig. 2(c), we observe an additional spectral contribution at the exact frequency of the lower duplet $f_- = 2.74$ GHz. By obtaining the mode profiles at f_- and f_+ from micromagnetic simulations [Fig. 2(d)]—especially in comparison with the profiles of spontaneous 3MS at the same excitation frequency f_D in Fig. 1(c)—we can confirm that the signals truly belong to azimuthal modes. As expected, these modes show different radial indices n. The profile of the mode excited at f_+ by the magnons in the waveguide is distorted. As the dipolar field of the waveguide generates a wide spectrum of $|m|$ components at the site of the disk, we attribute this to an excitation of multiple degenerate duplets at that frequency. However, the profile of the solely parametrically excited mode f_- almost perfectly resembles the profile of the lower duplet produced by spontaneous 3MS. Thus, we conclude that 3MS has been successfully stimulated below threshold.

In the remainder of this Letter, we want to explore three aspects of stimulated 3MS, namely the bandwidth of stimulation, the dependence on the excitation power within the waveguide, as well as the temporal evolution of the magnons subject to stimulated splitting.

To address the bandwidth, we excite the disk below threshold at f_D and vary the excitation frequency f_{WG} in the waveguide. Figure 3(a) shows the f_{WG}-dependent spectral response of the disk obtained by μBLS. The dashed diagonal line at f_{WG} is accompanied with an antidiagonal response over a wide range around the frequencies of the duplets. In fact, the stimulation efficiency as a function of waveguide frequency f_{WG} closely follows a Lorentzian curve of about 100 MHz half width at half maximum which, in first order, is approximately equal to the damping rate of the parametrically excited duplet at f_- (see Supplemental Material [29] for analytical details). This confirms that stimulated 3MS is possible even when f_{WG} does not exactly match the frequency of one of the secondary duplets [16,37].

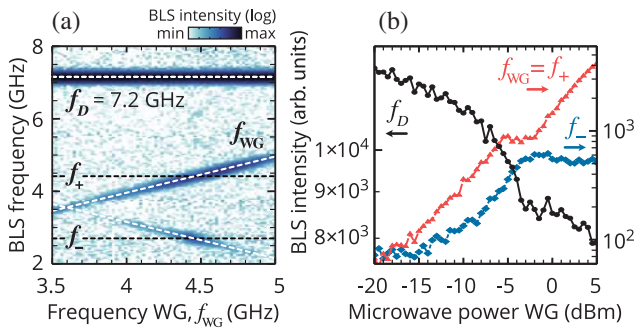

FIG. 3. (a) BLS spectra of the disk when excited below threshold at frequency f_D and the excitation frequency in the waveguide f_{WG} is varied. The response at f_- corresponds to the lower duplet, as a result of stimulated 3MS. In (b), the BLS response is extracted by integrating over a frequency interval around the respective frequencies when the disk is excited at $f_D = 7.2$ GHz below threshold and the excitation power in the waveguide is varied at constant frequency $f_{WG} = f_+ = 4.46$ GHz. Arrows indicate the corresponding logarithmic intensity axis.

Next, we address the influence of the power that the waveguide is excited with. In the experiment, we fix $f_{\mathrm{WG}} = f_+$ and vary the microwave power applied to the antenna on the waveguide. The BLS intensities of the modes in the disk were extracted by integrating over a certain linewidth around the respective frequencies. The results summarized in Fig. 3(b) confirm that stimulated splitting is possible even for low excitation powers in the waveguide. With increasing power of f_{WG}, the measured signal at f_- increases whereas the one at f_D decreases. This demonstrates the energetic interconnection between the different modes and is an indirect evidence that a splitting process is taking place. We observe a saturation in the power of the stimulated splitting above which the intensity of the parametrically excited duplet at f_- does not increase further. However, the resonantly excited duplet at $f_{\mathrm{WG}} = f_+$ still increases. As seen from the evolution of f_D in Fig. 3(b), above this power, the energy flux supplied by the directly excited radial mode is nearly exhausted. Naturally, the position of the saturation depends on the excitation power of this radial mode.

Finally, we focus on how stimulation provides means to control the timescale of 3MS. Parametric phenomena of this nature are known to exhibit a power-dependent delay. It takes a certain time before the directly excited mode reaches its threshold, before the secondary duplets start to grow, and even a longer time before these magnons reach their dynamic equilibrium. Since stimulated splitting is possible below threshold, the temporal evolution of the modes must change compared to spontaneous scattering. For this, we utilize rate equations derived from nonlinear spin-wave theory [4,38,39], combined with time-resolved μBLS (TRμBLS). Both methods allow us to track the temporal evolution of magnons (see Supplemental Material [29] for details). Only a qualitative comparison between theory and experiments is presented here because, first, the exact power arriving at the antenna is unknown in the experiment and, second, for the same reason, a synchronization of the microwave pulses at the sample is cumbersome. Moreover, in the theoretical model, an additional delay arising from the finite group velocity of the magnons excited in the waveguide is neglected.

Let us first focus on the case below threshold. In Figs. 4(a) and 4(b), we show the reference case when only the radial mode at f_D is excited with a rf field, marked with a box on top of the panels. As soon as the duplet at f_+ is excited as well, the parametrically excited duplet at f_- immediately follows [Figs. 4(c) and 4(d)]. This means that the response to stimulation is almost instant. Note that, here, we observe a feedback on the directly excited mode, i.e., a loss in its intensity due to the opening of the 3MS channel. This fast response can be used to shorten the power-dependent parametric time delay above threshold. If again only the radial mode is excited, now above threshold, we observe spontaneous 3MS. The secondary modes reach dynamic equilibrium at about 20 ns in the theoretical calculation [Fig. 4(e)] and at 15 ns in the experiment [Fig. 4(f)]. Also here, the secondary modes appear much

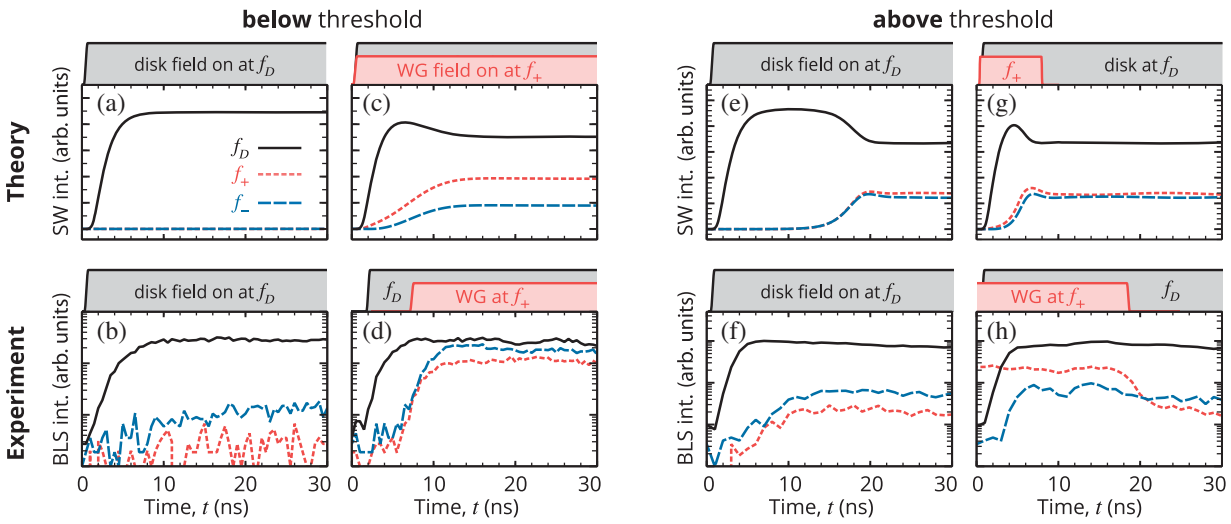

FIG. 4. Temporal evolution of the spin-wave intensities obtained by nonlinear spin-wave (SW) theory and TRμBLS, respectively. The time frames when the rf fields are turned on are marked by the boxes on top of the axes. In (a) and (b), only the radial mode at f_D is excited below threshold. In (c) and (d), an additional rf field is applied at f_+ in the waveguide, showing a successful stimulation of the mode at f_-. Panels (e) and (f) show spontaneous 3MS above threshold, whereas (g) and (h) show a shortening of the parametric time delay by applying a rf pulse at f_+ in the waveguide. The ratio between the intensity levels of different modes in the experiments deviates from the theoretical calculation, likely due to the spatial dependence of the duplets which form standing waves. Since TRμBLS measurements are time-consuming they were only performed at one position on the disk. Different scales were used for theory and experiments to highlight the feedback on the directly excited mode from theory, but also to show the small signals of TRμBLS.

earlier if stimulated 3MS takes place [Figs. 4(g) and 4(h)]. Additionally, in the theoretical calculation, the rf field in the waveguide at f_+ is only applied for a short duration at the beginning of the rf pulse at f_D; i.e., we stimulate only for a short time. Note that this time is much smaller than the time needed for the secondary modes to reach dynamical equilibrium in the case of spontaneous 3MS in Fig. 4(e). After the stimulation pulse at f_+ in Fig. 4(g) is turned off, spontaneous 3MS takes over and all modes relax slowly into their dynamic equilibrium. This illustrates that 3MS can be prematurely triggered above threshold even using only a short stimulation pulse.

In conclusion, we demonstrated that stimulated 3MS in a magnetic vortex can be achieved by coupling the dynamic fields of magnons propagating in an adjacent waveguide to the disk. Using micromagnetic simulations, nonlinear spin-wave theory, and Brillouin-light-scattering microscopy, we have predicted and confirmed that three-magnon splitting can be triggered below threshold by exciting one of the secondary modes or duplets. The BLS experiments have shown that stimulation is possible even at low powers and in a wide bandwidth around the frequencies of the secondary modes or duplets. Finally, we showed the instantaneous response to stimulation and the possibility to even prematurely trigger 3MS above threshold in a sustainable manner. Our theoretical predictions are not only verified experimentally but are qualitatively in good agreement. We believe that stimulated 3MS provides a new possibility to harness the potential of nonlinear spin-wave dynamics. The nonlinear system of coupled magnons, controlled by stimulated 3MS, could potentially serve as a basis for hardware neuromorphic computing. For example, an ensemble of vortex disks coupled to a network of waveguides could be utilized in magnon-based nonlinear networks, in which the individual disks or, alternatively, the magnon modes themselves act as neurons.

Financial support by the Deutsche Forschungsgemeinschaft within programs SCHU 2922/1-1 and KA 5069/1-1 is gratefully acknowledged. K. S. acknowledges funding within the Helmholtz Postdoc Programme. R. V. acknowledges support of NAS of Ukraine through Project No. 23-04/01-2020. The samples were fabricated at the Nanofabrication Facilities (NanoFaRo) at the Institute of Ion Beam Research and Materials Research at HZDR. We thank B. Scheumann for the film deposition.

L. K. and K. S. contributed equally to this work.

*l.koerber@hzdr.de
†k.schultheiss@hzdr.de

[1] N. Bloembergen and R. W. Damon, Phys. Rev. **85**, 699 (1952).
[2] R. W. Damon, Rev. Mod. Phys. **25**, 239 (1953).
[3] N. Bloembergen and S. Wang, Phys. Rev. **93**, 72 (1954).
[4] V. S. L'vov, *Wave Turbulence under Parametric Excitation: Applications to Magnets* (Springer Science & Business Media, New York, 2012).
[5] A. G. Gurevich and G. A. Melkov, *Magnetization Oscillations and Waves* (CRC Press, Boca Raton, FL, 1996).
[6] N. Bloembergen, *Nonlinear Optics*, Advanced Book Classics (Addison-Wesley Publishing Company, Reading, MA, 1991).
[7] A. Hasegawa, in *Proceedings of the Symposium on Physics and Applications of Optical Solitons in Fibres, Kyoto, Japan, 1995* (Springer Science & Business Media, New York, 2012), Vol. 3.
[8] D. Woods and T. J. Naughton, Nat. Phys. **8**, 257 (2012).
[9] G. Tanaka, T. Yamane, J. B. Hroux, R. Nakane, N. Kanazawa, S. Takeda, H. Numata, D. Nakano, and A. Hirose, Neural Netw. **115**, 100 (2019).
[10] D. Marković, N. Leroux, M. Riou, F. Abreu Araujo, J. Torrejon, D. Querlioz, A. Fukushima, S. Yuasa, J. Trastoy, P. Bortolotti *et al.*, Appl. Phys. Lett. **114**, 012409 (2019).
[11] J. Torrejon, M. Riou, F. A. Araujo, S. Tsunegi, G. Khalsa, D. Querlioz, P. Bortolotti, V. Cros, K. Yakushiji, A. Fukushima *et al.*, Nature (London) **547**, 428 (2017).
[12] K. Schultheiss, R. Verba, F. Wehrmann, K. Wagner, L. Körber, T. Hula, T. Hache, A. Kákay, A. A. Awad, V. Tiberkevich, A. N. Slavin, J. Fassbender, and H. Schultheiss, Phys. Rev. Lett. **122**, 097202 (2019).
[13] B. Zhang, Z. Wang, Y. Cao, P. Yan, and X. R. Wang, Phys. Rev. B **97**, 094421 (2018).
[14] M. Buess, R. Hőllinger, T. Haug, K. Perzlmaier, U. Krey, D. Pescia, M. R. Scheinfein, D.Weiss, and C. H. Back, Phys. Rev. Lett. **93**, 077207 (2004).
[15] M. Buess, T. P. J. Knowles, R. Hollinger, T. Haug, U. Krey, D. Weiss, D. Pescia, M. R. Scheinfein, and C. H. Back, Phys. Rev. B **71**, 104415 (2005).
[16] D. V. Slobodianiuk, G. A. Melkov, K. Schultheiss, H. Schultheiss, and R. V. Verba, IEEE Magn. Lett. **10**, 1 (2019).
[17] K. Y. Guslienko, A. N. Slavin, V. Tiberkevich, and S.-K. Kim, Phys. Rev. Lett. **101**, 247203 (2008).
[18] B. A. Ivanov and C. E. Zaspel, Phys. Rev. Lett. **94**, 027205 (2005).
[19] R. V. Verba, A. Hierro-Rodriguez, D. Navas, J. Ding, X. M. Liu, A. O. Adeyeye, K. Y. Guslienko, and G. N. Kakazei, Phys. Rev. B **93**, 214437 (2016).
[20] K. Y. Guslienko, B. A. Ivanov, V. Novosad, Y. Otani, H. Shima, and K. Fukamichi, J. Appl. Phys. **91**, 8037 (2002).
[21] A. Y. Galkin, B. A. Ivanov, and C. E. Zaspel, Phys. Rev. B **74**, 144419 (2006).
[22] D. D. Sheka, I. A. Yastremsky, B. A. Ivanov, G. M. Wysin, and F. G. Mertens, Phys. Rev. B **69**, 054429 (2004).
[23] B. A. Ivanov, H. J. Schnitzer, F. G. Mertens, and G. M. Wysin, Phys. Rev. B **58**, 8464 (1998).
[24] B. A. Ivanov and C. E. Zaspel, Appl. Phys. Lett. **81**, 1261 (2002).
[25] G. Lv, H. Zhang, X. Cao, F. Gao, and Y. Liu, Appl. Phys. Lett. **103**, 252404 (2013).
[26] I. Neudecker, K. Perzlmaier, F. Hoffmann, G. Woltersdorf, M. Buess, D. Weiss, and C. H. Back, Phys. Rev. B **73**, 134426 (2006).

[27] B. Taurel, T. Valet, V. V. Naletov, N. Vukadinovic, G. de Loubens, and O. Klein, Phys. Rev. B **93**, 184427 (2016).
[28] F. Hoffmann, G. Woltersdorf, K. Perzlmaier, A. N. Slavin, V. S. Tiberkevich, A. Bischof, D. Weiss, and C. H. Back, Phys. Rev. B **76**, 014416 (2007).
[29] See Supplemental Material http://link.aps.org/supplemental/10.1103/PhysRevLett.125.207203 for a description of the methods used, a demonstration of stimulated 3MS at different excitation frequencies and a theoretical discussion of the bandwidth of stimulation, which includes Refs. [30,31].
[30] R. Verba, V. Tiberkevich, and A. Slavin, Phys. Rev. B **98**, 104408 (2018).
[31] R. Verba, L. Körber, K. Schultheiss, H. Schultheiss, V. Tiberkevich, and A. Slavin, arXiv:2008.11812.
[32] B. A. Kalinikos and A. N. Slavin, J. Phys. C **19**, 7013 (1986).
[33] T. Sebastian, K. Schultheiss, B. Obry, B. Hillebrands, and H. Schultheiss, Front. Phys. **3**, 35 (2015).
[34] A. Vansteenkiste, J. Leliaert, M. Dvornik, M. Helsen, F. Garcia-Sanchez, and B. Van Waeyenberge, AIP Adv. **4**, 107133 (2014).
[35] A. Kákay, Curvilinear Micromagnetism, https://www.hzdr.de/db/Cms?pOid=55944&pNid=107.
[36] In simulations, the rf field was set to about 75% of the threshold field. In experiments, an excitation at about 50% of the threshold power was used.
[37] G. A. Melkov, D. V. Slobodianiuk, V. S. Tiberkevich, G. de Loubens, O. Klein, and A. N. Slavin, IEEE Magn. Lett. **4**, 4000504 (2013).
[38] P. Krivosik and C. E. Patton, Phys. Rev. B **82**, 184428 (2010).
[39] K. Livesey, in *Handbook of Surface Science* (Elsevier, New York, 2015), Vol. 5, pp. 169–214.

NANO LETTERS

pubs.acs.org/NanoLett Letter

Curvilinear One-Dimensional Antiferromagnets

Oleksandr V. Pylypovskyi,[†] Denys Y. Kononenko,[†] Kostiantyn V. Yershov, Ulrich K. Rößler, Artem V. Tomilo, Jürgen Fassbender, Jeroen van den Brink, Denys Makarov,* and Denis D. Sheka*

Cite This: *Nano Lett.* 2020, 20, 8157−8162 Read Online

ACCESS | Metrics & More | Article Recommendations | Supporting Information

ABSTRACT: Antiferromagnets host exotic quasiparticles, support high frequency excitations and are key enablers of the prospective spintronic and spin−orbitronic technologies. Here, we propose a concept of a curvilinear antiferromagnetism where material responses can be tailored by a geometrical curvature without the need to adjust material parameters. We show that an intrinsically achiral one-dimensional (1D) curvilinear antiferromagnet behaves as a chiral helimagnet with geometrically tunable Dzyaloshinskii−Moriya interaction (DMI) and orientation of the Néel vector. The curvature-induced DMI results in the hybridization of spin wave modes and enables a geometrically driven local minimum of the low-frequency branch. This positions curvilinear 1D antiferromagnets as a novel platform for the realization of geometrically tunable chiral antiferromagnets for antiferromagnetic spin−orbitronics and fundamental discoveries in the formation of coherent magnon condensates in the momentum space.

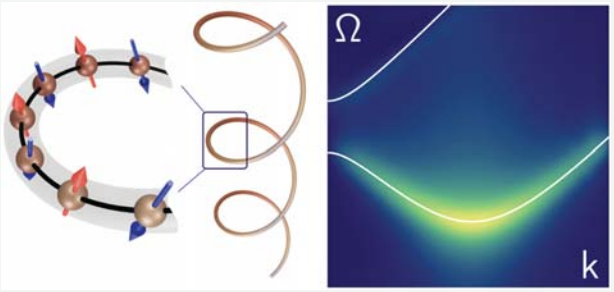

KEYWORDS: *antiferromagnetism, curvilinear spin chain, Dzyaloshinskii−Moriya interaction, spin−orbitronics, coherent magnon excitations*

■ INTRODUCTION

Antiferromagnets (AFMs) have emerged as a versatile material science platform that enabled numerous fundamental discoveries including observation of monopole quasiparticles in frustrated systems[1−3] and collective quantum effects, such as spin superfluidity[4−6] and Bose−Einstein condensation (BEC) of magnetic excitations.[5,7,8] This trend is even further facilitated by the advent of antiferromagnetic spintronics[6,9−11] and related novel physical concepts of staggered spin−orbit torques.[11−13] These effects are specific to AFMs possessing broken inversion symmetry in a local environment, which is also a source of DMI.[14−16] The presence of DMI can cause noncollinear AFM states, characterized by weak ferromagnetism and (or) chiral helimagnetism.[17,18] DMI significantly affects dynamics of solitary excitations in AFMs including much higher domain wall velocities[19] and absence of the gyroforce (Magnus force) for skyrmions.[20,21] The portfolio of material systems available for these studies is very limited due to the stringent requirement on symmetry, as DMI-induced chiral textures in an AFM can exist only in magnetic materials belonging to gyrotropic crystal classes.[15,17] In addition, the efficient manipulation of arbitrary textures of any kind by spin−orbit torques also requires broken inversion symmetry of the crystal lattice or staggered spin current polarization.[22] This requirement renders the progress in AFM-related fundamental and technological research to depend on time-consuming material screening and optimization of intrinsic chiral properties of AFMs.

For ferromagnets (FMs) chiral responses in nanowires and thin films can be tailored by using curvilinear geometries.[23−26] This framework, known as curvilinear magnetism,[27−30] allows induction of magnetochiral effects in otherwise conventional achiral FMs.[25,31,32] In contrast to FMs, no theory of curvilinear antiferromagnetism is available to date. Therefore, the appealing approaches to use geometrical curvatures to enable chiral properties in AFMs have not been explored. If available, it would be possible to decouple the design of chiral responses of AFMs and their intrinsic magnetic properties. We emphasize that the case of curvilinear AFMs is fundamentally different from curvilinear FMs primarily due to the necessity to self-consistently account for the mutual interplay of several (at least two for AFM vs one for FM) fields of magnetization with the geometrical curvature. This is directly related to the physical nature of the order parameter in AFMs. In contrast to FMs, where the opposite directions of the magnetization correspond to different magnetic states, the AFM order parameter is represented only by the axis of orientation, similarly to nematic directors.[33] The latter leads to specific types of domains, absent

Received: August 7, 2020
Revised: September 28, 2020
Published: September 28, 2020

https://dx.doi.org/10.1021/acs.nanolett.0c03246
Nano Lett. 2020, 20, 8157−8162

Nano Letters pubs.acs.org/NanoLett Letter

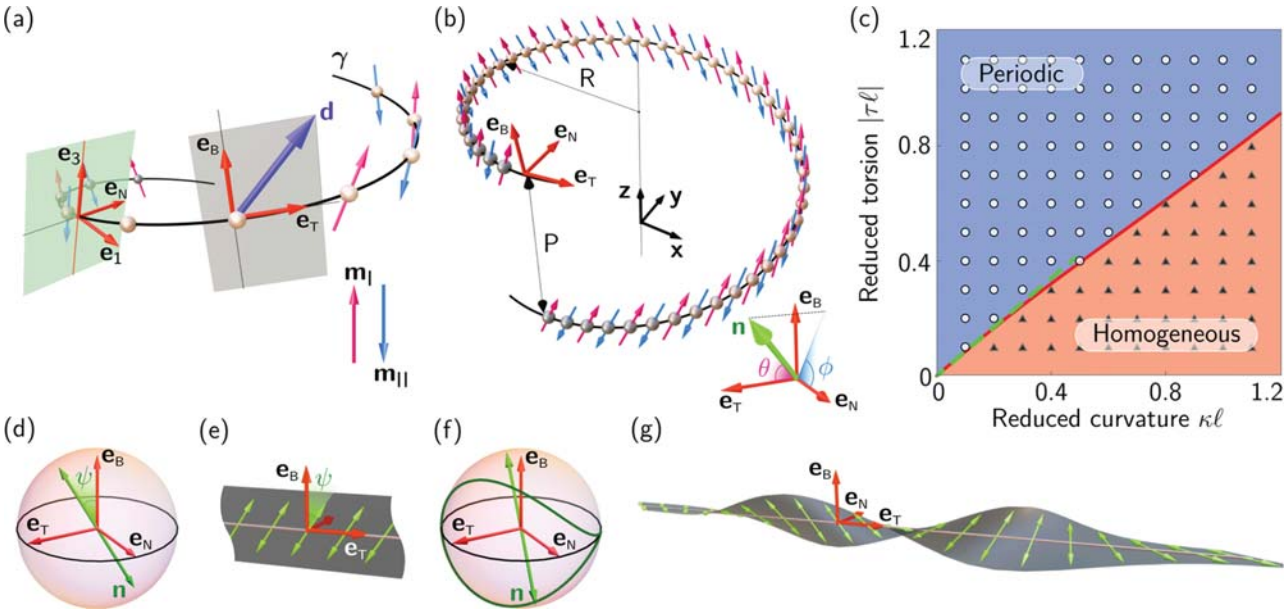

Figure 1. (a) Schematics of the antiferromagnetic spin chain $\boldsymbol{\gamma}$. Magnetic sublattices with magnetization $\boldsymbol{m}_{\mathrm{I}}$ and $\boldsymbol{m}_{\mathrm{II}}$ are shown by magenta and light-blue arrows. The Dzyaloshinskii vector $\boldsymbol{d}$ (dark-blue) lies in the TB plane given by the TNB basis $\boldsymbol{e}_{\mathrm{T,N,B}}$. Hard and easy anisotropy axes are labeled by $\boldsymbol{e}_1$ and $\boldsymbol{e}_3$, respectively. (b) Helix spin chain with radius R and pitch P. The AFM order parameter (Néel vector) $\boldsymbol{n}$ parametrized by angles θ and ϕ is shown by the green arrow. (c) Diagram of equilibrium states for a helix spin chain. Open symbols and triangles correspond to periodic and homogeneous states, respectively, obtained in spin−lattice simulations. The solid red curve shows the boundary between the states. The dashed green line shows the asymptotic of the boundary $\tau_b \approx 0.85\kappa$ for $\kappa\, l \ll 1$. Schematics of the (d, e) homogeneous and (f, g) periodic states in the TNB reference frame. (d, f) Bloch spheres illustrate the trajectories of $\boldsymbol{n}$. The tilt angle $\psi \approx l^2\kappa\tau$.

in FMs.[34,35] The staggered magnetic ordering also allows the magnetostatic interaction between neighboring AFM systems to be neglected and enhances the resonance frequencies.[36]

In this Letter, we put forth a fundamental foundation of curvilinear 1D AFMs. We explore curvature effects in a prototypical AFM system, namely, spin chain where spins are coupled via local exchange and long-range dipolar interactions. The nearest-neighbor exchange interaction brings about two geometry-induced responses: the intrinsically achiral curvilinear AFM spin chain behaves as a chiral helimagnet with a geometrically tunable DMI and a biaxial anisotropy. We show that generic curvilinear 1D AFMs exhibit the full set of Lifshitz invariants, whose strength is determined by the local torsion and curvature. We apply our theory to analyze static and dynamic responses of helical AFM spin chains to demonstrate consequences of the coupling between the geometry and the AFM order parameter. Spin chains arranged along space curves with nonzero torsion exhibit a magnetic phase transition from homogeneous to periodic states, which is tunable by controlling geometrical parameters. The appearance of the curvature-induced DMI results in the hybridization of spin wave modes in linear dynamics and opens a possibility to investigate a coherent and long-living magnon state in the DMI-induced minimum of the dispersion curve.

Model of a Curvilinear AFM. We start with a classical spin chain taking into account the AFM nearest-neighbor exchange and dipolar interaction. Its static and dynamic properties are determined by the Landau−Lifshitz equation $\hbar S \mathrm{d}\boldsymbol{m}_i/\mathrm{d}t = \boldsymbol{m}_i \times \partial\mathcal{H}/\partial\boldsymbol{m}_i$ with the Hamiltonian specific to the collinear intrinsically achiral AFM

$$\mathcal{H} = -\frac{JS^2}{2}\boldsymbol{m}_i\cdot\boldsymbol{m}_{i+1} - \frac{\mu}{2}\sum_i \boldsymbol{m}_i\cdot\boldsymbol{H}_i^d. \tag{1}$$

Here, $\boldsymbol{m}_i$ is the unit magnetic moment of ith site, $\hbar$ is the Planck constant, S is the spin length, $J < 0$ is the exchange integral, $\mu = g\mu_{\mathrm{B}}S$ is the total magnetic moment of one site with g being Landé factor, and μ_{B} is Bohr magneton. The dipolar field at the ith site reads $\boldsymbol{H}_i^d = -\mu\sum_{j=1+i}^{\infty}[\boldsymbol{m}_j r_{ij}^2 - 3\boldsymbol{r}_{ij}(\boldsymbol{m}_j\cdot\boldsymbol{r}_{ij})]/r_{ij}^5$ with $\boldsymbol{r}_{ij}$ being the radius-vector between the ith and jth sites and the distance between neighboring sites equal a. We assume that the positions of all magnetic sites are described by a space curve $\boldsymbol{\gamma}(s)$ with s being the arc-length characterized by the curvature $\kappa(s)$ and torsion $\tau(s)$. The local reference frame can be chosen as the Frenet−Serret frame with tangential, normal, and binormal vectors $\boldsymbol{e}_{\mathrm{T,N,B}}$, see Figure 1a.

The continuum counterpart of the spin−lattice model is formulated on the basis of two vector fields, namely, the total magnetization $\boldsymbol{m}(s) = (\boldsymbol{m}_{\mathrm{I}} + \boldsymbol{m}_{\mathrm{II}})/2$ and Néel vector $\boldsymbol{n}(s) = (\boldsymbol{m}_{\mathrm{I}} - \boldsymbol{m}_{\mathrm{II}})/2$. The fields $\boldsymbol{m}_{\mathrm{I,II}} = \boldsymbol{m}_{\mathrm{I,II}}(s)$ correspond to the two sublattices of the AFM. In the long-wave approximation, the density of Lagrangian $L = \int \mathcal{L}\mathrm{d}s$, corresponding to the curvilinear AFM reads

$$\mathcal{L} = \frac{M_s^2}{\gamma_0^2\Lambda}\dot{\boldsymbol{n}}^2 - \mathcal{E} \tag{2a}$$

with the overdot corresponding to the derivative with respect to time. The effective energy density $\mathcal{E}$ is written as

https://dx.doi.org/10.1021/acs.nanolett.0c03246
Nano Lett. 2020, 20, 8157−8162

$$\mathcal{E} = \mathcal{E}_x + \mathcal{E}_{\mathrm{DM}} + \mathcal{E}_{\mathrm{A}} + K(\boldsymbol{n}\cdot\boldsymbol{e}_{\mathrm{T}})^2$$
$$\mathcal{E}_x = An'_\alpha n'_\alpha,\ \mathcal{E}_{\mathrm{DM}} = A\mathcal{F}_{\alpha\beta}(n_\alpha n'_\beta - n_\beta n'_\alpha),$$
$$\mathcal{E}_{\mathrm{A}} = A\mathcal{K}_{\alpha\beta}n_\alpha n_\beta,\ \alpha, \beta \in \mathrm{T,N,B}, \tag{2b}$$

where $M_s = \mu/(2a)$ is the magnetization of one sublattice, γ_0 is the gyromagnetic ratio, $\Lambda = 2|J|S^2/a$ is the constant of the uniform exchange, $A = |J|S^2a/2$ is the exchange stiffness, and $K \approx 2.7\ \mu^2/a^4$ is the hard axis anisotropy constant induced by the dipolar interaction, see the Supporting Information. Model (2) is valid for $K \ll \Lambda$ and the space curve $\boldsymbol{\gamma}$ possessing consequent turns separated by a distance significantly larger than the lattice constant a. In this approximation, $|\boldsymbol{m}| \ll |\boldsymbol{n}|$ and $\boldsymbol{n}$ can be considered as a unit director. In model (2b), the Einstein summation rule is applied and prime means derivative with respect to s. The Frenet tensor $\mathcal{F}_{\alpha\beta}$ has four nonzero components $\mathcal{F}_{\mathrm{TN}} = -\mathcal{F}_{\mathrm{NT}} = \kappa$ and $\mathcal{F}_{\mathrm{NB}} = -\mathcal{F}_{\mathrm{BN}} = \tau$. The characteristic length and time scales are given by the magnetic length $l = \sqrt{A/K}$ and the frequency of the AFM resonance $\omega_0 = c/l$ with $c = \gamma_0\sqrt{\Lambda A}/M_s$ being the characteristic magnon speed. The exchange energy density expands into three terms, with only one, $\mathcal{E}_x$, possessing the form of a regular inhomogeneous exchange in straight spin chains.

The term $\mathcal{E}_{\mathrm{DM}}$ can be written as the functional form of a DMI, $\mathcal{E}_{\mathrm{DM}} = \boldsymbol{d}\cdot[\boldsymbol{n} \times \boldsymbol{n}']$. This term is allowed in crystals with magnetic symmetry groups C_n and S_4 acting on 1D magnetic textures.[15] However, its origin is not the spin−orbit interaction as for the case of intrinsic DMI but the exchange interaction. The vector $\boldsymbol{d} = \mathrm{d}_{\mathrm{T}}\boldsymbol{e}_{\mathrm{T}} + \mathrm{d}_{\mathrm{B}}\boldsymbol{e}_{\mathrm{B}}$ acts as the Dzyaloshinskii vector with components $\mathrm{d}_{\mathrm{T}} = 2A\tau$ and $\mathrm{d}_{\mathrm{B}} = 2A\kappa$. This DMI corresponds to the full set of Lifshitz invariants, allowed in a 1D magnet. The DMI vector $\boldsymbol{d}$ is linear with respect to τ and κ, which allows strong chiral effects in curvilinear 1D AFMs. The strength of the curvature-induced DMI can be estimated as the relation to the exchange stiffness. For instance, in the case of a Mn-DNA chain (A-DNA form) bent to the radius of 15 nm, the $ad_{\mathrm{T,B}}/A$ is about 0.05. (Magnetic parameters of Mn-DNA $S = 5/2$, $a = 0.344$ nm, and $|J| = 9.6 \times 10^{-25}$ J are taken from ref 37.) This value is comparable with the intrinsic chiral properties of $KMnF_3$ used for the discussion of dynamics of 1D solitons[19,38] ($aD/A = 0.036$ with D being the constant of the nonuniform DMI), where ultrafast motion of AFM domain walls was predicted.[19]

In addition to the linear in τ and κ DMI terms, the expression for energy density $\mathcal{E}$ contains weaker bilinear terms, representing a curvature-induced anisotropy $\mathcal{E}_{\mathrm{A}}$ whose coefficients are given by the tensor $\mathcal{K}_{\alpha\beta} = \mathcal{F}_{\alpha\gamma}\mathcal{F}_{\beta\gamma} \propto \kappa^2, \tau^2, \kappa\tau$. It contains nondiagonal terms, causing the tilt of $\boldsymbol{n}$ within the rectifying surface formed by $\boldsymbol{e}_{\mathrm{T}}$ and $\boldsymbol{e}_{\mathrm{B}}$. The presence of the two anisotropies (hard axis stemming from the dipolar interaction and easy axis stemming from the exchange interaction) renders a curvilinear AFM spin chain to behave as a biaxial AFM. The directions of the primary hard axis $\boldsymbol{e}_1$ and secondary easy axis $\boldsymbol{e}_3$ are determined by the diagonalization of the tensor of the total anisotropy $A\mathcal{K}_{\alpha\beta} + \delta_{1\alpha}\delta_{1\beta}K$ with $\delta_{\alpha\beta}$ being Kronecker delta, see Figure 1a. The axis $\boldsymbol{e}_1$ lies within the rectifying surface. The anisotropy induced by the dipolar interaction is the strongest one and defines the plane, where the Néel vector rotates. The direction of the vector $\boldsymbol{n}$ within the easy plane is given by the curvature-induced anisotropy $\mathcal{E}_{\mathrm{A}}$. The system has no competing easy axis anisotropy terms. This means that independent of the strength of $\mathcal{E}_{\mathrm{A}}$ it govern the orientation of the Néel vector even for $A\kappa^2$, $A\tau^2 \ll K$.

As a result, a generic curvilinear achiral 1D AFM will behave as a chiral helimagnet with the DMI strength and the orientation of the Néel vector determined by the geometrical parameters, i.e., curvature and torsion.

Ground State of AFM Helix Chains. To illustrate the behavior of curvilinear AFM spin chains, described by (2), we analyzed a helix chain as the prototypical curvilinear systems possessing a constant curvature and torsion. The geometry of a helix is characterized by the radius $R = \kappa/(\kappa^2 + \tau^2)$ and pitch $P = 2\pi\tau/(\kappa^2 + \tau^2)$, see Figure 1b. It is convenient to introduce the angular parametrization of the Néel vector $\boldsymbol{n} = \boldsymbol{e}_{\mathrm{T}}\cos\theta + \boldsymbol{e}_{\mathrm{N}}\sin\theta\cos\phi + \boldsymbol{e}_{\mathrm{B}}\sin\theta\sin\phi$ with $\theta = \theta(s, t)$ and $\phi = \phi(s, t)$ being polar and azimuthal angles, respectively. Taking into account the Néel vector is a director, states with (θ, ϕ) and $(\pi - \theta, \phi \pm \pi)$ are equivalent. The linear energy density then reads

$$\mathcal{E} = A(\theta' + \kappa\cos\phi)^2 + A[\sin\theta(\phi' + \tau) - \kappa\cos\theta\sin\phi]^2 + K\cos^2\theta. \tag{3}$$

As a biaxial chiral helimagnet, helix spin chains support homogeneous and periodic equilibrium states dependent on the strength of the DMI, see Figure 1c. For the case of the homogeneous state, which is realized for $\tau < \tau_b(\kappa) \approx 0.85\kappa$ at $\kappa l \ll 1$, see Figure 1d, e and the Supporting Information, the orientation of the Néel vector is given by $\theta_{\mathrm{hom}} = \pi/2 - \psi$ and $\phi_{\mathrm{hom}} = \pi/2$, where $\psi \approx l^2\kappa\tau$ and $\kappa l, |\tau| l \ll 1$.

The periodic state can be stabilized in systems possessing torsion $\tau > \tau_{\mathrm{b}}(\kappa)$. In the periodic state, the Néel vector is almost uniform in the plane perpendicular to the helix axis and modulated in the local reference frame, see Figure 1f, g. The emergence of the periodic state is a consequence of the exchange-induced DMI, $\mathcal{E}_{\mathrm{DM}}$, with the main contribution given by the torsion-related term d_{T}. When the curvature is much smaller than the torsion, the state can be described as the Dzyaloshinskii spiral[39] with $\theta_{\mathrm{per}} = \pi/2$ and $\phi_{\mathrm{per}} = -\tau s$. The boundary between the homogeneous and periodic states $\tau_b(\kappa)$ is plotted by the solid red line in Figure 1c.

It is instructive to compare the results above with FM spin chains, where dipolar interactions induce easy axis anisotropy. In contrast to a FM helices,[24] the phase transition between the periodic and homogeneous states in AFMs has no threshold in curvature. Hence, the transition to the periodic state in the case of AFM helical chains can be observed for very small curvatures. This is a consequence of the specificity of the curvilinear AFM systems where the stability of the state is given by the weak easy axis anisotropy stemming from the exchange interaction. Therefore, effects of curvilinearity in AFMs are much stronger than in FMs.

Linear Dynamics. To describe linear excitations in a curved AFM helix chain, we consider the homogeneous magnetic state. The Euler−Lagrange equations for the Lagrangian (2a) are linearized by $\theta(s, t) = \theta_{\mathrm{hom}} + \vartheta(s, t)$ and $\phi(s, t) = \phi_{\mathrm{hom}} + \varphi(s, t)/\sin\theta_{\mathrm{hom}}$. Here, $\vartheta(s, t)$ and $\varphi(s, t)$ are small deviations from the equilibrium state. The corresponding equations read

https://dx.doi.org/10.1021/acs.nanolett.0c03246
Nano Lett. 2020, 20, 8157−8162

$$A\vartheta'' - Ac^{-2}\vartheta = K_0\ddot{\vartheta} + D_3\varphi',$$
$$A\varphi'' - Ac^{-2}\varphi = K_3\ddot{\varphi} - D_3\vartheta', \quad (4)$$

where $K_{0,3}$ and D_3 are functions of curvature, acting as the effective anisotropy and DMI coefficients, respectively, see the Supporting Information. For a large curvature radius and small torsion, $K_0 \approx A(l^{-2} + \kappa^2 - \tau^2)$, $K_3 \approx A\kappa^2$ and $D_3 \approx 2A\kappa$. The dispersion law can be written using the substitution of plane waves $\vartheta(s, t) = \vartheta_k \cos(ks - \Omega t)$ and $\varphi(s, t) = \varphi_k \sin(ks - \Omega t)$, where ϑ_k and φ_k are small amplitudes, k is the wavenumber, and Ω is frequency. The dispersion reads

$$\frac{\Omega^2}{c^2} = k^2 + \frac{K_0 + K_3}{2A} + \frac{q}{2A}\sqrt{(K_0 - K_3)^2 + 4D_3^2k^2}. \quad (5)$$

We note that the dispersion curve is similar to flat biaxial AFMs with DMI[19] and remains symmetric with respect to the sign of the momentum k. Yet, the geometrical tunability of the anisotropy and DMI allows to unveil new physics of collective excitations in curvilinear 1D AFMs.

The spin-wave spectrum (5) superimposed with spin−lattice simulations (see the Supporting Information) is shown in Figure 2a for two helix geometries (Figure 2b). The high-frequency optical branch with $q = 1$ is always gapped and the change of the geometry affects only the gap due to the curvature-induced anisotropy, $\Omega^{\text{gap}}_{q=+1} = \omega_0 + cl(\kappa^2 - \tau^2)/2$. In contrast, there is a strong qualitative impact of the curvature on the low frequency branch. While it is gapless for a straight spin chain,[40] the gap $\Omega^{\text{gap}}_{q=-1} \approx c\kappa$ appears for any finite curvature as a results of the spin-wave hybridization, forming a low-frequency optical branch with $q = -1$, see Figure 2a. The curvature-induced DMI results in the emergence of a region with a negative group velocity followed by a local minimum at $k = k_{\text{min}}$ on the dispersion curve with the depth δ, see Figure 2a, c. The presence of a negative group velocity is also observed for multiferroics[41] and exchange-dipolar modes in AFM thin films.[42,43] The depth of the minimum increases with κ and τ, see Figure 2d. The possibility to realize magnon ground states not in equilibrium ($k \neq 0$ at minimum energy)[44] renders curvilinear 1D AFMs a flexible platform to study coherent excitations for spin superfluidity[45−47] and BEC of magnons[48−51] with taking into account a proper pumping and magnon thermodynamics.

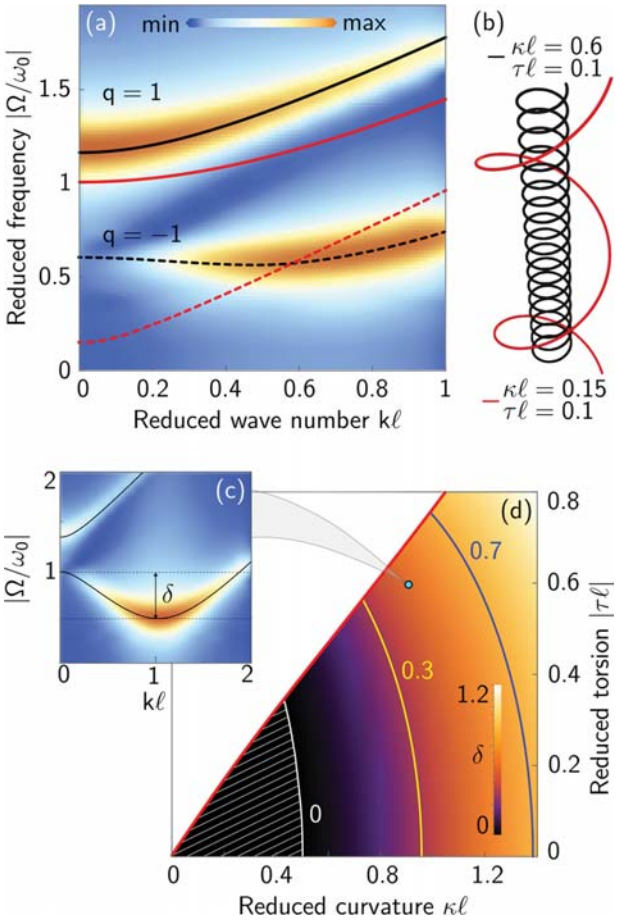

Figure 2. (a) Spin-wave dispersion (5) for helical AFM spin chains with $\tau l = 0.1$ and two curvatures $\kappa l = 0.6$ (black) and $\kappa l = 0.15$ (red). The result of spin−lattice simulations is shown by the background color for a helical spin chain with the geometry with $\tau l = 0.1$ and $\kappa l = 0.6$. (b) Helix geometries calculated in a. (c) Spin-wave dispersion (5) and simulations for $\kappa l = 0.9$ and $\tau l = 0.6$. The depth of the minimum in the acoustic branch is shown by δ. (d) The depth δ for different curvatures and torsions within the homogeneous ground state (below red line, same as in Figure 1c). Dashed line corresponds to the absence of minimum.

CONCLUSIONS

We develop a theory of curvilinear one-dimensional antiferromagnets. We demonstrate that the intrinsically achiral curvilinear AFM spin chain behaves as a biaxial chiral helimagnet with geometrically tunable DMI and anisotropy. The curvature-induced DMI results in the hybridization of magnon modes in the chain. The low-frequency branch possesses a local minimum supporting a long-living magnon state, which allows consideration of 1D curvilinear AFMs as the platform for the realization of BEC of magnons in k-space. Furthermore, the symmetry and strength of the geometry-induced DMI opens perspectives for applications in antiferromagnetic spin−orbitronics, e.g. for ultrafast dynamics of chiral domain walls.[19,38] We consider copper-based[52] and DNA-based metal−organic frameworks[53−56] as a promising materials for experimental validation of our predictions. For instance, one can expect the strength of curvature-induced DMI as $ad_{\text{T, B}}/A \approx 0.05$, which is comparable with AFMs supporting chiral domain walls.

ASSOCIATED CONTENT

Supporting Information

The Supporting Information is available free of charge at https://pubs.acs.org/doi/10.1021/acs.nanolett.0c03246.

Details on analytical calculations and numerical simulations, including (i) the geometry, (ii) the model of curvilinear antiferromagnet, (iii) dipolar interaction in spin chains as an effective anisotropy (both ferromagnetic and antiferromagnetic ordering, and curvilinear antiferromagnetic spin chains), (iv) the homogeneous state of antiferromagnetic helix chains, (v) the periodic state of antiferromagnetic helix chains, (vi) the boundary between states, (vii) The ground state of antiferromagnetic flat chains, (viii) spin waves in antiferromagnetic flat chains, (ix) spin waves in antiferromagnetic helices

https://dx.doi.org/10.1021/acs.nanolett.0c03246
Nano Lett. 2020, 20, 8157−8162

and stability of the homogeneous state, and (x) simulations (PDF)

AUTHOR INFORMATION

Corresponding Authors

Denys Makarov − *Helmholtz-Zentrum Dresden-Rossendorf e.V., Institute of Ion Beam Physics and Materials Research, Dresden 01328, Germany;* orcid.org/0000-0002-7177-4308; Email: d.makarov@hzdr.de

Denis D. Sheka − *Taras Shevchenko National University of Kyiv, Kyiv 01601, Ukraine;* orcid.org/0000-0001-7311-0639; Email: sheka@knu.ua

Authors

Oleksandr V. Pylypovskyi − *Helmholtz-Zentrum Dresden-Rossendorf e.V., Institute of Ion Beam Physics and Materials Research, Dresden 01328, Germany; Taras Shevchenko National University of Kyiv, Kyiv 01601, Ukraine;* orcid.org/0000-0002-5947-9760

Denys Y. Kononenko − *Taras Shevchenko National University of Kyiv, Kyiv 01601, Ukraine; Institute for Theoretical Solid State Physics, IFW Dresden, Dresden 01069, Germany;* orcid.org/0000-0002-4467-730X

Kostiantyn V. Yershov − *Institute for Theoretical Solid State Physics, IFW Dresden, Dresden 01069, Germany; Bogolyubov Institute for Theoretical Physics of National Academy of Sciences of Ukraine, Kyiv 03143, Ukraine;* orcid.org/0000-0003-2731-2808

Ulrich K. Rößler − *Institute for Theoretical Solid State Physics, IFW Dresden, Dresden 01069, Germany*

Artem V. Tomilo − *Taras Shevchenko National University of Kyiv, Kyiv 01601, Ukraine;* orcid.org/0000-0002-5390-2767

Jürgen Fassbender − *Helmholtz-Zentrum Dresden-Rossendorf e.V., Institute of Ion Beam Physics and Materials Research, Dresden 01328, Germany*

Jeroen van den Brink − *Institute for Theoretical Solid State Physics, IFW Dresden, Dresden 01069, Germany; Institute for Theoretical Physics, TU Dresden, Dresden 01069, Germany*

Complete contact information is available at: https://pubs.acs.org/10.1021/acs.nanolett.0c03246

Author Contributions

†O.V.P. and D.Y.K. contributed equally to this work.

Notes

The authors declare no competing financial interest.

ACKNOWLEDGMENTS

We thank U. Nitzsche for technical support. D.Y.K. and K.V.Y. acknowledge financial support from UKRATOP-project (funded by BMBF under reference 01DK18002). In part, this work was supported by the Program of Fundamental Research of the Department of Physics and Astronomy of the National Academy of Sciences of Ukraine (Project 0120U100855), by the Alexander von Humboldt Foundation (Research Group Linkage Programme), DFG MA 5144/22-1, DFG MA 5144/24-1, DFG MC 9/22-1, and by Taras Shevchenko National University of Kyiv (Project 19BF052-01).

DEDICATION

This paper is dedicated to the memory of the wonderful physicist Yuri Gaididei, who recently passed away.

REFERENCES

(1) Castelnovo, C.; Moessner, R.; Sondhi, S. L. Magnetic monopoles in spin ice. *Nature* **2008**, *451*, 42−45.

(2) Nagaosa, N.; Tokura, Y. Emergent electromagnetism in solids. *Phys. Scr.* **2012**, *T146*, 014020.

(3) Zvyagin, A. A. New physics in frustrated magnets: Spin ices, monopoles, etc. (Review Article). *Low Temp. Phys.* **2013**, *39*, 901−922.

(4) Takei, S.; Halperin, B. I.; Yacoby, A.; Tserkovnyak, Y. Superfluid spin transport through antiferromagnetic insulators. *Phys. Rev. B: Condens. Matter Mater. Phys.* **2014**, *90*, 094408.

(5) Proukakis, N., Snoke, D., Littlewood, P., Eds.; *Universal Themes of Bose−Einstein Condensation*; Cambridge University Press, 2017; pp 387−388.

(6) Baltz, V.; Manchon, A.; Tsoi, M.; Moriyama, T.; Ono, T.; Tserkovnyak, Y. Antiferromagnetic spintronics. *Rev. Mod. Phys.* **2018**, *90*, 015005.

(7) Rice, T. M. QUANTUM MECHANICS: To Condense or Not to Condense. *Science* **2002**, *298*, 760−761.

(8) Giamarchi, T.; Rüegg, C.; Tchernyshyov, O. Bose−Einstein condensation in magnetic insulators. *Nat. Phys.* **2008**, *4*, 198−204.

(9) Gomonay, O.; Jungwirth, T.; Sinova, J. Concepts of antiferromagnetic spintronics. *Phys. Status Solidi RRL* **2017**, *11*, 1700022.

(10) Šmejkal, L.; Mokrousov, Y.; Yan, B.; MacDonald, A. H. Topological antiferromagnetic spintronics. *Nat. Phys.* **2018**, *14*, 242−251.

(11) Manchon, A.; Železný, J.; Miron, I. M.; Jungwirth, T.; Sinova, J.; Thiaville, A.; Garello, K.; Gambardella, P. Current-induced spin-orbit torques in ferromagnetic and antiferromagnetic systems. *Rev. Mod. Phys.* **2019**, *91*, 035004.

(12) Zhang, X.; Liu, Q.; Luo, J.-W.; Freeman, A. J.; Zunger, A. Hidden spin polarization in inversion-symmetric bulk crystals. *Nat. Phys.* **2014**, *10*, 387−393.

(13) Železný, J.; Gao, H.; Výborný, K.; Zemen, J.; Mašek, J.; Manchon, A.; Wunderlich, J.; Sinova, J.; Jungwirth, T. Relativistic Néel-Order Fields Induced by Electrical Current in Antiferromagnets. *Phys. Rev. Lett.* **2014**, *113*, 157201.

(14) Dzialoshinskii, I. E. Thermodynamic theory of "weak" ferromagnetism in antiferromagnetic substances. *Sov. Phys. JETP* **1957**, *5*, 1259−1272.

(15) Bogdanov, A. N.; Yablonskiĭ, D. A. Thermodynamically stable "vortices" in magnetically ordered crystals. The mixed state of magnets. *Zh. Eksp. Teor. Fiz.* **1989**, *95*, 178−182.

(16) Qaiumzadeh, A.; Ado, I. A.; Duine, R. A.; Titov, M.; Brataas, A. Theory of the Interfacial Dzyaloshinskii-Moriya Interaction in Rashba Antiferromagnets. *Phys. Rev. Lett.* **2018**, *120*, 197202.

(17) Dzyaloshinskii, I. E. Theory of Helicoidal Structures in Antiferromagnets. I. Nonmetals. *Sov. Phys. JETP* **1964**, *19*, 960−971.

(18) Bogdanov, A. N.; Rößler, U. K.; Wolf, M.; Müller, K.-H. Magnetic structures and reorientation transitions in noncentrosymmetric uniaxial antiferromagnets. *Phys. Rev. B: Condens. Matter Mater. Phys.* **2002**, *66*, 214410.

(19) Qaiumzadeh, A.; Kristiansen, L. A.; Brataas, A. Controlling chiral domain walls in antiferromagnets using spin-wave helicity. *Phys. Rev. B: Condens. Matter Mater. Phys.* **2018**, *97*, No. 020402(R).

(20) Barker, J.; Tretiakov, O. A. Static and Dynamical Properties of Antiferromagnetic Skyrmions in the Presence of Applied Current and Temperature. *Phys. Rev. Lett.* **2016**, *116*, 147203.

(21) Shen, L.; Li, X.; Zhao, Y.; Xia, J.; Zhao, G.; Zhou, Y. Current-Induced Dynamics of the Antiferromagnetic Skyrmion and Skyrmionium. *Phys. Rev. Appl.* **2019**, *12*, 064033.

(22) Železný, J.; Wadley, P.; Olejník, K.; Hoffmann, A.; Ohno, H. Spin transport and spin torque in antiferromagnetic devices. *Nat. Phys.* **2018**, *14*, 220−228.
(23) Gaididei, Y.; Kravchuk, V. P.; Sheka, D. D. Curvature Effects in Thin Magnetic Shells. *Phys. Rev. Lett.* **2014**, *112*, 257203.
(24) Sheka, D. D.; Kravchuk, V. P.; Yershov, K. V.; Gaididei, Y. Torsion-induced effects in magnetic nanowires. *Phys. Rev. B: Condens. Matter Mater. Phys.* **2015**, *92*, 054417.
(25) Pylypovskyi, O. V.; Sheka, D. D.; Kravchuk, V. P.; Yershov, K. V.; Makarov, D.; Gaididei, Y. Rashba Torque Driven Domain Wall Motion in Magnetic Helices. *Sci. Rep.* **2016**, *6*, 23316.
(26) Sheka, D. D.; Pylypovskyi, O. V.; Landeros, P.; Gaididei, Y.; Kákay, A.; Makarov, D. Nonlocal chiral symmetry breaking in curvilinear magnetic shells. *Communications Physics* **2020**, *3*, 128.
(27) Streubel, R.; Fischer, P.; Kronast, F.; Kravchuk, V. P.; Sheka, D. D.; Gaididei, Y.; Schmidt, O. G.; Makarov, D. Magnetism in curved geometries (Topical Review). *J. Phys. D: Appl. Phys.* **2016**, *49*, 363001.
(28) Fernández-Pacheco, A.; Streubel, R.; Fruchart, O.; Hertel, R.; Fischer, P.; Cowburn, R. P. Three-dimensional nanomagnetism. *Nat. Commun.* **2017**, *8*, 15756.
(29) Fischer, P.; Sanz-Hernández, D.; Streubel, R.; Fernández-Pacheco, A. Launching a new dimension with 3D magnetic nanostructures. *APL Mater.* **2020**, *8*, 010701.
(30) Vedmedenko, E. Y.; Kawakami, R. K.; Sheka, D.; Gambardella, P.; Kirilyuk, A.; Hirohata, A.; Binek, C.; Chubykalo-Fesenko, O. A.; Sanvito, S.; Kirby, B.; Grollier, J.; Everschor-Sitte, K.; Kampfrath, T.; You, C.-Y.; Berger, A. The 2020 Magnetism Roadmap. *J. Phys. D: Appl. Phys.* **2020**, *53*, 453001.
(31) Otálora, J. A.; Yan, M.; Schultheiss, H.; Hertel, R.; Kákay, A. Curvature-Induced Asymmetric Spin-Wave Dispersion. *Phys. Rev. Lett.* **2016**, *117*, 227203.
(32) Vojkovic, S.; Carvalho-Santos, V. L.; Fonseca, J. M.; Nunez, A. S. Vortex-antivortex pairs induced by curvature in toroidal nanomagnets. *J. Appl. Phys.* **2017**, *121*, 113906.
(33) Yang, D.-K.; Wu, S.-T. *Fundamentals of Liquid Crystal Devices*; John Wiley & Sons: Chichester, U.K., 2014.
(34) Cheong, S.-W.; Fiebig, M.; Wu, W.; Chapon, L.; Kiryukhin, V. Seeing is believing: visualization of antiferromagnetic domains. *npj Quantum Materials* **2020**, *5*, 3.
(35) Castillo-Sepúlveda, S.; Escobar, R. A.; Altbir, D.; Krizanac, M.; Vedmedenko, E. Y. Magnetic Möbius stripe without frustration: Noncollinear metastable states. *Phys. Rev. B: Condens. Matter Mater. Phys.* **2017**, *96*, 024426.
(36) Gurevich, A. G.; Melkov, G. A. *Magnetization Oscillations and Waves*; CRC Press, Boca Raton, FL, 1996.
(37) Mizoguchi, K.; Tanaka, S.; Ogawa, T.; Shiobara, N.; Sakamoto, H. Magnetic study of the electronic states of B-DNA and M-DNA doped with metal ions. *Phys. Rev. B: Condens. Matter Mater. Phys.* **2005**, *72*, 033106.
(38) Pan, K.; Xing, L.; Yuan, H. Y.; Wang, W. Driving chiral domain walls in antiferromagnets using rotating magnetic fields. *Phys. Rev. B: Condens. Matter Mater. Phys.* **2018**, *97*, 184418.
(39) Dzyaloshinskii, I. E. The Theory of Helicoidal Structures in Antiferromagnets. II. Metals. *Sov. Phys. JETP* **1965**, *20*, 223.
(40) Ivanov, B. A.; Kolezhuk, A. K. Solitons in Low-Dimensional Antiferromagnets. *Low Temp. Phys.* **1995**, *21*, 275−301.
(41) de Sousa, R.; Moore, J. E. Optical coupling to spin waves in the cycloidal multiferroic $BiFeO_3$. *Phys. Rev. B: Condens. Matter Mater. Phys.* **2008**, *77*, 012406.
(42) Stamps, R. L.; Camley, R. E. Bulk and surface spin waves in thin-film antiferromagnets. *J. Appl. Phys.* **1984**, *56*, 3497−3502.
(43) Stamps, R. L.; Camley, R. E. Dipole-exchange spin-wave modes in very-thin-film antiferromagnets. *Phys. Rev. B: Condens. Matter Mater. Phys.* **1987**, *35*, 1919−1931.
(44) Demokritov, S. O., Slavin, A. N., Eds.; *Magnonics: From Fundamentals to Applications*; Topics in Applied Physics; Springer: Berlin, 2013.
(45) Yuan, W.; Zhu, Q.; Su, T.; Yao, Y.; Xing, W.; Chen, Y.; Ma, Y.; Lin, X.; Shi, J.; Shindou, R.; Xie, X. C.; Han, W. Experimental signatures of spin superfluid ground state in canted antiferromagnet Cr_2O_3 via nonlocal spin transport. *Science Advances* **2018**, *4*, No. eaat1098.
(46) Sonin, E. B. Superfluid spin transport in ferro- and antiferromagnets. *Phys. Rev. B: Condens. Matter Mater. Phys.* **2019**, *99*, 104423.
(47) Evers, M.; Nowak, U. Transport properties of spin superfluids: Comparing easy-plane ferromagnets and antiferromagnets. *Phys. Rev. B: Condens. Matter Mater. Phys.* **2020**, *101*, 184415.
(48) Demokritov, S. O.; Demidov, V. E.; Dzyapko, O.; Melkov, G. A.; Serga, A. A.; Hillebrands, B.; Slavin, A. N. Bose−Einstein condensation of quasi-equilibrium magnons at room temperature under pumping. *Nature* **2006**, *443*, 430−433.
(49) Serga, A. A.; Tiberkevich, V. S.; Sandweg, C. W.; Vasyuchka, V. I.; Bozhko, D. A.; Chumak, A. V.; Neumann, T.; Obry, B.; Melkov, G. A.; Slavin, A. N.; Hillebrands, B. Bose−Einstein condensation in an ultra-hot gas of pumped magnons. *Nat. Commun.* **2014**, *5*, 3452.
(50) Clausen, P.; Bozhko, D. A.; Vasyuchka, V. I.; Hillebrands, B.; Melkov, G. A.; Serga, A. A. Stimulated thermalization of a parametrically driven magnon gas as a prerequisite for Bose−Einstein magnon condensation. *Phys. Rev. B: Condens. Matter Mater. Phys.* **2015**, *91*, No. 220402(R).
(51) Bozhko, D. A.; Serga, A. A.; Clausen, P.; Vasyuchka, V. I.; Heussner, F.; Melkov, G. A.; Pomyalov, A.; L'vov, V. S.; Hillebrands, B. Supercurrent in a room-temperature Bose−Einstein magnon condensate. *Nat. Phys.* **2016**, *12*, 1057−1062.
(52) Zhang, X.; Li, B.; Zhang, J. An Efficient Strategy for Self-Assembly of DNA-Mimic Homochiral 1D Helical Cu(II) Chain from Achiral Flexible Ligand by Spontaneous Resolution. *Inorg. Chem.* **2016**, *55*, 3378−3383.
(53) Zhang, H. Y.; Calzolari, A.; Di Felice, R. On the Magnetic Alignment of Metal Ions in a DNA-Mimic Double Helix. *J. Phys. Chem. B* **2005**, *109*, 15345−15348.
(54) Yamaguchi, K.; Taniguchi, T.; Kawakami, T.; Hamamoto, T.; Okumura, M. Possibilities of magnetic modifications of DNA wires, sheets and related materials. *Polyhedron* **2005**, *24*, 2758−2766.
(55) Mizoguchi, K.; Tanaka, S.; Ojima, M.; Sano, S.; Nagatori, M.; Sakamoto, H.; Yonezawa, Y.; Aoki, Y.; Sato, H.; Furukawa, K.; Nakamura, T. AF-like Ground State of Mn-DNA and Charge Transfer from Fe to Base-π-Band in Fe-DNA. *J. Phys. Soc. Jpn.* **2007**, *76*, 043801.
(56) Samanta, P. K.; Pati, S. K. Structural and Magnetic Properties of a Variety of Transition Metal Incorporated DNA Double Helices. *Chem. - Eur. J.* **2014**, *20*, 1760−1764.

https://dx.doi.org/10.1021/acs.nanolett.0c03246
Nano Lett. 2020, 20, 8157−8162

Singh et al. *Light: Science & Applications* (2020)9:30
https://doi.org/10.1038/s41377-020-0265-4

Official journal of the CIOMP 2047-7538
www.nature.com/lsa

ARTICLE Open Access

Up to 70 THz bandwidth from an implanted Ge photoconductive antenna excited by a femtosecond Er:fibre laser

Abhishek Singh[1], Alexej Pashkin[1], Stephan Winnerl[1], Malte Welsch[1,2], Cornelius Beckh[3], Philipp Sulzer[3], Alfred Leitenstorfer[3], Manfred Helm[1,2] and Harald Schneider[1]

Abstract

Phase-stable electromagnetic pulses in the THz frequency range offer several unique capabilities in time-resolved spectroscopy. However, the diversity of their application is limited by the covered spectral bandwidth. In particular, the upper frequency limit of photoconductive emitters - the most widespread technique in THz spectroscopy – reaches only up to 7 THz in the regular transmission mode due to absorption by infrared-active optical phonons. Here, we present ultrabroadband (extending up to 70 THz) THz emission from an Au-implanted Ge emitter that is compatible with mode-locked fibre lasers operating at wavelengths of 1.1 and 1.55 μm with pulse repetition rates of 10 and 20 MHz, respectively. This result opens up the possibility for the development of compact THz photonic devices operating up to multi-THz frequencies that are compatible with Si CMOS technology.

Introduction

THz time-domain spectroscopy using broadband THz pulses has emerged as a powerful tool for probing low-energy excitations in condensed matter at the meV energy scale[1–3]. The spectrum of potential applications depends on the available spectral bandwidth, signal-to-noise ratio and data acquisition speed. In general, the techniques for THz generation and detection exploit either photoconductivity or optical nonlinearity[4,5]. Photoconductive techniques for THz emission and detection are widely used due to their simplicity, compactness and possibility of direct coupling to fiber optics. THz emission from photoconductivity was first demonstrated using Si[4,6,7]; however, the majority of current photoconductive antennas are based on GaAs or InGaAs (in case of the telecom wavelength) due to the high carrier mobility in these materials and well-established schemes for reducing the carrier lifetime[8]. Optical rectification techniques rely mostly on polar noncentrosymmetric materials with a strong second-order optical nonlinearity, such as ZnTe, GaP, GaSe, or *DSTMS*[9]. The polar nature of these materials renders their optical phonons strongly IR-active, leading to reststrahlen bands in the region between 5 and 10 THz. As a result, the spectral bandwidth of many THz emitters is limited to below 7 THz in the regular transmission mode. In particular, for InGaAs-based photoconductive emitters excited at a wavelength of 1.55 μm, gapless THz spectra up to 6.5 THz have been demonstrated[10]. Thin electro-optic crystals of GaSe and *DAST* have shown THz emission extending up to more than 100 THz towards the higher frequency end, but the THz intensity near their phonon frequencies is strongly suppressed[11–14]. Even in the reflection geometry available with photoconductive emitters, strong absorption and emission by polar TO and LO phonons, respectively, hinders their application for spectroscopy around the resonance frequencies[15,16].

Correspondence: Alexej Pashkin (a.pashkin@hzdr.de) or Harald Schneider (h.schneider@hzdr.de)
[1]Institute of Ion Beam Physics and Materials Research, Helmholtz-Zentrum Dresden-Rossendorf, 01328 Dresden, Germany
[2]Cfaed and Institute of Applied Physics, TU Dresden, 01062 Dresden, Germany
Full list of author information is available at the end of the article.

To satisfy the demand of a gapless ultrabroadband spectrum, novel techniques such as two-color air plasma[17] and spintronic THz emission[18] have been introduced. THz emission from air plasma achieves a bandwidth of more than 100 THz, but this technique requires high pump-pulse energies of several 100 μJ or higher that can be achieved only by rather complex and expensive laser amplifiers[17,19]. Spintronic emitters have shown great potential as a gapless broadband emitter reaching a bandwidth up to 30 THz that is compatible with nJ laser pulses from conventional femtosecond oscillators[18]. Recently, their scalability for the generation of higher THz fields was also demonstrated[20]. A similar study by Wu et al.[21] demonstrated efficient operation of such a THz emitter driven by a pump power as low as 0.15 mW. Nevertheless, THz generation using photoconductive antennas remains important for many applications due to the direct control of the THz field strength and polarity by an applied bias voltage. Moreover, specially designed electrode geometries enable the generation of radial or azimuthal THz polarizations[22] and a fully controllable angle of the linear polarization[23,24]. However, until recently, the bandwidth coverage of photoconductive emitters has been limited by the above-mentioned factors.

A breakthrough in the generation of a broadband THz spectrum beyond the reststrahlen band of III-V semiconductors was achieved recently by using a Ge-based photoconductive dipole antenna based on pure Ge[25]. This semiconductor has a direct interband absorption above 0.8 eV, which is very close to its indirect bandgap at 0.66 eV. The effective electron mass in the center of the Brillouin zone of Ge is fairly small, leading to a strong acceleration of photogenerated electrons and, correspondingly, to efficient THz emission. This property gives Ge a clear advantage over Si in applications for photoconductive THz devices. Moreover, the relatively small bandgap of Ge enables pumping with compact fiber lasers. Finally, Ge is known to be compatible with Si CMOS technology[26]; thus, it is attractive for integrated on-chip THz solutions for THz signal processing[27,28].

The absence of polar phonons in Ge enabled the generation of a gapless THz spectrum spreading up to 13 THz, and it has been demonstrated that the bandwidth of a Ge-based THz emitter is limited only by the duration of the excitation and detection laser pulses and, therefore, can be potentially extended to much higher frequencies[25]. However, the ultimate performance can hardly be reached for intrinsic Ge due to the relatively long carrier lifetime of several μs caused by the indirect character of the bandgap. The repetition rate of the driving laser must be low enough (250 kHz or less) to ensure full recombination of the carriers between the pulses, limiting the choice to complex and expensive regenerative laser amplifiers for which a sub-30 fs pulse duration is cumbersome to achieve, and the full pulse energy usually cannot be exploited due to the saturation of the THz emission by screening effects.

Results

To harness the full potential of Ge as a material for photoconductive THz emitters, we reduce the carrier lifetime down to the sub-nanosecond level by introducing deep traps via Au implantation. Although a shorter carrier lifetime is not an essential requirement for broadband THz emission, a sub-nanosecond lifetime ensures reliable operation of Ge:Au THz emitters at repetition rates up to a few hundred MHz, covering the specifications of most contemporary femtosecond oscillators. It is known that Au in Ge forms deep acceptor levels within the bandgap that possess large capture cross-sections and drastically reduce the carrier lifetime for very low doping

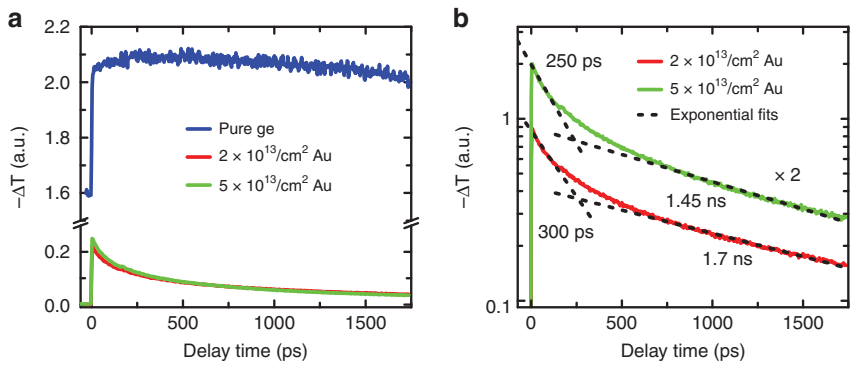

Fig. 1 Carrier recombination in Ge measured by optical pump/THz probe spectroscopy. a Pump-induced change in the THz transmission as a function of the pump-probe delay time for pure and Au-implanted Ge. The pump fluence is 12.5 μJ/cm^2, and the wavelength is 800 nm. **b** Bi-exponential fits of the decay dynamics for the Ge:Au samples. The curves for the 5 × 10^{13} ions/cm^2 dose are vertically shifted for clarity (multiplied by 2)

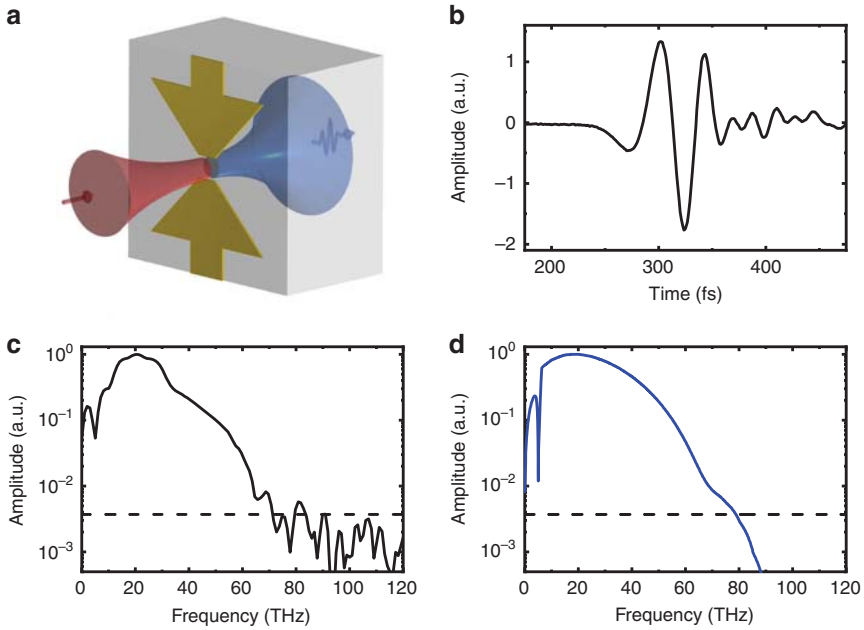

Fig. 2 Ultrabroadband THz emission from a Ge:Au antenna pumped at 1100 nm. a Schematic diagram of the Ge photoconductive emitter with bowtie-like electrodes. The pump and THz beams are shown in red and blue, respectively. **b** Recorded THz pulse for pumping with 11-fs pulses with a wavelength centered at 1100 nm. **c** Fourier transform of the recorded THz pulse. **d** Simulated THz spectrum calculated as a product of the THz field emitted by the photoinduced current in the Ge emitter and the ZnTe detector response function. The dashed lines show the experimental noise floor

concentrations[29,30]. Ge substrates were implanted with Au ions with an energy of 330 keV and doses of 5×10^{13} ions/cm^2 and 2×10^{13} ions/cm^2 followed by annealing at 900 °C for several hours to ensure a low homogeneous concentration of gold impurities near the surface of the Ge wafer. After annealing, the Au ions diffuse hundreds of μm deep inside the Ge substrate, resulting in a suitable doping density of approximately 10^{15} cm^{-3} (see Supplementary Information Fig. S1).

We have estimated the carrier lifetime in implanted Ge wafers using optical pump/THz probe spectroscopy. Figure 1 shows the photoinduced change in the THz transmission ΔT, which is approximately proportional to the density of the free charge carriers. The comparison between pure and Au-doped Ge clearly demonstrates a dramatic reduction in the recombination time. The pure Ge sample shows a step-like increase in the carrier density with a minor decrease in the following 1.5 ns. Moreover, there is a strong nonzero response at negative delay times, indicating a high density of carriers accumulated in the sample from the preceding pump pulse arriving 4 μs earlier. In stark contrast, Ge:Au samples show a strong decay within 1 ns after photoexcitation and a negligible offset at negative delay times. The recombination dynamics can be described using a bi-exponential decay, as shown in Fig. 1b. The faster decay time of ≈300 ps can be attributed to surface recombination and the slower nanosecond decay to trap-assisted recombination in the volume of the Ge:Au sample. Both implanted Ge substrates exhibit a carrier lifetime of less than 2 ns, which is approximately 3 orders of magnitude shorter than the typical carrier lifetime in pure germanium.

Bowtie electrode structures with a 10-μm gap and a 30-μm length for each electrode were fabricated on two implanted Ge:Au substrates using the same fabrication process and bowtie electrode geometry as in our previous work[25]. A schematic diagram showing THz emitter operation is presented in Fig. 2a. The near-infrared pump beam is focused onto the 10-μm gap between the electrodes. Photoexcited charge carriers are accelerated by the applied bias field, producing a transient current burst. The THz beam emitted by this current in the forward direction is collimated and refocused on an electro-optic crystal for field-resolved detection. The short carrier lifetime enables us to operate the Ge emitter at a repetition rate of tens of MHz using a femtosecond fiber laser system.

First, we test the THz emission induced by 11-fs short pulses with a central wavelength around 1100 nm (spectrum spanning from 900 to 1250 nm) and an energy of 7 nJ (at a repetition rate of 10 MHz). The emitter was fabricated on Ge:Au with an implantation dose of 2×10^{13} ions/cm^2. The generated THz transient is detected by electro-optic sampling using 8.42-fs short probe pulses

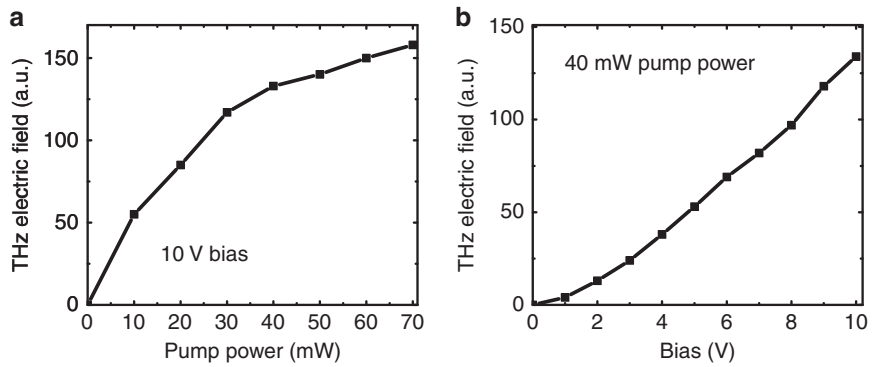

Fig. 3 Peak-to-peak electric field of the THz pulse. a THz peak-to-peak electric field variation at a constant bias of 10 V and various pump powers. At a high pump-pulse energy, the separation of photogenerated electron-hole pairs causes screening of the DC field applied to the emitter. Hence, the efficiency of the emitter is affected, causing saturation of the emitted THz field. **b** THz peak-to-peak electric field variation at a constant pump power of 40 mW and a varying bias applied to the emitter electrodes

in a (110) ZnTe crystal with a thickness of 14.3 μm. Figure 2b, c show the recorded THz pulse in the time domain and its Fourier spectrum, respectively. The obtained spectrum spans from the lowest detectable frequency up to 70 THz, demonstrating unprecedented bandwidth for a photoconductive antenna with a gapless spectrum. The small dip in the spectrum at approximately 5 THz is caused by the response function of the ZnTe detector, and the true THz emission spectrum is gapless, as has been confirmed in previous work[25]. The estimated peak electric field of the focused THz pulse is ~ 0.8 kV/cm, and the signal-to-noise ratio is ~300.

We have modeled the detected THz spectrum using the intensity and phase spectra of the pump and probe near-infrared pulses (see Supplementary Information). The emission from biased Ge:Au is calculated by solving the equation for the pump pulse propagation in Ge, which takes into account the absorption and dispersion of the refractive index. In this way, the temporal and depth profile of the photoinduced carrier concentration can be calculated. The total emitted THz field is estimated as a sum of the emission by currents across the full depth of the emitter. The resulting spectrum is multiplied by the detector response function (DRF) of the ZnTe detector, which takes into account the group velocity dispersion across the very large bandwidth of the probe pulse. Further details are given in the Supplementary Information. The effect of the diffraction-limited focusing of the THz beam on the detector is also taken into account. The result shown in Fig. 2d agrees well with the experimentally measured spectrum demonstrating that the roll-off at the higher frequency is mainly due to widths of the pump and probe pulses, and the roll-off towards the lower frequency is due to diffraction-limited focusing of the THz beam on the detector crystal. Thus, we observe a gapless spectrum extending up to 70 THz (wavelength of 4.3 μm).

The performance of the implanted Ge emitter is studied for various pump powers and applied bias. Figure 3a, b show the observed variation in the peak-to-peak electric field amplitude of the emitted THz pulse at different pump powers and applied bias, respectively. Usually, the peak-to-peak electric field amplitude of photoconductive emitters increases linearly with the pump power until saturation occurs due to the screening of the applied electric field. The implanted Ge emitter also exhibits similar behavior with the pump power, as shown in Fig. 3a. The THz field scales almost linearly for a pump pulse energy up to 3 nJ (30 mW of power at 10 MHz), exhibiting saturation beyond this limit. Similarly, the THz field is also expected to scale linearly with the applied bias field on the emitter electrodes. Figure 3b demonstrates an almost linear dependence with the signal vanishing at zero bias, thus confirming that the THz emission is produced solely by the photoinduced current in the Ge antenna.

In the following, we demonstrate the compatibility of the Ge:Au photoconductive antenna with the conventional telecom C-band covered by ubiquitous Er-doped femtosecond fiber lasers. The absorption edge of Ge at 0.66 eV ($\lambda \approx 1876$ nm) is well below the telecom band. However, the absorption is rather weak due to the indirect character of the bandgap and increases abruptly only for photon energies above 0.8 eV ($\lambda \approx 1550$ nm) corresponding to direct interband transitions near the Γ-point of the Brillouin zone[31]. The onset of the strong absorption in Ge coincides with the telecom wavelength of 1550 nm and, thus, should enable broadband emission from the Ge-based THz emitter.

The emitter fabricated on Ge:Au with an implantation dose of 5×10^{13} ions/cm^2 was pumped with 12-fs pulses with a central wavelength around 1550 nm and an energy of 3.5 nJ at a repetition rate of 20 MHz. The spectrum of the pump pulse is shown in Fig. 4a together with the

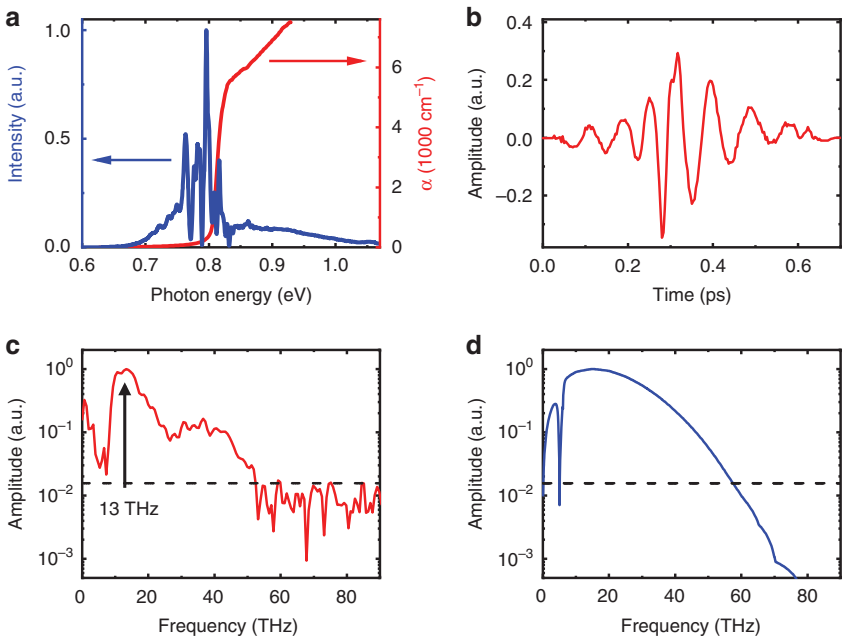

Fig. 4 Broadband THz emission from the Ge:Au antenna pumped at 1550 nm. a Spectrum of the pump pulse (blue) compared to the absorption coefficient of Ge (red) taken from Ref. [29]. **b** Recorded THz pulse for pumping with 12-fs laser pulses centered around 1550 nm. **c** Fourier transform of the recorded pulse. The arrow indicates the contribution of the narrowband part of the pulse at 13 THz. **d** Simulated THz spectrum. Only the broadband single-cycle pulse stems from the photocurrent. The dashed lines show the experimental noise floor

absorption coefficient of Ge, demonstrating that the part of the pump pulse with photon energies below 0.8 eV should contribute much less to the generation of the transient photocurrent than its high-energy part. Thus, even though the initial pulse duration and the energy are comparable to the previous case of pumping at 1100 nm, the expected THz bandwidth should be lower than 70 THz.

The emitted THz pulses are recorded with an 18-μm-thick ZnTe detector crystal by electro-optic sampling using 5.8-fs pulses with a central wavelength of 1200 nm (see Supplementary Information). The photoconductive antenna is pumped at a repetition rate of 20 MHz under an applied DC bias of 10 V. Figure 4b, c show the recorded THz waveform and its Fourier transform, respectively. The THz spectrum spans up to 50 THz, demonstrating that the Ge-based photoconductive antenna is capable of broadband THz emission when pumped at the telecom wavelength. As anticipated, the bandwidth and dynamic range of the THz waveform are lower than those for pumping at 1100 nm due to the nonuniform absorption of different parts of the excitation spectrum. The estimated peak electric field is ~ 0.12 kV/cm, and the signal-to-noise ratio is ~65. Furthermore, the pulse shape differs from the typical single-cycle THz waveform that is observed for pumping at 1100 nm (see Fig. 2b) and includes an additional multi-cycle THz component with a frequency of approximately 13 THz. The phase of this narrowband feature is nearly opposite to that of the broadband THz pulse at low frequencies, leading to the minimum in the detected spectrum below the 13 THz peak due to destructive interference.

Discussion

Although similar narrowband emission by LO phonons in polar semiconductors is well known and understood[15,32], such a component is not expected in nonpolar Ge. To verify whether this emission can be related to indirect interband absorption away from the surface of the photoconductive antenna, we performed a simulation of the recorded THz pulse using the same approach as that for 1100-nm pumping. The time-dependent current across the full depth of the Ge:Au wafer is calculated by numerically solving the pulse propagation equation (see Supplementary Information). The resulting THz spectrum depicted in Fig. 4d reasonably describes the decrease in the bandwidth to 50 THz due to the dominating role played by the carriers photoexcited via the direct interband transitions for photon energies above 0.8 eV. In fact, our simulation shows a negligible contribution of the spectral components below 0.8 eV. However, the THz emission is expected to be similar to the case of pumping at 1100 nm with a nearly single-cycle THz waveform. Thus, the narrowband emission at 13 THz cannot be attributed to a standard transient photocurrent in our structure. A more exotic mechanism such as coherent

polarizations due to the simultaneous generation of heavy-hole–light-hole wavepackets as recently reported in GaAs[33] may be considered. However, this discussion is beyond the scope of the present work and requires a larger amount of experimental data.

In conclusion, we have demonstrated a photoconductive THz emitter fabricated on Au-implanted Ge that is capable of emitting a gapless spectrum with an unprecedented bandwidth reaching 70 THz. The tested devices are fully compatible with femtosecond fiber lasers and demonstrate ultrabroadband THz emission by pumping at either 1100 or 1550 nm. Thus, Ge-based THz emitters may be used for the generation of a gapless spectrum in combination with standard Er-doped femtosecond fiber lasers at frequencies as high as 76 MHz. The demonstrated bandwidth is almost one order of magnitude higher than that of existing state-of-the-art photoconductive THz emitters fabricated on GaAs or InGaAs. Consequently, Ge-based THz devices can revolutionize THz technology due to their ultrabroad spectral bandwidth coverage and their potential compatibility with Si CMOS technology.

Materials and methods

Ge implantation

Au ions with an energy of 330 keV and doses of 2×10^{13} ions/cm^2 and 5×10^{13} ions/cm^2, respectively, were implanted into two nominally undoped (100) Ge substrates. A simulation using the SRIM software shows an initial implantation depth of approximately 150 nm (Supplementary Information Fig. S1). To distribute the Au ions uniformly over a length scale larger than the penetration depth of the pump light and to recover the lattice damage after ion irradiation, the samples were annealed in vacuum at 900 °C for 3 h (sample with a dose of 5×10^{13} ions/cm^2) and 10 h (sample with a dose of 2×10^{13} ions/cm^2). Annealing is expected to cause Au diffusion to a depth of more than 100 μm into the Ge wafers. After processing, the surfaces of the samples were polished to make them smooth enough for lithographic processing.

Optical pump/THz probe measurements

The measurements of the carrier lifetime in Ge:Au were performed using a THz setup equipped with a GaAs-based large-area photoconductive emitter and a ZnTe electro-optic detector covering frequencies up to 3 THz. The system is driven by a Ti:Sa amplifier laser operating at a repetition rate of 250 kHz and a wavelength of ~ 800 nm. Pump powers of 50 and 200 mW are used to pump the ≈3-mm-diameter area, resulting in fluences of 12.5 and 50 μJ/cm^2 for the excitation of pure and implanted Ge substrates, respectively. The THz pulse is focused to approximately 1 mm in size on the same spot, ensuring homogeneous pumping conditions. The change in the THz transmission is measured using lock-in detection at different pump-probe delay times. The data shown in Fig. 1 are recorded at the peak of the THz probe pulse and normalized with respect to the pump fluence in order to provide a direct comparison of the different curves.

Emitter fabrication

Bowtie-like electrodes were fabricated on the two implanted Ge substrates using standard electron beam lithography. Two layers of 5-nm Ti and 45-nm Au were deposited consecutively, and the bowtie geometry was formed by a lift-off process.

THz emitter characterization for pumping at 1550 and 1100 nm

The THz setup is based on ultrabroadband Er:fiber laser technology[34]. The repetition rates of the electro-optic sampling pulses with wavelengths of 1100 and 1550 nm are 20 and 40 MHz, respectively. The pump pulses with wavelengths of 1100 or 1550 nm are modulated at 10 and 20 MHz, respectively—half of the oscillator frequency, enabling excellent sensitivity of the system at the shot-noise limit using a lock-in detection technique. Further details can be found in the additional materials of recent publications that utilized the same fiber laser systems[35,36].

An 18-μm-thick ZnTe crystal was used for the electro-optic sampling of the emitted THz pulses when the emitter was pumped at a wavelength of 1550 nm, and 14.3-μm-thick ZnTe and 18.4-μm-thick GaSe were used to characterize the emitter when pumped at 1100 nm. The studied photoconductive emitters were biased by a static voltage, since the pump pulses were already modulated at half the probe repetition rate.

Acknowledgements
The support by R. Böttger and the Ion Beam Center (IBC) at HZDR is gratefully acknowledged. The authors would like to thank W. Skorupa for his valuable suggestions and I. Skorupa and U. Lucchesi for technical assistance.

Author details
[1]Institute of Ion Beam Physics and Materials Research, Helmholtz-Zentrum Dresden-Rossendorf, 01328 Dresden, Germany. [2]Cfaed and Institute of Applied Physics, TU Dresden, 01062 Dresden, Germany. [3]Department of Physics and Center for Applied Photonics, University of Konstanz, 78457 Konstanz, Germany

Author contributions
A.S. and A.P. conceived the experiments and performed the doping of the Ge wafers. A.S. measured the carrier lifetime, fabricated the antenna structure and obtained the THz signal using a Ti:Sa laser. C.B., P.S., and A.L. constructed the THz setups based on femtosecond Er:fiber lasers. C.B., P.S., and A.S. carried out the THz measurements using the fiber laser systems. A.S., M.W., and A.P. performed the numerical modeling of the THz signals. The paper was drafted by A.S. and A.P. All authors contributed to discussing the results and writing the paper.

Conflict of interest
The authors declare that they have no conflict of interest.

Supplementary information is available for this paper at https://doi.org/10.1038/s41377-020-0265-4.

Received: 2 September 2019 Revised: 31 January 2020 Accepted: 18 February 2020
Published online: 03 March 2020

References

1. Tonouchi, M. Cutting-edge terahertz technology. *Nat. Photonics* **1**, 97–105 (2007).
2. Jin, Z. M. et al. Accessing the fundamentals of magnetotransport in metals with terahertz probes. *Nat. Phys.* **11**, 761–766 (2015).
3. Markelz, A. G., Roitberg, A. & Heilweil, E. J. Pulsed terahertz spectroscopy of DNA, bovine serum albumin and collagen between 0.1 and 2.0 THz. *Chem. Phys. Lett.* **320**, 42–48 (2000).
4. Auston, D. H., Cheung, K. P. & Smith, P. R. Picosecond photoconducting Hertzian dipoles. *Appl. Phys. Lett.* **45**, 284–286 (1984).
5. Wu, Q. & Zhang, X. C. Free-space electro-optic sampling of terahertz beams. *Appl. Phys. Lett.* **67**, 3523–3525 (1995).
6. Smith, P. R., Auston, D. H. & Nuss, M. C. Subpicosecond photoconducting dipole antennas. *IEEE J. Quantum Electron.* **24**, 255–260 (1988).
7. Fattinger, C. & Grischkowsky, D. Point source terahertz optics. *Appl. Phys. Lett.* **53**, 1480–1482 (1988).
8. Gupta, S. et al. Subpicosecond carrier lifetime in GaAs grown by molecular beam epitaxy at low temperatures. *Appl. Phys. Lett.* **59**, 3276–3278 (1991).
9. Dhillon, S. S. et al. The 2017 terahertz science and technology Roadmap. *J. Phys. D* **50**, 043001 (2017).
10. Nandi, U. et al. 1550-nm driven ErAs:In(Al)GaAs photoconductor-based terahertz time domain system with 6.5 THz bandwidth. *J. Infrared Millim. Terahertz Waves* **39**, 340–348 (2018).
11. Kübler, C. et al. Ultrabroadband detection of multi-terahertz field transients with GaSe electro-optic sensors: approaching the near infrared. *Appl. Phys. Lett.* **85**, 3360–3362 (2004).
12. Ashida, M. Ultra-broadband terahertz wave detection using photoconductive antenna. *Jpn J. Appl. Phys.* **47**, 8221–8225 (2008).
13. Takayanagi, J. et al. Generation and detection of broadband coherent terahertz radiation using 17-fs ultrashort pulse fiber laser. *Opt. Express* **16**, 12859–12865 (2008).
14. Katayama, I. et al. Electric field detection of phase-locked near-infrared pulses using photoconductive antenna. *Opt. Express* **21**, 16248–16254 (2013).
15. Shen, Y. C. et al. Generation and detection of ultrabroadband terahertz radiation using photoconductive emitters and receivers. *Appl. Phys. Lett.* **85**, 164 (2004).
16. Hale, P. J. et al. 20 THz broadband generation using semi-insulating GaAs interdigitated photoconductive antennas. *Opt. Express* **22**, 26358–26364 (2014).
17. Thomson, M. D., Blank, V. & Roskos, H. G. Terahertz white-light pulses from an air plasma photo-induced by incommensurate two-color optical fields. *Opt. Express* **18**, 23173–23182 (2010).
18. Seifert, T. et al. Efficient metallic spintronic emitters of ultrabroadband terahertz radiation. *Nat. Photonics* **10**, 483–488 (2016).
19. Kim, K. Y. et al. Coherent control of terahertz supercontinuum generation in ultrafast laser–gas interactions. *Nat. Photonics* **2**, 605–609 (2008).
20. Seifert, T. et al. Ultrabroadband single-cycle terahertz pulses with peak fields of 300 kV cm^{-1} from a metallic spintronic emitter. *Appl. Phys. Lett.* **110**, 252402 (2017).
21. Wu, Y. et al. High-performance THz emitters based on ferromagnetic/non-magnetic heterostructures. *Adv. Mater.* **29**, 1603031 (2017).
22. Winnerl, S. et al. Terahertz Bessel-Gauss beams of radial and azimuthal polarization from microstructured photoconductive antennas. *Opt. Express* **17**, 1571–1576 (2009).
23. Mosley, C. D. W. et al. Scalable interdigitated photoconductive emitters for the electrical modulation of terahertz beams with arbitrary linear polarization. *AIP Adv.* **9**, 045323 (2019).
24. Maussang, K. et al. Large-area photoconductive switches as emitters of terahertz pulses with fully electrically controlled linear polarization. *Opt. Express* **27**, 14784–14797 (2019).
25. Singh, A. et al. Gapless broadband terahertz emission from a germanium photoconductive emitter. *ACS Photonics* **5**, 2718–2723 (2018).
26. Michel, J., Liu, J. F. & Kimerling, L. C. High-performance Ge-on-Si photodetectors. *Nat. Photonics* **4**, 527–534 (2010).
27. Jalali, B. & Fathpour, S. Silicon photonics. *J. Lightwave Technol.* **24**, 4600–4615 (2006).
28. Harter, T. et al. Silicon–plasmonic integrated circuits for terahertz signal generation and coherent detection. *Nat. Photonics* **12**, 625–633 (2018).
29. Johnson, L. & Levinstein, H. Infrared properties of gold in germanium. *Phys. Rev.* **117**, 1197–1203 (1960).
30. Williams, R. L. Carrier lifetimes in n-type gold-doped germanium. *J. Phys. Chem. Solids* **22**, 261–267 (1961).
31. Dash, W. C. & Newman, R. Intrinsic optical absorption in single-crystal germanium and silicon at 77 K and 300 K. *Phys. Rev.* **99**, 1151–1155 (1955).
32. Leitenstorfer, A. et al. Detectors and sources for ultrabroadband electro-optic sampling: experiment and theory. *Appl. Phys. Lett.* **74**, 1516–1518 (1999).
33. Ghalgaoui, A. et al. Resonant second-order nonlinear terahertz response of gallium arsenide. *Phys. Rev. Lett.* **121**, 266602 (2018).
34. Brida, D. et al. Ultrabroadband Er:fiber lasers. *Laser Photonics Rev.* **8**, 409–428 (2014).
35. Riek, C. et al. Subcycle quantum electrodynamics. *Nature* **541**, 376–379 (2017).
36. Storz, P. et al. Parametric amplification of phase-locked few-cycle pulses and ultraviolet harmonics generation in solids at high repetition rate. *Laser Photonics Rev.* **11**, 1700062 (2017).

^{60}Fe deposition during the late Pleistocene and the Holocene echoes past supernova activity

A. Wallner[a,b,1], J. Feige[c,d], L. K. Fifield[a], M. B. Froehlich[a], R. Golser[c], M. A. C. Hotchkis[e], D. Koll[a], G. Leckenby[a], M. Martschini[a,c], S. Merchel[b], S. Panjkov[a], S. Pavetich[a], G. Rugel[b], and S. G. Tims[a]

[a]Department of Nuclear Physics, Research School of Physics, Australian National University, Canberra, ACT 2601, Australia; [b]Institute of Ion Beam Physics and Materials Research, Helmholtz-Zentrum Dresden-Rossendorf, 01328 Dresden, Germany; [c]Isotope Physics, Faculty of Physics, Vienna Environmental Research Accelerator Laboratory, University of Vienna, 1090 Vienna, Austria; [d]Zentrum für Astronomie und Astrophysik, Technische Universität Berlin, 10623 Berlin, Germany; and [e]Centre for Accelerator Science, Australian Nuclear Science and Technology Organisation, Lucas Heights, NSW 2234, Australia

Edited by Mark Thiemens, University of California San Diego, La Jolla, CA, and approved July 13, 2020 (received for review October 5, 2019)

Nuclides synthesized in massive stars are ejected into space via stellar winds and supernova explosions. The solar system (SS) moves through the interstellar medium and collects these nucleosynthesis products. One such product is ^{60}Fe, a radionuclide with a half-life of 2.6 My that is predominantly produced in massive stars and ejected in supernova explosions. Extraterrestrial ^{60}Fe has been found on Earth, suggesting close-by supernova explosions ∼2 to 3 and ∼6 Ma. Here, we report on the detection of a continuous interstellar ^{60}Fe influx on Earth over the past ∼33,000 y. This time period coincides with passage of our SS through such interstellar clouds, which have a significantly larger particle density compared to the local average interstellar medium embedding our SS for the past few million years. The interstellar ^{60}Fe was extracted from five deep-sea sediment samples and accelerator mass spectrometry was used for single-atom counting. The low number of 19 detected atoms indicates a continued but low influx of interstellar ^{60}Fe. The measured ^{60}Fe time profile over the 33 ky, obtained with a time resolution of about ±9 ky, does not seem to reflect any large changes in the interstellar particle density during Earth's passage through local interstellar clouds, which could be expected if the local cloud represented an isolated remnant of the most recent supernova ejecta that traversed the Earth ∼2 to 3 Ma. The identified ^{60}Fe influx may signal a late echo of some million-year-old supernovae with the ^{60}Fe-bearing dust particles still permeating the interstellar medium.

Fe-60 | supernova | ISM | accelerator mass spectrometry | deep-sea sediments

The temperature and particle density of the interstellar medium (ISM) is shaped by winds from massive stars and stellar explosions. Near the solar system (SS), supernovae (SNe) have created a network of filaments, shells, and superbubbles (1–7). Superbubbles represent low-density cavities in space with typical densities of ∼0.005 hydrogen atoms per cm^3 (10^{-26} g·cm^{-3}) and exist for tens of millions of years. The SS has been located inside the Local Superbubble (LB) for at least the last 3 My and possibly more than 10 My (8). The LB extends for ∼60 to 100 pc from the sun in the galactic plane and forms an open structure perpendicular to the plane (galactic chimney) (3).

The LB does, however, contain some higher-density regions, and the SS is presently immersed in a small cluster of local interstellar clouds (CLIC). These are partially ionized individual clouds within the much-lower-density LB material, filling between 6 and 19% of the LB volume (4). Because the SS is moving at a considerable velocity sometimes exceeding 25 km·s^{-1} relative to these clouds, it has encountered them regularly, with the first encounter sometime between 44 and 150 ky BP (1, 6, 7). For a cloud length of ∼1 pc the cloud transit time becomes on the order of 40 ky. Presently, the SS is traversing the so-called local interstellar cloud (LIC) at a relative velocity of 25.7 km·s^{-1} (9). This small local cloud has a density of ∼0.2 hydrogen atoms per cm^3 (about 40 times the density of the LB) and has a size of ∼5 pc (1). The SS entered the LIC sometime between 4 and 40 ky BP, but it will be leaving the LIC within the next few thousand years because it is passing very near the edge (1) (Fig. 1).

As a consequence, the SS has traversed different regions of ISM during the past several million years, which may have affected the heliosphere, the inner SS, and also the flux of interstellar dust and galactic cosmic rays at Earth (1, 10–13). Several questions arise: What is the origin of these interstellar clouds? Are they enriched in material from SNe, or are they simply representative of the average ISM? Will passage through such clouds modulate the galactic cosmic-ray flux into the inner SS?

Several formation scenarios have been proposed for the CLIC, including the LIC. The CLIC could be a result of interactions between the LB and its neighboring Loop I superbubble (14) or an array of ISM structures consisting of material that originated from the inside surface of the LB wall and these structures were generated by a distorted magnetic field (magnetic flux tube) (15), or it may represent a dense cloud that survived a shock wave from an expanding bubble (1, 4, 7).

To address these questions, we searched for a geological radioisotope record that may allow the mapping of signatures of such cloud transitions. We have measured concentrations of the radioisotope ^{60}Fe in deep-sea sediments covering the last ∼33 ky.

Significance

Nearby supernova explosions shape the interstellar medium. Ejecta, containing fresh nucleosynthetic products, may traverse the solar system as a transient passage, or alternatively the solar system may traverse local clouds that may represent isolated remnants of supernova explosions. Such scenarios may modulate the galactic cosmic-ray flux intensity to which Earth is exposed. Varying conditions of the traversed interstellar medium could have impacts on climate and can be imprinted in the terrestrial geological record. Some radionuclides, such as ^{60}Fe, are not produced on Earth or within the solar system in significant quantities. Their existence in deep-sea sediments demonstrates recent production in close-by supernova explosions with a continued influx of ^{60}Fe until today.

Author contributions: A.W. and J.F. designed research; A.W., J.F., L.K.F., M.B.F., R.G., M.A.C.H., D.K., G.L., M.M., S.M., S. Panjkov, S. Pavetich, G.R., and S.G.T. performed research; J.F., M.B.F., D.K., and S.M. contributed new reagents/analytic tools; A.W., M.B.F., M.A.C.H., D.K., G.L., S. Panjkov, S. Pavetich, G.R., and S.G.T. analyzed data; and A.W. and L.K.F. wrote the paper.

The authors declare no competing interest.

This article is a PNAS Direct Submission.

[1]To whom correspondence may be addressed. Email: anton.wallner@anu.edu.au.

This article contains supporting information online at https://www.pnas.org/lookup/suppl/doi:10.1073/pnas.1916769117/-/DCSupplemental.

First published August 24, 2020.

ASTRONOMY

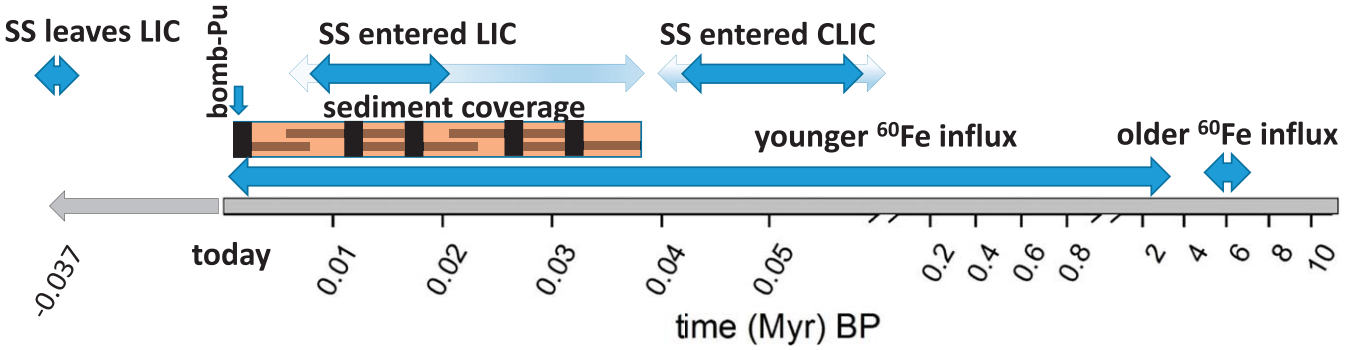

Fig. 1. Time line indicating recent enhanced ^{60}Fe influxes (5.5 to 7 Ma and from 3.2 Ma) and the passage of the SS through the local ISM structures CLIC and LIC. The blue horizontal arrows indicate the most probable time, and the pale blue in the back covers the entire possible time range. The orange box depicts the approximate location of the five sediment samples with respect to these transitions. The black rectangles represent the 1-cm length and the gray bars the time resolution if sediment mixing is taken into account.

^{60}Fe has a half-life of (2.61 ± 0.04) My (16–18). Because it is not naturally produced on Earth, the presence of ^{60}Fe is a sensitive indicator of supernova explosions within the last few million years. The ^{60}Fe can reach Earth because it is trapped in interstellar dust grains that can penetrate into the SS (10–13, 19–24). It has been shown that there was significantly enhanced ^{60}Fe deposition on Earth at 1.7 to 3.2 My (25–30) and ∼6 My BP (28) (Fig. 1), as well as a low present-day influx (31). ^{60}Fe has also been detected in lunar samples (32), in the galaxy via gamma rays associated with its radioactive decay (33) and in galactic cosmic rays (34). In particular, these multiple influxes during the last 10 My, as observed in deep-sea ferromanganese crusts and sediments, suggest that Earth may have been exposed to waves of SN ejecta, or alternatively it may have traversed clouds of ^{60}Fe-enriched dust. Passage through the CLIC could be a possible source for an enhanced ^{60}Fe influx during the past few tens of thousands of years. Alternatively, ^{60}Fe-bearing dust grains might permeate the interstellar space, including interstellar clouds unaffected by the ISM structure they pass. In such a scenario, the terrestrial ^{60}Fe-influx pattern would not be correlated with the changing mass density faced by the SS while moving through the ISM.

Results

Trace concentrations of ^{60}Fe were measured in five samples originating from two different piston cores, extracted during the Eltanin expeditions and provided by the Antarctic Marine Geology Research Facility at Florida State University. The cores, E45-21 (38°58.7′S, 103°43.1′E) and E50-02 (39°57.5′S, 104°55.7′E), were collected from sites ∼1,000 km southwest of Australia in the Indian Ocean at depths of ∼4,200 m (28, 35–39). E45-21 was one of the cores that showed enhanced ^{60}Fe depositions between 1.7 and 3.2 My at depths of 400 to 700 cm (28). Here, the emphasis was on the top 13 cm of these cores that covers the past ∼33 ky. Three samples of 1-cm thickness were taken from core E45-21 and two from E50-02. These five samples encompass the depth range 0 to 13 cm with 3- to 4-cm intervals between them (Table 1).

Iron and beryllium were leached from 3 g of these sediment samples at the Helmholtz-Zentrum Dresden-Rossendorf (HZDR) (39). A modified version of the method proposed by Bourlès et al. (41) and Merchel and Herpers (42) was applied (for more details see ref. 43). This gentle procedure extracts the authigenic fraction of the sample containing the soluble beryllium (^{10}Be and ^{9}Be) and iron (^{60}Fe and stable iron). We assume negligible losses of extraterrestrial ^{60}Fe relative to stable iron for that procedure (as tested by ref. 32). Purified beryllium oxide and iron oxide samples were mixed with Nb and Ag powder, respectively, for accelerator mass spectrometry (AMS) analysis (*Materials and Methods*) at HZDR (44) and the Australian National University (ANU) (17, 28). Since AMS measures the ^{60}Fe/Fe isotope ratio, the concentrations of the stable Fe were determined via inductively coupled plasma mass spectrometry (ICP-MS) at HZDR so that ^{60}Fe concentrations could then be derived.

A mean measurement background of ^{60}Fe/Fe = (0.27 ± 0.08) × 10^{-16} was determined over the past 5 y of ^{60}Fe AMS measurements on commercial iron oxide samples containing no ^{60}Fe, equivalent to less than one identified detector event over approximately one full day of measurement (see also ref. 28).

For deeper layers sedimentation rates between 3.7 (Eltanin 45-21) and 4.0 mm/ky (Eltanin 50-02) were determined from magnetostratigraphy and terrestrial ^{10}Be/^{9}Be dating (28, 35, 38). The ^{10}Be concentrations for the five surface sediment samples agree well with the decay-corrected data obtained for the deeper layers and confirm present-day ages of these samples (*SI Appendix*).

Assuming similar sedimentation rates for the first few centimeters of sediment as those measured in the deeper layers, the 1-cm-thick layers of the samples represent a time period of ∼2.5 ky per layer. Postdepositional particle redistribution by bioturbation and movement of the ^{60}Fe in solution in the pore waters, however, does degrade this time resolution (45). We refer to independent measurements of Lee et al. (46) and assume a constant 7-cm mixing length over the entire time period (45, 46); this yields a total of ±9 ky time resolution per individual 1-cm sample.

The three samples from Eltanin 45-21 and two from Eltanin 50-02, therefore, provided a time record that extended from the present to 27.3 (10 cm) and 32.5 ky (13 cm), respectively. Taking mixing into account, the time range covers ∼40 ky.

The five individual sediment samples gave between zero and seven ^{60}Fe events in the detector (Table 1). In total 19 ^{60}Fe events were detected compared to an expected background of 3.6 detector counts scaled from measurements of pure terrestrial iron samples (assumed to contain negligible ^{60}Fe). The individual ^{60}Fe events are listed together with the expected number of background events in Table 1. Correcting for background and applying counting statistics for a low number of detector events (40), we deduce an average isotope ratio of Fe/Fe_{60} = $(1.6^{+0.5}_{-0.4}) \times 10^{-16}$ (68% confidence interval) and significant above background with >99.99% confidence. The measured ^{60}Fe/Fe atom ratios for the individual samples are listed in Table 1. There is no significant difference within statistics between samples representing different time periods and hence no obvious trend with sample depth or age (Fig. 2).

Interstellar dust particles ablate during passage through the atmosphere and the interstellar ^{60}Fe atoms would therefore have

Table 1. Sediment characteristics, ^{60}Fe data from AMS measurements, and incorporation (inc.) rates

Sample ID	Core	Depth, cm	Time period, ka*	^{60}Fe detected	^{60}Fe-bgr expected†	^{60}Fe/Fe|$_{meas}$, 10^{-15} atom/atom	^{60}Fe/Fe|$_{corr}$, 10^{-15} atom/atom‡	Fe conc., mg·g^{-1}§	^{60}Fe conc., 10^3 atom·g^{-1}	^{60}Fe inc. rates, atom·cm^{-2}·y^{-1}
85	45-21	0–1	0–2.8	6	0.9	$0.25^{+0.14}_{-0.09}$	$0.20^{+0.13}_{-0.09}$	4.10	$8.2^{+5.3}_{-3.6}$	$3.5^{+2.3}_{-1.5}$
81	50-02	4–5	10–12.5	7	1.4	$0.19^{+0.09}_{-0.07}$	$0.16^{+0.10}_{-0.08}$	6.66	$10.9^{+6.4}_{-5.4}$	$5.1^{+3.0}_{-2.5}$
83	45-21	6–7	16.3–19.1	3	0.45	$0.24^{+0.18}_{-0.15}$	$0.19^{+0.17}_{-0.13}$	2.77	$5.4^{+4.8}_{-3.6}$	$2.3^{+2.1}_{-1.5}$
84	45-21	9–10	24.5–27.3	0	0.25	<0.17	<0.17	2.99	<5.1	<2.2
82	50-02	12–13	30.0–32.5	3	0.7	$0.15^{+0.12}_{-0.10}$	$0.12^{+0.12}_{-0.09}$	4.75	$5.9^{+5.9}_{-4.4}$	$2.7^{+2.7}_{-2.0}$
All¶		0–13	0.0–32.5	19	3.6	$0.19^{+0.05}_{-0.04}$	$0.16^{+0.05}_{-0.04}$	4.87	$7.8^{+2.5}_{-2.0}$	$3.5^{+1.1}_{-0.9}$
Blank	Terrestrial	—	—			$0.027^{+0.008}_{-0.008}$	< 0.01			
Mean#	47 samples		1.7–3.2 Ma	288						24.1 ± 1.8

All uncertainties (1-σ) are calculated using Feldman and Cousins statistics (40).

*Sedimentation rate of 3.7 mm/ky and 4.0 mm/ky for cores 45-21 and 50-02, respectively (38); we assumed for the top layers the same sedimentation rates as measured for the deeper layers (1.7 to 3.2 Ma).

†Background (bgr) events as expected from measured terrestrial blanks which are assumed to contain negligible amounts of ^{60}Fe.

‡Background-corrected.

§Stable Fe concentrations (conc.) were measured by ICP-MS at HZDR with a typical uncertainty of 5%.

¶Weighted with the total amount of analyzed material.

#For comparison we list the mean value for the time period 1.7 to 3.2 Ma as given in ref. 28.

been released from the dust particles when they arrived at the surface of the ocean (22). ^{60}Fe is then transferred in the same way as terrestrial stable Fe to the sediment archive, via scavenging processes. The measured ^{60}Fe/Fe isotope ratio can be converted into an incorporation rate for ^{60}Fe (atoms per square centimeter per year) using the stable (terrestrial) Fe content as measured by ICP-MS (Table 1), the mean density of the archives (1.16 g·cm^{-3}), and their sedimentation rates (3.7 and 4 mm·ky^{-1}) (28, 38).

Here, deep-sea sediments are assumed to incorporate all ^{60}Fe from the water column above due to the high particle reactivity which results in 100% transfer into the sediments. Hence, averaged over the entire time period we obtain a mean deposition rate of $(3.5^{+1.1}_{-0.9})$ ^{60}Fe atoms·cm^{-2}·y^{-1}, corresponding to an accumulated incorporation of $(1.13^{+0.34}_{-0.32}) \times 10^5$ atoms·cm^{-2} over 33 ky (Table 1). A previous preliminary value for a subset of this sediment gave a 2-σ upper limit of <3.6 ^{60}Fe atoms·cm^{-2}·y^{-1} (28), consistent with our new value if the same time period is assumed for the sediment samples.*

We can compare this result with those from deep-sea ferromanganese crusts, another geological record where ^{60}Fe has been successfully identified (26, 28). These crusts, however, have incorporation efficiencies for Fe that can be significantly lower than 100%. For example, "Crust-3," recovered from the Pacific Ocean, has an incorporation efficiency of ∼17%. It has recently been studied with ∼1-mm layer depth resolution. Its top layer averages over the most recent 370 ky and gives an incorporation rate of $(0.21^{+0.08}_{-0.06})$ ^{60}Fe atoms·cm^{-2}·y^{-1}. Corrected for the crust incorporation efficiency this corresponds to a deposition rate of $(1.24^{+0.55}_{-0.47})$ ^{60}Fe atoms·cm^{-2}·y^{-1}, indicating a ^{60}Fe influx averaged over this 10-times-longer period that is a factor of ∼2 to 3 lower than was found for the ∼33-ky average in the sediment. The top 1 mm layer of another crust (237KD) (26) suggests a similar result [assuming 10% incorporation (19, 28)] (Fig. 3). The detection of ^{60}Fe in Antarctic snow (31) suggests a present-day influx (<20-y accumulation) of $(1.2^{+0.6}_{-0.5})$ ^{60}Fe atoms·cm^{-2}·y^{-1} (Fig. 3), which is in line with the results from "Crust 3." Note that if the sedimentation rate of present-day sediments would be different from the 1.7- to 3.2-My average the ^{60}Fe deposition rate for the top layers would change accordingly.

The high-resolution data obtained here over a period of ∼33 ky would in principle allow a time-dependent ^{60}Fe flux into the SS to be probed on time scales of ∼10 ky, since the residence time of Fe in the ocean is negligible [∼100 y (22)]. However, owing to the low ^{60}Fe influx and the consequent detection of only a few ^{60}Fe events per sample, the data obtained here allow us to generate a meaningful value for the ^{60}Fe influx only for the average over 33 ky, but not for individual data points (Fig. 2).

Discussion

Our data demonstrate detection of an interstellar ^{60}Fe influx over the recent past of ∼33 ky that appears roughly constant over this time. Note that the Antarctic snow data (31) also confirm the existence of a present-day influx (<20 y) at 2.4 σ significance (Fig. 3). Assuming that extraterrestrial ^{60}Fe is homogeneously distributed over Earth's surface (5.1×10^{18} cm^2), we derive from our data that 5.9×10^{23} ^{60}Fe atoms (∼60 g) reached Earth during the past 33 ky.

ISM dust particles that incorporate ^{60}Fe are the most probable means for ^{60}Fe to enter the SS [neglecting the orders-of-magnitude lower ^{60}Fe influx as highly energetic cosmic ray particles (34)] and to be deposited in terrestrial archives; dust overcomes the solar wind pressure and the SS magnetic field. Satellite-borne instruments on the Ulysses, Galileo, and Cassini space missions (11–13, 47–49) have detected ISM dust inside the SS, and the data suggest that a mass fraction of 3 to 6% of interstellar dust particles is presently able to penetrate deep into the SS and reach Earth. Taking the median value of 4.5%, the observed terrestrial deposition of $(3.5^{+1.1}_{-0.9})$ ^{60}Fe atoms·cm^{-2}·y^{-1} can be converted to an ISM ^{60}Fe concentration of $(3.8 \pm 1.7) \times 10^{-12}$ ^{60}Fe atoms·cm^{-3} in dust for the local ISM. Note that it is necessary first to scale the deposition rate by a factor of 4 to take into account that deposition occurs over the surface of the globe, whereas the volume swept out by Earth's passage through the ISM is proportional to its cross-sectional area. Here, we assumed a velocity of the SS relative to the dust particles in the LIC of 25.7 km·s^{-1} and an uncertainty in the dust penetration efficiency of 33% (Table 2). Interestingly, this derived ^{60}Fe concentration,

*Note that in ref. 28 the time-averaged deposition rate of the top layers was originally calculated by assuming a much longer time period of <300 ky covered by these layers; that is, based on two detector events, this assumption resulted in <0.2 ^{60}Fe atoms·cm−2·y−1 (1-σ), which, however, changes to <1.8 atoms·cm−2·y−1 (1-σ) for the updated time period of 33 ky. The isotope ratio and ^{60}Fe concentration and total ^{60}Fe deposition are, however, independent of the time period.

ASTRONOMY

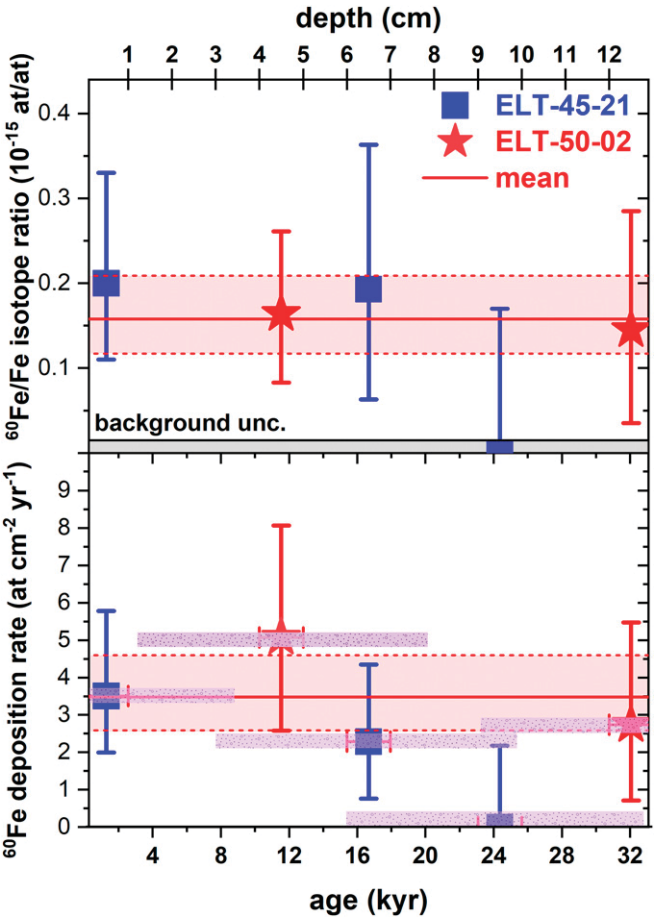

Fig. 2. ^{60}Fe/Fe isotope ratios and ^{60}Fe deposition rates (atoms·cm^{-2}·y^{-1}) for the five deep-sea layers representing the past 33 ky. The measurement background contributes to 1×10^{-17} in the uncertainty of the isotope ratio (black line, *Upper*). The mixing length in the deep-sea sediments was assumed to be ±3.5 cm. This length and the corresponding time resolution is indicated (*Lower*) by the horizontal bars. No obvious trend in the isotope ratio and in the deposition rate is visible for the samples versus depth and age.

which is representative of the local ISM during the past ~33 ky, is closely similar to the galaxy-averaged ^{60}Fe concentration in the ISM of $\sim 4 \times 10^{-12}$ atoms·cm^{-3} as deduced from the average SN rate in the galaxy and gamma-astronomy data (33).

The ^{60}Fe concentration of $(3.8 \pm 1.7) \times 10^{-12}$ atoms·cm^{-3} in the LIC measured in the present work is an order of magnitude lower than the value of $\sim 47 \times 10^{-12}$ atoms·cm^{-3} averaged over the 1.7-to-3.2-My peak. This elevated ^{60}Fe influx between 1.7 and 3.2 My (and between 5.5 and 7 My) is most readily interpreted in terms of transient SN ejecta passing Earth (28). Given the much lower influx during the last 33 ky, during which the SS spent at least some of the time within the LIC, it seems unlikely that the LIC (and possibly the CLIC as well) represents a residual structure of a broken-up SN ejecta shell from this younger event. Note that the ^{60}Fe influx over the past 33 ky seems comparable to the (not-decay-corrected) influx measured for the older, ~6- to 7-My event of ~1.5 ^{60}Fe atoms·cm^{-2}·y^{-1} in its peak (28). The intensity of the present-day influx would fit to a Super-AGB star production having typically much lower nucleosynthesis yields compared to SNe (50) but there are no stellar candidates within a few parsecs, and additionally the stable isotope signature in the local ISM, such as He and Ne, would not fit this scenario (51, 52).

Conclusions

Our data clearly show that there is ^{60}Fe in the local ISM, confirming present-day Antarctic snow data (31). Koll et al. (31) noted that a sharp increase in the flux of ^{60}Fe would be expected around the time when the SS entered the LIC, if the LIC is the origin of the detected ^{60}Fe. Our data, although based on low statistics, do not indicate such an increase during the past 33 ky, even though it is likely that the SS entered the LIC during this time (1, 4), and hence that at least the oldest sediment sample should represent a time period before entering the LIC.

Possible scenarios for the presence of ^{60}Fe in the local ISM might be as follows:

1) Gradual fading away of the transient passage of the supernova debris that produced the 1.7-to-3.1-My peak.
2) Echo of previous SNe with the dust particles having reflected from the boundary of the LB, thereby carrying ^{60}Fe "backward" toward the SS (see, e.g., refs. 49 and 53).
3) The LIC may be an independent ISM structure that survived the passage of the most recent SN ejecta (1.7 to 3.2 Ma) (54). If the ^{60}Fe observed here is coming from the LIC, it could represent the residue from an older event (note e.g., the enhanced ^{60}Fe influx ~6 Ma, where radioactive decay has reduced an originally higher ^{60}Fe concentration).

To discriminate between these possibilities, it will be necessary to extend the sediment data further into the past, and in particular to fill in the gap between the ~40 ky covered by the present work and ~1 Ma. If the ^{60}Fe influx is found to increase steadily toward the peak at 1.7 to 3.1 Ma, then the first explanation would be favored. If, on the other hand, the influx is found to be lower at >40 ky than at present, this would favor the LIC as the source of the ^{60}Fe and the third possibility would be the more likely. Existing crust data already cover this region in principle, but the time resolution is insufficient to distinguish between the above scenarios.

Materials and Methods

Sample Measurement. In general, individual samples contained between some 10^3 and ~10^4 ^{60}Fe atoms per g sediment, equivalent to one ^{60}Fe-decay

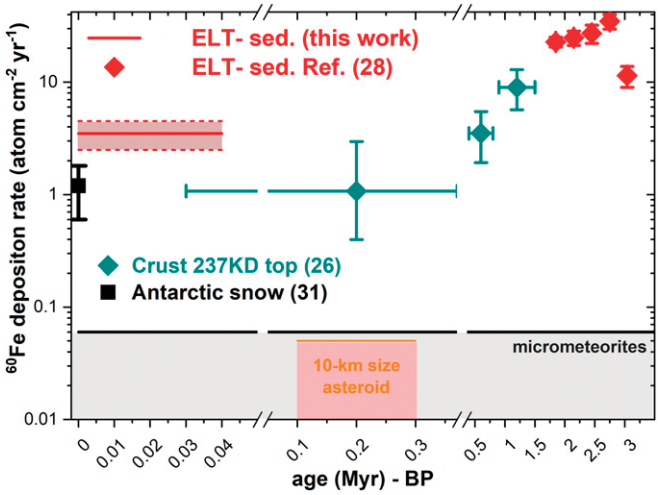

Fig. 3. Comparison of ^{60}Fe deposition rates averaged for different time periods over the past 3.5 My. Data are from measurements of deep-sea sediments and deep-sea crust samples (26, 28, 31). Also shown is the expected ^{60}Fe influx as deduced from the total extraterrestrial material flux onto Earth (constant) as well as for a single 10-km asteroid impact with the ^{60}Fe distributed over a deep-sea layer representing a time period of 200 ky (*Materials and Methods* and ref. 28). All interplanetary sources are a factor of ~50 to 100 lower than the measured recent deposition rate.

Table 2. Comparison of ^{60}Fe deposition and ISM concentrations between recent and older time periods

	0–0.02 ka	0–33 ka	0–10 Ma average	1.7–3.2 Ma
	Snow (31)	ELT	ELT and crust	ELT peak
Deposition rate, atom·cm^{-2}·y^{-1}	$1.2^{+0.6}_{-0.5}$	$3.5^{+1.1}_{-0.9}$	5.1 ± 0.5	24 ± 2
^{60}Fe-SS flux at 1 AU, atom·cm^{-2}·y^{-1}	$4.8^{+2.4}_{-2.0}$	14 ± 4	20 ± 2	98 ± 8
^{60}Fe ISM flux, 10^3 atom·cm^{-2}·y^{-1}	0.11 ± 0.06	0.31 ± 0.14	0.45 ± 0.15	2.1 ± 0.8
Velocity, km·s^{-1}*	25.7	25.7	∼15 ± 5	∼15 ± 5
Distance traversed per My, pc·My^{-1}	26	26	15 ± 5	15 ± 5
Distance traversed, pc	0.0005	0.9	153 ± 51	22 ± 7
^{60}Fe ISM particle conc., 10^{-12} ^{60}Fe·atom·cm^{-3}	1.3 ± 0.7	3.8 ± 1.7	9.6 ± 4.3	47 ± 22
ISM particle density, H-atom·cm^{-3}	0.2	0.2	0.005	—

The ^{60}Fe deposition rate for the 10-My case is a combined value deduced from the Eltanin sediment (ELT), crust (28), and Antarctic snow data (31). The ^{60}Fe ISM flux is calculated assuming a dust particle penetration probability from the ISM into the SS of (4.5 ± 1.5)%. For comparison of different influx scenarios, we assumed here the present density of the LB to be simply representative for the past 10 My (150 pc, with 1 pc = 3.086 × 10^{18} cm). This low value will not reflect the real average density over the past 10 My but will be representative for a large fraction of the time during the past 10 My. The dust penetration probability was assumed to be identical for the 0 to 33 ky and 0 to 10 My time periods.

*A mean velocity of 15 km·s^{-1} was assumed for the older time periods, taken as the average of the relative velocity in the ISM of 10 to 20 km·s^{-1} velocity (3, 4, 6, 7).

every 400 to 4,000 y in a 1-g sediment sample. Thus, we have applied the most sensitive technique, AMS (55–58), to directly count the minute amounts of ISM ^{60}Fe, via its isotope ratio ^{60}Fe/Fe. The corresponding ^{60}Fe concentrations were derived from the concentrations of the stable Fe determined via ICP-MS. The ^{60}Fe measurements were performed with the 14UD accelerator at the ANU (17, 28, 59, 60).

Details on the Determination of ^{60}Fe. The AMS measurements determine the atom ratio, for example ^{60}Fe/^{A}Fe, where ^{A}Fe (A = 54 or 56) is a stable isotope measured as an ion current in a Faraday cup in front of the particle detection system. We expect ^{60}Fe/^{56}Fe ratios between 10^{-17} and a few 10^{-16} from all samples. We have developed the capability to detect trace amounts of ^{60}Fe in terrestrial archives by AMS with an overall efficiency (atoms detected/atoms in the sample) of 0.5‰ (28), that is, one ^{60}Fe event in the detector would represent ∼2,000 ^{60}Fe atoms in the analyzed sample. The ANU setup has been optimized for high measurement efficiency and selectivity.

For such experiments where only a few counts are expected, it is crucial to suppress completely any interfering backgrounds due to stable elements of the same mass (e.g., ^{60}Ni in the case of ^{60}Fe), molecules of the same mass, and tails of the hugely more abundant stable isotopes (e.g., ^{54,56,57,58}Fe). This is achieved using the high energies of ∼170 MeV available from the 14UD tandem accelerator operating at ∼14 MV in combination with a gas-filled magnet detection system. At these ultralow levels, the elimination of interference from the stable isobar ^{60}Ni becomes extremely challenging. Although AMS completely destroys and removes molecular ions of mass 60 in the beam with the use of the accelerator and subsequent mass filters, the stable nuclide ^{60}Ni behaves in exactly the same way through the accelerator and subsequent analyzers and hence is still present at levels up to 10 orders of magnitude above the rare ^{60}Fe. Spatial separation of the ^{60}Fe and ^{60}Ni isobars was achieved in a gas-filled magnet, allowing the great majority of the ^{60}Ni to be blocked from entering the final particle detector (17, 28, 60). A multielectrode ionization chamber, which determines not only the energy but also the rate of energy loss of each ion and its position, then allows the few ^{60}Fe events to be clearly separated from the residual ^{60}Ni. The gas-filled magnet reduces the ^{60}Ni intensity (typically 10^5 to 10^6 counts per s) by a factor of ∼10^4 to a rate that the ionization detector can handle comfortably (61, 62). This setup provides a powerful means to reject the ^{60}Ni isobaric background but accepts essentially all of the ^{60}Fe events.

Due to the low number of expected ^{60}Fe events, the measurement background was carefully monitored with samples of iron oxides that contained negligible ^{60}Fe. The measurement background achieved for the system was ^{60}Fe/Fe = (2.7 ± 0.8) × 10^{-17}. The unknown samples were measured relative to standard-type samples (isotope ratios known with ∼10% accuracy) which were based on material from the Technical University of Munich and on material from recent meteorite studies (63). They had been previously cross-calibrated against a material from the Paul Scherrer Institute with well-known isotope ratios (64). These samples confirmed the validity of scaling the system settings between the different masses, with the data showing a reproducibility of ∼5%.

The measurement procedure was a slow sequence of 10-s measurements of the ^{54}Fe^{10+} ion current, alternating with counting periods of ^{60}Fe^{11+} ions that were typically 20 to 30 min for the real samples and blanks but were reduced to 3 to 5 min for the standard-type materials. All samples were measured repeatedly.

The five individual samples resulted in 6 to 20 mg of Fe_2O_3 which were subdivided into three to seven individual sputter samples for AMS. Sputtering times to fully consume the material were between 2 and 12 h per sample; this corresponds to a total counting time of ∼30 h and a similar time for blank samples. On average the crust samples gave ∼0.6 ^{60}Fe detector events per hour compared to <0.1 events per hour for blanks. Overall, distributed over three AMS beam times, 19 detector events were registered for the sediment samples compared to two detector events for blanks.

Arguments against a ^{60}Fe Influx from Meteorites or Micrometeorites in the Past 40 ky. Although we do not expect any significant ^{60}Fe production on Earth (28, 31), some ^{60}Fe will be deposited continuously through interplanetary material that bombards Earth. In space, highly energetic cosmic rays (predominantly galactic cosmic protons) will—via secondary neutrons and protons—produce ^{60}Fe through spallation reactions on Ni target atoms in interplanetary objects. Some earlier studies suggested that micrometeorites (MM) captured by Earth could also be responsible for the ^{60}Fe increase observed in crust 237KD in the period ∼2 to 3 My BP (65, 66).

We can estimate an interplanetary contribution to the total ^{60}Fe influx from the total amount of interplanetary material accreting on Earth: About (30,000 ± 20,000) tons of cosmic dust reaches Earth (67) per year, predominantly through MM and interplanetary dust particles. Objects that are more massive contribute less than 1% of the total mass flux. With measured concentrations of ^{60}Fe in micrometeorites or interplanetary dust of 0.51 dpm (decays per minute)·kg^{-1} Ni (1 × 10^{12} ^{60}Fe atoms·kg^{-1} Ni) (63, 68, 69) and a Ni content in cosmic dust (interplanetary particles) of ∼1% (CI chondrites) we calculate a flux of 0.06 ^{60}Fe atoms·cm^{-2}·y^{-1}, evenly spread over Earth's surface (Fig. 3). We measured a mean ^{60}Fe flux of 3.5 ± 1.0 ^{60}Fe atoms·cm^{-2}·y^{-1} for the past 33 ky, that is, the observed ^{60}Fe influx is 58 ± 17 times higher than expected from a constant influx of interplanetary particles.

We also measured the Ni content in the leachates of the five individual sediment samples by means of ICP-MS. The sediments contained on average 40 μg leachable Ni per g sediment, compared to 4,900 μg of leached Fe per g sediment (Table 1) (28). Thus, we obtain an element concentration ratio [Ni]/[Fe] of 0.008 atom/atom (see also refs. 28 and 39). With 1 × 10^{12} ^{60}Fe atoms per kg Ni, we calculate for the sediment samples a ^{60}Fe concentration of 4 × 10^4 atom·g^{-1}, which is five times higher than the measured ratio (Table 1). Thus, if 20% of the total Ni in the archives would be of (micro)meteoritic origin, we could account for the measured ^{60}Fe. The leachable Ni concentration was found to vary by less than 10% in all five sediment samples. For comparison, the 30,000 tons per year of cosmic dust influx (see also refs.

ASTRONOMY

70–73 indicating an even lower cosmic dust influx), assuming 10% is Fe (1% is Ni) and distributed equally across Earth's surface, corresponds to a stable ISM Fe (Ni) concentration in the sediments of 1.3 μg/g sediment (0.13 μg/g for Ni). The extraterrestrial stable Fe influx would be less than a per mille contribution to the total Fe in the sample (4,900 μg/g) and as a consequence the leached fraction of the sediment is completely dominated by stable Fe of terrestrial origin. Hence, we must assume a similar scenario for Ni. In summary, under the assumptions made above of ^{60}Fe production in (micro) meteorites, an interplanetary source for the elevated ^{60}Fe influx is not supported (see also the discussion in the supplement to ref. 28).

Arguments against a Significant ^{60}Fe Production from Solar Events in the past 40 ky. Independent from interstellar sources, extreme solar proton events can also lead to a significantly increased atmospheric production of cosmogenic radionuclides which eventually can become incorporated in terrestrial archives. Recent detections of excursions in the ^{14}C record at AD 774/775 and 993/994 as well as in ^{14}C, ^{10}Be, and ^{36}Cl at ∼660 BC have, for example, been found in tree rings and ice cores, respectively, which points to an extraterrestrial origin (refs. 74–77 and references therein). Such short-term solar events require time resolutions in the archive of the order of years. The total ^{60}Fe production for such events will be very low because of these short time scales and because of the scarcity of the required Ni target nuclei in the atmosphere needed for ^{60}Fe production. Therefore, such events would not be detectable in our samples.

Data Availability Statement. All relevant data are included in the paper and *SI Appendix*.

ACKNOWLEDGMENTS. We thank the Antarctic Marine Geology Research Facility, Florida State University (C. Sjunneskog) for providing the sediment cores. This work was funded by Austrian Science Fund project AI00428, through the European Science Foundation Collaborative Research Project CoDustMas; Australian Research Council projects DP140100136, DP180100495, and DP180100496; German Academic Exchange Service project 56266169; and The Group of Eight Australia–Germany Joint Research Cooperation Scheme. J.F. acknowledges a stipend from the University of Vienna and R.G. support from the European Cooperation in Science and Technology "ChETEC" Action (CA16117). We also acknowledge financial support from the Australian Government for the Heavy Ion Accelerator Facility at ANU through the National Collaborative Research Infrastructure Strategy. ICP-MS measurements were performed by S. Beutner (HZDR).

1. P. Frisch, V. V. Dwarkadas, "Effect of supernovae on the local interstellar material" in *Handbook of Supernovae*, A.W. Alsabti, P. Murdin, Eds. (Springer International Publishing AG, 2016).
2. D. P. Cox, P. R. Anderson, Extended adiabatic blast waves and a model of the soft X-ray background. *Astrophys. J.* **253**, 268 (1982).
3. R. K. Smith, D. P. Cox, Multiple supernova remnant models of the local bubble and the soft X-ray background. *Astrophys. J. Suppl. Ser.* **134**, 283 (2001).
4. P. C. Frisch *et al*., The galactic environment of the Sun: Interstellar material inside and outside of the heliosphere. *Space Sci. Rev.* **146**, 235–273 (2009).
5. D. Breitschwerdt *et al*., The locations of recent supernovae near the Sun from modelling $^{(60)}$Fe transport. *Nature* **532**, 73–76 (2016).
6. S. Redfield, J. L. Linsky, The structure of the local interstellar medium. IV. Dynamics, morphology, physical properties, and implications of cloud-cloud interactions. *Astrophys. J.* **673**, 283 (2008).
7. P. Frisch, D. G. York, *The Galaxy and the Solar System*, (University of Arizona Press, Tucson, 1986), pp. 83–100.
8. B. Fuchs, D. Breitschwerdt, M. A. de Avillez, C. Dettbarn, C. Flynn, The search for the origin of the Local Bubble redivivus. *Mon. Not. R. Astron. Soc.* **373**, 993 (2006).
9. R. Lallement, R. Ferlet, A. M. Lagrange, M. Lemoine, A. Vidal-Madjar, Local cloud structure from HST-GHRS. *Astron. Astrophys.* **304**, 461 (1995).
10. E. Gruen *et al*., Discovery of Jovian dust streams and interstellar grains by the Ulysses spacecraft. *Nature* **362**, 428 (1993).
11. A. J. Westphal *et al*.; 30714 Stardust@home dusters, Interstellar dust. Evidence for interstellar origin of seven dust particles collected by the Stardust spacecraft. *Science* **345**, 786–791 (2014).
12. I. Mann, Interstellar dust in the solar system. *Annu. Rev. Astron. Astrophys.* **48**, 173–203 (2010).
13. N. Altobelli *et al*., Interstellar dust flux measurements by the Galileo dust instrument between the orbits of Venus and Mars. *J. Geophys.* **110**, A07102 (2005).
14. D. Breitschwerdt, M. J. Freyberg, R. Egger, Origin of H I clouds in the local bubble. I. A hydromagnetic Rayleigh-Taylor instability caused by the interaction between the Loop I and the local bubble. *Astron. Astrophys.* **361**, 303 (2000).
15. P. D. Cox, L. Helenius, Flux-tube dynamics and model for the origin of the local fluff. *Astrophys. J.* **583**, 205 (2003).
16. G. Rugel *et al*., New measurement of the ^{60}Fe half-life. *Phys. Rev. Lett.* **103**, 072502 (2009).
17. A. Wallner *et al*., Settling the half-life of ^{60}Fe: Fundamental for a versatile astrophysical chronometer. *Phys. Rev. Lett.* **114**, 041101 (2015).
18. K. M. Ostiek *et al*., Activity measurement of ^{60}Fe through the decay of ^{60m}Co and confirmation of its half-life. *Phys. Rev. C* **95**, 055809 (2017).
19. A. Wallner *et al*., Abundance of live ^{244}Pu in deep-sea reservoirs on Earth points to rarity of actinide nucleosynthesis. *Nat. Commun.* **6**, 5956 (2015).
20. E. Dwek, The evolution of the elemental abundances in the gas and dust phases of the galaxy. *Astrophys. J.* **501**, 643–665 (1998).
21. J. Ellis, B. D. Fields, D. N. Schramm, Geological isotope anomalies as signatures of nearby supernovae. *Astrophys. J.* **470**, 1227 (1996).
22. B. J. Fry, B. D. Fields, J. R. Ellis, Radioactive iron rain: Transporting ^{60}Fe in SN dust to the ocean floor. *Astrophys. J.* **827**, 48 (2016).
23. G. Korschinek, T. Faestermann, K. Knie, C. Schmidt, ^{60}Fe, a promising AMS isotope for many applications. *Radiocarbon* **38**, 68 (1996).
24. T. Athanassiadou, B. D. Fields, Penetration of nearby supernova dust in the inner solar system. *New Astron.* **16**, 229–241 (2011).
25. K. Knie *et al*., Indication for supernova produced ^{60}Fe activity on earth. *Phys. Rev. Lett.* **83**, 18–21 (1999).
26. K. Knie *et al*., ^{60}Fe anomaly in a deep-sea manganese crust and implications for a nearby supernova source. *Phys. Rev. Lett.* **93**, 171103 (2004).
27. C. Fitoussi *et al*., Search for supernova-produced ^{60}Fe in a marine sediment. *Phys. Rev. Lett.* **101**, 121101 (2008).
28. A. Wallner *et al*., Recent near-Earth supernovae probed by global deposition of interstellar radioactive ^{60}Fe. *Nature* **532**, 69–72 (2016).
29. P. Ludwig *et al*., Time-resolved 2-million-year-old supernova activity discovered in Earth's microfossil record. *Proc. Natl. Acad. Sci. U.S.A.* **113**, 9232–9237 (2016).
30. G. Korschinek *et al*., Supernova-produced ^{53}Mn on Earth. *Phys. Rev. Lett.* **125**, 031101 (2020).
31. D. Koll *et al*., Interstellar ^{60}Fe in Antarctica. *Phys. Rev. Lett.* **123**, 072701 (2019).
32. L. Fimiani *et al*., Interstellar ^{60}Fe on the surface of the moon. *Phys. Rev. Lett.* **116**, 151104 (2016).
33. R. Diehl, Nuclear astrophysics lessons from INTEGRAL. *Rep. Prog. Phys.* **76**, 026301 (2013).
34. W. R. Binns *et al*., Observation of the ^{60}Fe nucleosynthesis-clock isotope in galactic cosmic rays. *Science* **352**, 677–680 (2016).
35. E. Allison, M. T. Ledbetter, Timing of bottom-water scour recorded by sedimentological parameters in the south Australian basin. *Mar. Geol.* **46**, 131–147 (1982).
36. L. A. Frakes, USNS Eltanin sediment descriptions, cruises 32-45 (Contribution 33, Sedimentary Research Laboratory, Florida State University, Tallahassee, 1971).
37. L. A. Frakes, USNS Eltanin sediment descriptions, cruises 4-54 (Contribution 37, Sedimentary Research Laboratory, Florida State University, Tallahassee, 1973).
38. J. Feige *et al*., Limits on supernova-associated ^{60}Fe/^{26}Al nucleosynthesis ratios from AMS measurements of deep-sea sediments. *Phys. Rev. Lett.* **121**, 221103 (2018).
39. J. Feige *et al*., The search for supernova-produced radionuclides in terrestrial deep-sea archives. *Publ. Astron. Soc. Aust.* **29**, 109–114 (2012).
40. G. J. Feldman, R. D. Cousins, Unified approach to the classical statistical analysis of small signals. *Phys. Rev. D Part. Fields* **57**, 3873–3889 (1998).
41. D. Bourlès, G. M. Raisbeck, F. Yiou, ^{10}Be and ^{9}Be in marine sediments and their potential for dating. *Geochim. Cosmochim. Acta* **53**, 443–452 (1989).
42. S. Merchel, U. Herpers, An update on radiochemical separation techniques for the determination of long-lived radionuclides via accelerator mass spectrometry. *Radiochim. Acta* **84**, 215–219 (1999).
43. J. Feige *et al*., "AMS measurements of cosmogenic and supernova-ejected radionuclides in deep-sea sediment cores" in *EPJ Web of Conferences*, (2013), Vol. 63, 10.1051/epjconf/20136303003.
44. S. Akhmadaliev, R. Heller, D. Hanf, G. Rugel, S. Merchel, The new 6MV AMS-facility DREAMS at Dresden. *Nucl. Instr. Method. B* **294**, 5 (2013).
45. L. R. Teal, M. T. Bulling, E. R. Parker, M. Solan, Global patterns of bioturbation intensity and mixed depth of marine soft sediments. *Aquat. Biol.* **2**, 207–218 (2008).
46. H. Lee *et al*., Distribution and inventories of ^{90}Sr, ^{137}Cs, ^{241}Am and Pu isotopes in sediments of the Northwest Pacific Ocean. *Mar. Geol.* **216**, 249 (2005).
47. N. Altobelli *et al*., Cassini between venus and earth: Detection of interstellar dust. *J. Geophys. Res.* **108**, 8032 (2003).
48. A. Li, "Interstellar grains - The 75th anniversary" in *Light, Dust, and Chemical Evolution*, R. Saija, C. Cecchi-Pestellini, Eds. (Journal of Physics: Conference Series, IOP Publishing, Bristol, UK, 2005), Vol. 6, pp. 229–248.
49. B. J. Fry, B. D. Fields, J. R. Ellis, No escape from the supernova! Magnetic imprisonment of dusty pinballs by a supernova remnant. *Astrophys. J.* **894**, 109 (2020).
50. C. L. Doherty, P. Gil-Pons, H. H. B. Lau, J. C. Lattanzio, L. Siess, Super and massive AGB stars - II. Nucleosynthesis and yields - Z = 0.02, 0.008 and 0.004. *Mon. Not. R. Astron. Soc.* **437**, 195 (2014).
51. E. Salerno *et al*., Measurement of ^{3}He/^{4}He in the local interstellar medium: The collisa experiment on *Mir*. *Astrophys. J.* **585**, 840–849 (2003).
52. G. Gloeckler, L. Fisk, *Composition of Matter*, (Springer, 2007), Vol. 27.
53. M. M. Schulreich, D. Breitschwerdt, J. Feige, C. Dettbarn, Numerical studies on the link between radioisotopic signatures on Earth and the formation of the Local Bubble. I. ^{60}Fe transport to the solar system by turbulent mixing of ejecta from nearby supernovae into a locally homogeneous ISM. *Astron. Astrophys.* **604**, A81 (2017).
54. J. D. Slavin, The origins and physical properties of the complex of local interstellar clouds. *Space Sci. Rev.* **143**, 311 (2009).
55. H.-A. Synal, "Developments in accelerator mass spectrometry" in *100 Years of Mass Spectrometry*, K. Blaum, Y. Litvinov, Eds. (Int. J. Mass Spectrom, 2013), Vol. 349–350, pp. 192–202.

56. W. Kutschera, "Applications of accelerator mass spectrometry" in *100 Years of Mass Spectrometry*, K. Blaum, Y. Litvinov, Eds. (Int. J. Mass Spectrom, 2013), Vol. 349-350, pp. 203–218.
57. P. Steier *et al*., Analysis and application of heavy isotopes in the environment. *Nucl. Instrum. Methods Phys. Res. B* **268**, 1045 (2010).
58. A. Wallner *et al*., Novel method to study neutron capture of 235U and 238U simultaneously at keV energies. *Phys. Rev. Lett.* **112**, 192501 (2014).
59. L. K. Fifield, S. G. Tims, T. Fujioka, W. T. Hoo, S. E. Everett, Accelerator mass spectrometry with the 14UD accelerator at the Australian National University. *Nucl. Instrum. Methods Phys. Res. B* **268**, 858–862 (2010).
60. M. Martschini *et al*., New and upgraded ionization chambers for AMS at the Australian National University. *Nucl. Instrum. Meth. B* **438**, 141 (2019).
61. M. Paul *et al*., Heavy ion separation with a gas-filled magnetic spectrograph. *Nucl. Instrum. Methods Phys. Res. A* **277**, 418 (1989).
62. K. Knie *et al*., High-sensitivity AMS for heavy nuclides at the Munich tandem accelerator. *Nucl. Instrum. Meth. B* **172**, 717 (2000).
63. I. Leya *et al*., ^{53}Mn and ^{60}Fe in iron meteorites - new data and model calculations. *Meteorit. Planet. Sci.* (2020) in press.
64. D. Schumann, N. Kivel, R. Dressler, Production and characterization of ^{60}Fe standards for accelerator mass spectrometry. *PLoS One* **14**, e0219039 (2019).
65. S. Basu, F. M. Stuart, C. Schnabel, V. Klemm, Galactic-cosmic-ray-produced ^{3}He in a ferromanganese crust: Any supernova ^{60}Fe excess on Earth? *Phys. Rev. Lett.* **98**, 141103 (2007).
66. F. M. Stuart, M. R. Lee, Micrometeorites and extraterrestrial He in a ferromanganese crust from the Pacific Ocean. *Chem. Geol.* **322–323**, 209 (2012).
67. S. G. Love, D. E. Brownlee, Heating and thermal transformation of micrometeoroids entering the Earth's atmosphere. *Icarus* **89**, 26–43 (1991).
68. R. Trappitsch, I. Leya, Cosmogenic production rates and recoil loss effects in micrometeorites and interplanetary dust particles. *Meteorit. Planet. Sci.* **48**, 195–210 (2013).
69. K. Knie *et al*., Accelerator mass spectrometry measurements and model calculations of iron-60 production rates in meteorites. *Meteorit. Planet. Sci.* **34**, 729–734 (1999).
70. B. Peucker-Ehrenbrink, Accretion of extraterrestrial matter during the last 80 million years and its effect on the marine osmium isotope record. *Geochim. Cosmochim. Acta* **60**, 3187–3196 (1996).
71. P. Gabrielli *et al*., Meteoric smoke fallout over the Holocene epoch revealed by iridium and platinum in Greenland ice. *Nature* **432**, 1011–1014 (2004).
72. J. M. C. Plane, Cosmic dust in the earth's atmosphere. *Chem. Soc. Rev.* **41**, 6507–6518 (2012).
73. G. Cremonese, P. Borin, E. Martellato, F. Marzari, M. Bruno, New calibration of the micrometeoroid flux on earth. *Astrophys. J.* **749**, L40 (2012).
74. F. Miyake, K. Nagaya, K. Masuda, T. Nakamura, A signature of cosmic-ray increase in AD 774-775 from tree rings in Japan. *Nature* **486**, 240–242 (2012).
75. F. Miyake, K. Masuda, T. Nakamura, Another rapid event in the carbon-14 content of tree rings. *Nat. Commun.* **4**, 1748 (2013).
76. F. Mekhaldi *et al*., Multiradionuclide evidence for the solar origin of the cosmic-ray events of AD 774/5 and 993/4. *Nat. Commun.* **6**, 8611 (2015).
77. P. O'Hare *et al*.; ASTER Team, Multiradionuclide evidence for an extreme solar proton event around 2,610 B.P. (~660 BC). *Proc. Natl. Acad. Sci. U.S.A.* **116**, 5961–5966 (2019).

ARTICLES
https://doi.org/10.1038/s41928-020-0412-1
nature electronics

Intrinsic plasticity of silicon nanowire neurotransistors for dynamic memory and learning functions

Eunhye Baek[1,2,3] ✉, Nikhil Ranjan Das[4], Carlo Vittorio Cannistraci[5,6], Taiuk Rim[7], Gilbert Santiago Cañón Bermúdez[8], Khrystyna Nych[1], Hyeonsu Cho[7], Kihyun Kim[9], Chang-Ki Baek[7], Denys Makarov[8], Ronald Tetzlaff[10], Leon Chua[11], Larysa Baraban[1,2,12] ✉ and Gianaurelio Cuniberti[1,2] ✉

Neuromorphic architectures merge learning and memory functions within a single unit cell and in a neuron-like fashion. Research in the field has been mainly focused on the plasticity of artificial synapses. However, the intrinsic plasticity of the neuronal membrane is also important in the implementation of neuromorphic information processing. Here we report a neurotransistor made from a silicon nanowire transistor coated by an ion-doped sol–gel silicate film that can emulate the intrinsic plasticity of the neuronal membrane. The neurotransistors are manufactured using a conventional complementary metal–oxide–semiconductor process on an 8-inch (200 mm) silicon-on-insulator wafer. Mobile ions allow the film to act as a pseudo-gate that generates memory and allows the neurotransistor to display plasticity. We show that multiple pulsed input signals of the neurotransistor are non-linearly processed by sigmoidal transformation into the output current, which resembles the functioning of a neuronal membrane. The output response is governed by the input signal history, which is stored as ionic states within the silicate film, and thereby provides the neurotransistor with learning capabilities.

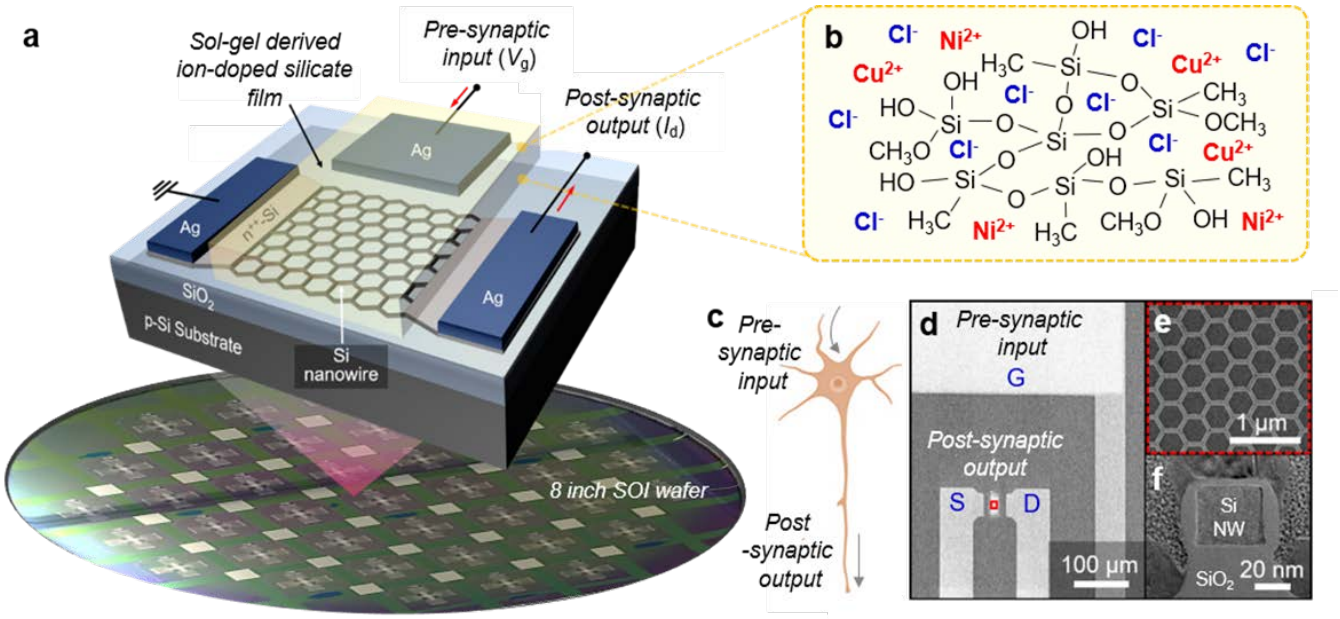

[1]Institute for Materials Science and Max Bergmann Center of Biomaterials, TU Dresden, Dresden, Germany. [2]Center for Advancing Electronics Dresden, TU Dresden, Dresden, Germany. [3]Center for Brain-Inspired Computing Research (CBICR), Beijing Innovation Center for Future Chip, Tsinghua University, Beijing, China. [4]Department of Radio Physics and Electronics, University of Calcutta, Kolkata, India. [5]Biomedical Cybernetics Group, Biotechnology Center (BIOTEC), Center for Molecular and Cellular Bioengineering (CMCB), Center for Systems Biology Dresden (CSBD), Cluster of Excellence Physics of Life (PoL), TU Dresden, Dresden, Germany. [6]Center for Complex Network Intelligence (CCNI), Tsinghua Laboratory of Brain and Intelligence, Tsinghua University, Beijing, China. [7]Department of Creative IT Engineering, Pohang University of Science and Technology, Pohang, Korea. [8]Institute of Ion Beam Physics and Materials Research, Helmholtz-Zentrum Dresden-Rossendorf e.V., Dresden, Germany. [9]Division of Electronic Engineering, Jeonbuk National University, Jeonju, Korea. [10]Chair of Fundamentals of Electrical Engineering, Technische Universität Dresden, Dresden, Germany. [11]University of California, EECS Department, Berkeley, Berkeley, USA. [12]Institute of Radiopharmaceutical Cancer Research, Helmholtz-Zentrum Dresden-Rossendorf e.V., Dresden, Germany. ✉e-mail: ebaek@tsinghua.edu.cn; l.baraban@hzdr.de; gianaurelio.cuniberti@tu-dresden.de

FULL PAPER

ADVANCED OPTICAL MATERIALS
www.advopticalmat.de

Efficient Modulation of Photonic Bandgap and Defect Modes in All-Dielectric Photonic Crystals by Energetic Ion Beams

Guiqiang Du, Xiachen Zhou, Chi Pang, Kaiyuan Zhang, Yunpeng Zhao, Guang Lu, Fen Liu, Ailing Wu, Shavkat Akhmadaliev, Shengqiang Zhou, and Feng Chen**

The photonic bandgap and localization in photonic crystals can be effectively modulated by energetic ion beams owing to the induced modification of the thickness and refractive indices of the materials. In this work, the modulation of photonic bandgap and defect modes in 1D all-dielectric photonic crystals is investigated theoretically and experimentally by using carbon (C^{5+}) ion irradiation. It is found that the photonic bandgap and defect mode have a remarkable hypsochromic shift under the C^{5+} ion irradiation. The degree of the blueshift mainly depends on the reduction of the material thickness that is nearly proportional to the fluences of C^{5+} ions. The blueshift of the band edges and defect modes shows a step-like behavior from transparency to opacifica-tion (near-zero transmittance or high reflectance) or a converse trend. The work paves a new way to tailor the photonic crystals toward the development of novel devices with tunable specific wavelengths and wavebands.

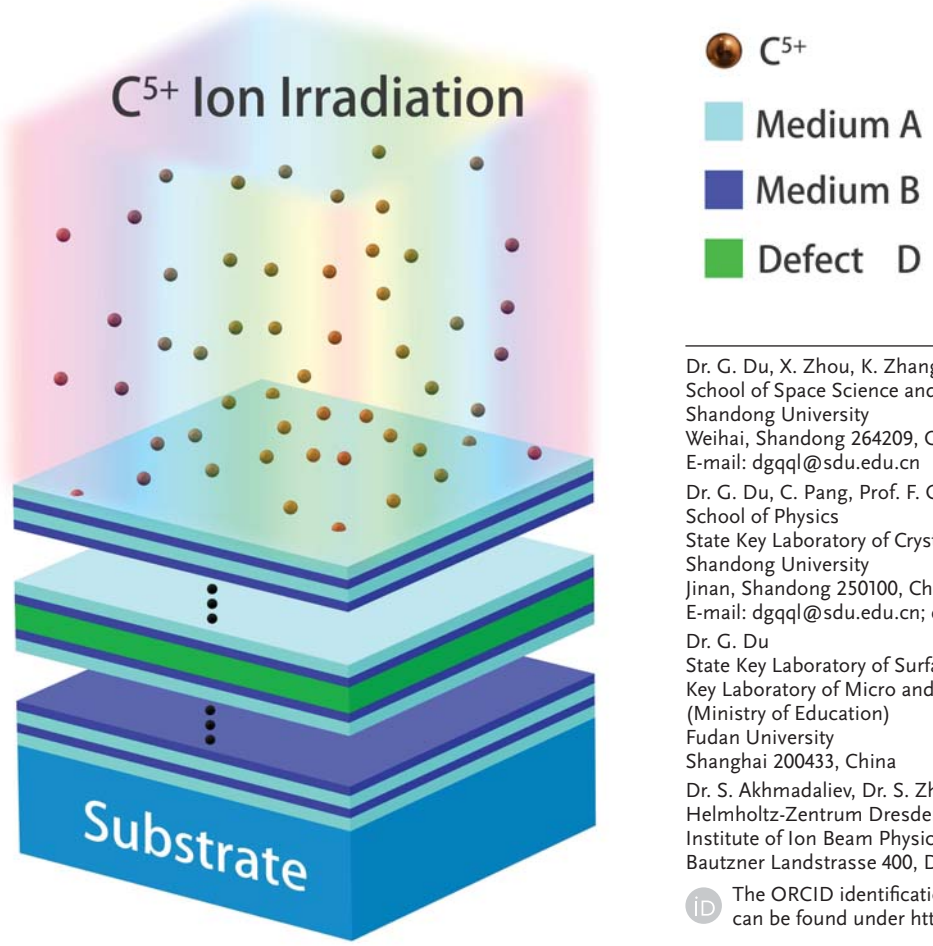

Dr. G. Du, X. Zhou, K. Zhang, Y. Zhao, Dr. G. Lu, Dr. F. Liu, Prof. A. Wu
School of Space Science and Physics
Shandong University
Weihai, Shandong 264209, China
E-mail: dgqql@sdu.edu.cn

Dr. G. Du, C. Pang, Prof. F. Chen
School of Physics
State Key Laboratory of Crystal Materials
Shandong University
Jinan, Shandong 250100, China
E-mail: dgqql@sdu.edu.cn; drfchen@sdu.edu.cn

Dr. G. Du
State Key Laboratory of Surface Physics and Department of Physics
Key Laboratory of Micro and Nano-Photonic Structures
(Ministry of Education)
Fudan University
Shanghai 200433, China

Dr. S. Akhmadaliev, Dr. S. Zhou
Helmholtz-Zentrum Dresden-Rossendorf
Institute of Ion Beam Physics and Materials Research
Bautzner Landstrasse 400, Dresden 01328, Germany

The ORCID identification number(s) for the author(s) of this article can be found under https://doi.org/10.1002/adom.202000426.

DOI: 10.1002/adom.202000426

REVIEW

ADVANCED ENERGY MATERIALS

Noble Metal Foams

www.advenergymat.de

Engineering Self-Supported Noble Metal Foams Toward Electrocatalysis and Beyond

Ran Du, Xinyi Jin, René Hübner, Xuelin Fan, Yue Hu, and Alexander Eychmüller**

Noble metals, despite their expensiveness, display irreplaceable roles in widespread fields. To acquire novel physicochemical properties and boost the performance-to-price ratio for practical applications, one core direction is to engineer noble metals into nanostructured porous networks. Noble metal foams (NMFs), featuring self-supported, 3D interconnected networks structured from noble-metal-based building blocks, have drawn tremendous attention in the last two decades. Inheriting structural traits of foams and physicochemical properties of noble metals, NMFs showcase a variety of interesting properties and impressive prospect in diverse fields, including electrocatalysis, heterogeneous catalysis, surface-enhanced Raman scattering, sensing and actuation, etc. A number of NMFs have been created and versatile synthetic approaches have been developed. However, because of the innate limitation of specific methods and the insufficient understanding of formation mechanisms, flexible manipulation of compositions, structures, and corresponding properties of NMFs are still challenging. Thus, the correlations between composition/structure and properties are seldom established, retarding material design/optimization for specific applications. This review is devoted to a comprehensive introduction of NMFs ranging from synthesis to applications, with an emphasis on electrocatalysis. Challenges and opportunities are also included to guide possible research directions in this field and promote the interest of interdisciplinary scientists.

1. Introduction

Noble metals are a group of oxidation-resistant transition metals, which are usually considered to consist of gold (Au), silver (Ag), ruthenium (Ru), rhodium (Rh), palladium (Pd), osmium (Os), iridium (Ir), and platinum (Pt). They are quite expensive (≈15 USD per ounce for Ag; 200–400 USD per ounce for Ru, Os; 800–1500 USD per ounce for Pt, Au, Pd, Ir; ≈3000 USD per ounce for rhodium. Data are acquired on May 12, 2019.[1] owing to their low mass abundance in the earth's crust (0.001–2 ppm[2]). Despite their inertness in bulk, noble metals become extremely active when the feature size reaches the nanoscale.[3] With the onset and advance of nanotechnology, they have exhibited irreplaceable functions in widespread fields, including electrocatalysis, heterogeneous catalysis, plasmonics, biology, etc.[4–6] Especially, exceptional performance is found in quite a few energy- and environment-related heterocatalytic and electrocatalytic reactions. Thus, many noble-metal-based materials, in spite of their high cost, have been commercialized in market, such as for catalysis and astronautics.

However, several issues exist in the development and practical use of noble metal nanomaterials. First, the melting point of noble metals considerably decreases with reduced feature size, which can incur and aggravate the aggregation and performance decline of noble metal nanoparticles (NPs) during storage or application. Second, certain strategies for suppressing aggregation (e.g., introduction of ligands or supporting substrates) work well in some cases, while the existence of additional components can affect the long-term stability and the unbiased evaluation of the true performance of noble metals. Third, to improve the performance-to-price ratio, both the increase of the utilization efficiency of noble metals and the search for their replacements[7,8] need to be explored. Because of certain unique physicochemical properties of noble metals which cannot be realized by other materials (e.g., electronic structures and plasmonic effects), under certain circumstances, improving the utilization efficiency and fully releasing the innate potential of noble metals are particularly favorable. Bearing the above concerns in mind, the engineering of noble metals into self-supported, nanostructured solid foams, i.e., noble metal foams (NMFs), serves as a promising solution

Dr. R. Du, X. Y. Jin, X. L. Fan, Prof. A. Eychmüller
Physical Chemistry
Technische Universität Dresden
Bergstr. 66b, Dresden 01062, Germany
E-mail: Ran.Du@chemie.tu-dresden.de;
alexander.eychmueller@chemie.tu-dresden.de

X. Y. Jin
Department of Polymer Science and Engineering
Zhejiang University
Hangzhou 310027, P. R. China

Dr. R. Hübner
Helmholtz-Zentrum Dresden-Rossendorf
Institute of Ion Beam Physics and Materials Research
Bautzner Landstrasse 400, Dresden 01328, Germany

Dr. Y. Hu
College of Chemistry and Materials Engineering
Wenzhou University
Wenzhou 325000, P. R. China

The ORCID identification number(s) for the author(s) of this article can be found under https://doi.org/10.1002/aenm.201901945.

DOI: 10.1002/aenm.201901945

nature physics

ARTICLES

https://doi.org/10.1038/s41567-020-01040-y

Inertial spin dynamics in ferromagnets

Kumar Neeraj[1,12], Nilesh Awari[2,12], Sergey Kovalev[2], Debanjan Polley[1], Nanna Zhou Hagström[1], Sri Sai Phani Kanth Arekapudi[3], Anna Semisalova[4,5], Kilian Lenz[5], Bertram Green[2], Jan-Christoph Deinert[2], Igor Ilyakov[2], Min Chen[2], Mohammed Bawatna[2], Valentino Scalera[6], Massimiliano d'Aquino[7], Claudio Serpico[6], Olav Hellwig[3,5], Jean-Eric Wegrowe[8], Michael Gensch[9,10] and Stefano Bonetti[1,11] ✉

The understanding of how spins move and can be manipulated at pico- and femtosecond timescales has implications for ultrafast and energy-efficient data-processing and storage applications. However, the possibility of realizing commercial technologies based on ultrafast spin dynamics has been hampered by our limited knowledge of the physics behind processes on this timescale. Recently, it has been suggested that inertial effects should be considered in the full description of the spin dynamics at these ultrafast timescales, but a clear observation of such effects in ferromagnets is still lacking. Here, we report direct experimental evidence of intrinsic inertial spin dynamics in ferromagnetic thin films in the form of a nutation of the magnetization at a frequency of ~0.5 THz. This allows us to reveal that the angular momentum relaxation time in ferromagnets is on the order of 10 ps.

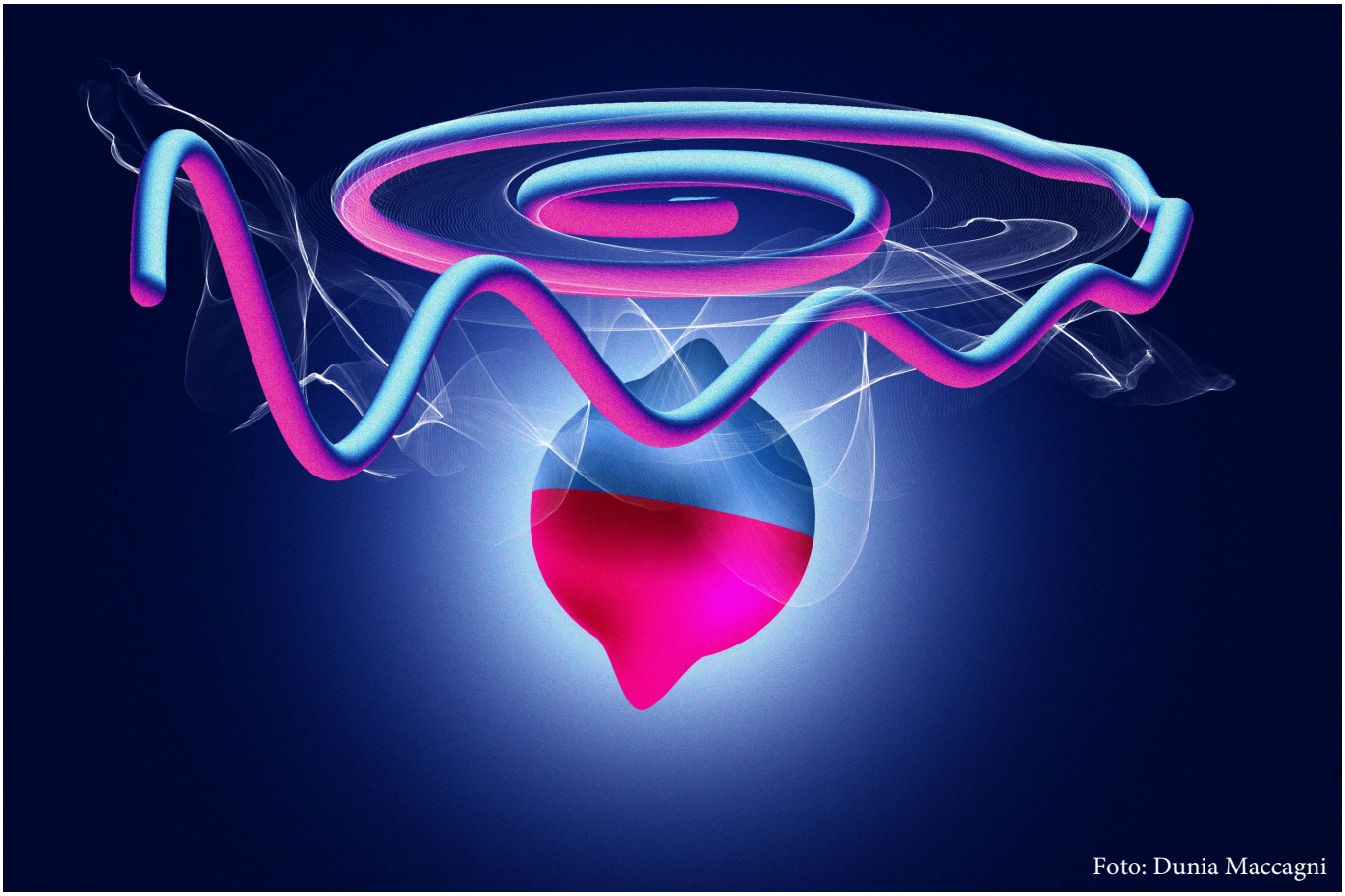

Foto: Dunia Maccagni

[1]Department of Physics, Stockholm University, Stockholm, Sweden. [2]Institute of Radiation Physics, Helmholtz-Zentrum Dresden-Rossendorf, Dresden, Germany. [3]Institute of Physics, Chemnitz University of Technology, Chemnitz, Germany. [4]Faculty of Physics and CENIDE, University of Duisburg-Essen, Duisburg, Germany. [5]Institute of Ion Beam Physics and Materials Research, Helmholtz-Zentrum Dresden-Rossendorf, Dresden, Germany. [6]DIETI, University of Naples Federico II, Naples, Italy. [7]Department of Engineering, University of Naples 'Parthenope', Naples, Italy. [8]LSI, École Polytechnique, CEA/DRF/IRAMIS, CNRS, Institut Polytechnique de Paris, Palaiseau, France. [9]Institute of Optical Sensor Systems, German Aerospace Center (DLR), Berlin, Germany. [10]Institute of Optics and Atomic Physics, TU Berlin, Berlin, Germany. [11]Department of Molecular Sciences and Nanosystems, Ca' Foscari University of Venice, Venezia-Mestre, Italy. [12]These authors contributed equally: K. Neeraj, N. Awari. ✉e-mail: stefano.bonetti@fysik.su.se

Soltani et al. *Light: Science & Applications* (2020)9:97
https://doi.org/10.1038/s41377-020-0321-0

Official journal of the CIOMP 2047-7538
www.nature.com/lsa

LETTER Open Access

Direct nanoscopic observation of plasma waves in the channel of a graphene field-effect transistor

Amin Soltani[1], Frederik Kuschewski[2], Marlene Bonmann[3], Andrey Generalov[3,6], Andrei Vorobiev[3], Florian Ludwig[1], Matthias M. Wiecha[1], Dovilė Čibiraitė[1], Frederik Walla[1], Stephan Winnerl[4], Susanne C. Kehr[2], Lukas M. Eng[2,5], Jan Stake[3] and Hartmut G. Roskos[1]

Abstract

Plasma waves play an important role in many solid-state phenomena and devices. They also become significant in electronic device structures as the operation frequencies of these devices increase. A prominent example is field-effect transistors (FETs), that witness increased attention for application as rectifying detectors and mixers of electromagnetic waves at gigahertz and terahertz frequencies, where they exhibit very good sensitivity even high above the cut-off frequency defined by the carrier transit time. Transport theory predicts that the coupling of radiation at THz frequencies into the channel of an antenna-coupled FET leads to the development of a gated plasma wave, collectively involving the charge carriers of both the two-dimensional electron gas and the gate electrode. In this paper, we present the first direct visualization of these waves. Employing graphene FETs containing a buried gate electrode, we utilize near-field THz nanoscopy at room temperature to directly probe the envelope function of the electric field amplitude on the exposed graphene sheet and the neighboring antenna regions. Mapping of the field distribution documents that wave injection is unidirectional from the source side since the oscillating electrical potentials on the gate and drain are equalized by capacitive shunting. The plasma waves, excited at 2 THz, are overdamped, and their decay time lies in the range of 25–70 fs. Despite this short decay time, the decay length is rather long, i.e., 0.3-0.5 μm, because of the rather large propagation speed of the plasma waves, which is found to lie in the range of $3.5–7 \times 10^6$ m/s, in good agreement with theory. The propagation speed depends only weakly on the gate voltage swing and is consistent with the theoretically predicted $\frac{1}{4}$ power law.

Plasma waves in solid-state materials and device structures have regained much attention with the emergence of graphene and the direct observation of plasmon polariton excitation and propagation on this two-dimensional material at infrared frequencies[1,2]. The capability to control the carrier density and thus the plasma frequency by doping as well as by the application of a gate voltage allowed the discovery of a plethora of physical phenomena related to plasmons, such as plasmon–phonon coupling[3], strong electronic correlations measured via the precise determination of the propagation velocity of the plasmons[4], negative local resistance[5], and material interactions that limit the propagation distance of the plasmon polaritons[6]. Plasma-wave excitations are also expected to play a significant role in graphene field-effect transistors (FETs), which are widely explored for the detection of terahertz radiation[7–9]. This formation of plasma waves is not specific to graphene but is expected for any type of gated two-dimensional electron gas (2DEG) in the channel of an FET. Such channel plasma waves have gained considerable attention, as FETs became of practical interest for detection[10–13] and generation[14–17] of

Correspondence: Amin Soltani (soltani@physik.uni-frankfurt.de) or Hartmut G. Roskos (roskos@physik.uni-frankfurt.de)
[1]Physikalisches Institut, Johann Wolfgang Goethe-Universität, Max-von-Laue-Str. 1, D-60438 Frankfurt am Main, Germany
[2]Institut für Angewandte Physik, Technische Universität Dresden, Nöthnitzer Str. 61, D-01187 Dresden, Germany
Full list of author information is available at the end of the article
These authors contributed equally: Amin Soltani, Frederik Kuschewski, Marlene Bonmann

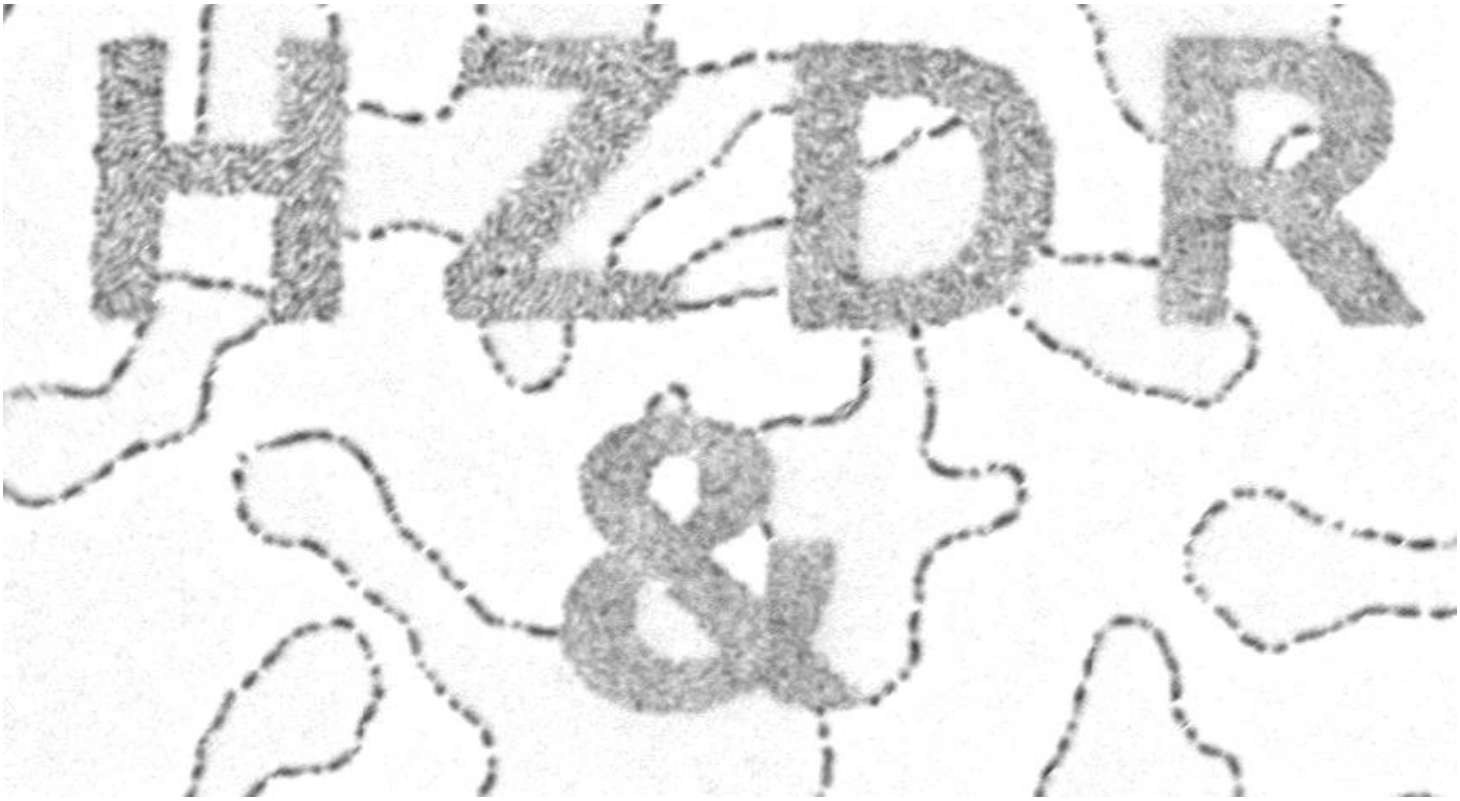

Statistics

Image: HZDR / F. Samad, O. Hellwig

User facilities and services

Ion Beam Center (IBC)

The Ion Beam Center (IBC) at HZDR combines various machines (electrostatic accelerators, ion implanters, low-energy and focused ion beam systems) into a unique facility used for ion beam modification and ion beam analysis of materials. The available energy range spans from a few eV to 60 MeV with a respective interaction depth in solids between 0.1 nm to 10 µm. In addition to standard broad beams also focused (down to 1 nm) and highly-charged (charge state up to 45+) ion beams are available. In combination with an allocated ion beam experiment, users can also profit from structural analysis (electron microscopy and spectroscopy, X-ray scattering techniques) and sample or device processing under clean-room conditions. At the 6 MV tandem accelerator, the DREAMS (DREsden AMS = accelerator mass spectrometry) facility is used for the determination of long-lived radionuclides, like ^{7,10}Be, ^{26}Al, ^{36}Cl, ^{41}Ca, ^{55}Fe, ^{129}I, and others. A schematic overview of the IBC including the description of the main beam lines and experimental stations is given on page 81 of this Annual Report. In 2020, about 16.000 beam time hours were delivered for about 130 proposals from users of more than 20 countries worldwide performing experiments at IBC or using the capabilities for ion beam services.

The IBC has provided ion beam technology as a user and competence center for ion beam applications for more than 30 years. With respect to user beam time hours, the IBC is internationally leading, and has been supported by numerous national and European grants, and by industry.

The research activities cover both ion beam modification and ion beam analysis (IBA).

The operation of IBC is accompanied by a strong in-house research at the affiliated host “Institute of Ion Beam Physics and Materials Research”, both in experiment and theory. Furthermore, the IBC strongly supports the commercial exploitation of ion beam technology of partners from industry, which is essential for materials science applications. For ion beam services, the HZDR Innovation GmbH (spin-off of the HZDR) – www.hzdr-innovation.de – provides a direct and fast access to the IBC facilities based on individual contracts.

Recently, new ion beam tools and end stations have been commissioned which will attract new users by state-of-the-art experimental instrumentation. In a new end station for Rutherford-backscattering spectrometry, solid-liquid interfaces can now be investigated in-situ in an electro-chemical cell. An ion microscope *ORION NanoFab* (He/Ne ions, 10 – 40 keV) provides unique

possibilities for surface imaging, nano-fabrication, and for the first time, elemental analysis based on ion beam techniques. The cluster tool at the 6 MV accelerator allows *in-situ* deposition and analysis investigations at temperatures of up to 800 °C. Medium-energy ion scattering (MEIS) is now available for investigation of elemental compositions and depth profiles of ultra-thin layers at the new 100 kV accelerator.

IBC activities are efficiently integrated into various Helmholtz programmes within the research field “Matter”, but also in the Helmholtz cross-programme activities “Mineral Resources”, “Materials Research for Energy Technologies”, and “Helmholtz Energy Materials Foundry”. Since 2013, the IBC has been recognized as a large-scale facility within the “BMBF Verbundforschung” promoting long-term collaborations with universities. In addition, as of 2019 the IBC is coordinating the EU Integrated Infrastructure Initiative (I3) project RADIATE, which provides trans-national access to the largest ion beam centers in Europe (www.ionbeamcenters.eu).

Following the rules of a European and national user facility, access for scientific experiments to IBC is provided on the basis of a proposal procedure (www.hzdr.de/IBC) via the common HZDR user facility portal **HZDR-GATE** (gate.hzdr.de), and for RADIATE via www.ionbeamcenters.eu. IBC users from EU countries are eligible to receive support through the RADIATE initiative. Due to the availability of multiple machines and versatile instrumentation, IBC proposals can be submitted continuously. The scientific quality of the proposals is evaluated and ranked by an external international User Selection Panel. For successfully evaluated proposals, users get free access to IBC facilities for their experiments. The use of the IBC facilities includes the scientific and technical support during planning, execution and evaluation of the experiments. For AMS samples preparation, two chemistry laboratories are available.

For more detailed information, please contact Dr. Stefan Facsko (s.facsko@hzdr.de) or Dr. Rene Heller (r.heller@hzdr.de), and visit the IBC webpage: www.hzdr.de/IBC.

Free Electron Laser FELBE

FELBE is an acronym for the free-electron laser (FEL) at the Electron Linear accelerator with high Brilliance and low Emittance (ELBE) located at the Helmholtz-Zentrum Dresden-Rossendorf. The heart of ELBE is a superconducting linear accelerator operating in continuous-wave (cw) mode with a pulse repetition rate of 13 MHz. The electron beam (40 MeV, 1 mA max.) is guided to several laboratories where secondary beams (particle and electromagnetic) are generated. Two free-electron lasers (U37-FEL and U100-FEL) produce intense, coherent electromagnetic radiation in the mid and far infrared, which is tunable over a wide wavelength range (5 –250 µm) by changing the electron energy or the undulator magnetic field. Main parameters of the infrared radiation produced by FELBE are as follows:

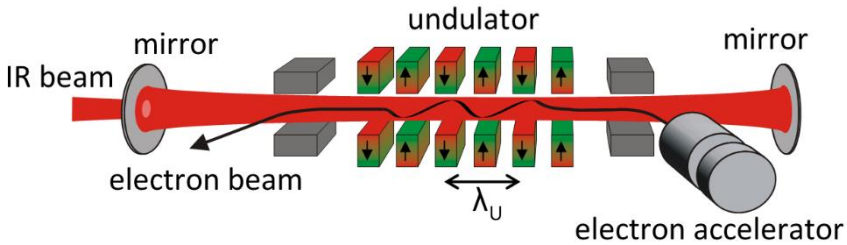

Wavelength λ	5 – 40 µm 18 – 250 µm	FEL with undulator U37 FEL with undulator U100
Pulse energy	0.01 – 2 µJ	depends on wavelength
Pulse length	1 – 25 ps	depends on wavelength
Repetition rate	13 MHz	3 modes: • cw • macropulsed (> 100 µs, < 25 Hz) • single pulsed (Hz … kHz)

In addition, there is the THz beamline TELBE that is run by the Institute of Radiation Physics. TELBE delivers high-power pulses (up to 10 µJ) in the low THz range (0.1 to 1.5 THz) at a repetition rate of 100 kHz. ELBE is a user facility and applications for beam time can be submitted twice a year, typically by April 15 and October 15. FELBE and TELBE users from EU countries are eligible to receive support through the HORIZON 2020 Integrated Infrastructure Initiative (I3) CALIPSOplus (**C**onvenient **A**ccess to **Li**ght Sources O**p**en to Innovation, **S**cience and to the W**o**rld) which started in May 2017.

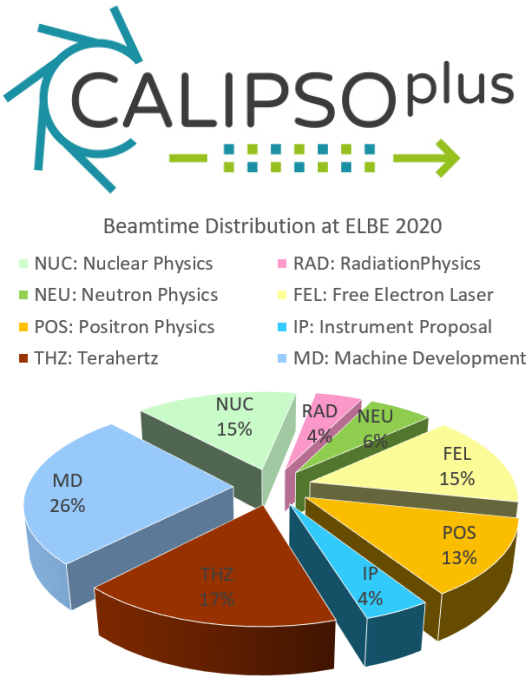

Typical applications are picosecond pump-probe spectroscopy (also in combination with several other femtosecond lasers, which are synchronized to the FEL), near-field microscopy, and nonlinear optics. The FELBE facility also serves as a far-infrared source for experiments at the Dresden High Magnetic Field Laboratory (HLD) involving pulsed magnetic fields up to 70 T.

The statistics shows that the FEL used about 800 hours beam time of the ELBE accelerator. This corresponds to 15 % of total beam time, which is again distributed among internal and external users.

For further information, please contact Prof. Manfred Helm (m.helm@hzdr.de) or visit the FELBE webpage www.hzdr.de/FELBE.

Experimental equipment

Accelerators, ion implanters, and other ion processing tools

Van de Graaff Accelerator (VdG)	2 MV	*TuR Dresden, DE*
Tandetron Accelerator (T1)	3 MV	*HVEE, NL*
Tandetron Accelerator (T2)	6 MV	*HVEE, NL*
Low-Energy Ion Implanter	0.1 – 40 kV	*Danfysik, DK*
Low-Energy Ion Platform	20 – 130 kV	*HVEE, NL*
High-Energy Ion Implanter	20 – 500 kV	*HVEE, NL*
Mass-Separated Focused Ion Beam (FIB) (15 nm, variable ions, Laser stage)	10 – 30 keV >10 A/cm^2	*Orsay Physics, FR*
Mass-Separated Focused Ion Beam (FIB) (variable ions, UHV, Lithography)	10 – 30 keV >10 A/cm^2	*Orsay Physics, FR*
ORION NanoFab HIM (including GIS, Nanopatterning, TOF-SIMS, µ-manipulators and heater)	He, Ne ions, 10 – 35 kV, Resolution ~ 0.5/1.8 nm	*Carl Zeiss Microscopy, DE*
ORION PLUS HIM modified for STIM	He ions, 10 - 35 kV, Resolution 0.35 nm	*Carl Zeiss Microscopy, DE*
Highly-Charged Ion Facility	25 eV – 6 keV × Q Q = 1 … 40 (Xe)	*DREEBIT, DE; PREVAC, PL*
Surface Modifications by Low-Energy Ion Irradiation	200 – 1200 eV	*Home-built*
UHV Ion Irradiation (Ar, He, etc.)	0 – 5 kV Scan 10 × 10 mm^2	*Cremer, DE; VG, USA*

Ion beam analysis (IBA)

A wide variety of advanced IBA techniques are available at the MV accelerators (see figure).

RBS	Rutherford Backscattering Spectrometry	(A1), (A2), (5), (9), (11), (14)	*VdG, T1, T2, HIM*
RBS/C	RBS – Channeling	(A1)	*VdG*
Liquid-RBS	Liquid Rutherford Backscattering Spectrometry	(A2)	*VdG*
MEIS	Medium Energy Ion Scattering	MEIS	
ERDA	Elastic Recoil Detection Analysis	(2), (9)	*T2*
PIXE	Particle-Induced X-ray Emission	(A1), (A2), (5), (14)	*VdG, T1, T2*
PIGE	Particle-Induced gamma Emission	(5), (14)	*T1, T2*
NRA	Nuclear Reaction Analysis	(1), (14)	*T1, T2*
NMP	Nuclear Microprobe	(14)	*T1*
AMS	Accelerator Mass Spectrometry (focused to long-lived radionuclides: ^{7}Be, ^{10}Be, ^{26}Al, ^{36}Cl, ^{41}Ca, ^{129}I)	(B2)	*T2*

Some stations are equipped with additional process facilities enabling *in-situ* IBA investigations during ion irradiation, sputtering, deposition, annealing, investigations at solid-liquid interfaces, etc.

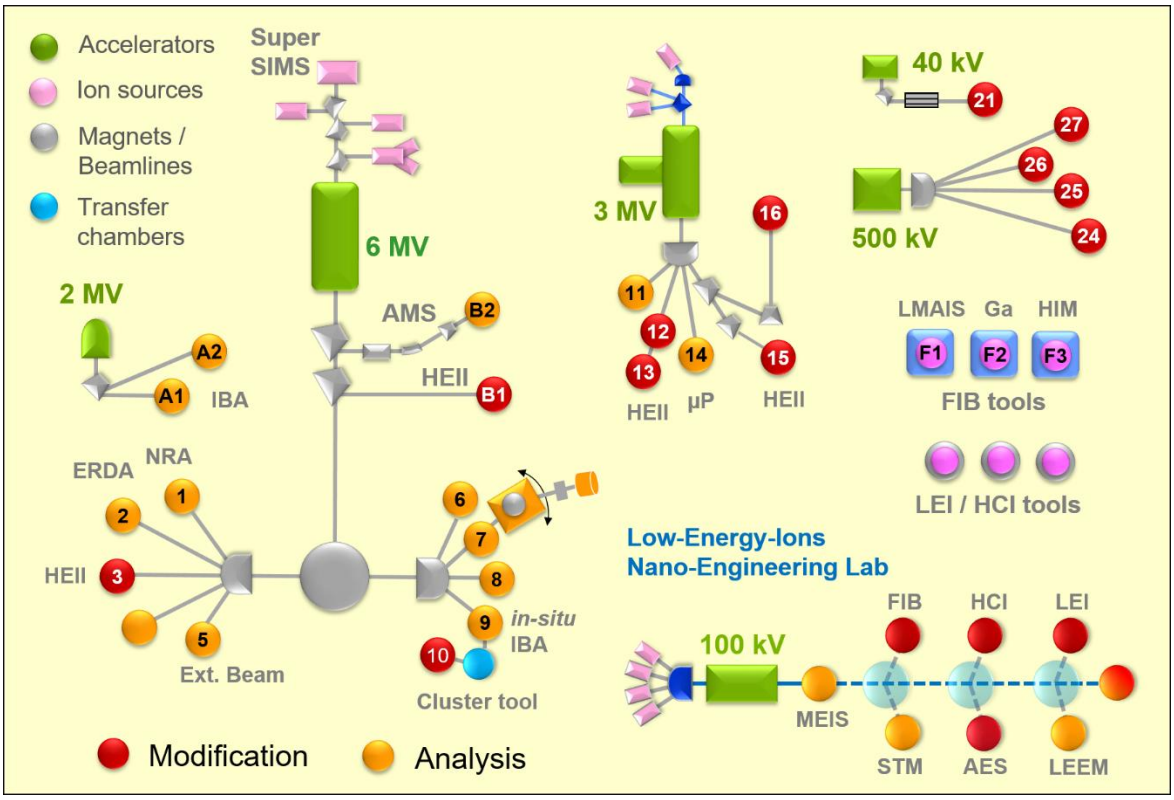

Schematic overview of the HZDR Ion Beam Center

Other particle-based analytical techniques

SEM	Scanning Electron Microscope (S4800 II)	1 – 30 keV + EDX	*Hitachi, JP*
TEM	Transmission Electron Microscope (Titan 80-300 with Image Corrector)	80 – 300 keV + EDX, EELS	*FEI, NL*
TEM	Transmission Electron Microscope (Talos F200X)	20 – 200 keV + SuperX EDX	*FEI, NL*
FIB/SEM	Focused Ion/Electron Cross Beam (NVision 40)	1 – 30 keV + EDX, EBSD	*Carl Zeiss Microscopy, DE*
FIB/SEM	Focused Ion/Electron Instrument (Helios 5 CX DualBeam)	0.5 – 30 keV	*Thermo Fisher Sci. - FEI, US*
AES	Auger Electron Spectroscopy	+ SAM, SEM, XPS, EDX, CL	*Scienta Omicron, DE*
LEEM	Low-Energy Electron Microscope (Spec-LEEM-III)	0 eV – 4.5 keV Resolution < 6 nm + AES	*Elmitec, DE*

Photon-based analytical techniques

XRD/XRR	X-Ray Diffractometers	Cu-Kα	
	θ-θ Powder D8 θ-2θ 4-Circle D5005 θ-θ 4-Circle Empyrean θ-2θ 4+2-Circle SEIFERT XRD3003-HR θ-θ Smart Lab 3kW		*Bruker, DE* *Siemens, DE* *PANalytical, NL* *General Electric, US* *Rigaku, JP*
SE	Angle Dependent Spectroscopic Ellipsometry	250 – 1700 nm	*Woollam, US*
UV-Vis	Solid Spec 3700 DUV	190 – 3300 nm	*Shimadzu, JP*
FTIR	Fourier-Transform Infrared Spectrometer	50 – 15000 cm^{-1}	*Bruker, DE*
	Ti:Sapphire Femtosecond Laser	78 MHz	*Spectra Physics, US*
	Femtosecond Optical Parametric Osci.		*APE, DE*
	Ti:Sapphire Femtosecond Amplifier	1 kHz, 250 kHz	*Coherent, US*
	Femtosecond Optical Parametric Amplifier		*Light Conversion, LT*
THz-TDS	Terahertz Time-Domain Spectroscopy	0.1 – 4 THz	*Home-built*
Raman	Raman Spectroscopy	> 10 cm^{-1}	*Jobin-Yvon-Horiba, FR*
	In-situ Raman Spectroscopy	> 100 cm^{-1}	*Jobin-Yvon-Horiba, FR*
PL	Photoluminescence (10 – 300 K)	405 – 1550 nm	*Jobin-Yvon-Horiba, FR*
	Micro-Photoluminescence	< 0.5 µm	*Jobin-Yvon-Horiba, FR*
TRPL	Time-Resolved Photoluminescence	τ = 3 ps – 2 ns τ > 5 ns	*Hamamatsu Phot., JP* *Stanford Res., US*
EL	Electroluminescence	300 – 1600 nm	*Jobin-Yvon-Horiba, FR*
	Optical Split-Coil Supercond. Magnet	7 T	*Oxford Instr., UK*
PR	Photomodulated Reflectivity	300 – 1600 nm	*Jobin-Yvon-Horiba, FR*
PLE	Photoluminescence Excitation	300 – 1600 nm	*Jobin-Yvon-Horiba, FR*
OES	Optical Emission Spectroscopy	250 – 800 nm	*Jobin-Yvon-Horiba, FR*
Confocal	Confocal scanning photoluminescence microscope	~1 µm resol. 5 – 300 K	*Attocube, DE*
SSPD	Superconducting single photon detectors	800 – 1500 nm	*Single Quantum, NL*

Magnetic thin film analysis

MFM	Magnetic Force Microscope	~ 50 nm resol.	*VEECO; DI, US*
AFM/MFM	Magnetic Force Microscope	~ 50 nm resol.	*BRUKER ICON tool, US*
SQUID VSM	Vibrating Sample Magnetometer	± 7 T	*Quantum Design, US*
Vector-VSM	Vibrating Sample Magnetometer	± 2 T	*Microsense, US*
MOKE	Magneto-Optic Kerr Effect (in-plane)	± 0.35 T	*Home-built*
MOKE	Magneto-Optic Kerr Effect (perpend.)	± 2 T	*Home-built*
FR-MOKE	Frequency-Resolved Magneto-Optic KE	± 1.1 T	*Home-built*
SKM	Scanning Kerr Microscope		*Home-built*
	Kerr Microscope		*Evico Magnetics, DE*
VNA-FMR	Vector Network Analyzer Ferromagnetic Resonance	50 GHz	*Agilent, DE; Home-built*
Cryo-FMR	Variable-Temperature Ferromagnetic Resonance	3 – 300 K	*Attocube, DE; Home-built*
ME	Magnetoellipsometer		*LOT, DE; AMAC, US*
µBLS	Brillouin Light Scattering Microscope	± 0.8 T, 491 & 532 nm	*Home-built*
SKM	Scanning Kerr Microscope with RF Detection (Spectrum Analyzer)	± 0.5 T, 40 GHz	*Home-built*
MT-50G	High Frequency Magneto-Transport Setup	± 1.5 T, 50 GHz 250 ps	*Home-built*

Other analytical and measuring techniques

STM/AFM	UHV Scanning Probe Microscope (variable T)		*Omicron, DE*
AFM	Atomic Force Microscope (Contact, Tapping, Spreading)		*Bruker, US*
AFM	Atomic Force Microscope (with c-AFM, SCM-Module)		*Bruker, US*
	Dektak Surface Profilometer		*Bruker, US*
	Micro Indenter/Scratch Tester		*Shimatsu, JP*
MPMS	Mechanical Properties Measurement System – Stretcher		*Home-built*
MS	Mass Spectrometers (EQP-300, HPR-30)		*HIDEN, UK*
	Wear Tester (pin-on disc)		*Home-built*
LP	Automated Langmuir Probe		*Impedans, IE*
HMS	Hall Measurement System	2 – 400 K, ≤ 9 T	*LakeShore, US*
	Van-der-Pauw HMS Ecopia	LNT & 300 K, 0.5 T	*Bridge Technol., US*
MTD	Magneto-Transport Device	300 K, ≤ 3 T	*Home-built*
RS	Sheet-Rho-Scanner		*AIT, KR*
Redmag	Redmag Tensormeter System	280 – 350 K, 2.5 T	*Home-built*
Greymag	Greymag Tensormeter System	300 K, 0.7 T (360°)	*Home-built*
Greenmag	Tensormeter System (TMCS)	30 – 320 K,	*Tensor Instruments*

		1.3 T (360°)	*(HZDR Inno), DE*
SEM	Scanning Electron Microscope (Phenom XL)	5 – 15 keV + EDS	*Thermo Fisher Sci., US*
IV / CV	I-V and C-V Semi-Automatic Prober	-60 – 300 °C	*Süss, DE; Keithley, US*
IV / CV	I-V and C-V Analyzer		*Keithley, US*
GC	Gas Chromatography (GC-2010)		*Shimadzu, JP*
ECW	Electrochemical workstation (CHI 760e)		*CH instruments, US*
FDA	Force-displacement analysis machine		*Sauter, DE*
IV / VNA	I-V and VNA Prober for VHF, LCR and frequency analysis measurements	20 – 120 MHz	*Süss, DE; Cascade, US; Keysight, US*
OSCI	4-channel real time oscilloscope	1.5 GHz (BW), 5 GSa/s	*Keysight, US*
IR-Cam	TrueIR Thermal Imager	-20 – 350 °C	*Keysight, US*
CM	Confocal Microscope (Smartproof 5)	405 nm LED, z drive res. ~ 1 nm	*Carl Zeiss, DE*
FAS	Fluidic Analytic Setup – microscope, high speed camera, and fluidic pumps	2 GB 120 kfps, 5 modules	*Zeiss, DE; Photron, US; Cetoni, DE*

Deposition and processing techniques

Physical Deposition	2x DC / 2x RF Magnetron Sputter System, up to 4x 6” substrates	*Nordiko, UK*
	Thermal (2 sources) / Electron Beam (12 pockets) Evaporation System	*CREAVAC, DE*
	Thermal Evaporation	*Bal-Tec, LI*
	Thermal (1 source) / Electron Beam (7 pockets) Evaporation System	*BESTEC, DE*
	DC/RF Magnetron Sputter System, 4x 3’’ + 4x 2’’ magnetrons, substrate heating: RT – 950 °C, up to 4” wafers	*BESTEC, DE*
	DC/RF Magnetron Sputter System, 6x 2’’ confocal magnetrons, substrate heating: RT – 650 °C, up to 3” wafers	*AJA International, US*
	Dual Ion Beam Sputtering (IBAD), 6" targets, RT – 500 °C	*Home-built*
	High Power Impulse Magnetron Sputtering	*Melec, DE*
	Magnetron Sputter System (2 targets)	*Home-built*
PLD	Pulsed Laser Deposition	*SURFACE, DE*
Molecular Beam Epitaxy	III-V Semiconductors	*Riber, FR*
	Metals	*CreaTec Fischer, DE*
Chemical Vapor Deposition	Plasma Enhanced CVD: a-Si, a-Ge, SiO_2, SiON, Si_3N_4	*Oxford Instr., UK*
Atomic Layer Deposition	Al_2O_3, HfO_2, SiO_2, ZnO	*Ultratech, US*
Dry Etching	ICP-RIE, ∅ 6”: CF_4, SF_6, C_4F_8 with interferometric etch-stop monitor	*Sentech, DE*
	RIBE, ∅ 6”: Ar, CF_4 with SIMS etch-stop monitor	*Roth & Rau, DE*

	Barrel reactor, ∅ 4”: O_2, Ar	*Diener electronic, DE*
Etching/Cleaning	incl. Anisotropic Selective KOH Etching, Metal-Assisted Chemical Etching, Photoelectrochemical Etching	
Photolithography	Mask-Aligner MA6, ∅ 6”, < 2 µm accuracy; with two-side alignment	*Süss, DE*
	Direct Laser Writer DWL 66FS, ∅ 8”x8”, 2 µm accuracy	*Heidelberg Instr., DE*
	Laser Micro Writer ML, 10 µm accuracy	*Durham Magneto Optics, UK*
Electron Beam Lithography	Raith 150-TWO: ∅ 6”, 10 nm resolution	*Raith, DE*
	e-Line Plus: ∅ 4”, 10 nm resolution	*Raith, DE*
Thermal Treatment	Room Temperature – 2000 °C	
Oxidation and annealing furnace		*INNOTHERM, DE*
Rapid Thermal Annealing JETFIRST 100		*JIPELEC, FR*
Rapid Thermal Annealing AW 610		*Allwin21, USA*
Flash-Lamp Units (0.5 – 20 ms)		*Home-built; FHR/DTF, DE*
Combined Flash Lamp Sputter Tool (Magnetron sputtering plus flash lamp annealing 0.3 – 3 ms, up to 10 Hz)		*ROVAK GmbH, DE*
RF Heating (Vacuum)		*JIPELEC, FR*
Laser Annealing (CW, 808 nm, 450 W)		*LIMO, DE*
Laser Annealing (30 ns pulse,10 Hz, 308 nm, 500 mJ)		*COHERENT, USA*
CVD Tube furnace (RT– 1200 ^{o}C, three channel gas)		*NBD, CN*
Vacuum oven (RT – 250 ^{o}C, Vacuum < 133 Pa)		*LAB-KITS, CN*
Vacuum oven (RT – 800 ^{o}C, Vacuum < 10^{-7} mbar)		*Home-built*
Bonding Techniques	Ultrasonic Wire Bonding	*Kulicke & Soffa, US*
	Semi-automatic Wire-bonder: Gold-ball and wedge-wedge bonding Ultrasonic generator: 60 kHz, 140 kHz Wire deformation control software	*F & S Bondtec, AT*
Cutting, Grinding, Polishing		*Bühler, DE*
TEM Sample Preparation	Plan View and Cross Section incl. Ion Milling Equipment	*Gatan, US*
SEM / HIM Sample Preparation	Mechanical milling, sawing, grinding, polishing	*Leica, AUT*
	Argon cross-section milling, surface polishing	*Hitachi, JP*
Disperse and mixer	Mixer for pastes and emulsions	*IKA, DE*
Centrifuge	Max. 17850 rpm, -10 – 40 °C	*Thermo Scientific, US*

Doctoral training programme

International Helmholtz Research School NANONET

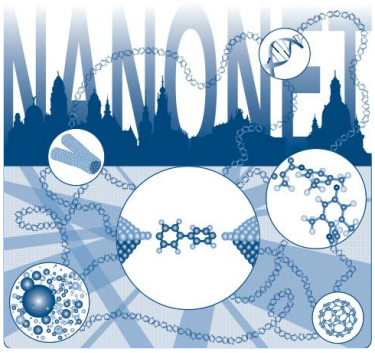

The Institute of Ion Beam Physics and Materials Research is coordinating the International Helmholtz Research School for Nanoelectronic Networks (IHRS NANONET) supported by the Initiative and Networking Fund of the Helmholtz Association. The project started in October 2012. The total funding is 1.2 Mio. € for a period of 8 years.

The IHRS NANONET is an international, interdisciplinary and thematically focused doctoral programme in the field of molecular electronics. The research school aims at attracting and promoting excellence by educating promising doctoral candidates with backgrounds in physics, chemistry, materials science and electrical engineering. During a period of three years, PhD candidates benefit from well-structured, comprehensive training curricula and multiple mentorship, while performing cutting edge research projects within one of the 15 NANONET research groups. The doctoral candidates have the unique opportunity to contribute to the advancement of molecular electronics by developing strategies for the integration of single nano-sized building blocks into large interconnected networks.

The IHRS NANONET fosters not only professional qualification but also personal development by equipping young graduates with competencies for successful careers in a wide variety of positions in academia and industry. The NANONET Annual Workshop was held in Oberbärenburg/Altenberg just inbetween the first and second Corona waves and was attended by 32 participants of 9 nationalities.

Five senior students concluded their PhD degrees in 2020: Congratulations to Dr. Wenbo Sheng, Dr. Seddigheh Nikipar, Dr. Yuriy Aleksandrov, Dr. Himani Arora (all at TU Dresden), and Dr. Türkan Bayrak Kelling at Univ Leipzig.

The consortium

- Helmholtz-Zentrum Dresden-Rossendorf (HZDR)
- Technische Universität (TU) Dresden
- Leibniz Institute of Polymer Research (IPF) Dresden
- Fraunhofer Institute for Ceramic Technologies and Systems (IKTS) Dresden
- Nanoelectronic Materials Laboratory (NaMLab) gGmbH Dresden

For further information, please contact the NANONET coordinator, Dr. Peter Zahn (nanonet@hzdr.de), or visit the IHRS NANONET website: www.hzdr.de/nanonet.

Publications and patents

Books and chapters

1. Bali, R.
Ferromagnetism in B2-Ordered Alloys Induced via Lattice Defects
in Ling, F.C.-C.; Zhou, S.; Kuznetsov, A. (eds.): Defects in Functional Materials, Hong Kong: World Scientific Publishing Co. (2020), ISBN: 978-981-120-316-9, pp. 201-239

2. Hafarov, A.; Prokopenko, O.; Sidorenko, S.; Makarov, D.; Vladymyrskyi, I.
$L1_0$ Ordered Thin Films for Spintronic and Permanent Magnet Applications
in Kaidatzis, A.; Sidorenko, S.; Vladymyrskyi, I.; Niarchos, D. (eds.): Modern Magnetic and Spintronic Materials. NATO Science for Peace and Security Series B: Physics and Biophysics, Dordrecht: Springer (2020), ISBN: 978-94-024-2033-3, pp. 73-94

3. Jeanneret, P.; Moreiras, S.M.; Merchel, S.; Gärtner, A.; Binnie, S.; Orgeira, M.J.; Aumaître, G.; Bourlès, D.; Keddadouche, K.
Novel cosmogenic datings in landslide deposits, San Juan, Argentina
in: Understanding and Reducing Landslide Disaster Risk. WLF 2020. ICL Contribution to Landslide Disaster Risk Reduction, Cham: Springer (2020), pp. 361-370

4. Ling, F.C.-C.; Zhou, S.; Kuznetsov, A. (eds.)
Defects in Functional Materials
Singapore: World Scientific Publishing Co. (2020), ISBN: 978-981-120-316-9

5. Tauchnitz, T.
Novel Methods for Controlled Self-Catalyzed Growth of GaAs Nanowires and GaAs/ Al_xGa_{1-x} As Axial Nanowire Heterostructures on Si Substrates by Molecular Beam Epitaxy
Wissenschaftlich-Technische Berichte HZDR-108, Helmholtz-Zentrum Dresden-Rossendorf (2020), ISSN: 2191-8708, eISSN: 2191-8716

Publications in journals

1. Ajayakumar, M.; Fu, Y.; Liu, F.; Komber, H.; Tkachova, V.; Xu, C.; Zhou, S.; Popov, A.; Liu, J.; Feng, X.
Tailoring Magnetic Features in Zigzag-Edged Nanographenes by Controlled Diels–Alder Reactions
Chemistry - A European Journal **26**, 7497 (2020)

2. Almotasem, A.T.; Posselt, M.; Polcar, T.
Deformation behavior of nanocrystalline body-centered cubic iron with segregated, foreign interstitial: A molecular dynamics study
Materials **13**, 5351 (2020)

3. Andany, S.H.; Hlawacek, G.; Hummel, S.; Brillard, C.; Kangül, M.; Fantner, G.E.
An atomic force microscope integrated with a helium ion microscope for correlative nanocharacterization
Beilstein Journal of Nanotechnology **11**, 1272 (2020)

4. Arora, H.; Dong, R.; Venanzi, T.; Zscharschuch, J.; Schneider, H.; Helm, M.; Feng, X.; Cánovas, E.; Erbe, A.
Demonstration of a Broadband Photodetector Based on a Two-Dimensional Metal-Organic Framework
Advanced Materials **32**, 16644666 (2020)

5. Arora, H.; Park, S.; Dong, R.; Erbe, A.
2D MOFs: A New Platform for Optics?
Optics and Photonics News **31**, 36 (2020)

6. Awari, N.; Semisalova, A.; Deinert, J.-C.; Lenz, K.; Lindner, J.; Fullerton, E.; Uhlir, V.; Li, J.; Clemens, B.; Carley, R.; Scherz, A.; Kovalev, S.; Gensch, M.
Monitoring laser-induced magnetization in FeRh by transient terahertz emission spectroscopy
Applied Physics Letters **117**, 122407 (2020)

7. Baek, E.; Ranjan Das, N.; Vittorio Cannistraci, C.; Rim, T.; Cañón Bermúdez, G.S.; Nych, K.; Cho, H.; Kim, K.; Baek, C.-K.; Makarov, D.; Tetzlaff, R.; Chua, L.; Baraban, L.; Cuniberti, G.
Intrinsic plasticity of silicon nanowire neurotransistors for dynamic memory and learning functions
Nature Electronics **3**, 398 (2020)

8. Begeza, V.; Mehner, E.; Stöcker, H.; Xie, Y.; García, A.; Hübner, R.; Erb, D.; Zhou, S.; Rebohle, L.
Formation of Thin NiGe Films by Magnetron Sputtering and Flash Lamp Annealing
Nanomaterials **10**, 648 (2020)

9. Bergmann, U.; Apelt, S.; Khojasteh, N.B.; Heller, R.
Solid–liquid interface analysis with in-situ Rutherford backscattering and electrochemical impedance spectroscopy
Surface and Interface Analysis **52**, 1111 (2020)

10. Bischoff, L.; Klingner, N.; Mazarov, P.; Pilz, W.; Meyer, F.
Boron Liquid Metal Alloy Ion Sources for Special FIB Applications
Journal of Vacuum Science & Technology B **38**, 042801 (2020)

11. Bishnupad, M.; Wei, Y.; Ghorbani Asl, M.; Krasheninnikov, A.; Parasmani, R.; Bikash, K.J.
Revealing the defect-dominated oxygen evolution activity of hematene
Journal of Materials Chemistry A **8**, 6709 (2020)

12. Blaschke, D.; Munnik, F.; Grenzer, J.; Rebohle, L.; Zahn, P.; Schmidt, H.; Gemming, S.
A correlation study of layer growth rate, thickness uniformity, stoichiometry, and hydrogen impurity level of ALD grown HfO_2 thin films
Applied Surface Science **506**, 144188 (2020)

13. Bommanaboyena, S.P.; Bergfeldt, T.; Heller, R.; Kläui, M.; Jourdan, M.
High quality epitaxial Mn_2Au (001) thin films grown by molecular beam epitaxy
Journal of Applied Physics **127**, 243901 (2020)

14. Cajzl, J.; Jeníčková, K.; Nekvindová, P.; Michalcová, A.; Veselý, M.; Macková, A.; Malinský, P.; Jágerová, A.; Mikšová, R.; Akhmadaliev, S.
Creation of Gold Nanoparticles in ZnO by Ion Implantation–DFT and Experimental Studies
Nanomaterials **10**, 2392 (2020)

15. Cajzl, J.; Nekvindova, P.; Jeníčková, K.; Jagerová, A.; Malinský, P.; Remeš, Z.; Neykova, N.; Chang, Y.-Y.; Oswald, J.; Kentsch, U.; Macková, A.
Erbium-ion implantation of single- and nano-crystalline ZnO
Nuclear Instruments and Methods in Physics Research B **464**, 65 (2020)

16. Chen, C.; Lu, Q.; Akhmadaliev, S.; Zhou, S.
Diamond-blade diced trapezoidal ridge waveguides in YCOB crystal for second harmonic generation
Optics and Laser Technology **126**, 106128 (2020)

17. Chepkasov, I.; Ghorbani Asl, M.; Zakhar, I.P.; Jurgen, H.S.; Krasheninnikov, A.
Alkali metals inside bi-layer graphene and MoS_2: insights from first-principles calculations
Nano Energy **75**, 104927 (2020)

18. Ciano, C.; Persichetti, L.; Montanari, M.; Di Gaspare, L.; Capellini, G.; Baldassarre, L.; Ortolani, M.; Pashkin, O.; Helm, M.; Winnerl, S.; Virgilio, M.; de Seta, M.
Electron-phonon coupling in n-type Ge two-dimensional systems
Physical Review B **102**, 205302 (2020)

19. Ciano, C.; Virgilio, M.; Bagolini, L.; Baldassarre, L.; Pashkin, O.; Helm, M.; Montanari, M.; Persichetti, L.; Di Gaspare, L.; Capellini, G.; Paul, D.J.; Scalari, G.; Faist, J.; de Seta, M.; Ortolani, M.
Terahertz absorption-saturation and emission from electron-doped germanium quantum wells
Optics Express **28**, 7245 (2020)

20. Ciano, C.; Virgilio, M.; Bagolini, L.; Baldassarre, L.; Rossetti, A.; Pashkin, O.; Helm, M.; Montanari, M.; Persichetti, L.; Di Gaspare, L.; Capellini, G.; Paul, D.J.; Scalari, G.; Faist, J.; de Seta, M.; Ortolani, M.
Electron Population Dynamics in Optically Pumped Asymmetric Coupled Ge/SiGe Quantum Wells: Experiments and Models
Photonics **7**, 2 (2020)

21. Ciesielski, K.; Synoradzki, K.; Veremchuk, I.; Skokowski, P.; Szymanski, D.; Grin, Y.; Kaczorowski, D.
Thermoelectric Performance of the Half-Heusler Phases RNiSb (R = Sc, Dy, Er, Tm, Lu): High Mobility Ratio between Majority and Minority Charge Carriers
Physical Review Applied **14**, 054046 (2020)

22. Creutzburg, S.; Schwestka, J.; Niggas, A.; Inani, H.; Tripathi, M.; George, A.; Heller, R.; Kozubek, R.; Madauß, L.; Facsko, S.; Kotakoski, J.; Schleberger, M.; Turchanin, A.; Grande, P.L.; Aumayr, F.; Wilhelm, R.A.
Vanishing influence of the band gap on charge exchange of slow highly charged ions in freestanding single layer MoS_2
Physical Review B **102**, 045408 (2020)

23. Cutroneo, M.; Torrisi, L.; Badziak, J.; Rosinski, M.; Torrisi, A.; Fazio, M.; Sofer, Z.E.; Böttger, R.; Akhmadaliev, S.
Hybrid graphene-based material promising target in laser matter interaction
Journal of Instrumentation **15**, C01021 (2020)

24. Darbandy, G.; Dollinger, F.; Formánek, P.; Hübner, R.; Resch, S.; Roemer, C.; Fischer, A.; Leo, K.; Kloes, A.; Kleemann, H.
Unraveling Structure and Device Operation of Organic Permeable Base Transistors
Advanced Electronic Materials **6**, 2000230 (2020)

25. Das, A.; Chekhonin, P.; Altstadt, E.; Bergner, F.; Heintze, C.; Lindau, R.
Microstructural characterization of inhomogeneity in 9Cr ODS EUROFER steel
Journal of Nuclear Materials **533**, 152083 (2020)

26. Das, A.; Chekhonin, P.; Altstadt, E.; McClintock, D.; Bergner, F.; Heintze, C.; Lindau, R.
Microstructure and fracture toughness characterization of three 9Cr ODS EUROFER steels with different thermo-mechanical treatments
Journal of Nuclear Materials **542**, 152464 (2020)

27. Deng, T.; Xing, T.; Brod, M.K.; Sheng, Y.; Qiu, P.; Veremchuk, I.; Song, Q.; Wei, T.-R.; Yang, J.; Snyder, G.J.; Grin, Y.; Chen, L.; Shi, X.
Discovery of high-performance thermoelectric copper chalcogenide using modified diffusion-couple high-throughput synthesis and automated histogram analysis technique
Energy & Environmental Science **13**, 3041 (2020)

28. Dieny, B.; Prejbeanu, I.L.; Garello, K.; Gambardella, P.; Freitas, P.; Lehndorff, R.; Raberg, W.; Ebels, U.; Demokritov, S.O.; Akerman, J.; Deac, A.; Pirro, P.; Adelmann, C.; Anane, A.; Chumak, A.V.; Hiroata, A.; Mangin, S.; Cengiz Onbaşlı, M.; D'Aquino, M.; Prenat, G.; Finocchio, G.; Lopez Diaz, L.; Chantrell, R.; Chubykalo-Fesenko, O.; Bortolotti, P.
Opportunities and challenges for spintronics in the microelectronic industry
Nature Electronics **3**, 446 (2020)

29. Dobroserdova, A.B.; Sanchez Romero, P.A.; Shapochkin, V.E.; Smagin, D.A.; Zverev, V.S.; Odenbach, S.; Kantorovich, S.S.
Measuring FORCs diagrams in computer simulations as a mean to gain microscopic insight
Journal of Magnetism and Magnetic Materials **501**, 166393 (2020)

30. Du, G.; Zhou, X.; Pang, C.; Zhang, K.; Zhao, Y.; Lu, G.; Liu, F.; Wu, A.; Akhmadaliev, S.; Zhou, S.; Chen, F.
Efficient Modulation of Photonic Bandgap and Defect Modes in All-Dielectric Photonic Crystals by Energetic Ion Beams
Advanced Optical Materials **8**, 2000426 (2020)

31. Du, R.; Jin, W.; Hübner, R.; Zhou, L.; Hu, Y.; Eychmüller, A.
Engineering Multimetallic Aerogels for pH-Universal HER and ORR Electrocatalysis
Advanced Energy Materials **10**, 1903857 (2020)

32. Du, R.; Jin, X.; Hübner, R.; Fan, X.; Hu, Y.; Eychmüller, A.
Engineering Self-Supported Noble Metal Foams Toward Electrocatalysis and Beyond
Advanced Energy Materials **10**, 1901945 (2020)

33. Du, R.; Joswig, J.-O.; Fan, X.; Hübner, R.; Spittel, D.; Hu, Y.; Eychmüller, A.
Disturbance-Promoted Unconventional and Rapid Fabrication of Self-Healable Noble Metal Gels for (Photo-)Electrocatalysis
Matter **2**, 908 (2020)

34. Du, R.; Joswig, J.-O.; Hübner, R.; Zhou, L.; Wei, W.; Hu, Y.; Eychmüller, A.
Freeze–Thaw-Promoted Fabrication of Clean and Hierarchically Structured Noble-Metal Aerogels for Electrocatalysis and Photoelectrocatalysis
Angewandte Chemie - International Edition **59**, 8293 (2020)

35. Du, R.; Wang, J.; Wang, Y.; Hübner, R.; Fan, X.; Senkovska, I.; Hu, Y.; Kaskel, S.; Eychmüller, A.
Unveiling reductant chemistry in fabricating noble metal aerogels for superior oxygen evolution and ethanol oxidation
Nature Communications **11**, 1590 (2020)

36. Dubale, A.A.; Zheng, Y.; Wang, H.; Hübner, R.; Li, Y.; Yang, J.; Zhang, J.; Sethi, N.K.; He, L.; Zheng, Z.; Liu, W.
High-Performance Bismuth-Doped Nickel Aerogel Electrocatalyst for the Methanol Oxidation Reaction
Angewandte Chemie - International Edition **59**, 13891 (2020)

37. Dubs, C.; Surzhenko, O.; Thomas, R.; Osten, J.; Schneider, T.; Lenz, K.; Grenzer, J.; Hübner, R.; Wendler, E.
Low damping and microstructural perfection of sub-40nm-thin yttrium iron garnet films grown by liquid phase epitaxy
Physical Review Materials **4**, 024416 (2020)

38. Dunne, P.; Fowley, C.; Hlawacek, G.; Kurian, J.; Atcheson, G.; Colis, S.; Teichert, N.; Kundys, B.; Venkatesan, M.; Lindner, J.; Deac, A.M.; Hermans, T.; Coey, J.; Doudin, B.
Helium Ion Microscopy for Reduced Spin Orbit Torque Switching Currents
Nano Letters **20**, 7036 (2020)

39. Eggert, B.; Schmeink, A.; Lill, J.; Liedke, M.O.; Kentsch, U.; Butterling, M.; Wagner, A.; Pascarelli, S.; Potzger, K.; Lindner, J.; Thomson, T.; Fassbender, J.; Ollefs, K.; Keune, W.; Bali, R.; Wende, H.
Magnetic response of FeRh to static and dynamic disorder
RSC Advances **10**, 14386 (2020)

40. Ehrler, J.; Sanyal, B.; Grenzer, J.; Zhou, S.; Böttger, R.; Wende, H.; Lindner, J.; Faßbender, J.; Leyens, C.; Potzger, K.; Bali, R.
Magneto-structural correlations in a systematically disordered B2 lattice
New Journal of Physics **22**, 073004 (2020)

41. Eichler-Volf, A.; Huang, T.; Vazquez Luna, F.; Alsaadawi, Y.; Stierle, S.; Cuniberti, G.; Steinhart, M.; Baraban, L.; Erbe, A.
Comparative Studies of Light-Responsive Swimmers: Janus Nanorods versus Spherical Particles
Langmuir **36**, 12504 (2020)

42. El-Said, A.S.; Rao, S.; Akhmadaliev, S.; Facsko, S.
Tuning Tailored Single-Walled Carbon Nanotubes by Highly Energetic Heavy Ions
Physical Review Applied **13**, 044073 (2020)

43. Erb, D.; de Schultz, R.; Ilinov, A.; Nordlund, K.; Bradley, M.R.; Facsko, S.
Nanopatterning of the (001) surface of crystalline Ge by ion irradiation at off-normal incidence: Experiment and simulation
Physical Review B **102**, 165422 (2020)

44. Fallarino, L.; Stienen, S.; Gallardo, R.A.; Arregi, J.A.; Uhlíř, V.; Lenz, K.; Hübner, R.; Oelschlägel, A.; Hellwig, O.; Lindner, J.
Higher order ferromagnetic resonances in out-of-plane saturated magnetic multilayers
Physical Review B **102**, 094434 (2020)

45. Fan, X.; Zerebecki, S.; Du, R.; Hübner, R.; Marzum, G.; Jiang, G.; Hu, Y.; Barcikowki, S.; Reichenberger, S.; Eychmüller, A.
Promoting the Electrocatalytic Performance of Noble Metal Aerogels by Ligand-Directed Modulation
Angewandte Chemie - International Edition **59**, 5706 (2020)

46. Flajšman, L.; Wagner, K.; Vaňatka, M.; Gloss, J.; Křižáková, V.; Schmid, M.; Schultheiß, H.; Urbánek, M.
Zero-field propagation of spin waves in waveguides prepared by focused ion beam direct writing
Physical Review B **101**, 014436 (2020)

47. Fuchs, F.; Khan, B.; Deb, D.; Pohl, D.; Schuster, J.; Weber, W.M.; Mühle, U.; Löffler, M.; Georgiev, Y.M.; Erbe, A.; Gemming, S.
Formation and crystallographic orientation of $NiSi_2$-Si interfaces
Journal of Applied Physics **128**, 085301 (2020)

48. Gaderbauer, W.; Truglas, T.; Arndt, M.; Steck, T.; Klingner, N.; Stifter, D.; Faderl, J.; Groiß, H.
Effects of Alloying Elements on Surface Oxides of Hot–Dip Galvanized Steel
Surface & Coatings Technology **404**, 126466 (2020)

49. Gago, R.; Prucnal, S.; Esteban-Mendoza, D.
Soft X-ray absorption study of tantalum incorporation in titanium oxide films: Impact of flash-lamp annealing
Ceramics International **46**, 15772 (2020)

50. Galle, L.; Ehrling, S.; Lochmann, S.; Kaskel, S.; Bischoff, L.; Grothe, J.
Conductive ITO interfaces for optoelectronic applications based on highly ordered inverse opal thin films
ChemNanoMat **6**, 560 (2020)

51. Gärtner, A.; Merchel, S.; Niedermann, S.; Braucher, R.; ASTER-Team; Steier, P.; Rugel, G.; Scharf, A.; Le Bras, L.; Linnemann, U.
Nature does the averaging – in-situ produced ^{10}Be, ^{21}Ne, and ^{26}Al in very young river terraces
Geosciences **10**, 237 (2020)

52. Ghaderzadeh, S.; Ghorbani Asl, M.; Kretschmer, S.; Hlawacek, G.; Krasheninnikov, A.
Channeling effects in gold nano-clusters under He ion irradiation: insights from molecular dynamics simulations
Nanotechnology **31**, 035302 (2020)

53. Ghaderzadeh, S.; Ladygin, V.; Ghorbani Asl, M.; Hlawacek, G.; Schleberger, M.; Krasheninnikov, A.
Freestanding and Supported MoS_2 Monolayers under Cluster Irradiation: Insights from Molecular Dynamics Simulation
ACS Applied Materials and Interfaces **12**, 37454 (2020)

54. Griggs, W.; Eggert, B.; Liedke, M.O.; Butterling, M.; Wagner, A.; Kentsch, U.; Hirschmann, E.; Grimes, M.; Caruana, A.J.; Kinane, C.; Wende, H.; Bali, R.; Thomson, T.
Depth selective magnetic phase coexistence in FeRh thin films
APL Materials **8**, 121103 (2020)

55. Hache, T.; Li, Y.; Weinhold, T.; Scheumann, B.; Trindade Goncalves, F.J.; Hellwig, O.; Faßbender, J.; Schultheiß, H.
Bipolar spin Hall nano-oscillators
Applied Physics Letters **116**, 192405 (2020)

56. Hache, T.; Vaňatka, M.; Flajšman, L.; Weinhold, T.; Hula, T.; Ciubotariu, O.; Albrecht, M.; Arkook, B.; Barsukov, I.; Fallarino, L.; Hellwig, O.; Faßbender, J.; Urbánek, M.; Schultheiß, H.
Freestanding and positionable microwave-antenna device for magneto-optical spectroscopy experiments
Physical Review Applied **13**, 054009 (2020)

57. Hain, K.; Steier, P.; Froehlich, M.B.; Golser, R.; Hou, X.; Lachner, J.; Nomura, T.; Qiao, J.; Quinto, F.; Sakaguchi, A.
^{233}U/^{236}U signature allows to distinguish environmental emissions of civil nuclear industry from weapons fallout
Nature Communications **11**, 1275 (2020)

58. He, S.; Yang, Q.; Li, X.; Liu, H.; Cao, L.; Akhmadaliev, S.; Wang, X.; Ren, Y.; Zhou, S.; Wu, P.
Para-ferroelectric phase transition driven by swift heavy-ion irradiation in KTN crystal
Applied Surface Science **519**, 146261 (2020)

59. Hernandez-Minguez, A.; Poshakinskiy, A.V.; Hollenbach, M.; Santos, P.V.; Astakhov, G.
Anisotropic spin-acoustic resonance in silicon carbide at room temperature
Physical Review Letters **125**, 107702 (2020)

60. Hillbrand, J.; Opačcak, N.; Piccardo, M.; Schneider, H.; Strasser, G.; Capasso, F.; Schwarz, B.
Mode-locked short pulses from an 8 µm wavelength semiconductor laser
Nature Communications **11**, 5788 (2020)

61. Hiller, D.; Julin, J.A.; Chnani, A.; Strehle, S.
Silicon Surface Passivation by ALD-Ga_2O_3: Thermal vs. Plasma-Enhanced Atomic Layer Deposition
IEEE Journal of Photovoltaics **10**, 959 (2020)

62. Hiller, D.; Markevich, V.P.; de Guzman, J.A.T.; König, D.; Prucnal, S.; Bock, W.; Julin, J.; Peaker, A.R.; MacDonald, D.; Grant, N.E.; Murphy, J.D.
Kinetics of Bulk Lifetime Degradation in Float-Zone Silicon: Fast Activation and Annihilation of Grown-In Defects and the Role of Hydrogen versus Light
Physica Status Solidi (A) **217**, 2000436 (2020)

63. Hollenbach, M.; Berencen, Y.; Kentsch, U.; Helm, M.; Astakhov, G.
Engineering telecom single-photon emitters in silicon for scalable quantum photonics
Optics Express **28**, 26111 (2020)

64. Hu, L.; Xu, M.; Li, X.; Wang, Y.; Wang, Y.; Dong, H.; Schneider, H.
Performance investigation of bulk photoconductive semiconductor switch based on reversely biased p^+-i-n^+ structure
IEEE Transactions on Electron Devices **67**, 4963 (2020)

65. Hu, X.; Zhao, Y.; Shen, X.; Krasheninnikov, A.; Chen, Z.; Sun, L.
Enhanced Ferromagnetism and Tunable Magnetism in Fe_3GeTe_2 Monolayer by Strain Engineering
ACS Applied Materials and Interfaces **12**, 26367 (2020)

66. Huang, T.; Gobeil, S.; Wang, X.; Misko, V.; Nori, F.; de Malsche, W.; Faßbender, J.; Makarov, D.; Cuniberti, G.; Baraban, L.
Anisotropic exclusion effect between photocatalytic Ag/AgCl Janus particles and passive beads in a dense colloidal matrix
Langmuir **36**, 7091 (2020)

67. Hula, T.; Schultheiß, K.; Buzdakov, A.; Körber, L.; Bejarano, M.; Flacke, L.; Liensberger, L.; Weiler, M.; Shaw, J.M.; Nembach, H.T.; Faßbender, J.; Schultheiß, H.
Nonlinear losses in magnon transport due to four-magnon scattering
Applied Physics Letters **117**, 042404 (2020)

68. Jadidi, M.M.; Kargarian, M.; Mittendorff, M.; Aytac, Y.; Shen, B.; König-Otto, J.; Winnerl, S.; Ni, N.; Gaeta, A.L.; Murphy, T.E.; Drew, H.D.
Nonlinear Optical Control of Chiral Charge Pumping in a Topological Weyl Semimetal
Physical Review B **102**, 245123 (2020)

69. Jäger, N.; Meindlhumer, M.; Spor, S.; Hruby, H.; Julin, J.; Stark, A.; Nahif, F.; Keckes, J.; Mitterer, C.; Daniel, R.
Microstructural evolution and thermal stability of AlCr(Si)N hard coatings revealed by in-situ high-temperature high-energy grazing incidence transmission X-ray diffraction
Acta Materialia **186**, 545 (2020)

70. Janke, D.; Munnik, F.; Julin, J.A.; Hübner, R.; Grenzer, J.; Wüstefeld, C.; Gemming, S.; Rafaja, D.; Krause, M.
Directionality of metal-induced crystallization and layer exchange in amorphous carbon/nickel thin film stacks
Carbon **159**, 656 (2020)

71. John, J.; Dhyani, V.; Georgiev, Y.; Gangnaik, A.; Biswas, S.; Holmes, J.; Das, A.; Ray, S.; Das, S.
Ultra-High Negative Infrared Photoconductance in Highly As-doped Germanium Nanowires Induced by Hot Electron Trapping
ACS Applied Electronic Materials **2**, 1934 (2020)

72. Kainz, C.; Schalk, N.; Tkadletz, M.; Saringer, C.; Winkler, M.; Stark, A.; Schell, N.; Julin, J.; Czettl, C.
Thermo-physical properties of coatings in the Ti(B,N) system grown by chemical vapor deposition
Surface & Coatings Technology **384**, 125318 (2020)

73. Kaiser, M.; Martinez, Y.; Schmidt, A.M.; Sanchez Romero, P.A.; Kantorovich, S.S.
Diffusion of single active-dipolar cubes in applied fields
Journal of Molecular Liquids **304**, 112688 (2020)

74. Kasper, C.; Klenkert, D.; Shang, Z.; Simin, D.; Sperlich, A.; Kraus, H.; Schneider, C.; Zhou, S.; Trupke, M.; Kada, W.; Ohshima, T.; Dyakonov, V.; Astakhov, G.
Influence of irradiation on defect spin coherence in silicon carbide
Physical Review Applied **13**, 044054 (2020)

75. Kern, Z.; Ruszkiczay-Rüdiger, Z.; Perșoiu, A.; Merchel, S.; Gärtner, A.; Rugel, G.; Lachner, J.; Steier, P.
Testing cave ice deposits as archives of past atmospheric ^{10}Be deposition
Aragonit Journal **25**, 45 (2020)

76. Kiani, M.; Du, N.; Vogel, M.; Raff, J.; Hübner, U.; Skorupa, I.; Bürger, D.; Schulz, S.E.; Schmidt, O.G.; Blaschke, D.; Schmidt, H.
Disturbing-free determination of yeast concentration in DI water and in glucose using impedance biochips
Biosensors **10**, 7 (2020)

77. Kiani, M.; Tannert, A.; Du, N.; Hübner, U.; Skorupa, I.; Bürger, D.; Zhao, X.; Blaschke, D.; Rebohle, L.; Cherkouk, C.; Neugebauer, U.; Schmidt, O.G.; Schmidt, H.
Towards Bacteria Counting in DI Water of Several Microliters or Growing Suspension Using Impedance Biochips
Biosensors **10**, 82 (2020)

78. Kislyuk, V.; Kotrechko, S.; Trachevskij, V.; Melnyk, A.; Pud, A.; Ogurtsov, N.; Noskov, Y.; Osiponok, M.; Lytvyn, P.; Dzyazko, Y.; Nierobisch, F.; Schneider, A.; Ludewig, F.; Akhmadaliev, S.; Aniol, R.; Kentsch, U.; Krause, M.; Facsko, S.
Impact of low energy ion beam on the properties of rr-P3HT films
Applied Surface Science **535**, 147619 (2020)

79. Klinghammer, S.; Voitsekhivska, T.; Licciardello, N.; Kim, K.; Baek, C.-K.; Cho, H.; Wolter, K.-J.; Kirschbaum, C.; Baraban, L.; Cuniberti, G.
Nanosensor-Based Real-Time Monitoring of Stress Biomarkers in Human Saliva Using a Portable Measurement System
ACS Sensors **5**, 4081 (2020)

80. Klingner, N.; Hlawacek, G.; Mazarov, P.; Pilz, W.; Meyer, F.; Bischoff, L.
Imaging and Milling Resolution of Light Ion Beams from HIM and Liquid Metal Alloy Ion Source driven FIBs
Beilstein Journal of Nanotechnology **11**, 1742 (2020)

81. Koch, L.; Samad, F.; Lenz, M.; Hellwig, O.
Manipulating the Energy Balance of Perpendicular-Anisotropy Synthetic Antiferromagnets by He^+-Ion Irradiation
Physical Review Applied **13**, 024029 (2020)

82. Kokot, H.; Kokot, B.; Sebastijanović, A.; Voss, C.; Podlipec, R.; Zawilska, P.; Berthing, T.; Ballester López, C.; Høgh Danielsen, P.; Contini, C.; Ivanov, M.; Krišelj, A.; Čotar, P.; Zhou, Q.; Ponti, J.; Zhernovkov, V.; Schneemilch, M.; Doumandji, Z.; Pušnik, M.; Umek, P.; Pajk, S.; Joubert, O.; Schmid, O.; Urbančič, I.; Irmler, M.; Beckers, J.; Lobaskin, V.; Halappanavar, S.; Quirke, N.; Lyubartsev, A.P.; Vogel, U.; Koklič, T.; Stoeger, T.; Štrancar, J.
Chronic Inflammation Prediction for Inhaled Particles, the Impact of Material Cycling and Quarantining in the Lung Epithelium
Advanced Materials **32**, 2003913 (2020)

83. Körber, L.; Schultheiß, K.; Hula, T.; Verba, R.; Faßbender, J.; Kakay, A.; Schultheiß, H.
Nonlocal stimulation of three-magnon splitting in a magnetic vortex
Physical Review Letters **125**, 207203 (2020)

84. Korniienko, A.; Kakay, A.; Sheka, D.D.; Kravchuk, V.P.
Effect of curvature on the eigenstates of magnetic skyrmions
Physical Review B **102**, 014432 (2020)

85. Korschinek, G.; Faestermann, T.; Poutivstev, M.; Arazi, A.; Knie, K.; Rugel, G.; Wallner, A.
Supernova-produced ^{53}Mn on earth
Physical Review Letters **125**, 031101 (2020)

86. Kou, Z.; Hashemi, A.; Puska, M.; Krasheninnikov, A.; Komsa, H.-P.
Simulating Raman spectra by combining first-principles and empirical potential approaches with application to defective MoS_2
npj Computational Materials **6**, 59 (2020)

87. Kowalska, E.; Sluka, V.; Kakay, A.; Fowley, C.; Lindner, J.; Fassbender, J.; Deac, A.M.
Spin-transfer dynamics in MgO-based magnetic tunnel junctions with an out-of-plane magnetized free layer and an in-plane polarizer
Physical Review B **101**, 024430 (2020)

88. Krasheninnikov, A.
Are two-dimensional materials radiation tolerant?
Nanoscale Horizons **5**, 1447 (2020)

89. Kretschmer, S.; Lehnert, T.; Kaiser, U.; Krasheninnikov, A.
Formation of Defects in Two-Dimensional MoS_2 in the Transmission Electron Microscope at Electron Energies below the Knock-on Threshold: The Role of Electronic Excitations
Nano Letters **20**, 2865 (2020)

90. Kumar, L.; Singh, S.; Horechyy, A.; Formanek, P.; Hübner, R.; Albrecht, V.; Weißpflog, J.; Schwarz, S.; Puneet, P.; Nandan, B.
Hollow Au@TiO_2 porous electrospun nanofibers for catalytic applications
RSC Advances **10**, 6592 (2020)

91. Lachner, J.; Ploner, M.; Steier, P.; Sakaguchi, A.; Usui, A.
Accumulation of ferromanganese crusts derived from carrier-free ^{10}Be/^{9}Be
Nuclear Instruments and Methods in Physics Research B **467**, 146 (2020)

92. Leya, I.; David, J.-C.; Faestermann, T.; Froehlich, M.; Kivel, N.; Koll, D.; Korschinek, G.; Mcintyre, S.; Merchel, S.; Pavetich, S.; Rugel, G.; Schumann, D.; Smith, T.; Wallner, A.
^{53}Mn and ^{60}Fe in iron meteorites – new data and model calculations
Meteoritics & Planetary Science **55**, 818 (2020)

93. Lin, X.; Zhu, H.; Zhao, Z.; You, C.; Kong, Y.; Zhao, Y.; Liu, J.; Chen, H.; Shi, X.; Makarov, D.; Mei, Y.
Hydrogel-based Janus Micromotors Capped with Functional Nanoparticles for Environmental Applications
Advanced Materials Technologies **5**, 2000279 (2020)

94. Liu, Y.; Lin, G.; Chen, Y.; Mönch, J.I.; Makarov, D.; Walsh, B.J.; Jin, D.
Coding and decoding stray magnetic fields for multiplexing kinetic bioassay platform
Lab on a chip **20**, 4561 (2020)

95. Lively, M.A.; Holybee, B.; Toriyama, M.; Facsko, S.; Allain, J.P.
Nonlinear compositional and morphological evolution of ion irradiated GaSb prior to nanostructure formation
Scientific Reports **10**, 8253 (2020)

96. Llandro, J.; Love, D.M.; Kovács, A.; Caron, J.; Vyas, K.N.; Kakay, A.; Salikhov, R.; Lenz, K.; Faßbender, J.; Scherer, M.R.J.; Cimorra, C.; Steiner, U.; Barnes, C.H.W.; Dunin-Borkowski, R.E.; Fukami, S.; Ohno, H.
Visualizing Magnetic Structure in 3D Nanoscale Ni–Fe Gyroid Networks
Nano Letters **20**, 3642 (2020)

97. Lumetzberger, J.; Buchner, M.; Pile, S.; Ney, V.; Gaderbauer, W.; Daffé, N.; Moro, M.V.; Primetzhofer, D.; Lenz, K.; Ney, A.
Influence of structure and cation distribution on magnetic anisotropy and damping in Zn/Al doped nickel ferrites
Physical Review B **102**, 054402 (2020)

98. Mansouri, M.; Fallarino, L.; M'Nassri, R.; Cheikhrouhou-Koubaa, W.; Cheikhrouhou, A.
Structural, Magnetocaloric, and Critical Behavior of $La_{0.5}Ca_{0.5}Mn_{1-x}V_xO_3$ Manganites Prepared by High-Energy Ball Milling
Journal of Superconductivity and Novel Magnetism **33**, 995 (2020)

99. Martschini, M.; Lachner, J.; Merchel, S.; Priller, A.; Steier, P.; Wallner, A.; Wieser, A.; Golser, R.
The quest for AMS of ^{182}Hf – why poor gas gives pure beams
European Physical Journal Web of Conferences **232**, 02003 (2020)

100. Mayordomo, N.; Rodriguez Hernandez, D.M.; Schild, D.; Molodtsov, K.; Johnstone, E.V.; Hübner, R.; Shams Aldin Azzam, S.; Brendler, V.; Müller, K.
Technetium retention by gamma alumina nanoparticles and the effect of sorbed Fe^{2+}
Journal of Hazardous Materials **833**, 122066 (2020)

101. McKinnon, T.; Hübner, R.; Heinrich, B.; Girt, E.
The role of boron on exchange coupling in NiFe/$Ru_{1-x}B_x$/FeCo trilayer structures
Journal of Applied Physics **127**, 053902 (2020)

102. Meerbach, C.; Klemmed, B.; Spittel, D.; Bauer, C.; Park, Y.J.; Hübner, R.; Jeong, H.Y.; Erb, D.; Shin, H.S.; Lesnyak, V.; Eychmüller, A.
General Colloidal Synthesis of Transition-Metal Disulfide Nanomaterials as Electrocatalysts for Hydrogen Evolution Reaction
ACS Applied Materials and Interfaces **12**, 13148 (2020)

103. Melzer, M.; Makarov, D.; Schmidt, O.G.
A review on stretchable magnetic field sensorics
Journal of Physics D: Applied Physics **53**, 083002 (2020)

104. Meng, F.; Thomson, M.D.; Ul-Islam, Q.; Klug, B.; Pashkin, O.; Schneider, H.; Roskos, H.G.
Intracavity third-harmonic generation in Si:B pumped by intense terahertz pulses
Physical Review B **102**, 075205 (2020)

105. Meyer, M.; Gliganic, L.A.; May, J.-H.; Merchel, S.; Rugel, G.; Schlütz, F.; Aldenderfer, M.; Krainer, K.
Landscape dynamics and human-environment interactions in the northern foothills of Cho Oyu and Mount Everest (southern Tibet) during the Late Pleistocene and Holocene
Quaternary Science Reviews **229**, 106127 (2020)

106. Mientus, R.; Weise, M.; Seeger, S.; Heller, R.; Ellmer, K.
Electrical and Optical Properties of Amorphous SnO_2:Ta Films, Prepared by DC and RF Magnetron Sputtering: A Systematic Study of the Influence of the Type of the Reactive Gas
Coatings **10**, 204 (2020)

107. Mostarac, D.; Vaughan, L.; Sanchez Romero, P.A.; Kantorovich, S.S.
The influence of crosslinkers and magnetic particle distribution along the filament backbone on the magnetic properties of supracolloidal linear polymer-like chains
Journal of Magnetism and Magnetic Materials **497**, 166029 (2020)

108. Mousley, M.; Möller, W.; Philipp, P.; Hlawacek, G.; Wirtz, T.; Eswara, S.
Structural and chemical evolution of Au-silica core-shell nanoparticles during 20 keV helium ion irradiation: a comparison between experiment and simulation
Scientific Reports **10**, 12058 (2020)

109. Murray, C.; van Efferen, C.; Jolie, W.; Fischer, J.A.; Hall, J.; Rosch, A.; Krasheninnikov, A.; Komsa, H.-P.; Michely, T.
Band Bending and Valence Band Quantization at Line Defects in MoS_2
ACS Nano **14**, 9176 (2020)

110. Myint, P.; Erb, D.; Zhang, X.; Wiegart, L.; Zhang, Y.; Fluerasu, A.; Headrick, R.; Facsko, S.; Ludwig, K.
Measurement of Ehrlich-Schwoebel barrier contribution to the self-organized formation of ordered surface patterns on Ge(001)
Physical Review B **102**, 201404(R) (2020)

111. Nasdala, L.; Akhmadaliev, S.; Burakov, B.E.; Chanmuang Nasdala, C.; Škoda, R.
The absence of metamictisation in natural monazite
Scientific Reports **10**, 14676 (2020)

112. Nentwich, M.; Zschornak, M.; Sonntag, M.; Gumeniuk, R.; Gemming, S.; Leisegang, T.; Meyer, D.C.
Structure variations within RSi_2 and R_2TSi_3 silicides. Part I. Structure overview
Acta Crystallographica Section B **76**, 177 (2020)

113. Niggas, A.; Schwestka, J.; Creutzburg, S.; Gupta, T.; Eder, D.; Bayer, B.C.; Aumayr, F.; Wilhelm, R.A.
The role of contaminations in ion beam spectroscopy with freestanding 2D materials: A study on thermal treatment
Journal of Chemical Physics **153**, 014702 (2020)

114. Nord, M.; McGrouther, D.; Potzger, K.; Bali, R.
Ionenstrahlen erzeugen periodische, magnetische Domänenstrukturen
Physik in unserer Zeit **51**, 58 (2020)

115. Novakovic-Marinkovic, N.; Mawass, M.-A.; Volkov, O.; Makushko, P.; Engel, W.D.; Makarov, D.; Kronast, F.
From stripes to bubbles: Deterministic transformation of magnetic domain patterns in Co/Pt multilayers induced by laser helicity
Physical Review B **102**, 174412 (2020)

116. Novikau, I.S.; Minina, E.S.; Sanchez Romero, P.A.; Kantorovich, S.S.
Suspensions of magnetic nanogels at zero field: Equilibrium structural properties
Journal of Magnetism and Magnetic Materials **498**, 166152 (2020)

117. Novikau, I.S.; Sanchez Romero, P.A.; Kantorovich, S.S.
The influence of an applied magnetic field on the self-assembly of magnetic nanogels
Journal of Molecular Liquids **307**, 112902 (2020)

118. Obied, L.H.; Roorda, S.; Prucnal, S.; Zhou, S.; Crandles, D.A.
An Infrared Transmission Study of Ge:Mn Thick Films Prepared by Ion Implantation and Post-Annealing
Journal of Applied Physics **127**, 103902 (2020)

119. Oder, M.; Koklič, T.; Umek, P.; Podlipec, R.; Štrancar, J.; Dobeic, M.
Photocatalytic biocidal effect of copper doped TiO_2 nanotube coated surfaces under laminar flow, illuminated with UVA light on Legionella pneumophila
PLOS ONE **15**, e0227574 (2020)

120. Orús, P.; Córdoba, R.; Hlawacek, G.; de Teresa, J.M.
Superconducting properties of in-plane W-C nanowires grown by He^+ Focused Ion Beam Induced Deposition
Nanotechnology **32**, 085301 (2020)

121. Pan, S.; Mondal, S.; Zelent, M.; Szwierz, R.; Pal, S.; Hellwig, O.; Krawczyk, M.; Barman, A.
Edge localization of spin waves in antidot multilayers with perpendicular magnetic anisotropy
Physical Review B **101**, 014403 (2020)

122. Patel, D.; Richardson, M.D.; Jim, B.; Akhmadaliev, Sh.; Goodall, R.; Gandy, A.S.
Radiation damage tolerance of a novel metastable refractory high entropy alloy $V_{2.5}Cr_{1.2}WMoCo_{0.04}$
Journal of Nuclear Materials **531**, 152005 (2020)

123. Peter, R.; Salamon, K.; Omerzu, A.; Grenzer, J.; Badovinac, I.J.; Saric, I.; Petravic, M.
Role of Hydrogen-Related Defects in Photocatalytic Activity of ZnO Films Grown by Atomic Layer Deposition
Journal of Physical Chemistry C **124**, 165116 (2020)

124. Pile, S.; Buchner, M.; Ney, V.; Schaffers, T.; Lenz, K.; Narkovic, R.; Lindner, J.; Ohldag, H.; Ney, A.
Direct imaging of the AC component of the pumped spin polarization with element specificity
Physical Review Applied **14**, 034005 (2020)

125. Podlipec, R.; Arsov, Z.; Koklic, T.; Strancar, J.
Characterization of blood coagulation dynamics and oxygenation in ex-vivo retinal vessels by fluorescence hyperspectral imaging
Journal of Biophotonics **13**, e202000021 (2020)

126. Pourteau, M.-L.; Gharbi, A.; Brianceau, P.; Dallery, J.-A.; Laulagnet, F.; Rademaker, G.; Tiron, R.; Engelmann, H.-J.; Borany, J.; Heinig, K.-H.; Rommel, M.; Baier, L.
Sub-20 nm multilayer nanopillar patterning for hybrid SET/CMOS integration
Micro and Nano Engineering **9**, 100074 (2020)

127. Prucnal, S.; Liedke, M.O.; Wang, X.; Butterling, M.; Posselt, M.; Knoch, J.; Windgassen, H.; Hirschmann, E.; Berencen, Y.; Rebohle, L.; Wang, M.; Napoltani, E.; Frigerio, J.; Ballabio, A.; Isella, G.; Hübner, R.; Wagner, A.; Bracht, H.; Helm, M.; Zhou, S.
Dissolution of donor-vacancy clusters in heavily doped n-type germanium
New Journal of Physics **22**, 123036 (2020)

128. Prucnal, S.; Żuk, J.; Hübner, R.; Duan, J.; Wang, M.; Pyszniak, K.; Drozdziel, A.; Turek, M.; Zhou, S.
Electron Concentration Limit in Ge Doped by Ion Implantation and Flash Lamp Annealing
Materials **13**, 1408 (2020)

129. Przezdziecka, E.; Chusnutdinow, S.; Wierzbicka, A.; Guziewicz, M.; Prucnal, S.; Stachowicz, M.; Zaleszczyk, W.; Zhou, S.; Kozanecki, A.
Current Transport Mechanisms in Zinc Oxide/Silicon Carbide Heterojunction Light-Emitting Diodes
Physica Status Solidi (B) **257**, 2000133 (2020)

130. Pylypovskyi, O.; Kononenko, D.Y.; Yershov, K.; Rößler, U.K.; Tomilo, A.; Faßbender, J.; van den Brink, J.; Makarov, D.; Sheka, D.
Curvilinear One-Dimensional Antiferromagnets
Nano Letters **20**, 8157 (2020)

131. Pylypovskyi, O.; Kravchuk, V.P.; Volkov, O.; Faßbender, J.; Sheka, D.; Makarov, D.
Unidirectional tilt of domain walls in equilibrium in biaxial stripes with Dzyaloshinskii–Moriya interaction
Journal of Physics D: Applied Physics **53**, 395003 (2020)

132. Qarra, H.H.; Knowles, K.M.; Vickers, M.E.; Zapata-Solvas, E.; Akhmadaliev, S.
Heavy ion irradiation damage in $Zr_3(Al_{0.9}Si_{0.1})C_2$ MAX phase
Journal of Nuclear Materials **540**, 152360 (2020)

133. Radic, D.; Hilke, S.; Peterlechner, M.; Posselt, M.; Wilde, G.; Bracht, H.
Comparison of experimental STEM conditions for fluctuation electron microscopy
Microscopy and Microanalysis **26**, 1100 (2020)

134. Rajbhar, M.K.; Das, P.; Satpati, B.; Möller, W.; Ramgir, N.; Chatterjee, S.
Moisture repelling perovskite nanowires for higher stability in energy applications
Applied Surface Science **527**, 146683 (2020)

135. Rajbhar, M.K.; Möller, W.; Satpati, B.; Manju, U.; Chaudhary, Y.S.; Chatterjee, S.
Broad Beam-Induced Fragmentation and Joining of Tungsten Oxide Nanorods: Implications for Nanodevice Fabrication and the Development of Fusion Reactors
ACS Applied Nano Materials **3**, 9064 (2020)

136. Ramasubramanian, L.; Kákay, A.; Fowley, C.; Yildirim, O.; Matthes, P.; Sorokin, S.; Titova, A.; Hilliard, D.; Böttger, R.; Hübner, R.; Gemming, S.; Schulz, S.E.; Kronast, F.; Makarov, D.; Faßbender, J.; Deac, A.M.
Tunable magnetic vortex dynamics in ion-implanted permalloy disks
ACS Applied Materials and Interfaces **12**, 27812 (2020)

137. Rana, R.; Balaghi, L.; Fotev, I.; Schneider, H.; Helm, M.; Dimakis, E.; Pashkin, O.
Nonlinear Charge Transport in InGaAs Nanowires at Terahertz Frequencies
Nano Letters **20**, 3225 (2020)

138. Ratajczak, R.; Mieszczynski, C.; Prucnal, S.; Krajewski, T.A.; Guziewicz, E.; Wozniak, W.; Kopalko, K.; Heller, R.; Akhmadaliev, S.
Correlations between the structural transformations and concentration quenching effect for RE-implanted ZnO systems
Applied Surface Science **521**, 146421 (2020)

139. Redondo-Cubero, A.; Palomares, F.J.; Hübner, R.; Gago, R.; Vázquez, L.
Highly ordered silicide ripple patterns induced by medium-energy ion irradiation
Physical Review B **102**, 075423 (2020)

140. Reichhelm, A.; Hübner, R.; Damm, C.; Nielsch, K.; Eychmüller, A.
Increasing the Diversity and Understanding of Semiconductor Nanoplatelets by Colloidal Atomic Layer Deposition
Physica Status Solidi (RRL) **14**, 2000282 (2020)

141. Reissig, F.; Zarschler, K.; Hübner, R.; Pietzsch, H.-J.; Kopka, K.; Mamat, C.
Sub-10 nm Radiolabeled Barium Sulfate Nanoparticles as Carriers for Theranostic Applications and Targeted Alpha Therapy
ChemistryOpen **9**, 797 (2020)

142. Riisager, K.; Borge, M.J.G.; Briz, J.A.; Carmona-Gallardo, M.; Forstner, O.; Fraile, L.M.; Fynbo, H.O.U.; Garzon Camacho, A.; Johansen, J.G.; Jonson, B.; Lund, M.V.; Lachner, J.; Madurga, M.; Merchel, S.; Nacher, E.; Nilsson, T.; Steier, P.; Tengblad, O.; Vedia, V.
Search for beta-delayed proton emission from ^{11}Be
European Physical Journal A **56**, 100 (2020)

143. Sanchez Romero, P.A.; Miller, J.; Kantorovich, S.S.; Richter, R.
Unknotting of quasi-two-dimensional ferrogranular networks by in-plane homogeneous magnetic fields
Journal of Magnetism and Magnetic Materials **499**, 166182 (2020)

144. Schmidt, J.; Winnerl, S.; Dimakis, E.; Hübner, R.; Schneider, H.; Helm, M.
All-THz pump-probe spectroscopy of the intersubband AC-Stark effect in a wide GaAs quantum well
Optics Express **28**, 25358 (2020)

145. Schöffmann, P.; Pütter, S.; Schubert, J.; Zander, W.; Barthel, J.; Zakalek, P.; Waschk, M.; Heller, R.; Brückel, T.
Tuning the Co/Sr stoichiometry of $SrCoO_{2.5}$ thin films by RHEED assisted MBE growth
Materials Research Express **7**, 116404 (2020)

146. Schütt, J.; Illing, R.; Volkov, O.; Kosub, T.; Granell, P.N.; Nhalil, H.; Faßbender, J.; Klein, L.; Grosz, A.; Makarov, D.
Two Orders of Magnitude Boost in the Detection Limit of Droplet-Based Micro-Magnetofluidics with Planar Hall Effect Sensors
ACS Omega **5**, 20609 (2020)

147. Schütt, J.; Sandoval Bojorquez, D.I.; Avitabile, E.; Oliveros Mata, E.S.; Milyukov, G.; Colditz, J.; Delogu, L.G.; Rauner, M.; Feldmann, A.; Koristka, S.; Middeke, J.M.; Sockel, K.; Faßbender, J.; Bachmann, M.; Bornhäuser, M.; Cuniberti, G.; Baraban, L.
Nanocytometer for smart analysis of peripheral blood and acute myeloid leukemia: a pilot study
Nano Letters **20**, 6572 (2020)

148. Schwestka, J.; Inani, H.; Tripathi, M.; Niggas, A.; McEvoy, N.; Libisch, F.; Aumayr, F.; Kotakoski, J.; Wilhelm, R.A.
Atomic-Scale Carving of Nanopores into a van der Waals Heterostructure with Slow Highly Charged Ions
ACS Nano **14**, 10536 (2020)

149. Selau, F.F.; Trombini, H.; Marmitt, G.G.; de Andrade, A.M.H.; Morais, J.; Grande, P.L.; Alencar, I.; Vos, M.; Heller, R.
Stopping and straggling of 60–250-keV backscattered protons on nanometric Pt films
Physical Review A **102**, 032812 (2020)

150. Serralta Hurtado De Menezes, E.; Klingner, N.; de Castro, O.; Mousley, M.; Eswara, S.; Duarte Pinto, S.; Wirtz, T.; Hlawacek, G.
Scanning transmission imaging in the helium ion microscope using a microchannel plate with a delay line detector
Beilstein Journal of Nanotechnology **11**, 1854 (2020)

151. Shang, Z.; Hashemi, A.; Berencen, Y.; Komsa, H.-P.; Erhart, P.; Zhou, S.; Helm, M.; Krasheninnikov, A.; Astakhov, G.
Local vibrational modes of Si vacancy spin qubits in SiC
Physical Review B **101**, 144109 (2020)

152. Sharma, A.; Hoffmann, M.A.; Matthes, P.; Hellwig, O.; Kowol, C.; Schulz, S.E.; Zahn, D.R.T.; Salvan, G.
Crystallization of optically thick films of $Co_xFe_{80-x}B_{20}$: Evolution of optical, magneto-optical, and structural properties
Physical Review B **101**, 054438 (2020)

153. Sharma, A.; Matthes, P.; Soldatov, I.; Arekapudi, S.S.P.K.; Böhm, B.; Lindner, M.; Selyshchev, O.; Thi, N.H.N.; Mehring, M.; Tegenkamp, C.; Schulz, S.E.; Zahn, D.R.T.; Paltiel, Y.; Hellwig, O.; Salvan, G.
Control of magneto-optical properties of cobalt-layers by adsorption of α-helical polyalanine self-assembled monolayers
Journal of Materials Chemistry C **8**, 11822 (2020)

154. Sheka, D.D.; Pylypovskyi, O.; Landeros, P.; Gaididei, Y.; Kakay, A.; Makarov, D.
Nonlocal chiral symmetry breaking in curvilinear magnetic shells
Communications Physics **3**, 128 (2020)

155. Shevchenko, N.; Grenzer, J.; Keplinger, O.; Rack, A.; Eckert, S.
Observation of sidearm splitting studied by high resolution X-ray radiography
International Journal of Materials Research **111**, 11 (2020)

156. Singh, A.; Pashkin, O.; Winnerl, S.; Welsch, M.; Beckh, C.; Sulzer, P.; Leitenstorfer, A.; Helm, M.; Schneider, H.
Up to 70 THz bandwidth from an implanted Ge photoconductive antenna excited by a femtosecond Er:fibre laser
Light: Science and Applications **9**, 30 (2020)

157. Singh, A.; Welsch, M.; Winnerl, S.; Helm, M.; Schneider, H.
Non-plasmonic improvement in photoconductive THz emitters using nano- and micro-structured electrodes
Optics Express **28**, 35490 (2020)

158. Slavkovská, Z.; Wallner, A.; Reifarth, R.; Pavetich, S.; Brückner, B.; Al-Khasawneh, K.; Merchel, S.; Volknandt, M.; Weigand, M.
Investigation of $^{54}Fe(n,\gamma)^{55}Fe$ and $^{35}Cl(n,\gamma)^{36}Cl$ reaction cross sections at keV energies by Accelerator Mass Spectrometry
European Physical Journal Web of Conferences **232**, 02005 (2020)

159. Smith, A.; Sobotkiewich, K.; Khan, A.; Montoya, E.A.; Yang, L.; Duan, Z.; Schneider, T.; Lenz, K.; Lindner, J.; An, K.; Li, X.; Krivorotov, I.N.
Dimensional crossover in spin Hall oscillators
Physical Review B **102**, 054422 (2020)

160. Soltani, A.; Kuschewski, F.; Bonmann, M.; Generalov, A.; Vorobiev, A.; Ludwig, F.; Wiecha, M.M.; Cibaraite, D.; Walla, F.; Winnerl, S.; Kehr, S.C.; Eng, L.M.; Stake, J.; Roskos, H.G.
Direct nanoscopic observation of plasma waves in the channel of a graphene feld-effect transistor
Light: Science and Applications **9**, 97 (2020)

161. Song, Y.; Xu, Z.; Li, R.; Wang, H.; Fan, Y.; Rommel, M.; Liu, J.; Astakhov, G.; Hlawacek, G.; Li, B.; Xu, J.; Fang, F.
Photoluminescence and Raman Spectroscopy Study on Color Centers of Helium Ion-Implanted 4H–SiC
Nanomanufacturing and Metrology **3**, 205 (2020)

162. Sorokin, S.; Gallardo, R.; Fowley, C.; Lenz, K.; Titova, A.; Dennehy, G.; Atcheson, G.; Rode, K.; Faßbender, J.; Lindner, J.; Deac, A.M.
Magnetization dynamics in synthetic antiferromagnets: the role of dynamical energy and mutual spin-pumping
Physical Review B **101**, 144410 (2020)

163. Sruthil Lal, S.B.; Devaraj, M.; Posselt, M.; Sharan, A.
Accurate determination of quasi-particle electronic and optical spectra of anatase titanium dioxide
AIP Conference Proceedings **2265**, 030375 (2020)

164. Stadlmayr, R.; Szabo, P.S.; Mayer, D.; Cupak, C.; Dittmar, T.; Bischoff, L.; Möller, S.; Rasinski, M.; Wilhelm, R.A.; Möller, W.; Aumayr, F.
Sputtering of nanostructured tungsten and comparison to modelling with TRI3DYN
Journal of Nuclear Materials **532**, 152019 (2020)

165. Steffenssen, G.; Müller, A.; Munnik, F.; Friis, H.; Erambert, M.; Kristoffersen, M.; Rosing-Schow, N.
Unusual scandium enrichments of the Tørdal pegmatites, south Norway. Part I: Garnet as Sc exploration pathfinder
Ore Geology Reviews **126**, 103729 (2020)

166. Strauss, F.; Hüger, E.; Julin, J.A.; Munnik, F.; Schmidt, H.
Lithium Diffusion in Ion-Beam Sputter-Deposited Lithium-Silicon Layers
Journal of Physical Chemistry C **124**, 8616 (2020)

167. Sun, Z.; Cai, M.; Hübner, R.; Ansorge-Schumacher, M.B.; Wu, C.
Tailoring Particle-enzyme Nanoconjugates for Biocatalysis at the Organic-organic Interface
ChemSusChem **13**, 6523 (2020)

168. Thieme, M.; Bergmann, U.; Kiesewetter, A.; Wehry, T.; Potzger, K.; Zarzycki, A.; Marszalek, M.; Worch, H.
Investigation of Mild Steel Corrosion in the Cement Production Associated with the Usage of Secondary Fuels
International Journal of Corrosion **2020**, 7341029 (2020)

169. Tiwari, S.; Schneider, J.D.; Wintz, S.; Arekapudi, S.S.P.K.; Lenz, K.; Andres, C.; Lindner, J.; Hellwig, O.; Gregory, P.C.; Robert, N.C.
Coupling of Lamb Waves and Spin Waves in Multiferroic Heterostructures
Journal of Microelectromechanical Systems **29**, 1121 (2020)

170. Trindade Goncalves, F.J.; Shimamoto, Y.; Sogo, T.; Paterson, G.W.; Kousaka, Y.; Togawa, Y.
Field driven recovery of the collective spin dynamics of the chiral soliton lattice
Applied Physics Letters **116**, 012403 (2020)

171. Uddin, W.; Maity, S.; Dhyani, V.; Ahmad, G.; Georgiev, Y.; Das, S.
Resonant Tunneling and Hole Transport Behavior in Low Noise Silicon Tri-gate Junctionless Single Hole Transistor
Semiconductor Science and Technology **35**, 065011 (2020)

172. Šujan, M.; Braucher, R.; Šujan, M.; Hók, J.; Povinec, P.P.; Šipka, F.; Rugel, G.; Scharf, A.
The tectono-sedimentary evolution of a major seismogenic zone with low slip rate activity: A geochronological and sedimentological investigation of the Dobrá Voda Depression (Western Carpathians)
Sedimentary Geology **383**, 248 (2020)

173. Valerius, P.; Kretschmer, S.; Senkovskiy, B.V.; Wu, S.; Hall, J.; Herman, A.; Ehlen, N.; Ghorbani Asl, M.; Grüneis, A.; Krasheninnikov, A.; Michely, T.
Reversible crystalline-to-amorphous phase transformation in monolayer MoS_2 under grazing ion irradiation
2D Materials **7**, 025005 (2020)

174. Vallinayagam, M.; Posselt, M.; Chandra, S.
Electronic structure and thermoelectric properties of Mo-based dichalcogenide monolayers locally and randomly modified by substitutional atoms
RSC Advances **10**, 43035 (2020)

175. Vasin, A.V.; Rusavsky, A.V.; Bortchagovsky, E.G.; Gomeniuk, Y.V.; Nikolenko, A.S.; Strelchuk, V.V.; Yatskiv, R.; Tiagulskyi, S.; Prucnal, S.; Skorupa, W.; Nazarov, A.N.
Methane as a novel doping precursor for deposition of highly conductive ZnO thin films by magnetron sputtering
Vacuum **174**, 109199 (2020)

176. Vegesna, S.V.; Bath, V.J.; Bürger, D.; Dellith, J.; Skorupa, I.; Schmidt, O.G.; Schmidt, H.
Increased static dielectric constant in ZnMnO and ZnCoO thin films with bound magnetic polarons
Scientific Reports **10**, 6698 (2020)

177. Venanzi, T.; Arora, H.; Winnerl, S.; Pashkin, O.; Chava, P.; Patanè, A.; Kovalyuk, Z.D.; Kudrynskyi, Z.R.; Watanabe, K.; Taniguchi, T.; Erbe, A.; Helm, M.; Schneider, H.
Photoluminescence dynamics in few-layer InSe
Physical Review Materials **4**, 044001 (2020)

178. Vogel, K.; Heintze, C.; Chekhonin, P.; Akhmadaliev, S.; Altstadt, E.; Bergner, F.
Relationships between depth-resolved primary radiation damage, irradiation-induced nanostructure and nanoindentation response of ion-irradiated Fe-Cr and ODS Fe-Cr alloys
Nuclear Materials and Energy **24**, 100759 (2020)

179. von Reppert, A.; Willig, L.; Pudell, J.-E.; Zeuschner, S.; Sellge, G.; Ganss, F.; Hellwig, O.; Ander Arregi, J.; Uhlíř, V.; Crut, A.; Bargheer, M.
Spin stress contribution to the lattice dynamics of FePt
Science Advances **6**, eaba1142 (2020)

180. Wallner, A.; Feige, J.; Fifield, K.; Froehlich, M.B.; Golser, R.; Hotchkis, M.A.C.; Koll, D.; Leckenby, G.; Martschini, M.; Merchel, S.; Panjkov, S.; Pavetich, S.; Rugel, G.; Tims, S.G.
^{60}Fe deposition during the late Pleistocene and the Holocene echoes supernova activity
PNAS Proceedings of the National Academy of Sciences of the United States of America **117**, 21873 (2020)

181. Wang, B.; Zhang, D.; Wang, H.; Zhao, H.; Liu, R.; Li, Q.; Zhou, S.; Du, J.; Xu, Q.
Enhanced room temperature ferromagnetism in MoS_2 by N plasma treatment
AIP Advances **10**, 015243 (2020)

182. Wang, C.; Chang, C.-H.; Herklotz, A.; Chen, C.; Ganss, F.; Kentsch, U.; Chen, D.; Gao, X.; Zeng, Y.-J.; Hellwig, O.; Helm, M.; Gemming, S.; Chu, Y.-H.; Zhou, S.
Topological Hall effect in single thick $SrRuO_3$ layers induced by defect engineering
Advanced Electronic Materials **6**, 2000184 (2020)

183. Wang, M.; Debernardi, A.; Zhang, W.; Xu, C.; Yuan, Y.; Xie, Y.; Berencén, Y.; Prucnal, S.; Helm, M.; Zhou, S.
Critical behavior of the insulator-to-metal transition in Te-hyperdoped Si
Physical Review B **102**, 085204 (2020)

184. Wang, M.; Shi, H.; Zhang, P.; Liao, Z.; Wang, M.; Zhong, H.; Schwotzer, F.; Shaygan Nia, A.; Zschech, E.; Zhou, S.; Kaskel, S.; Dong, R.; Feng, X.
Phthalocyanine-Based 2D Conjugated Metal-Organic Framework Nanosheets for High-Performance Micro-Supercapacitors
Advanced Functional Materials **30**, 2002664 (2020)

185. Wang, M.; Wang, M.; Lin, H.-H.; Ballabio, M.; Zhong, H.; Bonn, M.; Zhou, S.; Heine, T.; Canovas, E.; Dong, R.; Feng, X.
High-Mobility Semiconducting Two-Dimensional Conjugated Covalent Organic Frameworks with p-Type Doping
Journal of the American Chemical Society **142**, 21622 (2020)

186. Wang, X.; Faßbender, J.; Posselt, M.
Mutual dependence of oxygen and vacancy diffusion in bcc Fe and dilute iron alloys
Physical Review B **101**, 174107 (2020)

187. Wang, X.; Mao, G.; Ge, J.; Michael, D.; Cañón Bermúdez, G.S.; Wirthl, D.; Illing, R.; Kosub, T.; Bischoff, L.; Wang, C.; Faßbender, J.; Kaltenbrunner, M.; Makarov, D.
Untethered and Ultrafast Soft-bodied Robots
Communications Materials **1**, 67 (2020)

188. Wang, Z.; Wang, G.; Qi, H.; Wang, M.; Wang, M.; Park, S.; Wang, H.; Yu, M.; Kaiser, U.; Fery, A.; Zhou, S.; Dong, R.; Feng, X.
Ultrathin two-dimensional conjugated metal–organic framework single-crystalline nanosheets enabled by surfactant-assisted synthesis
Chemical Science **11**, 7665 (2020)

189. Waqar, A.; Cai-Qin, L.; Xu, C.; Zhou, S.; Wagner, A.; Butterling, M.; Muhammad, Y.; Francis, C.-C.L.
Ferromagnetism in Undoped ZnO Grown by Pulsed Laser Deposition
Materials Research Express **7**, 056102 (2020)

190. Wehmeier, L.; Nörenberg, T.; de Oliveira, T.V.A.G.; Klopf, J.M.; Yang, S.-Y.; Martin, L.W.; Ramesh, R.; Eng, L.M.; Kehr, S.C.
Phonon-induced near-field resonances in multiferroic $BiFeO_3$ thin films at infrared and THz wavelengths
Applied Physics Letters **116**, 071103 (2020)

191. Wei, Y.; Ghorbani Asl, M.; Krasheninnikov, A.
Tailoring the Electronic and Magnetic Properties of Hematene by Surface Passivation: Insights from First-principles Calculations
Journal of Physical Chemistry C **124**, 22784 (2020)

192. Werbrouck, A.; Mattelaer, F.; Minjauw, M.; Nisula, M.; Julin, J.A.; Munnik, F.; Dendooven, J.; Detavernier, C.
Reaction Pathways for Atomic Layer Deposition with Lithium Hexamethyl Disilazide, Trimethyl Phosphate, and Oxygen Plasma
Journal of Physical Chemistry C **124**, 27829 (2020)

193. Wheatcroft, L.; Klingner, N.; Heller, R.; Hlawacek, G.; Ozkaya, D.; Cookson, J.; Inkson, B.J.
Visualisation and Chemical Characterisation of the Cathode Electrolyte Interphase in High Voltage Li-ion Battery Material $LiCoPO_4$ using He-ion Microscopy and in-situ Time-of-Flight Secondary Ion Mass Spectroscopy
ACS Applied Energy Materials **3**, 8822 (2020)

194. Wilske, C.; Suckow, A.; Mallast, U.; Meier, C.; Merchel, S.; Merkel, B.; Pavetich, S.; Rödiger, T.; Rugel, G.; Sachse, A.; Weise, S.; Siebert, C.
A multi-environmental tracer study to determine groundwater residence times and recharge in a structurally complex multi-aquifer system
Hydrology and Earth System Sciences **24**, 249 (2020)

195. Wojewoda, O.; Hula, T.; Flajšman, L.; Vaňatka, M.; Gloss, J.; Holobrádek, J.; Staňo, M.; Stienen, S.; Körber, L.; Schultheiß, K.; Schmid, M.; Schultheiß, H.; Urbánek, M.
Propagation of spin waves through a Néel domain wall
Applied Physics Letters **117**, 022405 (2020)

196. Xu, X.; Heinig, K.-H.; Möller, W.; Engelmann, H.-J.; Klingner, N.; Gharbi, A.; Tiron, R.; Borany, J.; Hlawacek, G.
Morphology modification of Si nanopillars under ion irradiation at elevated temperatures: plastic deformation and controlled thinning to 10 nm
Semiconductor Science and Technology **35**, 015021 (2020)

197. Yang, L.; Wang, C.; Zeng, M.; Hou, Z.; Fan, Z.; Chen, D.; Qin, M.; Lu, X.; Li, Q.; Gao, X.
Polarization tunability in multiferroic $DyMn_2O_5$: Influence of Y and Eu co-doping and 3d-4f exchange
Solid State Communications **307**, 113809 (2020)

198. Yang, Q.; Kou, L.; Hu, X.; Wang, Y.; Lu, C.; Krasheninnikov, A.; Sun, L.
Strain robust spin gapless semiconductors/half-metals in transition metal embedded $MoSe_2$ monolayer
Journal of Physics: Condensed Matter **32**, 365305 (2020)

199. Yi, A.; Zheng, Y.; Huang, H.; Lin, J.; Yan, Y.; You, T.; Huang, K.; Zhang, S.; Shen, C.; Zhou, M.; Huang, W.; Zhang, J.; Zhou, S.; Ou, H.; Ou, X.
Wafer-scale 4H-silicon carbide-on-insulator (4H–SiCOI) platform for nonlinear integrated optical devices
Optical Materials **107**, 109990 (2020)

200. Yildirim, O.; Hilliard, D.; Arekapudi, S.S.P.K.; Fowley, C.; Cansever, H.; Koch, L.; Ramasubramanian, L.; Zhou, S.; Böttger, R.; Lindner, J.; Faßbender, J.; Hellwig, O.; Deac, A.M.
Ion-irradiation-induced cobalt/cobalt oxide heterostructures: printing 3D interfaces
ACS Applied Materials and Interfaces **12**, 9858 (2020)

201. Yuan, Y.; Liu, Y.; Xu, C.; Kang, J.; Wang, W.; Wang, Q.; Song, B.; Zhou, S.; Wang, X.
3D-Ising critical behavior in antiperovskite-type ferromagneticlike Mn_3GaN
Journal of Applied Physics **127**, 073903 (2020)

202. Zehner, J.; Soldatov, I.; Schneider, S.; Heller, R.; Khojasteh, N.B.; Schiemenz, S.; Fähler, S.; Nielsch, K.; Schäfer, R.; Leistner, K.
Voltage-Controlled Deblocking of Magnetization Reversal in Thin Films by Tunable Domain Wall Interactions and Pinning Sites
Advanced Electronic Materials **6**, 2000406 (2020)

203. Zhang, G.; Samuely, T.; Iwahara, N.; Kačmarčík, J.; Wang, C.; May, P.W.; Jochum, J.K.; Onufriienko, O.; Szabó, P.; Zhou, S.; Samuely, P.; Moshchalkov, V.V.; Chibotaru, L.F.; Rubahn, H.-G.
Yu-Shiba-Rusinov bands in ferromagnetic superconducting diamond
Science Advances **6**, eaaz2536 (2020)

204. Zhang, X.; Zhang, Z.; Akhmadaliev, S.; Zhou, S.; Wu, Y.; Guo, B.
Structural and magnetic properties of swift heavy-ion irradiated SiC
Vacuum **184**, 109849 (2020)

205. Zhong, H.; Ghorbani-Asl, M.; Ly, K.H.; Ge, J.; Zhang, J.; Wang, M.; Liao, Z.; Makarov, D.; Zschech, E.; Brunner, E.; Weidinger, I.M.; Zhang, J.; Krasheninnikov, A.; Kaskel, S.; Dong, R.; Feng, X.
Synergistic Electroreduction of Carbon Dioxide to Carbon Monoxide on Bimetallic Layered Conjugated Metal-Organic Frameworks
Nature Communications **11**, 1409 (2020)

Patents

1. Bogusz, A.; Rayapati, V.R.; Skorupa, I.; Schmidt, H.; Bürger, D.; Krüger, S.; Rebohle, L.
   P1813 - Schichtabfolge zur Erzeugung von Elektrolumineszenz und deren Verwendung
   DE102018117210 - Offenlegung 20.02.2020
2. Bürger, D.; Krüger, S.; Skorupa, I.; Schmidt, H.; Du, N.
   P1819 - Verfahren zur Herstellung eines keramischen Materials mit lokal einstellbarem Permeabilitätsgradienten, dessen Anwendung in einem Beschichtungsverfahren sowie dessen Verwendung
   DE102018125270 - Offenlegung 16.04.2020; Nachanmeldungen: WO
3. Illing, R.; Makarov, D.
   P1812 - Fluidik-Detektionssystem
   DE102018116918 - Offenlegung 16.01.2020; Nachanmeldungen: WO

Concluded scientific degrees

PhD theses

1. Aleksandrov, Y. I.
   Spin dynamics in confined sub-micron magnetic structures
   TU Dresden, 15.10.2020
2. Arora, H.
   Charge transport in two-dimensional materials and their electronic applications
   TU Dresden, 09.12.2020
3. Ehrler, J.
   Magneto-structural correlations in $Fe_{60}Al_{40}$ thin films
   TU Dresden, 25.08.2020
4. Kretschmer, S.
   Effects of electron and ion irradiation on two-dimensional molybdenum-disulfide
   TU Dresden, 15.01.2020
5. Prüfer, T.
   Formation of Si nanocrystals for single electron transistors by ion beam mixing and self-organization – modeling and simulation
   TU Dresden, 10.03.2020
6. Schmeink, A.
   Pulsed laser induced magneto-structural transition in $Fe_{49}Rh_{51}$ thin films and structural dependence of electronic transport in $Fe_{60}Al_{40}$ thin wires
   TU Dresden, 23.11.2020
7. Vallinayagam, M.
   First-principles studies on oxide nanoclusters in bcc Fe
   TU Dresden, 21.07.2020
8. Venanzi, T.
   Optical and infrared properties of atomically thin semiconductors
   TU Dresden, 14.10.2020
9. Wang, C.
   Tuning physical properties of epitaxial $SrRuO_3$ films by ion irradiation
   TU Dresden, 16.07.2020
10. Wang, X.
    Multiscale modeling of oxygen and vacancy diffusion in dilute ferritic iron alloys
    TU Dresden, 26.10.2020

Bachelor/Master/Diploma theses

1. Bachmann, E.
   Inbetriebnahme und Einarbeitung des in situ Reflektometers im Cluster Tool des HZDR
   TU Dresden (B.Sc.), 16.04.2020
2. Gao, Y.
   Confocal microscopy of irradiation induced defects in silicon carbide
   TU Dresden (M.Sc.), 06.01.2020
3. Ghosh, S.
   Fabrication and electrical characterization of Top-Gated RFETs
   TU Dresden (M.Sc.), 29.04.2020

4. Hoppe, M.
Untersuchungen zur Struktur von SnO_2:Ta – Dünnschichten
TU Dresden (B.Sc.), 16.04.2020

5. Hozaien, N.
Top-down Fabrication and Characterization of SiGe Reconfigurable Field Effect Transistors
TU Dresden (M.Sc.), 20.10.2020

6. Jain, A.
Fabrication and electrical characterization of DNA templated nanowires and double-stranded DNA
TU Chemnitz (M.Sc.), 23.04.2020

7. Moebus, F.
Optical Spectroscopy on highly mismatched GaAs/$In_xAl_{1-x}As$ Core/Shell Nanowires
TU Dresden (M.Sc.), 12.06.2020

8. Oelschlägel, A.
Charakterisierung der Resonanzmoden in ferromagnetischen Mikrostreifen mittels ferromagnetischer Resonanz
TU Dresden (M.Sc.), 18.09.2020

9. Quasebarth, G.
Calculation of spin-wave eigenmodes in confined nanostructures using a dynamic matrix approach
TU Dresden (B.Sc.), 28.09.2020

10. Shaikh, M. S.
Thermal stability of Te-hyperdoped Si
TU Chemnitz (M.Sc.), 02.06.2020

11. Sharma, D.
Doping of 2D transition-metal dichalcogenides using ion implantation and flash lamp annealing
TU Chemnitz (M.Sc.), 22.09.2020

12. Sonnenberg, J.
Untersuchung zur PVD-Abscheidung von Kupfer-Chrom-Oxid-Absorberschichten für solarthermische Turmkraftwerke
TU Dresden (Diplom), 23.01.2020

13. Zahn, F.
Performance dependence of GPU accelerated sparse linear system solvers on the finite element mesh structure in micromagnetic simulations
TU Dresden (B.Sc.), 06.11.2020

Awards and honors

1. **García Valenzuela, Aurelio**

   Postdoc at the department “Nanoelectronics” received the Premio Jóvenes Investigadores IUMA-2020 (**Young Researchers Award IUMA-2020**) for his work on “SiO_x by magnetron sputtered revisited: Tailoring the photonic properties of multilayers” as part of his PhD project, published in Applied Surface Science **488**, 791 – 800 (2019).

2. **Körber, Lukas**

   PhD student in the Emmy-Noether group “Magnonics” won the **Lohrmann-Medaille of TU Dresden** for “hervorragende Studienleistungen und besonderes gesellschaftliches Engagement auf Vorschlag des Studierendenrates“.

3. **Krasheninnikov, Arkady**

   Head of the group “Atomistic Simulations of Irradiation-induced Phenomena” was once again announced as **Highly Cited Researcher 2020** by Clarivate Analytics (Web of Science), Philadelphia, PA, USA.

4. **Kretschmer, Silvan**

   Former PhD student at the Ion Beam Center received the 2020 Microscopy & Microanalysis **Postdoctoral Scholar Award** for his presentation “Electron irradiation of two-dimensional MoS_2: insights into the influence of electronic excitations from first-principle calculations”.

5. **Makarov, Denys**

   Head of the department “Intelligent Materials and Systems” was admitted as a member of the **Young Academy of Europe** (YAE).

6. **Serralta, Eduardo**

   PhD student at the Ion Beam Center received a **Travel Grant** of the picoFIB network to visit the Luxembourg Institute of Science and Technology (LIST).

Invited conference contributions

1. Ghorbani Asl, M.
Defect engineering in two-dimensional materials: from fundamentals to applications
IV International Symposium Modern Materials Science, 17.11.2020, Moscow, Russia

2. Helm, M.; Fotev, I.; Balaghi, L.; Lang, D.; Rana, R.; Winnerl, S.; Schneider, H.; Dimakis, E.; Pashkin, A.
Nonlinear IR and THz Spectroscopy of Semiconductor Nanowires
45th International Conference on Infrared, Millimeter, and Terahertz Waves (IRMMW-THz 2020), 08. – 13.11.2020, Buffalo, USA

3. Hlawacek, G.; Barrahma, R.; Bouton, O.; Biesemeier, A.; Serralta Hurtado De Menezes, E.; Klingner, N.; de Castro, O.; Gnauck, P.; Lucas, F.; Duarte Pinto, S.; Wirtz, T.
A Focused Ion Beam based in-situ cryo high resolution instrument for multimodal analysis in nano-biology
IAEA Technical Meeting on Imaging Using Ionizing Radiation to Address Biological Challenges, 30.11. – 03.12.2020, Vienna, Austria

4. Makarov, D.
Curvilinear Magnetism: Fundamentals and Applications
The 2020 Magnetism and Magnetic Materials Conference, 04.11.2020, Palm Beach, USA

5. Makarov, D.
From shapeable magnetoelectronics to soft robotics with embedded magnetic cognition
2020 TMS Annual Meeting & Exhibition, Symposium: Advanced Magnetic Materials for Energy and Power Conversion Applications, 24.02.2020, San Diego, USA

6. Makarov, D.
Flexible magnetic field sensors
MSM2020: 15th International Conference Mechatronic Systems and Materials, 01.07.2020, Bialystok, Poland

7. Makarov, D.
Implantable Highly Compliant Devices for Heating of Internal Organs
International Conference on Advances in Biological Science and Technology (ICABST2020), 28.10.2020, Sanya, China

8. Makarov, D.
Overview of recent advances in flexible highly compliant magnetoelectronics
2020 IEEE Electron Devices Technology and Manufacturing Conference (EDTM), 06.04.2020, Penang, Malaysia

9. Sato, N.; Schultheiß, K.; Körber, L.; Puwenberg, N.; Mühl, T.; Awad, A.A.; Arekapudi, S.S.P.K.; Hellwig, O.; Faßbender, J.; Schultheiß, H.
Domain wall-based spin-Hall nano-oscillators
65th Annual Conference on Magnetism and Magnetic Materials (MMM 2020), 02. – 06.11.2020, Palm Beach, Florida (virtual), USA

10. Schneider, H.
Ion-implanted Ge photoconductive antennae for terahertz emission
Radiation Effects of Materials and Devices (REMD-2020), 12. – 15.01.2020, Harbin, China

11. Schneider, H.
THz nonlinear electronic response in GaAs/InGaAs semiconductor nanowires
Synchrotron and Free electron laser Radiation: generation and application (SFR-2020), 13. – 16.07.2020, Novosibirsk, Russian Federation

12. Singh, A.; Winnerl, S.; Welsch, M.; Beckh, C.; Sulzer, P.; Leitenstorfer, A.; Helm, M.; Schneider, H.
70 THz bandwidth from a Au-implanted Ge photoconductive emitter pumped by a modelocked Er:fibre laser
SPIE Optics + Photonics Digital Forum, 24. – 28.08.2020, San Diego, USA

13. Volkov, O.
Curvature-driven Chiral Effects in Nanomagnetism
MMM 2020 Virtual Conference, 02. – 06.11.2020, Palm Beach, Florida, USA

14. Zhou, S.
Ion implantation + sub-second annealing: a route towards hyperdoped semiconductors
6th International Virtual Conference on Ion Beams in Materials Engineering and Characterizations, 08. – 11.12.2020, New Delhi, India

15. Zhou, S.
Pushing the doping limit for future FETs
International Virtual School on Ion Beams in Materials Science, 01. – 05.12.2020, New Delhi, India

Conferences, workshops, colloquia and seminars

Organization of conferences and workshops

1. Inkson, B.; Hlawacek, G.
   Advances in Gas-ion Microscopy - the 3rd International Workshop of the PicoFIB Network
   20.01.2020, Sheffield, UK
2. Kotakoski, J.; Hlawacek, G.; Ovchinnikova, O.; Krasheninnikov, A.
   Microscopy & Microanalysis 2020, Symposium A10 Structural Changes in Hard, Soft, and Biological Samples During Imaging: From Transmission Electron to Helium Ion Microscopy
   03. – 07.08.2020, virtual event
3. Cuniberti, G.; Gemming, S.
   DCMS Materials 4.0 Summer School 2020: Materials Genome Engineering
   17. – 21.08.2020, virtual event
4. Cordoba, R.; Philipp, P.; Hlawacek, G.
   CMD2020GEFES (EPS), Mini-colloquium: Focused Ion Beam Induced Processing
   31.08. – 01.09.2020, virtual event
5. Erbe, A.; Zahn, P.
   NANONET Annual Workshop 2020
   07. – 09.10.2020, Altenberg, Germany

Colloquia

1. Kläui, M.
   Johannes Gutenberg-University Mainz, Germany
   Antiferromagnetic Insulatronics: Spintronics without magnetic fields and moving electrons
   17.12.2020
2. Koopmans, B.
   Eindhoven University of Technology, The Netherlands
   Femto-magnetism meets spintronics: Towards integrated magneto-photonics
   11.12.2020
3. Shiraishi, M.
   Kyoto University, Japan
   Spins in low-dimensional materials systems: Transport, gate-control and conversion
   13.03.2020

Seminars

1. Gliga, S.
   Swiss Light Source, Paul Scherrer Institut, Villigen, Switzerland
   Artificial spin ices: building blocks for functional materials
   19.02.2020
2. Katona, G.
   University of Debrecen, Department of Solid State Physics, Hungary
   Diffusion in thin films
   21.01.2020
3. Kotakoski, J.
   Vienna University of Technology, Austria
   Atomic-scale study and engineering of low-dimensional materials
   14.01.2020

4. Kronast, F.
Helmholtz-Zentrum Berlin für Materialien und Energie, Berlin, Germany
Spatially resolved investigation of all-optical magnetization switching
09.10.2020

5. Ogawa, S.
Nano-electronics Research Institute, AIST, Japan
Applications of the helium ion microscopy to graphene nano-patterning and cell observation
23.01.2020

6. Pantazopoulos, P.-A.
National and Kapodistrian University of Athens, Greece
Controlling light with static and dynamic magnetization fields
11.03.2020

7. Ronning, C.
Friedrich-Schiller-Universität Jena, Germany
Ion beam designed metasurfaces
11.03.2020

8. Vladymyrskyi, I.
National Technical University of Ukraine “Igor Sikorsky Kyiv Polytechnic Institute”, Metals Physics Department
Structural phase transitions in Pt/Fe-based layer stacks
23.01.2020

Projects

The projects are listed by funding institution and project starting date. In addition, the institute has several bilateral service collaborations with industrial partners and research institutions. These activities are not included in the following overview.

European Projects

1. 02/2016 – 10/2020 European Union EU
IONS4SET – Single Electron Transistor
Dr. J. v. Borany Phone: 0351 260 3378 j.v.borany@hzdr.de

2. 01/2017 – 09/2021 European Union EU
TRANSPIRE –Terahertz Radio Communication
Dr. A. Deac Phone: 0351 260 3709 a.deac@hzdr.de

3. 01/2017 – 06/2021 European Union EU
npSCOPE – Nanoparticle Characterization
Dr. G. Hlawacek Phone: 0351 260 3409 g.hlawacek@hzdr.de

4. 05/2017 – 10/2021 European Union EU
CALIPSOplus – Coordinated Access to Lightsources
Prof. M. Helm Phone: 0351 260 2260 m.helm@hzdr.de

5. 01/2019 – 12/2022 European Union EU
RADIATE – Research And Development with Ion Beams - Advancing Technology in Europe
Prof. J. Fassbender Phone: 0351 260 3096 j.fassbender@hzdr.de

6. 10/2020 – 09/2023 European Union EU
BIONANOSENS – Deeping collaboration on novel biomolecular electronics based on "smart" nanomaterials
Dr. D. Makarov Phone: 0351 260 3273 d.makarov@hzdr.de

7. 11/2020 – 10/2021 European Union EU
FIT4NANO – Focused Ion Technology for Nanomaterials
Dr. G. Hlawacek Phone: 0351 260 3409 g.hlawacek@hzdr.de

8. 11/2020 – 10/2024 European Union EU
RADICAL – Fundamental Breakthrough in Detection of Atmospheric Free Radicals
Dr. Y. Georgiev Phone: 0351 260 2321 y.georgiev@hzdr.de

9. 10/2020 – 09/2023 NATO NATO
natoMYP – Spintronic Devices for Microwave Detection and Energy Harvesting Applications
Dr. D. Makarov Phone: 0351 260 3273 d.makarov@hzdr.de

Helmholtz Association Projects

1. 10/2012 – 12/2020 Helmholtz-Gemeinschaft HGF
NANONET – International Helmholtz Research School on Nanoelectronics
Dr. A. Erbe Phone: 0351 260 2366 a.erbe@hzdr.de

2. 10/2017 – 12/2020 Helmholtz-Gemeinschaft HGF
Helmholtz Exzellenznetzwerk – cfaed 2 + 3
Dr. A. Erbe Phone: 0351 260 2366 a.erbe@hzdr.de

3. 10/2017 – 02/2020 Helmholtz-Gemeinschaft HGF
Helmholtz ERC Recognition Award
Dr. H. Schultheiß Phone: 0351 260 3243 h.schultheiss@hzdr.de

4. 01/2019 – 12/2020 Helmholtz-Gemeinschaft HGF
Helmholtz Exzellenznetzwerk – DCM-MatDNA Phase 3
Prof. S. Gemming Phone: 0351 260 2470 s.gemming@hzdr.de

5. 01/2019 – 12/2021 Helmholtz-Gemeinschaft HGF
CROSSING – Crossing borders and scales - an interdisciplinary approach
Dr. J. v. Borany Phone: 0351 260 3378 j.v.borany@hzdr.de

6. 02/2019 – 06/2020 Helmholtz-Gemeinschaft HGF
Helmholtz Enterprise – Tensormeter
Dr. T. Kosub Phone: 0351 260 2900 t.kosub@hzdr.de

7. 07/2019 – 12/2020 Helmholtz-Gemeinschaft HGF
Helmholtz Enterprise Plus – Tensormeter
Dr. T. Kosub Phone: 0351 260 2900 t.kosub@hzdr.de

8. 12/2019 – 11/2024 Helmholtz-Gemeinschaft HGF
Helmholtz Innovation Lab – FlexiSens
Dr. D. Makarov Phone: 0351 260 3273 d.makarov@hzdr.de

9. 02/2020 – 01/2025 Helmholtz-Gemeinschaft HGF
Helmholtz Innovation Lab – UltraTherm
Dr. L. Rebohle Phone: 0351 260 3368 l.rebohle@hzdr.de

German Science Foundation Projects

1. 05/2014 – 08/2021 Deutsche Forschungsgemeinschaft DFG
Emmy Noether Junior Research Group – Magnonics
Dr. H. Schultheiß Phone: 0351 260 3243 h.schultheiss@hzdr.de

2. 03/2017 – 08/2020 Deutsche Forschungsgemeinschaft DFG
MUMAGI – Disorder induced magnetism
Dr. R. Bali Phone: 0351 260 2919 r.bali@hzdr.de

3. 07/2017 – 11/2020 Deutsche Forschungsgemeinschaft DFG
HELEX2D – Interaction of highly charged ions with 2D materials
Dr. R. Wilhelm Phone: 0351 260 3378 r.wilhelm@hzdr.de

4. 08/2017 – 07/2020 Deutsche Forschungsgemeinschaft DFG
FlexCom – Magnetic field sensitive flexible communication system
Dr. D. Makarov Phone: 0351 260 3273 d.makarov@hzdr.de

5. 09/2017 – 11/2020 Deutsche Forschungsgemeinschaft DFG
Lane Formation
Dr. A. Erbe Phone: 0351 260 2366 a.erbe@hzdr.de

6. 11/2017 – 07/2021 Deutsche Forschungsgemeinschaft DFG
ULTRACRITICAL – High-temperature superconductors
Dr. A. Pashkin Phone: 0351 260 3287 o.pashkin@hzdr.de

7. 04/2018 – 06/2021 Deutsche Forschungsgemeinschaft DFG
Confined Microswimmers
Dr. A. Erbe Phone: 0351 260 2366 a.erbe@hzdr.de

8. 04/2018 – 02/2022 Deutsche Forschungsgemeinschaft DFG
IMASTE – Graphene encapsulated quasi-2D materials
Dr. A. Krasheninnikov Phone: 0351 260 3148 a.krasheninnikov@hzdr.de

9. 10/2018 – 07/2021 Deutsche Forschungsgemeinschaft DFG
Doping by ALD and FLA
Dr. L. Rebohle Phone: 0351 260 3368 l.rebohle@hzdr.de

10. 01/2019 – 07/2021 Deutsche Forschungsgemeinschaft DFG
Quantum control of single spin centers in silicon carbide coupled to optical microcavities
Dr. G. Astakhov Phone: 0351 260 3894 g.astakhov@hzdr.de

11. 01/2019 – 01/2022 Deutsche Forschungsgemeinschaft DFG
Printable giant magnetoresistive sensors with high sensitivity at small magnetic fields
Dr. D. Makarov Phone: 0351 260 3273 d.makarov@hzdr.de

12. 06/2019 – 06/2022 Deutsche Forschungsgemeinschaft DFG
Interacting Magnonic Currents and Chiral Spin Textures for Energy Efficient Spintronics
Dr. H. Schultheiß Phone: 0351 260 3243 h.schultheiss@hzdr.de

13. 07/2019 – 06/2022 Deutsche Forschungsgemeinschaft DFG
3D tailoring of all-oxide heterostructures by ion beams
Dr. S. *Zhou Phone: 0351 260 2484 s.zhou@hzdr.de*

14. 07/2019 – 06/2022 Deutsche Forschungsgemeinschaft DFG
Lab-on-chip Systems Carrying Artificial Motors for Multiplexed and Multiparametric Biochemical Assays
Dr. D. Makarov Phone: 0351 260 3273 d.makarov@hzdr.de

15. 10/2019 – 11/2022 Deutsche Forschungsgemeinschaft DFG
3D transport of spin waves in curved nano-membranes
Dr. A. Kakay Phone: +49 351 260 2689 a.kakay@hzdr.de

16. 11/2019 – 10/2022 Deutsche Forschungsgemeinschaft DFG
Functionalization of Ultrathin MoS_2 by Defect Engineering
Dr. A. Krasheninnikov Phone: 0351 260 3148 a.krasheninnikov@hzdr.de

17. 02/2020 – 01/2023 Deutsche Forschungsgemeinschaft DFG
TRIGUS - Friction-induced interface and structure-changing processes in dry lubrication systems under defined atmospheres
Dr. M. Krause Phone: 0351 260 3578 matthias.krause@hzdr.de

18. 04/2020 – 04/2023 Deutsche Forschungsgemeinschaft DFG
CurvMag – Non-Local Chiral Interactions In Corrugated Magnetic Nanoshells
Dr. D. Makarov Phone: 0351 260 3273 d.makarov@hzdr.de

19. 07/2020 – 06/2024 Deutsche Forschungsgemeinschaft DFG
SFB 1415 – "Chemistry of Synthetic Two-Dimensional Materials"
Dr. A. Krasheninnikov Phone: 0351 260 3148 a.krasheninnikov@hzdr.de

20. 08/2020 – 07/2023 Deutsche Forschungsgemeinschaft DFG
AMSIGE – Topological order and its correlation to self-atom transport in amorphous materials:silicon and germanium as model systems
Dr. M. Posselt Phone: 0351 260 3279 m.posselt@hzdr.de

21. 09/2020 – 08/2023 Deutsche Forschungsgemeinschaft DFG
3Dmag – Krümmungsinduzierte Effekte in magnetischen Nanostrukturen
Dr. D. Makarov Phone: 0351 260 3273 d.makarov@hzdr.de

22. 11/2020 – 10/2023 Deutsche Forschungsgemeinschaft DFG
miracuSi – Room-temperature broadband MIR photodetector based on Si:Te for wafer-scale integration
Dr. M. Wang Phone: 0351 260 2833 m.wang@hzdr.de

23. 11/2020 – 10/2023 Deutsche Forschungsgemeinschaft DFG
eSensus – Compliant and breathable magnetoelectronics: towards electronic proprioception
Dr. D. Makarov Phone: 0351 260 3273 d.makarov@hzdr.de

24. 11/2020 – 10/2023 Deutsche Forschungsgemeinschaft DFG
TOPCURVE – Curvature-induced Effects in Magnetic Nanostructures
Dr. A. Kakay Phone: +49 351 260 2689 a.kakay@hzdr.de

25. 12/2020 – 11/2023 Deutsche Forschungsgemeinschaft DFG
MUMAGI II – Microscopic understanding of disorder induced ferromagnetism in B2-alloy thin films II
Dr. R. Bali Phone: 0351 260 2919 r.bali@hzdr.de

Federally and Saxony State Funded Projects

1. 01/2018 – 10/2020 DECHEMA e.V. DECHEMA
High temperature oxidation resistance for nickel-based alloys by fluorine implantation
Dr. W. Skorupa Phone: 0351 260 3612 w.skorupa@hzdr.de
2. 11/2018 – 10/2021 Bundesministerium für Bildung und Forschung BMBF
Metal-germanium interface: Schottky barrier and ohmic contacts
Dr. S. Prucnal Phone: 0351 260 2065 s.prucnal@hzdr.de
3. 03/2019 – 03/2021 Arbeitsgemeinschaft industrielle Forschung AiF
Improvement of the dynamic properties of GaAs power diodes by proton irradiation
Dr. J. v. Borany Phone: 0351 260 3378 j.v.borany@hzdr.de
4. 03/2019 – 09/2020 Bundesministerium für Wirtschaft und Energie BMWi
Electrostatically functionalized materials with bio-sensitive adsorption properties
Dr. L. Rebohle Phone: 0351 260 3368 l.rebohle@hzdr.de
5. 05/2019 – 02/2021 Bundesministerium für Wirtschaft und Energie BMWi
Magnetoelectrical detector
Dr. D. Makarov Phone: 0351 260 3273 d.makarov@hzdr.de
6. 07/2019 – 01/2022 Sächsische Aufbaubank SAB
Innovative product platform for space-based Global Navigation Satellite Systems (GNSS)
Dr. J. v. Borany Phone: 0351 260 3378 j.v.borany@hzdr.de
7. 10/2019 – 09/2023 Bundesministerium für Bildung und Forschung BMBF
Group IV-heterostructures for most advanced nanoelectronics devices
Dr. Y. Georgiev Phone: 0351 260 2321 y.georgiev@hzdr.de
Dr. S. Prucnal Phone: 0351 260 2065 s.prucnal@hzdr.de
8. 10/2019 – 09/2023 Bundesministerium für Bildung und Forschung BMBF
Black phosphorus in sensitive, selective and stable sensors
Dr. A. Erbe Phone: 0351 260 2366 a.erbe@hzdr.de
9. 06/2020 – 05/2022 EFDS e.V. EFDS
Novel Eddy current sensors based on flexible GMR sensor arrays for the analysis of components of complex shape
Dr. D. Makarov Phone: 0351 260 3273 d.makarov@hzdr.de
10. 03/2020 – 02/2022 Arbeitsgemeinschaft industrielle Forschung AiF
Magnetic Nanostructures
Dr. L. Bischoff Phone: 0351 260 2866 l.bischoff@hzdr.de
11. 10/2020 – 09/2023 Bundesministerium für Wirtschaft und Energie BMWi
RoSiLIB – Nanoporous Si anodes of lithium ion batteries by microdroplet quenching
Dr. K.-H. Heinig Phone: 0351 260 3288 k.h.heinig@hzdr.de
12. 12/2020 – 01/2022 Sächsische Aufbaubank SAB
NanoNeuroNet – Nanostructures for Neural Networks
Dr. A. Erbe Phone: 0351 260 2366 a.erbe@hzdr.de

Personnel Exchange Projects and Society Chairs

1. 05/2017 – 12/2022 Institute of Electrical and Electronics Engineers IEEE
   Magnetics Society German Chapter Chair
   Dr. H. Schultheiß Phone: 0351 260 3243 h.schultheiss@hzdr.de
2. 07/2017 – 12/2021 Alexander-von-Humboldt-Stiftung AvH
   Humboldt fellowship Prof. Sheka
   Dr. D. Makarov Phone: 0351 260 3273 d.makarov@hzdr.de
3. 04/2018 – 03/2020 Deutscher Akademischer Austauschdienst DAAD
   ULTIMAT – Superlattices of ultra-thin $In_xGa_{1-x}N$/GaN quantum wells
   Dr. E. Dimakis Phone: 0351 260 2765 e.dimakis@hzdr.de
4. 11/2019 – 02/2020 Deutscher Akademischer Austauschdienst DAAD
   Visit Karen Lizbeth Cardos Tisnado
   Dr. A. Erbe Phone: 0351 260 2366 a.erbe@hzdr.de
5. 10/2020 – 09/2021 Alexander-von-Humboldt-Stiftung AvH
   Feodor Lynen Return Grant for Dr. Rico Friedrich
   Dr. A. Krasheninnikov Phone: 0351 260 3148 a.krasheninnikov@hzdr.de

Organization chart

Institute of Ion Beam Physics and Materials Research

Prof. Dr. Jürgen Faßbender *Prof. Dr. Manfred Helm*

Ion Beam Center
Dr. Stefan Facsko, Dr. René Heller

- **Ion Accelerators** *Dr. Shavkat Akhmadaliev*
- **Ion Implantation and Modification of Materials** *Ulrich Kentsch*
- **Ion Beam Analysis** *Dr. René Heller*
- **Ion Induced Nanostructures** *Dr. Gregor Hlawacek*
- **Structural Analysis** *Dr. René Hübner*
- **Atomistic Simulations** *Dr. Arkady Krasheninnikov*

Magnetism
Dr. Jürgen Lindner

- **Micromagnetic Modeling** *Dr. Attila Kákay*
- **Magnonics** *Dr. Helmut Schultheiß*

Intelligent Materials and Systems
Dr. Denys Makarov

- **Intelligent Materials and Systems** *Dr. Denys Makarov*

Accelerator Mass Spectrometry
Prof. Dr. Anton Wallner

- **AMS** *Prof. Dr. Anton Wallner*

Nanoelectronics
Dr. Artur Erbe

- **Nanomaterials and Transport** *Dr. Artur Erbe, Dr. Matthias Krause*
- **Nanofabrication and Analysis** *Dr. Ciaran Fowley, Dr. Yordan Georgiev*

Semiconductor Materials
Dr. Shengqiang Zhou

- **Semiconductor Materials** *Dr. Shengqiang Zhou*
- **Quantum Materials and Technology** *Dr. Georgy Astakhov*

Spectroscopy
Dr. Harald Schneider

- **Spectroscopy** *Dr. Harald Schneider*

International Helmholtz Research School for Nanoelectronic Networks (IHRS NANONET)

Speaker: Dr. Artur Erbe | Teaching Director: Dr. Peter Zahn

List of personnel 2020

DIRECTORS	OFFICE
Prof. Dr. M. Helm, Prof. Dr. J. Faßbender	S. Gebel, S. Kirch

SCIENTIFIC STAFF

Permanent staff

Dr. C. Akhmadaliev
Dr. G. Astakhov
Dr. L. Bischoff
Dr. J. von Borany
Dr. A. Deac
Dr. E. Dimakis
Dr. A. Erbe
Dr. S. Facsko
Dr. C. Fowley
Prof. Dr. S. Gemming
Dr. Y. Georgiev
Dr. J. Grenzer
Dr. R. Heller
Dr. G. Hlawacek
Dr. R. Hübner
Dr. A. Kákay
Dr. A. Krasheninnikov
Dr. M. Krause
Dr. J. Lachner
Dr. K. Lenz
Dr. J. Lindner
Dr. D. Makarov
Dr. S. Merchel
Dr. F. Munnik
Dr. A. Pashkin
Dr. M. Posselt
Dr. K. Potzger
Dr. S. Prucnal
Dr. L. Rebohle
Dr. G. Rugel
Dr. H. Schneider
Prof. Dr. A. Wallner
Dr. S. Winnerl
Dr. P. Zahn
Dr. S. Zhou

Non-permanent

Dr. H. Arora (P)
Dr. R. Bali
Dr. Y. Berencén
Dr. D. Blaschke (P)
Dr. G. S. Canon Bermudez
Dr. H. Cansever (P)
Dr. C. Cherkouk (P)
Dr. A. Eichler-Volf (P)
Dr. H.-J. Engelmann (P)
Dr. D. Erb
Dr. C. Folgner (P)
Dr. R. Friedrich (P)
Dr. A. Froideval (P)
Dr. A. Garcia Valenzuela (P)
Dr. M. Ghorbani Asl
Dr. O. Gladii (P)
Dr. F. Goncalves (P)
Dr. M. Grobosch (P)
Dr. M. Ha (P)
Dr. C. Habenicht (P)
Dr. K.-H. Heinig (P)
Prof. Dr. O. Hellwig
Dr. V. Iurchuk (P)
R. Kaltofen (P)
Dr. N. Klingner (P)
Dr. S. Kretschmer (P)
Dr. T. Kosub
Dr. C. Lei (P)
Dr. A. Lindner (P)
Prof. Dr. W. Möller (P)
Dr. I. Mönch (P)
Dr. J.P. Navarro
Dr. R. Podlipec (P)
Dr. O. Pylypovskyi
Dr. R. Rana
Dr. R. Salikhov
Dr. H. Schultheiß
Dr. K. Schultheiß (P)
Dr. J. Schütt (P)
Dr. A. Singh
Dr. W. Skorupa (P)
Dr. S. Stienen
Dr. A. Titova
Dr. T.T. Trinh
Dr. I. Veremchuk
Dr. O. Volkov (P)
Dr. C. Wagner
Dr. M. Wang
Dr. R. Wilhelm
Dr. R. Yankov

(P) Projects

TECHNICAL STAFF

Permanent staff

Rb. Aniol
Rm. Aniol
E. Christalle
S. Eisenwinder
H. Gude
J. Heinze
A. Henschke
H. Hilliges
Dr. R. Illing
U. Kentsch
S. Klare
J. Kreher
A. Kunz
K. Lang
H. Lange
U. Lucchesi
F. Ludewig
R. Mester
Dr. R. Narkovic
C. Neisser
F. Nierobisch
T. Putzke
A. Reichel
B. Scheumann
G. Schnabel
A. Schneider
A. Scholz
T. Schönherr
T. Schumann
I. Skorupa
M. Steinert
A. Thiel
T. Voitsekhivska
J. Wagner
A. Weise
A. Weißig
J. Winkelmann
R. Ziegenrücker
L. Zimmermann
J. Zscharschuch

Non-permanent

A. Berens (P)
T. Döring (P)
M. Görlich
R. Krause
S. Krüger (P)
A. Legrand
T. Naumann
L. Ramasubramanian (P)
C. Schubert (P)
J. Schulz
T. Tarnow

(P) Projects

PhD STUDENTS

Y. Alsaadawi
T. Bayrak
V. Begeza
M. Bejarano
P. Chava
S. Creutzburg
J. Duan
A. Echresh
Z. Fekri
I. Fotev
S. Ghaderzadeh
S. Ghosh
T. Hache
D. Hilliard
M. Hollenbach
T. Hula
S. Jazavandi Ghamsari
T. Joseph
M. B. Khan
M. M. Khan
F. Kilibarda
L. Körber
Zi. Li
A. Luferau
P. Makushko
E.S. Oliveros Mata
F. Samad
A. Schmeink
R. de Schulz
A. Seidl
E. Serralta Hurtado
M.S. Shaikh
Z. Shang
S. Sorokin
O. Steuer
A. Strobel
D. Tucholski
M. Vallinayagam
T. Venanzi
C. Wang
X. Wang
Y. Wei
Y. Xie
X. Xu
N. Yuan

STUDENTS (Diploma / MSc / BSc)

Y. Gao
M. Hoppe
N. Hozaien
N. Jagtap
A. Jain
F. Moebus
A. Oelschlägel
G. Quasebarth
T. Seidel
D. Sharma
P. Singh
J. Sonnenberg
S. Stierle
J. Vekariya
F. Zahn

Wissenschaftlich-Technische Berichte
HZDR-112 | 2021 | ISSN 2191-8708

HELMHOLTZ ZENTRUM
DRESDEN ROSSENDORF

Institute of Ion Beam Physics and Materials Research
Bautzner Landstrasse 400
01328 Dresden/Germany
Phone +49 351 260-2345
Fax +49 351 260-3285
https://www.hzdr.de

Member of the Helmholtz Association